



HAL
open science

On the design of a new test method to characterize the delamination of thermosetting polymer under thermal mixed mode loading

Lucas Durix

► **To cite this version:**

Lucas Durix. On the design of a new test method to characterize the delamination of thermosetting polymer under thermal mixed mode loading. Engineering Sciences [physics]. Université de Valenciennes et du Hainaut-Cambrésis, 2010. English. NNT: . tel-03071730

HAL Id: tel-03071730

<https://uphf.hal.science/tel-03071730>

Submitted on 16 Dec 2020

HAL is a multi-disciplinary open access archive for the deposit and dissemination of scientific research documents, whether they are published or not. The documents may come from teaching and research institutions in France or abroad, or from public or private research centers.

L'archive ouverte pluridisciplinaire **HAL**, est destinée au dépôt et à la diffusion de documents scientifiques de niveau recherche, publiés ou non, émanant des établissements d'enseignement et de recherche français ou étrangers, des laboratoires publics ou privés.



THESE DE DOCTORAT PRESENTÉE À L'UNIVERSITÉ DE
VALENCIENNES ET DU HAINAUT CAMBRESIS

EN VUE DE L'OBTENTION D'UN DOCTORAT EN GÉNIE
MÉCANIQUE

ON THE DESIGN OF A NEW TEST METHOD TO CHARACTERIZE THE DELAMINATION OF THERMOSETTING POLYMER UNDER THERMAL MIXED MODE LOADING

**Conception d'un nouveau protocole experimental pour la
caractérisation du délaminage des polymères thermodurcissables
sous chargement thermique en mode mixte**

Soutenance le 20/12/2010

- Version préliminaire -

Par

Lucas Durix





LAMIH
LABORATOIRE
D'AUTOMATIQUE
DE MECANIQUE ET
D'INFORMATIQUE
INDUSTRIELLES
ET HUMAINES



Laboratoire d'Automatique, de Mécanique et d'Informatique Industrielles et Humaines
FRE CNRS 3304
Université de Valenciennes et du Hainaut-Cambrésis
Le Mont-Houy
59313 Valenciennes Cedex 9
FRANCE



AND

Invented for life



BOSCH

Robert Bosch GmbH
Corporate Sector Research and Advance Engineering
Advance Production Technology 1
Plastic Engineering

Postfach 1131
71301 Waiblingen
GERMANY



ACKNOWLEDGMENT

I would like to address my very special thanks to the people who help me to success during these last four years:

Dr. Marc Dreßler (Bosch CR/APP2) for the every day valuable support and substantial help in my professional life, but also in my private life,

Dr. Kurt Hornberger (Bosch CR/APP2) for the opportunity he gave me to join the Group Bosch and to realize this PhD work,

Prof. Daniel Coutellier (Université Valenciennes), for having guided me from my master thesis to the accomplishment of this PhD work,

Dr. Markus Andre for the valuable explanation concerning FEM simulations involving viscoelastic materials,

Ulrich Schaaf, Frieder Sundermeier, Andreas Kugler, Ruben Wahl, Kai Von Garnier (Bosch CR/APP4) for the valuable help and machines they left at my disposal to realize all tests described in this document, and Dr. Metin Koyuncu for quantities of molding compound furnished for the tests,

Julien Roger (Bosch CR/ARU), for the precious tricks to success in my every day life when I came to Germany,

Bernd Weber (Bosch AE/EVR), for borrowing flow measuring devices, expected to characterize the convection in a thermal shock chamber, which broke down because of thermal shocks...,

Mohamed Hossein Shirangi (Mahle-Bosch joint venture), for the valuable advice and sympathy,

Gert Schlottig (Fraunhofer IZM Berlin, Infineon Technologies AG.) for the time he spent reviewing my publications,

Alain Lecocq (Université Valenciennes), one of the significant men I met in my life, who placed my life on the rail I followed until there,

...and all people who help me in different ways, my parents, friends in Stuttgart who introduced me in particular to a now very important person, the Fraunhofer IZM colleagues for their friendly greeting and Bosch colleagues for their unconditional sympathy and assistance.

ABSTRACT

Crack propagation in integrated circuits is a major failure cause of electronic components. In the automotive branch, a highly competitive market, failure is not allowed and reliability can make the difference to gain market shares. For this reason, many efforts and researches were conducted in this field during the last decades.

In automotive applications, electronic parts have to challenge heavy life conditions, such as vibrations, wide temperature variations, humidity, oil aggressions, etc. In particular, cyclic thermal variations bring incompatible thermal strains along materials interfaces, and leads to interfacial crack propagation (delamination) between copper leadframes used as conductor and polymeric molding compound used to encapsulate devices. Delamination causes then the cracking of the encapsulant and finally the failure of the electronic component.

Predicting the interfacial delamination in electronic packages is key to enhance reliability.

As detailed in this work, delamination strength of interfaces involving molding compounds depends on many influences. Its characterization required numerous kinds of test, involving heavy costs and long testing periods. In this work, a low cost test setup is proposed to characterize the molding compound/copper interface regarding the different influences already mentioned.

The delamination toughness of the copper/polymeric molding compound is characterized with a classic molding compound of the market with respect to the mode mixity (ratio of loading mode II/mode I), temperature, and load rate. Moisture effect is also investigated. The critical energy release rate for the investigated interface is estimated using the classical numerical-experimental correlation used in fracture mechanics. For the investigated material pair, the interfacial toughness exhibits viscoelastic properties and an own time-temperature superposition principle.

Obtained interfacial parameters are defined in Abaqus. The latter is widely benchmarked for problems involving delamination and viscoelastic materials.

In the case of cracking between two dissimilar materials, the analytical solution of the stress and strain fields at delamination front depends on a characteristic reference length. The choice of this reference length, conditioning the the mode mixity estimation, is also addressed. The reference length is experimentally characterized for the different investigated temperature.

RÉSUMÉ

La propagation des fissures dans les circuits intégrés est l'une des causes principales de défaillance de ces circuits. Sur le marché automobile fortement concurrentiel, les défaillances ne sont pas permises, et la fiabilité demeure un critère pouvant faire la différence pour gagner des parts de marché. Pour cette raison, de nombreux efforts et recherches ont vu le jour durant les dernières décennies.

Dans le cas des applications liées à l'automobile, les composants électroniques sont confrontés à de lourdes contraintes, telles que vibrations, importants changements de température, projections d'eau ou de dérivés pétroliers, etc.

Les variations de température génèrent en particulier des déformations thermiques souvent incompatibles au niveau des interfaces entre matériaux, ce qui provoque dans les circuits intégrés le décollement des conducteurs cuivrés de l'enrobage polymérique utilisé pour la protection du composant (délaminage). Le délaminage aboutit par la suite à la fissuration propre de l'encapsulant puis à la défaillance du composant.

L'amélioration de la fiabilité des composants requiert par conséquent de pouvoir prédire le délaminage aux interfaces cuivre/matériau d'encapsulation.

Tel que démontré dans ces travaux, la ténacité interfaciale dépend de plusieurs influences. Une caractérisation complète requiert de nombreux tests, mettant en jeu différents types d'appareillages et d'éprouvettes, ce qui génère de nombreux coûts et un temps d'exécution important. Une méthode de test à faible coût est proposée dans ce document pour la caractérisation des interfaces cuivre/encapsulant dans les différentes conditions évoquées. Cette méthode a été mise en pratique avec succès pour caractériser un matériau d'encapsulation classiquement utilisé dans l'industrie automobile. L'influence de la mixité des modes de rupture, de la température, de la vitesse de chargement ainsi que de l'humidité ont été étudiées. Les techniques habituelles en mécanique de la rupture de corrélation résultats expérimentaux-simulations ont été utilisées pour déterminer le taux de restitution d'énergie critique dans les différents cas. La ténacité de l'interface cuivre/matériau d'encapsulation s'est révélée suivre un comportement viscoélastique, incluant des propriétés propres de superposition temps-température.

Les paramètres interfaciaux obtenus ont finalement été définis dans l'outil de simulation MEF Abaqus. Ce dernier a d'ailleurs été l'objet de nombreuses vérifications en ce qui concerne la simulation des problèmes de délaminage des matériaux viscoélastiques.

Dans le cas de la fissuration entre deux matériaux hétérogènes, la description analytique des champs de contrainte et de déformation en pointe de fissure fait appel à une longueur de référence. Le choix de cette longueur de référence est abordé dans ce document. Cette dernière est déterminée expérimentalement pour les différentes températures testées.

TABLE OF CONTENT

I. GENERAL CONTEXT	1
I.1 INTRODUCTION	1
I.2 APPROACH IN THIS WORK	2
II. THEORETICAL BACKGROUND	4
II.1 FRACTURE MECHANICS	4
II.2 CRACK INITIATION	5
II.3 STRESS INTENSITY – BASED FRACTURE CRITERION	7
II.3.1 CRACKS IN HOMOGENEOUS MEDIA	7
II.3.1.1 Definition	7
II.3.1.2 Criterion of Crack Propagation	8
II.3.2 STRESS INTENSITY FACTOR FOR INTERFACIAL CRACKS	8
II.3.3 DISPLACEMENT FIELD AHEAD CRACK TIP	10
II.4 ENERGY-BASED FRACTURE CRITERION	12
II.4.1 ENERGY RELEASE RATE FOR ISOTROPIC CASES	12
II.4.2 VIRTUAL CRACK CLOSURE TECHNIQUE	13
II.4.3 VCCT DISCRETIZATION FOR FINITE ELEMENT ANALYSIS	15
II.4.4 ENERGY RELEASE RATE FROM OSCILLATORY STRESS INTENSITY FACTOR	15
II.5 MODE MIXITY AT CRACK TIP	17
II.5.1 OSCILLATORY SIF-BASED PHASE ANGLE ESTIMATION	17
II.5.2 EXTENDED SIF-BASED MIXED-MODE ANGLE ESTIMATION METHOD	18
II.5.3 NON-OSCILLATORY ERR-BASED MIXED MODE SEPARATION	19
II.5.4 OSCILLATORY ERR-BASED MIXED MODE SEPARATION METHOD	19
II.5.5 PHASE ANGLE ESTIMATION FROM VCCT AND SIF	21
II.5.6 DISCUSSING ABOUT THE CHOICE OF A METHOD	23
II.6 TEMPERATURE AND STRAIN RATE EFFECTS ON CRACK TIP FIELD	24
II.6.1 PHENOMENOLOGICAL DESCRIPTION	25
II.6.2 MATERIAL CONSTITUTIVE LAWS FOR LINEAR VISCOELASTICITY	26
II.6.2.1 Kelvin-Voigt Spring-dashpot-model	27
II.6.2.2 Maxwell spring-dashpot-model	28
II.6.2.3 Generalized Maxwell-model	28
II.6.2.4 Generalized Kelvin-Voigt-model	30
II.6.2.5 Material Response to Sinusoidal Excitations	31
II.6.3 TIME-TEMPERATURE CORRESPONDENCE	33
II.6.3.1 Time-Temperature Superposition Principle	33
II.6.3.2 Shift Function	34
II.6.3.3 Poisson’s Ratio	35
II.6.4 USING LINEAR ELASTIC FRACTURE MECHANICS WITH TIME-DEPENDENT MATERIALS	36
II.7 MOISTURE INFLUENCE ON ADHESION STRENGTH	36
III. NUMERICAL BACKGROUND	37
III.1 VCCT IMPLEMENTATION IN ABAQUS	37
III.1.1 GENERAL FEM METHODOLOGY	37
III.1.2 ABAQUS 6.8 VCCT IMPLEMENTATION	37
III.1.3 CONTACT INTERACTION: BACKGROUND OF VCCT IMPLEMENTATION	38

III.1.3.1	Contact Discretization	38
III.1.3.2	Contact Tracking	40
III.1.3.3	Contact Enforcement	40
III.1.4	APPARENT IMPLEMENTATION OF THE ABAQUS VCCT	41
III.2	CRACK PROPAGATION ANALYSIS WITH ABAQUS	43
III.2.1	PRINCIPLE	43
III.2.2	THE BK-LAW	43
III.2.3	REEDER AND POWER LAWS	45
III.3	NUMERICAL VERIFICATION	46
III.3.1	CONTACT INTERACTION INFLUENCE ON THE NEAR-STRESS-FIELD	46
III.3.2	MESH REFINEMENT AND CONVERGENCE CONDITION	47
III.3.3	VCCT VS. J-INTEGRAL AND ANALYTICAL SOLUTION	49
III.3.4	RENDERING OF LINEAR VISCOELASTIC PROPERTIES	50
IV.	INTERFACIAL DELAMINATION TOUGHNESS CHARACTERIZATION	53
IV.1	PREEXISTING TEST SETUPS	53
IV.2	APPROACH	53
IV.3	THE TRIANGLE BUTTON SHEAR SPECIMEN	55
IV.3.1	CONCEPT	55
IV.3.2	SPECIMEN FABRICATION	56
IV.3.3	CRACK INITIATION	56
IV.4	EXPERIMENTAL PROCEDURE FOR TESTING AT ROOM TEMPERATURE	57
IV.4.1	TEST EQUIPMENT	57
IV.4.2	CLAMPING AND SHEARING TOOL	58
IV.4.3	SHEARING TOOL/SPECIMEN FRICTION COEFFICIENT	58
IV.4.4	CRACK LENGTH MEASUREMENT	59
IV.4.5	FRACTURE PATTERN ANALYZE	61
IV.4.5.1	Verification of the Cohesive Crack Propagation Hypothesis	61
IV.4.5.2	Afterwards-Measurement of the initial Delamination Length	62
IV.5	MATERIAL CHARACTERIZATION	63
IV.5.1	EMC TENSILE MODULUS	63
IV.5.2	POISSON'S RATIO CHARACTERIZATION	64
IV.5.3	COPPER LEADFRAME	66
IV.6	NUMERICAL MODELING	67
IV.6.1	BOUNDARY CONDITIONS	67
IV.6.2	SHEARING TOOL	67
IV.6.3	ELEMENTS	67
IV.6.4	CRACK MODELING	67
IV.6.5	MESH TECHNIQUE	68
IV.6.6	MATERIAL MODELING	69
IV.6.7	RESIDUAL AND THERMAL STRESS ESTIMATION	69
IV.6.8	RESIDUAL AND THERMAL STRESS IMPLEMENTATION	71
IV.7	NUMERICAL RESULTS	72
IV.7.1	LOADING CONDITIONS ALONG THE DELAMINATION FRONT	72
IV.7.2	FROM SHEARING HEIGHT TO MODE MIXITY	73
IV.7.3	MIXED MODE RATIO	74
IV.7.3.1	General Trend	74
IV.7.3.2	Maximum reachable Mode II Amount	75
IV.7.3.3	Negative Mode II Loading	76
IV.7.4	PHASE ANGLE (FROM SIF) AND ERR RATIO	77
IV.7.5	ENERGY RELEASE RATE AT DELAMINATION FRONT	78

IV.7.5.1	Expected Behavior	78
IV.7.5.2	Obtained Behavior	79
IV.8	EXPERIMENTAL INVESTIGATION OF THE MODE MIXITY INFLUENCE ON THE DELAMINATION STRENGTH AT ROOM TEMPERATURE	82
IV.8.1	EXPERIMENTALLY OBTAINED CRITICAL SHEAR FORCES	82
IV.8.2	EXPERIMENTAL DISPERSION	83
IV.9	EXPERIMENTAL INVESTIGATION OF THE TEMPERATURE INFLUENCE ON THE DELAMINATION TOUGHNESS	85
IV.9.1	TEST SET-UP	85
IV.9.2	NUMERICAL RESULTS	86
IV.9.3	TEST METHODOLOGY AND RESULTS	87
IV.9.4	EXPERIMENTAL DISPERSION	89
IV.10	EXPERIMENTAL INVESTIGATION OF THE LOAD-RATE INFLUENCE ON THE DELAMINATION STRENGTH	91
IV.10.1	TEST SET-UP	91
IV.10.2	TEST METHODOLOGY AND RESULTS	92
IV.10.3	EXPERIMENTAL DISPERSION	93
IV.10.4	APPLYING THE TIME TEMPERATURE SUPERPOSITION TO THE INTERFACIAL TOUGHNESS	94
IV.11	INVESTIGATION OF THE MOISTURE INFLUENCE	95
IV.11.1	TEST PREPARATION	95
IV.11.2	TEST RESULTS	96
V.	<u>INTERFACIAL FRACTURE TOUGHNESS RESULTS</u>	98
V.1	EXPERIMENTAL/NUMERICAL CORRELATION	98
V.1.1	EXPERIMENTAL/NUMERICAL CORRELATION FOR THE MODE MIXITY INVESTIGATION AT ROOM TEMPERATURE	98
V.1.2	CORRELATION FOR TESTS AT HIGHER TEMPERATURES THAN ROOM TEMPERATURE	100
V.2	MODE MIXITY EFFECT AT ROOM TEMPERATURE	101
V.2.1	EXPERIMENTAL/NUMERICAL CORRELATION	101
V.2.2	REFERENCE LENGTH DETERMINATION	102
V.2.3	RESULT IMPLEMENTATION	103
V.2.4	GENERAL COMMENTS	104
V.3	TEMPERATURE INFLUENCE ON THE DELAMINATION TOUGHNESS	105
V.3.1	REFERENCE LENGTH ESTIMATION	105
V.3.2	EXPERIMENTAL NUMERICAL CORRELATION	105
V.3.3	RESULT IMPLEMENTATION	108
V.4	STRAIN RATE EFFECT	109
V.4.1	EXPERIMENTAL/NUMERICAL CORRELATION	109
V.4.2	STRAIN RATE/TEMPERATURE SUPERPOSITION	110
V.5	FINAL BENCHMARK BY MEANS OF DCB TEST	112
V.5.1	EXPERIMENTAL PROCEDURE	112
V.5.2	NUMERICAL MODEL	115
V.5.3	NUMERICAL RESULTS	116
V.5.3.1	Specimen Compliance-Crack Length Relation	116
V.5.3.2	Reproducing the Delamination	117
V.6	CONCLUSION	119
VI.	<u>FATIGUE AND LIFE TIME ASSESSMENT</u>	120
VI.1	THERMAL LOADED TWO-LAYER QUAD SPECIMEN	120
VI.1.1	TEST CONCEPT	120

VI.1.2	SPECIMEN PREPARATION AND TEST METHOD	120
VI.1.3	SMILE AND CRY FATIGUE CONCEPT	122
VI.1.4	DELAMINATION AREA MEASUREMENT	123
VI.1.5	EXPERIMENTAL RESULTS	125
VI.1.6	NUMERICAL MODELING	126
VI.1.7	NUMERICAL RESULTS	127
VI.1.8	CONCLUSION	129

VII. OUTLOOK **131**

VIII. APPENDIX **134**

LIST OF SYMBOLS

Latin Symbols

a	Delamination length or crack length
A	Delaminated Area (surface)
b	Relative element width at delamination front
da	Elementary crack propagation length
dA	Elementary crack propagation area
E_{ij}	Abaqus variable referring to the strain component ij in the strain tensor
f	Coefficient of friction
F	Applied shear loading to the specimen
\overline{F}_C	Average critical shear force
g	Gravitational acceleration
G	Total energy release rate (ERR)
G_1	Apparent mode 1 energy release rate amount
G_{1C}	Critical ERR for the apparent pure mode 1 loading case
G_I	True mode 1 energy release rate amount
G_2	Apparent mode 2 energy release rate amount
G_{2C}	Critical ERR for the (theoretical) apparent pure mode 2 loading case
G_{II}	True mode 2 energy release rate amount
G_C	Critical energy release rate for the considered material/interface
G_C^{BK}	Equivalent critical energy release rate of Benzeggagh and Kenane
h	Shearing height
i	Complex number given by $i \times i = -1$
k_i	Stiffness of elementary element i in the spring-dashpot viscoelastic models
K	Stress intensity factor (SIF)
K_I	SIF part corresponding to the Mode 1 Loading
K_{II}	SIF part corresponding to the Mode 2 Loading
K_C	Critical stress intensity factor for the considered interface
L	Reference Length for the estimation of the phase angle crack tip
L^0	Arbitrarily chosen reference length
L_T^1	Experimentally determined reference length at temperature T
m	Weight
p	Laplace variable
r	Distance considered ahead delamination front
R	Reaction force during the friction coefficient measurement
R_N	Normal reaction force during the friction coefficient measurement
R_f	Coulomb force during the friction coefficient measurement
S_{ij}	Abaqus variable referring to the stress component ij in the stress tensor
T	Temperature
T_G	Glass transition temperature
T_M	Molding Temperature
T_S	Thermal strain-free free temperature for 2-layer specimens

u_x^i	Displacement of node i in the x -direction
u_y^i	Displacement of node i in the y -direction
U_i	Abaqus variable referring to the displacement component in the direction i

Greek Symbols

α^i	Coefficient of thermal expansion (CTE) of material i
α_r	Size of the crack tip process zone
α	First parameter of Dunders
β	Second Dunders Parameter
δ_{CTE}	CTE-mismatch
Δa	Crack extension
ΔA	Delamination surface increase
ΔG	Fatigue energy release rate
ΔT_S	EMC temperature variation leading to the equivalent material retraction as the material shrinkage
Δu_x	Relative Crack Flank sliding (projected on the x -direction)
Δu_y	Relative Crack Flank opening (projected on the y -direction)
ε	Interface Parameter
φ	ERR Phase Angle given from the apparent mode 1 and 2 Energy Release Rate Ratio
η	Curvature Parameter in the BK-Law
μ	Elastic Shear Modulus
σ	Standard Deviation
$\bar{\sigma}$	Stress tensor
σ_y	Yield strength
τ_i	Damping of elementary element i in the spring-dashpot viscoelastic models
ω	Difference between φ and ψ
ψ	Phase angle estimated toward crack tip from oscillatory stress intensity factor
ψ_r	Oscillatory SIF phase angle estimated at distance r ahead crack tip

Note:

In the document, if variables G , K or ψ are used in conjunction with the subscript 1 or 2, they refer respectively to the apparent loading mode I or mode II estimated for example with the ratio of energy release rate $G_{\text{II}}/G_{\text{I}}$.

If the former variables are used in conjunction with the subscript I or II, they refer respectively to the "true" loading mode I or mode II estimated from the stress intensity factor (section II.5.2).

I. General Context

I.1 Introduction

Higher reliability and the miniaturization of electronic packaging in automotive applications are more and more demanded. These packages are exposed to harsh environments, such as extreme temperature, fast temperature changes, shocks, vibrations, humidity and hazarding liquids.

Today the common solution answering this problem is the encapsulation of the electronic packages in highly filled epoxy resins, also known as molding compounds. This encapsulation of electronic components provides a powerful solution to these challenges.

Electronic packages are made of various different materials, and more particularly polymeric molding compound, copper lead-frame, silicon, ceramic and epoxy printed board. Each of

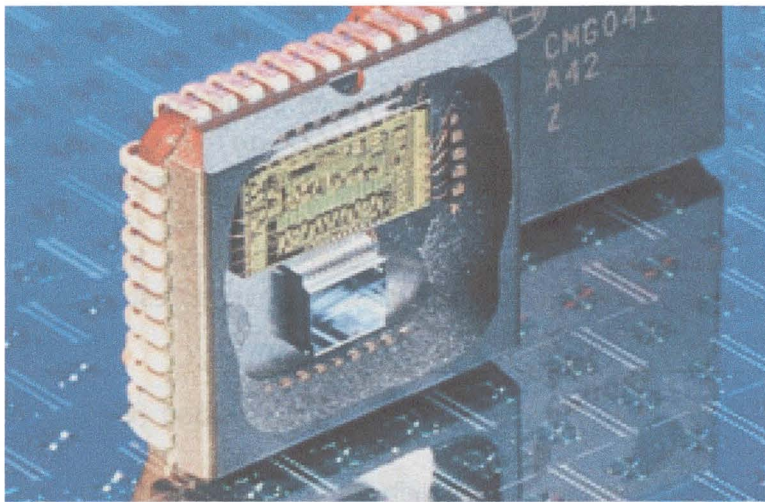


Figure 1: Typical encapsulated Component

these materials has its own material properties, and especially each one has its own coefficient of thermal expansion (CTE).

Considering two layers of different materials of this package faced to thermal change, for example a metallic pin encapsulated in molding compound, the CTE-mismatch leads to incompatible strains at their interface. Both layers are bonded and are consequently not free to expand thermally as

they would do, free of constraint. Significant stresses can consequently appear at all material interfaces submitted to large temperature changes.

Interfacial stresses lead to the interfacial crack initiation (delamination), which will propagate in the packages until the component fail. The fracture can be reached by different ways. Either loading conditions are critical, fracture occurs within a short time, or the loading conditions leads to fatigue delamination growth along the interface, failure occurs after a given life time of the component.

Delamination propagates until a boundary of the interface is reached. Interfacial cracks then kink in the encapsulant material (corner crack), leading to the complete failure of the encapsulation function and to the component failure.

Molding compounds are composed of a thermosetting plastic epoxy resin matrix filled with microparticles of silicon dioxide. The filler represents between 75 or 92 percent of the total weight. Molding compounds are used because of their low coefficient of thermal expansion comparatively to other compounds such as thermoplastic resins. Other advantages are their low chemical shrinkage after molding, i.e. their retraction at solidification process remains low, which allows the reduction of residual stress in the package after molding. And of course, the main reason of their use is their high permeability to media such as water or oil.

Concerning their mechanical properties, molding compounds generally exhibit an instantaneous elastic modulus between 16 and 25 GPa at room temperature. They show a glass transition in most cases at temperatures situated between 130 and 190 °C. Their coefficient of thermal expansion is in the range 8 to 13 Parts per Million per Kelvin (PPM/K) below the glass transition temperature T_G and about 35 PPM/K above T_G .

I.2 Approach in this Work

The aim of this work is to focus on the delamination of thermosetting polymer based on molding compound/copper leadframe interface.

This work takes place in an industrial framework at the Robert Bosch GmbH company near Stuttgart in Germany. In this context, the developed methods have to respond to the industrial requirements rather than academic ones. For this reason, this work proposes new tests setups which can be easily performed in research departments and labs from industries. The developed methodologies are simple, cost-effective, and can be rapidly executed. The main goal of this work can be formulated as follows: "A single test setup to characterize the delamination toughness, whatever the investigated influence."

The main focus is on the overcritical delamination between molding compound (EMC) and copper used to encapsulate electronic devices.

The Bosch Company is also concerned by the long-time reliability of its products. For this reason, it was tried during the last months to assess the life-time of the studied interface using two-layer specimens, which are for other purpose already at disposal in the Bosch labs. Electronic devices developed for automotive applications are typically submitted to a certain number of thermal shocks, which that they have to survive to be validated. Classically, these devices are submitted to thermal cycles between 150 °C and -40°C. For this reason, the developed fatigue test concept is based on thermal fatigue using the same thermal shocks. Moreover, using these thermal shocks is for economical purposes particularly interesting since thermal shocks chambers are continuously in activity, so that tests can anytime carried out by adding the required specimen in a functioning thermal chamber. It doesn't involve additional machine cost and doesn't requisition tensile machines during several days as traditional fatigue tests do.

The required theoretical backgrounds in fracture mechanics and a reasonable description of the linear viscoelasticity are presented in the part II of this document. A part of this work

deals with finite-element-method (FEM). The tool Abaqus is used in this work. The implantation of interfacial fracture mechanics in Abaqus is investigated and discussed in part III.

The part IV of this work mainly focuses on the experimental determination of the overcritical delamination toughness using the test setup, based on the triangle button shear specimen (TBSS). This concept is presented at the beginning of part IV.

Experimental results can not be correctly interpreted without the numerical investigation of the test. For this reason, the numerical results are presented in the part IV before the experimental results, which are presented at the end.

The numerical correlation between experimental and numerical results and the determination of the overcritical delamination toughness of the EMC-copper interface is presented in part V. At the end of the part V, a study is performed with a modified double cantilever beam specimen (DCB) to check if the delamination propagation under critical loading is correctly reproduced in FEA.

Finally, an overview of the investigated fatigue test concept and the obtained results are presented in part VI.

II. Theoretical Background

II.1 Fracture Mechanics

The first fundamental hypothesis in fracture mechanics is an initial existence of a crack. Themes dealing with the following question: «How does a crack appear, why and where?» belong to the damage mechanic sciences.

The crack propagation depends strongly on the loading conditions at the crack tip. Namely, three different modes of fracture are distinguished, known as mode I, mode II and mode III of fracture. Each one corresponds to different loading mechanisms, which explains why they are not critical in the same manner.

The description of these fracture modes only considers the load condition at the crack tip and has no consideration for the general far-fields of stress and strain. In all cases, the loading conditions at the crack tip can be described thanks to a combination of these three modes.

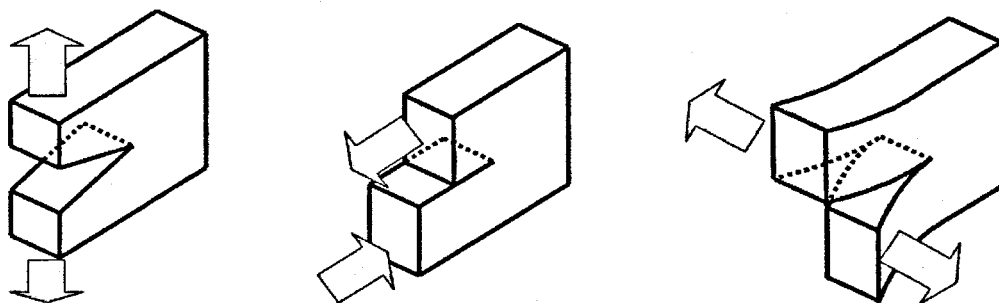


Figure 2: Loading modes at crack Tipp

- a. mode I
- b. mode II
- c. mode III

Mode I of fracture corresponds to the part of opening, i.e. loading in the normal direction to the crack plane. It leads to the separation of both crack flanks and is more critical than the others. Mode II of fracture corresponds to the part of longitudinal shear loading. It leads to crack flanks relative shifting in the crack plane and in the direction orthogonal to the crack front. Mode III of fracture corresponds to the part of transversal shear loading. It leads to the crack flanks relative twist in the crack plane and parallel to the crack front.

Many works only consider the mode I and the mode II loading. The first reason is that the mode III usually plays a negligible role in comparison to the other modes. Another reason is that the mode mixity is often estimated on the specimen and loading symmetry plane, which

is also a symmetry plane for the stress and strain fields. In such a plane, the plane strain condition can be assumed, and no mode III loading exists at crack tip.

II.2 Crack Initiation

Fracture mechanics basically assumes that a crack already exists. It means that the location where the cracks are, their dimensions and forms are already known before the study. In some industrial contexts, the place where a crack occurs is generally known a-posteriori thanks to the feedback from the use and test of prototypes. As explained in [Lemaitre 2007], damage can occur under various different conditions (static loading, low cycle fatigue, or high cycle fatigue as well) and at different scales (macroscopic, microscopic). Ductile damaging occurs under static loading, creep damaging under high temperature. Fracture in highly filled epoxy resin occurs thanks to brittle damage under monotonic loading or low/high cycle loading damage when they undergo large numbers of repeated loading.

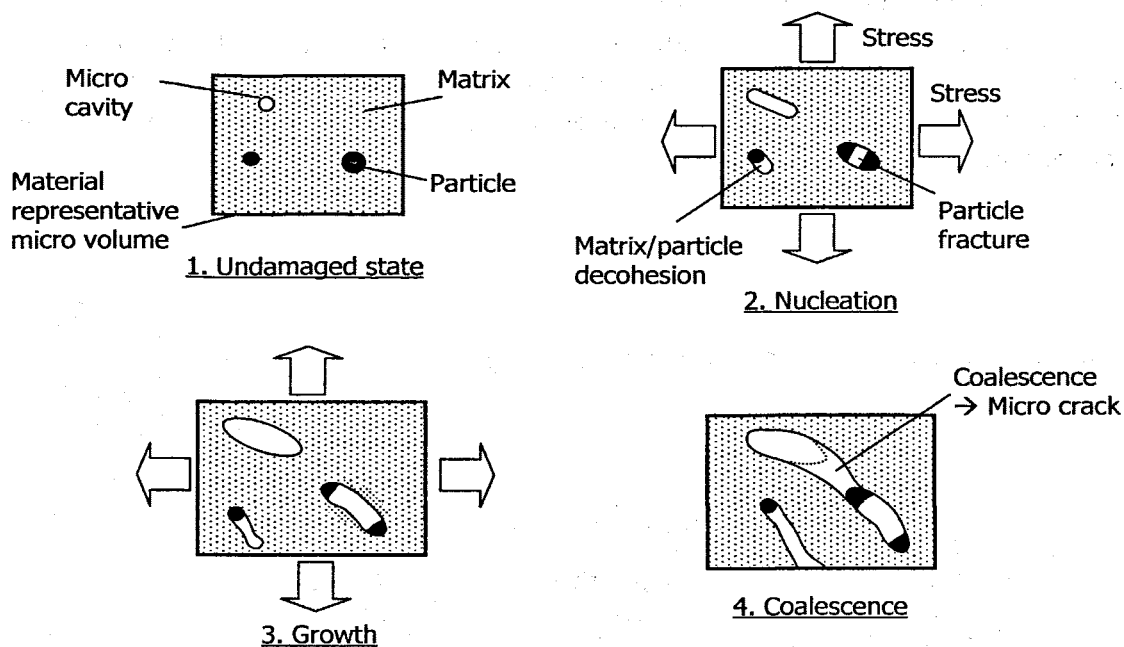


Figure 3: Damaging and crack initiation

In all cases, damaging always initiates near discontinuities such as particles, impurities, etc. Damaging can roughly be divided into three phases (see Figure 3). In damaging, the micro scale is considered. The first part is the nucleation phase. The matrix-particles decohesion, the existence of nano cavities and the fracture of inclusions lead to the appearance of micro cavities. In a second phase, micro cavities grow because of material strain. Finally, different micro cavities join each other in the coalescence phase which causes a micro crack.

Initiation occurs at stress concentration places, i.e. where parts are prone to weakness, for example strong sectional reductions, important curvatures, tuckings and cuttings, etc. In orthotropic parts (multi material assemblies), cracking frequently appears at interface corners, and leads to both homogenous materials cracking (bulk cracking) and interfacial delamination. It is frequently assumed that micro bulk crack initiates in the direction of the maximal stress, and then propagates in the direction which combined with external loading induces mode I cracking, which is also energetically the cheapest path [Roger 2007]. Delamination follows interfaces and rarely kinks out of the interface as the weakest crack toughness is often located at interfaces, whatever the mode mixity at crack tip.

A potential failure cause of electronic packages such as IC packages (integrated circuits, Figure 4) is the delamination.

Such packages are constituted from many different materials. Hence, cracks initiate because of thermal loading, at places where the material CTE-mismatch and the geometry induces the biggest stress. Cracking occurs at the copper/molding compound interface and propagates along this interface until a corner is reached. It then propagates further along another face constituting a material interface.

As the leadframe is sufficiently delaminated, larger strains are rendered possible. At singularities, i.e. part corners, crack jumps from the interface in the molding compound, and propagates until encapsulant outside face. It allows then moisture intrusion and may cause component failure.

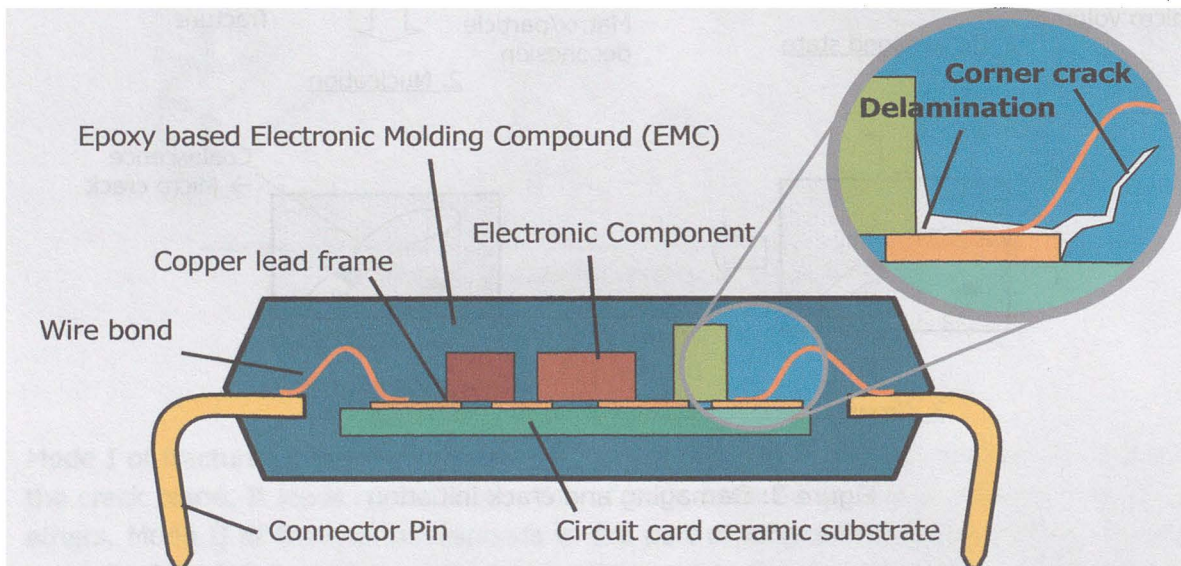


Figure 4: Example of Failure Mechanisms in Electronic Packages

II.3 Stress Intensity – based Fracture Criterion

II.3.1 Cracks in Homogeneous Media

II.3.1.1 Definition

The stress intensity factors (SIF) are originally defined by [Irwin 1957] as criterion to predict crack propagation in homogenous elastic media. The stress intensity factors can be used within the LEFM (linear elastic fracture mechanics) which assumes that no plastic deformation occurs. It is often used if the size of plastic deformations at crack tip is negligible compared to all other dimensions. It can especially be applied for brittle media such as epoxy based thermosetting polymers. The SIF quantify the stress concentration at crack tip.

A crack in an elastic homogeneous body is considered. The stress field in the vicinity of the crack is expressed using polar coordinates (r , θ).

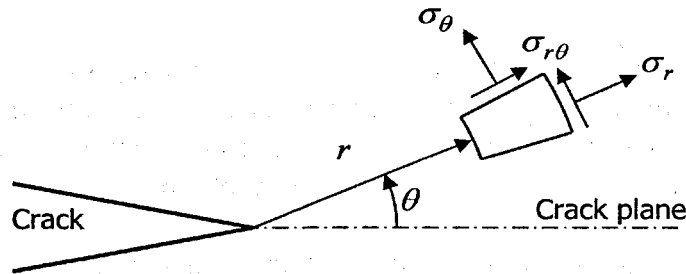


Figure 5: Stress Field at Crack Tip

In 2D problem, if plane stress condition is assumed, σ_z is equal to zero. Considering that stress becomes singular at crack tip, i.e. $\sigma_i \rightarrow \infty$ when $r \rightarrow 0$, Irwin proposes the formulation of the near crack tip stress field in the form of eq. II-1, where r is the distance to crack tip, m a positive number, F_r , F_θ and $F_{r\theta}$ three functions of the polar direction θ :

$$\sigma_r = F_r(\theta)r^{-m}, \quad \sigma_\theta = F_\theta(\theta)r^{-m}, \quad \sigma_{r\theta} = F_{r\theta}(\theta)r^{-m}. \quad \text{eq. II-1}$$

Using this general formulation, stress effectively increases as the distance to crack tip diminishes. Following formulations, compatible with eq. II-1, define the stress intensity factors K_I , K_{II} and K_{III} . Subscript I, II and III refer to the respective mode I, II and III load amount. The parameter m takes the value $1/2$.

$$\sigma_r = K_I \frac{1}{2\sqrt{2\pi r}} \cos \frac{\theta}{2} (3 - \cos \theta) - K_{II} \frac{1}{2\sqrt{2\pi r}} \sin \frac{\theta}{2} (1 - 3 \cos \theta). \quad \text{eq. II-2}$$

$$\sigma_{r\theta} = K_I \frac{1}{2\sqrt{2\pi r}} \sin \frac{\theta}{2} (1 + \cos \theta) - K_{II} \frac{1}{2\sqrt{2\pi r}} \cos \frac{\theta}{2} (1 - 3 \cos \theta). \quad \text{eq. II-3}$$

$$\sigma_{\theta} = K_I \frac{1}{2\sqrt{2\pi r}} \cos \frac{\theta}{2} (1 + \cos \theta) - K_{II} \frac{3}{2\sqrt{2\pi r}} \sin \frac{\theta}{2} (1 + \cos \theta). \quad \text{eq. II-4}$$

Expressed on the crack plane ($\theta = 0$), the general expression of stress singularity at crack tip is found:

$$\sigma_r = \frac{K_I}{\sqrt{2\pi r}}, \quad \sigma_{\theta} = \frac{K_I}{\sqrt{2\pi r}} \quad \text{and} \quad \sigma_{r\theta} = \frac{K_{II}}{\sqrt{2\pi r}}. \quad \text{eq. II-5}$$

Thus, general stress intensity factors are defined using the form in the eq. II-6, where the subscript i refers to I, II or III, σ is the far field stress and f a function of the geometry.

$$K_i = \sigma_{ii} \sqrt{\pi a} f(\text{geometry}). \quad \text{eq. II-6}$$

II.3.1.2 Criterion of Crack Propagation

A crack submitted to pure mode I loading propagates if $K_I > K_{IC}$. K_I refers to the stress intensity at crack tip, and K_{IC} is the material crack toughness for mode I loading. For pure modes II and pure mode III loading, propagation occurs if respectively $K_{II} > K_{IIC}$ or $K_{III} > K_{IIIC}$, K_{IC} , K_{IIC} and K_{IIIC} being material properties.

For mixed mode loading, several extended fracture criteria exist to define the critical combinations $(K_I, K_{II}, K_{III})_c$. Most of them are summarized in [Roger 2007].

II.3.2 Stress Intensity Factor for Interfacial Cracks

In the case of interfacial crack between two dissimilar materials, the previous definition of the stress intensity factors is not valid.

Williams ([Williams 1959]) first investigated crack between two dissimilar media for geological purpose. He determined the form of the stress singularity by solving the Eigenvalues problem, and found that this stress singularity could not be in the form $r^{-1/2}$ but should rather be in a complex form r^{λ} with $\lambda = \lambda_r + i\lambda_j$, suggesting oscillatory stress and strain fields at crack tip.

England ([England 1965]) found a solution for the stress field at crack tip and crack tip opening by resolving the so called Hilbert problem. He also confirmed Williams result and verified that stress and displacement fields at crack tip were of oscillatory nature.

Erdogan ([Erdogan 1965]) investigated further this problematic and formulated the stress field solution in the case of straight cracking between plates.

Rice ([Rice 1965]) found one crack tip stress field solution using the Eigen-value method of Williams with the mathematical theories of Muskhelishvili ([Muskhelishvili 1953]) and extended the Irwin stress intensity factors to interfacial crack problems.

Dundurs ([Dundurs 1969]) established that stress field in a body composed of two isotropic layers under surface traction depends on two parameters α and β . These parameters are functions of the elastic constants of both materials constituting the interface. The latter permits to define the interfacial constant ε .

SIF extension to interfacial cracking is finally proposed by [Rice 1988] (eq. II-7). The near stress field expression is similar to the one for bulk cracking (cracking in homogeneous media, eq. II-5). In eq. II-7, the exponent i refers to the complex number ($i^2=-1$):

$$\sigma_{yy} + i\sigma_{xy} = \frac{K}{\sqrt{2\pi r}} r^{i\varepsilon}. \quad \text{eq. II-7}$$

The interfacial stress intensity factor is defined as a complex quantity (eq. II-8.a, eq. II-8.b). The parameter ψ is the complex argument of the SIF and represents the mixed mode angle at crack, i.e. the amount of mode I and mode II loading at distance r from crack tip. Identically, K_I and K_{II} can be related to the respective contribution of mode I and mode II loading.

$$K = |K|e^{i\psi} = K_I + iK_{II} \quad \text{eq. II-8}$$

The r -singularity is complex in the form $\lambda = -1/2 + i\varepsilon$. Expanded and separated in real and imaginary parts, the eq. II-7 leads to the expression of the stress field near the singularity (eq. II-9).

$$\begin{aligned} \sigma_{yy} &= \frac{1}{\sqrt{2\pi r}} [K_I \cos(\varepsilon \ln r) - K_{II} \sin(\varepsilon \ln r)] \\ \sigma_{xy} &= \frac{1}{\sqrt{2\pi r}} [K_I \sin(\varepsilon \ln r) + K_{II} \cos(\varepsilon \ln r)]. \end{aligned} \quad \text{eq. II-9}$$

According to eq. II-9.a and eq. II-9.b, the stress concentration at crack tip decreases in a \sqrt{r} -manner but also oscillates inside this envelope.

The nature of these oscillations is widely studied in [Williams 1959], [Erdogan 1965], [England 1965], [Rice 1968b], [Rice 1988], [Hutchinson 1992].

Considering the eq. II-9, the period of the oscillations is given by:

$$T_r = r_1 - r_0; \quad \varepsilon \ln r_1 = 2\pi + \varepsilon \ln r_0. \quad \text{eq. II-10}$$

Stress oscillation frequency varies with the distance r to crack tip. It is given by:

$$f_r = \frac{1}{r \left(\exp \frac{2\pi}{\varepsilon} - 1 \right)}. \quad \text{eq. II-11}$$

Considering eq. II-11, stress field oscillation pseudo period increases as r also increases.

Assuming ε in the range of 0.1 for the EMC/copper interface, at a distance r equal to 10^{-26} m, the pseudo period of the oscillation is approximately equal to 20 mm. Oscillations are consequently expected to appear at a distance to crack front inferior to 10^{-26} m.

[Dugdale 1960] suggests that stress distribution is uniform in the process zone at crack and is equal to the material yield stress when the crack propagation condition is met ($K = K_C$). The size of the process zone is given by the eq. II-12, where σ_y is the yield strength:

$$\alpha_r = \frac{\pi}{8} \left(\frac{K_I}{\sigma_y} \right)^2. \quad \text{eq. II-12}$$

Considering a yield strength of 100 MPa for a thermosetting polymer, 300 MPa for the copper substrate and a delamination strength K_{IC} of $1700 \text{ Pa}\cdot\text{m}^{1/2}$ for the thermosetting polymer/copper interface, the process zone size is in the range of 10^{-10} m in the polymer and 10^{-11} m in copper.

But at a distance r of 10^{-10} m from crack tip, the oscillations period is theoretically supposed to be in the range of 10^{18} m. As a consequence, if the Dugdale assumption is admitted, there is no possible oscillation of the stress field at crack tip for the EMC/copper interface.

II.3.3 Displacement field ahead crack tip

Displacement field at crack tip (eq. II-13) is proposed by [Hutchinson 1987], [Sun 1987] and [Suo 1988]. Furthermore it is adopted in several works until now ([Matos 1988], [Charalamb. 1989], [Hutchinson 1992], [Agrawal 1996], [Sun 1997a], [Yeung 2000], [Tay 2003]).

$$\Delta u_y + i\Delta u_x = 8 \frac{K \sqrt{r} r^{i\varepsilon}}{E^* \sqrt{2\pi} (1 + 2i\varepsilon) \cosh(\pi\varepsilon)}. \quad \text{eq. II-13}$$

The expression in eq. II-13 relates the relative crack flanks displacement at a distance r ahead of crack tip to the complex stress intensity factor (Figure 6). E^* is the equivalent interfacial elasticity (eq. II-14) and ε the interface parameter (eq. II-16 to eq. II-19). The displacement field ahead of crack tip is also affected by the $i\varepsilon$ -exponent, which suggests the same problematic as for the stress field (stress intensity factor definition).

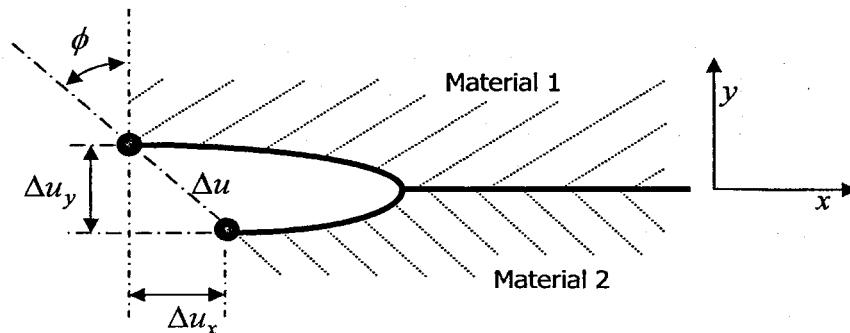


Figure 6: Displacement Field at Crack Tip

The equivalent interfacial elastic module E^* is defined by the relation:

$$\frac{1}{E^*} = \frac{1}{2} \left(\frac{1}{E_1} + \frac{1}{E_2} \right). \quad \text{eq. II-14}$$

Quantities \overline{E}_1 and \overline{E}_2 are defined in eq. II-15.a and eq. II-15.b. The parameter i refers to material 1 or 2.

$$\begin{aligned} \overline{E}_i &= \frac{E_i}{1-\nu_i^2} \quad \text{for plane strain,} \\ \overline{E}_i &= E_i \quad \text{for plane stress.} \end{aligned} \quad \text{eq. II-15}$$

In eq. II-13, ε is the interfacial parameter defined by

$$\varepsilon = \frac{1}{2\pi} \ln \frac{1-\beta}{1+\beta}, \quad \text{eq. II-16}$$

β is the second Dunders parameter ([Dunders 1969]):

$$\beta = \frac{\mu_1(\kappa_2 - 1) - \mu_2(\kappa_1 - 1)}{\mu_1(\kappa_2 + 1) + \mu_2(\kappa_1 + 1)}. \quad \text{eq. II-17}$$

The parameters κ_1 and κ_2 were also defined by:

$$\begin{aligned} \kappa_i &= 3 - 4\nu_i \quad \text{for plane strain,} \\ \kappa_i &= \frac{3 - \nu_i}{1 + \nu_i} \quad \text{for plane stress.} \end{aligned} \quad \text{eq. II-18}$$

μ_1 and μ_2 refer to the shear modulus of material 1 and material 2, and can be derived from other elastic quantities:

$$\mu_i = \frac{E_i}{2 + 2\nu_i} \quad \text{eq. II-19}$$

Henceforth, the angle ϕ defines the crack flanks relative displacements (crack tip sliding/crack opening): $\phi = \arctan(\Delta u_x / \Delta u_y)$. This angle corresponds to the mode mixity at crack tip in the case where both materials are identical, and for crack propagation in homogeneous materials.

The expression in eq. II-13 is reformulated in module-arguments complex number in order to establish eq. II-20 and eq. II-21:

$$\Delta u e^{i\phi} = \Lambda |K| e^{i\psi} \sqrt{r} e^{i\varepsilon \ln(r)} \sqrt{1 + 4\varepsilon^2} e^{i \arctan(-2\varepsilon)}, \quad \text{eq. II-20}$$

$$\Lambda = \frac{8}{E^* \sqrt{2\pi} (1 + 4\varepsilon^2) \cosh(\pi\varepsilon)}. \quad \text{eq. II-21}$$

Separating the complex modules and the arguments permits relating the modulus and phase of the stress intensity factor to the near crack tip displacements considered at distance r from crack tip (eq. II-22 and eq. II-23).

$$|K| = \frac{\Delta u}{\Lambda \sqrt{r} \sqrt{1+4\varepsilon^2}} \quad \text{eq. II-22}$$

$$\psi = \phi + \arctan(2\varepsilon) - \varepsilon \ln(r). \quad \text{eq. II-23}$$

The determination of the K -factor using the near crack tip displacement is r -dependent.

II.4 Energy-Based Fracture Criterion

II.4.1 Energy Release Rate for isotropic Cases

The energy release rate (ERR) is defined by [Griffith 1921] within the LEFM (linear elastic fracture mechanics), and can be consequently used for brittle materials. This criterion assumes that the system is energetically conservative and reversible.

The whole system energy is considered, namely, elastic strain energy, work of external loads, finally dissipative phenomenon can be taken into account.

Considering an equilibrated 2D problem containing a crack of length a , if this crack propagates by an infinitesimal length da (Figure 7), new surfaces are created in the system, corresponding to the crack flanks extension equal to $2bda$ (for a crack extension da , two crack walls are extended from da). Variable b refers to the system thickness.

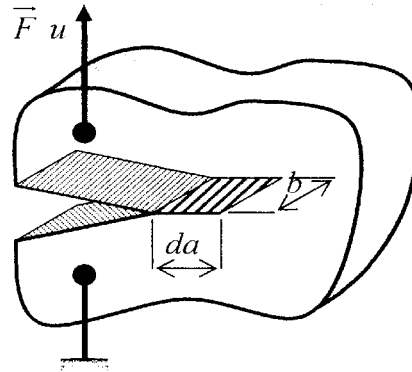


Figure 7: The Energy Release Rate

Let be Π_1 and Π_2 the whole system energy respectively before and after crack propagation. The former is defined by eq. II-24, in which E is the whole system strain energy before the crack propagation,

$$\Pi_1 = E. \quad \text{eq. II-24}$$

An infinitesimal load increase brings a work dW and leads to crack propagation da . The system strain energy varies by dE . At crack propagation, a part of the system strain energy is released, so that dW does not equilibrate dE . To be conservative, the system must

involve a further energetic quantity. The energy of surface creation per unit of area dU_S is considered in addition. System energy after crack propagation is then defined by:

$$\Pi_2 = E + dE + dW + dU_S. \quad \text{eq. II-25}$$

The system being conservative, the relation in the eq. II-26 is verified

$$\frac{\partial \Pi}{\partial a} = \Pi_2 - \Pi_1 = dE + dW + dU_S = 0. \quad \text{eq. II-26}$$

And consequently, considering the surface created dA equal to $2bda$:

$$\frac{\partial U_S}{\partial A} = -\frac{\partial W + \partial E}{\partial A} \quad \text{eq. II-27}$$

Griffith introduced the energy release rate G , representing the system energy loss per area increment of crack propagation as:

$$G = -\frac{\partial W + \partial E}{\partial A}. \quad \text{eq. II-28}$$

The energy of crack surface creation per unit is called the critical energy release rate G_C . This quantity is a material intrinsic property, which can be partially related to the atomic bond and atom density per volume unit, etc.

$$G_C = \frac{\partial U_S}{\partial A}. \quad \text{eq. II-29}$$

The crack is assumed to propagate if G reaches G_C . The ERR can also be split into three parts G_I , G_{II} and G_{III} corresponding to the load contributions of mode I, mode II and mode III at crack tip. G is defined as the sum of the three terms.

As mentioned for the SIF, the critical energy leading to crack propagation G_C (which can also be referred as crack toughness) varies depending on the ratio of mode I, mode II and mode III loading at crack tip.

II.4.2 Virtual Crack Closure Technique

Several methods exist to estimate the ERR for crack propagating at the interface of two dissimilar materials. One is the Virtual Crack Closure Technique (VCCT) proposed by Rybicky and Kanninen [Rybicki 1977].

The formulation of the VCCT is also reviewed in details in [Krueger 2002], where similar methods and enhancements to the original VCCT are proposed.

The VCCT assumes crack propagation as a thermodynamically reversible phenomenon. The energy needed to propagate a crack by Δa is considered equal to the energy needed to reclose it over a length Δa . The method consists then in the estimation of the energy required to reclose the crack.

The two-dimensional fracture problem is considered (Figure 8). Variable δ is the crack opening. It also corresponds to the path followed by crack flanks to be joined together (crack closure). The initial interfacial stress at crack tip is defined by σ , whereas σ^* makes reference to the interfacial stress at crack tip, hence the latter is reclosed.

The elementary work required to reclose the crack from da is then equal to:

$$dW = \sigma_y^*(-da)\delta_y(-da)da + \sigma_x^*(-da)\delta_x(-da)da. \quad \text{eq. II-30}$$

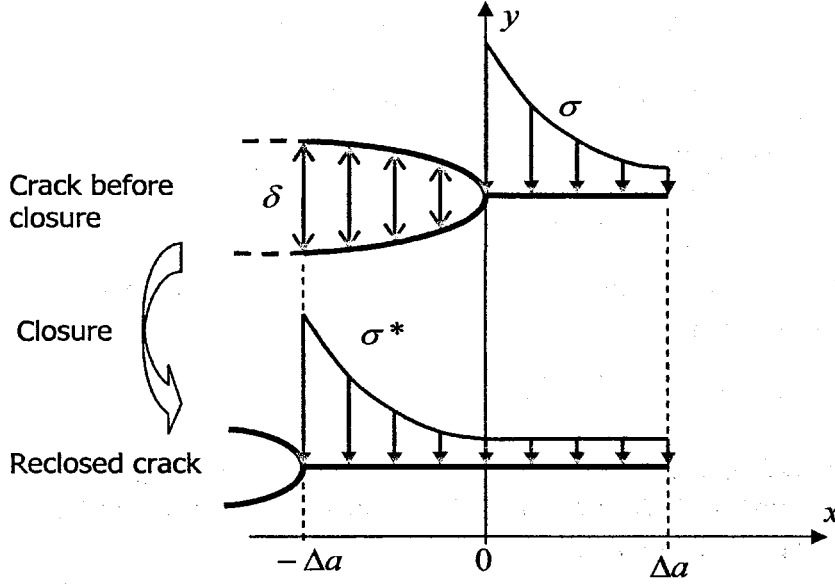


Figure 8: Virtual Crack Closure Technique

Identically, the work required to reclose the crack over a length Δa corresponds to:

$$W = \int_0^{\Delta a} \sigma_y^*(-x)\delta_y(-x)dx + \int_0^{\Delta a} \sigma_x^*(-x)\delta_x(-x)dx. \quad \text{eq. II-31}$$

This work corresponds to the energy required for the creation of the crack flanks surface $2b\Delta a$ (b is the crack width). The energy release rate is given by:

$$G = \lim_{\Delta a \rightarrow 0} \frac{W}{2b\Delta a}. \quad \text{eq. II-32}$$

So far, estimating the ERR requires on one hand to determine the strain field, in order to get δ ; and on the other and the stress field σ^* , hence the crack is reclosed. In this form, the VCCT requires to compute two times the stress and strain fields, i.e. before and after the crack extension Δa .

To prevent a double computation, the VCCT assumes that crack extension from a to $a + da$ does not alter significantly the strain and stress field (self-similar crack extension hypothesis). In principle this assumption is correct if the crack extension da remains negligible compared to the crack length.

If this hypothesis is verified, stress fields σ^* and σ can be assumed identical. The virtual crack closure technique defines consequently the energy release rate as:

$$G = G_1 + G_2, \quad \text{eq. II-33}$$

$$G_1 = \lim_{\Delta a \rightarrow 0} \frac{1}{2b\Delta a} \int_0^{\Delta a} \sigma_y(\Delta a - x) \delta_y(-x) dx, \quad \text{eq. II-34}$$

$$G_2 = \lim_{\Delta a \rightarrow 0} \frac{1}{2b\Delta a} \int_0^{\Delta a} \sigma_x(\Delta a - x) \delta_x(-x) dx. \quad \text{eq. II-35}$$

For cracks in homogenous materials, G_1 and G_2 can be directly related to the mode I and mode II loading contributions.

For interfacial cracks between two dissimilar materials, G_1 and G_2 do not exactly correspond to modes I and II loading because of the oscillatory behavior at crack tip (refer to section II.3.2). The oscillatory behavior at crack tip causes the estimation of the ratio G_2/G_1 to be Δa -dependent ([Beuth 1996]). This assumption is verified in section III.3.2. For interfacial cracks, this ratio should be considered carefully and the mode mixity estimated using other physical quantities. The total energy release rate G is expected to be Δa -independent.

II.4.3 VCCT Discretization for Finite Element Analysis

Several forms of the virtual crack closure technique implementations are given by [Krueger 2002]. For the two-dimensional case, the VCCT is implemented for finite element models using first order quad elements, as follows:

$$G_1 = \frac{1}{2b\Delta a} F_y^k (u_y^i - u_y^j) \quad \text{and} \quad G_2 = \frac{1}{2b\Delta a} F_x^k (u_x^i - u_x^j) \quad \text{eq. II-36}$$

In eq. II-36, F_x^k refers to the nodal force at crack tip in the direction of crack propagation, and F_y^k to the nodal force in the direction normal to the crack plane (Figure 9). Variables u^i and u^j correspond to the nodal displacements in front of the crack tip.

For three-dimensional problems (Figure 10), the ERR of mode III is defined additionally as:

$$G_3 = \frac{1}{2b\Delta a} F_z^k (u_z^i - u_z^j) \quad \text{eq. II-37}$$

II.4.4 Energy Release Rate from Oscillatory Stress Intensity Factor

Energy release rate and stress intensity factors can be directly related (as long as LEFM is assumed). This relation is established by [Malyshev 1965]:

$$G = \frac{1 - \beta^2}{E^*} |K|^2. \quad \text{eq. II-38}$$

E^* is the equivalent interfacial elastic modulus (eq. II-14), β is the second Dunders parameter (eq. II-17).

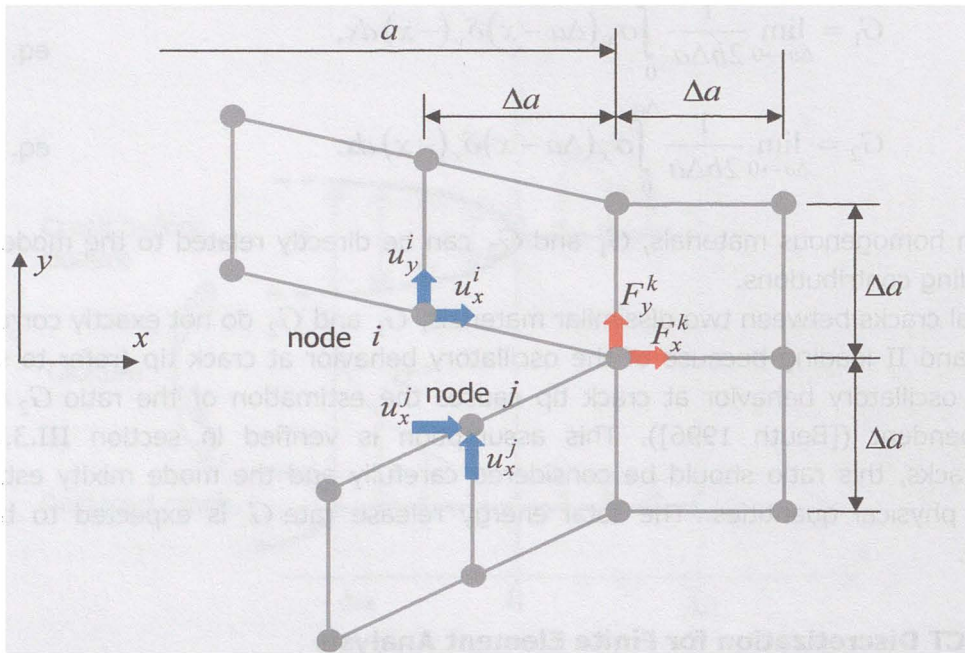


Figure 9: 2D VCCT for Finite Element Modeling with 1st Order Elements

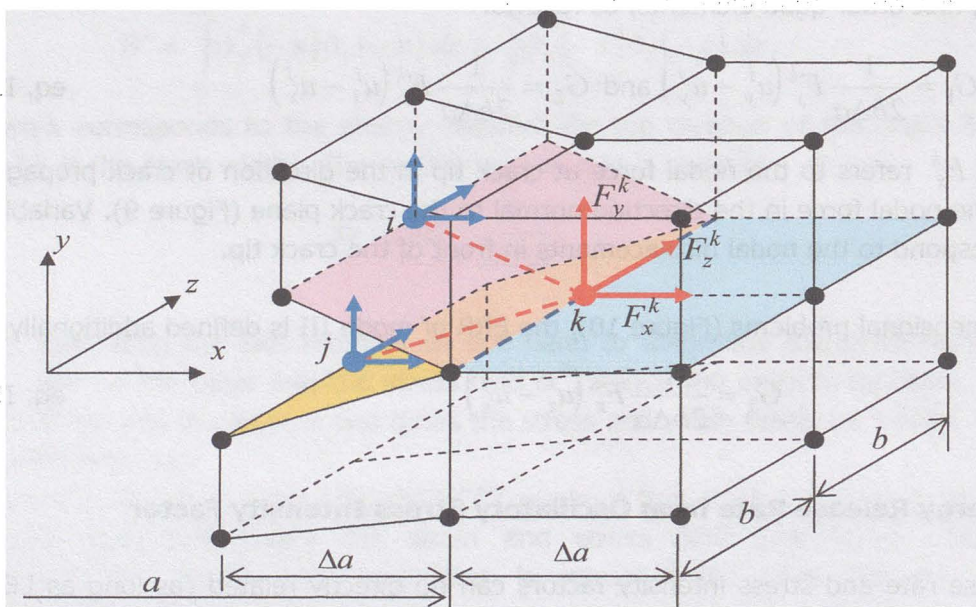


Figure 10: 3D VCCT for Finite Element Modeling with 1st Order Elements

II.5 Mode Mixity at Crack Tip

II.5.1 Oscillatory SIF-based Phase Angle Estimation

As shown by eq. II-23, the phase angle ψ depends on ϕ , latter defined by the arctangent of $\Delta u_x / \Delta u_y$. Separating equation eq. II-13 into its real and imaginary part permits to express each term of the relative crack flank displacement according both longitudinal and transversal direction to the crack tip,

$$\Delta u_y = \Lambda [(K_I + 2\varepsilon K_{II}) \cos(\varepsilon \ln r) - (K_{II} - 2\varepsilon K_I) \sin(\varepsilon \ln r)], \quad \text{eq. II-39}$$

and

$$\Delta u_x = \Lambda [(K_I + 2\varepsilon K_{II}) \sin(\varepsilon \ln r) + (K_{II} - 2\varepsilon K_I) \cos(\varepsilon \ln r)]. \quad \text{eq. II-40}$$

It shows that relation between crack flanks displacement and stress intensity factors is composed of terms of pseudo period r -dependant given by (section II.3.2):

$$T = r \left(\exp \frac{2\pi}{\varepsilon} - 1 \right). \quad \text{eq. II-41}$$

Admitting the interface parameter ε in the range of 0.1, oscillation period reaches enormous lengths incomparable to the problem dimensions as r reaches nano millimeters. These oscillations can not be observed physically. Anyhow, phase angle estimated from eq. II-23 depends on the choice of r , the distance taken for the crack flanks relative displacement.

[Rice 1988] suggested normalizing this distance r by a problem representative length L (or normalizing length), so that the obtained term in the log is dimensionless. Consequently, eq. II-23 becomes:

$$\psi = \arctan \frac{\Delta u_x}{\Delta u_y} + \arctan(2\varepsilon) - \varepsilon \ln \frac{\Delta a}{L}. \quad \text{eq. II-42}$$

Δa corresponds to the considered distance r to crack tip. Since ψ is an angle situated between $-\pi/2$ and $\pi/2$, it is meaningful that the last term in eq. II-42 fulfills the relation:

$$\varepsilon \ln \frac{\Delta a}{L} \in \left[\frac{-\pi}{2} - \arctan 2\varepsilon, \frac{\pi}{2} - \arctan 2\varepsilon \right]. \quad \text{eq. II-43}$$

The Δa -dependency of the mixed-mode angle estimation is since the first works in this field an unresolved problem. [Agrawal 1997] suggested resolving this problem by determining the critical energy release rate for a given interface with two different test set-ups. Considering that different set-up should lead to the same interfacial toughness for a given material combination. The used reference length must be adjusted until numerical correlations of both tests give same result. This solution has the main disadvantage that it requires performing two experiments, resulting in double cost and time.

II.5.2 Extended SIF-based Mixed-Mode Angle Estimation Method

[Tay 2003] estimated the stress intensity factor on different distances ahead of the crack tip. He shows that, far enough from the crack tip, the obtained stress intensity factors show a linear trend, which one can be extrapolated to zero to estimate the stress intensity factors at crack tip. This method can also be applied for the phase angle.

Considering that the mode mixity at crack tip is estimated using FEM, relative displacement of crack flanks can be taken at distance Δa , $2 \Delta a$, $3 \Delta a$, $4 \Delta a \dots n \Delta a$, where Δa is the element length at crack tip (see Figure 9). Considering that the singularity is not adequately described in FEM, displacement of first node pairs may not be considered. Then, enough node pairs must be considered to get a linear trend of the phase angle as function of the reference length. Then it can be identified and properly extrapolated to distance zero. Node pairs should anyway be chosen, so that all nodes are situated into the near-crack-tip field, and so that the estimated mode mixity describes the mode mixity at crack tip. For the curve in Figure 11, nodes chosen are situated in at a maximal distance of $50 \mu\text{m}$ from crack tip.

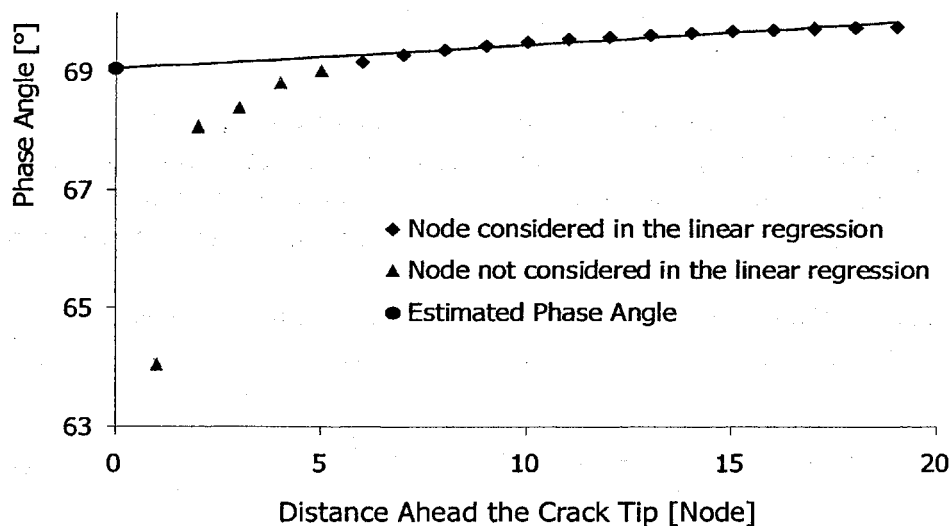


Figure 11: Extended SIF-based mixed-mode estimation

This method furnishes a pseudo Δa -independent estimation of the mixed-mode angle. Equation eq. II-42 is taken to estimate the mode mixity at each node pairs. For each pair, Δa corresponds to the load-free distance of node pair to the crack tip. The result issued from this extrapolation depends on the normalizing length L chosen. A variation ΔL of the reference length leads (in Figure 11) to a vertical shifting $\varepsilon \ln \Delta L$ of the curve.

II.5.3 Non-Oscillatory ERR-based mixed mode separation

Using the virtual crack closure technique permits to estimate each component of the energy release rate G_1 and G_2 . For isotropic crack problems, each one can be related to their respective load contribution: tension, longitudinal shearing and transversal shearing at crack tip. Consequently, the mode mixity can be simply defined as:

$$\psi_G = \arctan \sqrt{\frac{G_2}{G_1}}. \quad \text{eq. II-44}$$

Considering for the case of crack propagation in isotropic media, energy release rate and stress intensity factors can be related using the relations:

$$G_1 = \frac{K_I^2}{E} \quad \text{and} \quad G_2 = \frac{K_{II}^2}{E}. \quad \text{eq. II-45}$$

This phase angle definition (eq. II-44) verify for isotropic crack propagation the following relation:

$$\tan(\psi_G) = \frac{K_{II}}{K_I}. \quad \text{eq. II-46}$$

In the case of interfacial cracks, the ratio of G_2/G_1 is not constant along the distance ahead crack tip (as verified in section III.3.2). This method leads to an approximation of the mixed mode angle but no unambiguous value.

II.5.4 Oscillatory ERR-based mixed mode separation method

Proposed by [Beuth 1996], following method aims unambiguously estimation of the mode mixity for interfacial problems. That is to say, a method which provides the phase angle for interfacial crack independently from the length ahead of the crack tip taken to 'measure' the relative crack tip sliding and opening.

Using a work of Suo (1990), Beuth adopt the following stress quantity at a distance x in front of the crack tip:

$$\sigma_H(x,0) \equiv \sqrt{\frac{H_{22}}{H_{11}}} \sigma_{yy} + i\sigma_{xx} = \frac{(K_I + iK_{II})x^{i\varepsilon}}{\sqrt{2\pi x}}. \quad \text{eq. II-47}$$

Formulation in eq. II-47 is similar to eq. II-7 except in the parameters H_{11} and H_{22} brought by Suo and defined further. Moreover, another crack tip opening quantity similar to eq. II-13 is adopted:

$$\delta_H(x,0) \equiv \sqrt{\frac{H_{11}}{H_{22}}} \delta_y + i\delta_x = \frac{2H_{11}(K_I + iK_{II})|x|^{1/2+i\varepsilon}}{\sqrt{2\pi}(1+2i\varepsilon)\cosh(\pi\varepsilon)}. \quad \text{eq. II-48}$$

Quantities H_{11} and H_{22} are functions of the material elastic properties constituting the interface. These quantities are given in [Beuth 1996] and are not required for the comprehension.

The following energy quantities are then proposed, in which the overbar denotes the complex conjugate, and Δa an infinitesimal crack extension:

$$\Phi_1 \equiv \operatorname{Re} \left[\int_0^{\Delta a} \sigma_H(x) \overline{\delta_H(\Delta a - x)} dx \right] \quad \text{eq. II-49.a}$$

$$\Phi_2 \equiv \operatorname{Re} \left[\int_0^{\Delta a} \sigma_H(x) \delta_H(\Delta a - x) dx \right]. \quad \text{eq. II-49.b}$$

The energy release rate at crack tip is thus formulated as:

$$G_1^b = \lim_{\Delta a \rightarrow 0} \frac{1}{4\Delta a} [\Phi_1 + \Phi_2] \quad \text{eq. II-50.a}$$

$$G_2^b = \lim_{\Delta a \rightarrow 0} \frac{1}{4\Delta a} [\Phi_1 - \Phi_2] \quad \text{eq. II-50.b}$$

The equations eq. II-50.a and eq. II-50.b verify the VCCT-definition given in section II.4.2. Equations eq. II-34 and eq. II-35 defining G_1^b and G_2^b can be reestablished using the left parts of eq. II-47 and eq. II-48, with eq. II-49.a and eq. II-49.b.

Thus, σ_H and δ_H can also be defined using the oscillatory stress intensity factor, i.e. using the right parts in eq. II-47 and eq. II-48. Beuth shows that Φ_1 can be expressed as a non-oscillatory function, that is to say without the power in $i\varepsilon$:

$$\Phi_1 = \frac{\Delta a H_{11}}{2 \cosh^2(\pi\varepsilon)} K \bar{K}. \quad \text{eq. II-51}$$

Obtaining Φ_2 in a similar form (with oscillatory term) is not possible, so that Beuth simply proposed an alternative Φ'_2 , which is the Φ_2 -function in which he 'eliminated' the oscillatory term

$$\Phi'_2 = \operatorname{Re} \left[\left(\frac{\Delta a}{h} \right)^{-2i\varepsilon} \int_0^{\Delta a} \sigma_H(x) \delta_H(\Delta a - x) dx \right]. \quad \text{eq. II-52}$$

In eq. II-52, h is a normalizing length equal to the thinner layer thickness constituting the interface. Using these formula, G_1 and G_2 can be determined using eq. II-50.a and eq. II-50.b. This solution is unaffected by the $i\varepsilon$ -singularity and then pseudo Δa -independent, that is to say, the solution does not oscillate with the distance Δa ahead crack tip.

Adapted for FEM, eq. II-49.a and eq. II-52 leads to the following definition of Φ_1 and Φ_2 :

$$\begin{aligned} \Phi_1 &= \operatorname{Re} \left[F_{H_k} \overline{\delta_{H_{ij}}} \right] \\ \Phi'_2 &= \operatorname{Re} \left[\left(\frac{\Delta a}{h} \right)^{-2i\varepsilon} F_{H_k} \delta_{H_{ij}} \right] \end{aligned} \quad \text{eq. II-53}$$

with:

$$F_{H_k} = \sqrt{\frac{H_{22}}{H_{11}}} F_{y_k} + i F_{x_k} \quad \text{eq. II-54.a}$$

$$\delta_{H_{ij}} = \sqrt{\frac{H_{11}}{H_{22}}} \delta_{y_{ij}} + i \delta_{x_{ij}}. \quad \text{eq. II-54.b}$$

In eq. II-54.a, F_{x_k} and F_{y_k} make reference to the nodal forces at crack tip in the respective directions x and y (refer to Figure 9). In eq. II-54.b, $\delta_{x_{ij}}$ and $\delta_{y_{ij}}$ make reference to the crack tip opening at the first node pair ahead crack tip, i.e. distance projected in the respective direction x and y between nodes i and j (refer to Figure 9).

Hence G_1 and G_2 are found using this modified VCCT-formulation of Beuth, the mixed mode angle can be determined by

$$\psi_{\text{Beuth}} = \arctan \sqrt{\frac{G_2^b}{G_1^b}}, \quad \text{eq. II-55}$$

in which equation, G_1 and G_2 are those defined in eq. II-50.a and eq. II-50.b.

II.5.5 Phase Angle Estimation from VCCT and SIF

The following method to estimate mode mixity at crack tip was previously reported by [Agrawal 1996]. This method determines the mixed-mode angle using the energy release rate ratio G_2/G_1 in combination with the stress intensity factor definition suggested by Rice ([Rice 1965]) to take the oscillatory behavior into account.

$$\sigma_{yy} + i\sigma_{xy} = \frac{K_I + iK_{II}}{\sqrt{2\pi r}} r^{i\varepsilon} \quad \text{eq. II-56}$$

Separating eq. II-56 into real and imaginary part leads to the following expression of the stress at crack tip:

$$\sigma_{yy} = \frac{1}{\sqrt{2\pi r}} [K_I \cos(\varepsilon \ln r) - K_{II} \sin(\varepsilon \ln r)] \quad \text{eq. II-57.a}$$

$$\sigma_{xy} = \frac{1}{\sqrt{2\pi r}} [K_{II} \cos(\varepsilon \ln r) + K_I \sin(\varepsilon \ln r)]. \quad \text{eq. II-57.b}$$

Then, eq. II-13 defining the displacement field at crack tip is considered. Displacement in each direction can be separated by separating real and imaginary parts. It leads to eq. II-39 and eq. II-40. Both equations eq. II-39 and eq. II-40 are injected with eq. II-57.a, eq. II-57.b into the VCCT formulation eq. II-34 and eq. II-35. It permits establishing eq. II-58.a and eq. II-58.b

$$G_1 = \frac{\Lambda}{4\sqrt{2\pi}} [f_C I_C - f_S I_S + (K_I^2 + K_{II}^2) I_0]$$

$$G_2 = \frac{\Lambda}{4\sqrt{2\pi}} [-f_C I_C + f_S I_S + (K_I^2 + K_{II}^2) I_0].$$

eq. II-58

Parameter Λ is defined by eq. II-21. I_C , I_S and I_0 are integral functions of the crack tip opening over the length Δa :

$$I_C = \frac{1}{\Delta a} \int_0^{\Delta a} \cos[\varepsilon \ln(r(\Delta a - r))] \sqrt{\frac{r}{\Delta a - r}} dr$$

$$I_S = \frac{1}{\Delta a} \int_0^{\Delta a} \sin[\varepsilon \ln(r(\Delta a - r))] \sqrt{\frac{r}{\Delta a - r}} dr$$

$$I_0 = \frac{1}{\Delta a} \int_0^{\Delta a} \left\{ \cos \left[\varepsilon \ln \left(\frac{\Delta a - r}{r} \right) \right] - 2\varepsilon \sin \left[\varepsilon \ln \left(\frac{\Delta a - r}{r} \right) \right] \right\} \sqrt{\frac{r}{\Delta a - r}} dr$$

eq. II-59

and

$$f_C = K_I^2 - K_{II}^2 + 4\varepsilon K_I K_{II}$$

$$f_S = 2[K_I K_{II} + \varepsilon(K_{II}^2 - K_I^2)].$$

eq. II-60

The mixed mode energy release rate ratio G_2/G_1 is then obtained by dividing eq. II-58.a with eq. II-58.b and then substituting f_C and f_S with eq. II-60.a and eq. II-60.b. With clever mathematical manipulation, eq. II-61 can be formulated:

$$\frac{G_1}{G_2} = \frac{(k^2 - 1 + 4\varepsilon k)I_C - 2I_S(k + \varepsilon - \varepsilon k^2) + (k^2 + 1)I_0}{-(k^2 - 1 + 4\varepsilon k)I_C + 2I_S(k + \varepsilon - \varepsilon k^2) + (k^2 + 1)I_0} = g.$$

eq. II-61

Defining $g = G_1/G_2$, and $k = K_I/K_{II}$, eq. II-61 is reorganized into the k -polynomial form eq. II-62:

$$\begin{aligned} & [(I_C + 2\varepsilon I_S)(1 + g) + I_0(g - 1)] k^2 \\ & + (4\varepsilon I_C - 2I_S)(1 + g) k \\ & - [(I_C + 2\varepsilon I_S)(1 + g) - I_0(g - 1)] = 0 \end{aligned}$$

eq. II-62

Finally, solving the k -polynomial eq. II-62 leads to a couple of solution k_1 and k_2 . One of the two given solution must be incompatible with the loading conditions at crack tip (crack flanks penetration, sign of crack flanks sliding) and must be eliminated.

Thus, the mixed mode angle can be defined as:

$$\psi_{ki} = \arctan \frac{1}{k_i}$$

eq. II-63

II.5.6 Discussing about the choice of a method

For all existing mixed-mode estimation methods, the mixed-mode ratio at crack tip is unlikely defined because of the reference length. The purpose is not to define, which one gives "true" results and which others "wrong" results because they are all approximations.

The advantage of the "extended SIF-based method" is the consideration of the oscillatory behavior of the stress and strain fields, and moreover the Δa -independency obtained using estimation of the phase angle at multiple distances to the crack tip and then extrapolation at $\Delta a = 0$. This method is moreover easy to implement as post-processing in the simulation.

For this work, we decide to choose the extended SIF-based method presented in section II.5.2.

II.6 Temperature and Strain Rate Effects on Crack Tip Field

Thermosetting polymers used to encapsulate electronic packages are linear viscoelastic. Studying crack propagation at their interfaces involves understanding what the viscoelasticity is and how it can affect crack propagation. Viscoelasticity means in a few words that the material elastic properties show temperature and load-rate dependencies. Moreover, elastic constants show a strong drop at the glass transition temperature T_G (Figure 12). The glass transition temperature for thermosetting polymers is generally situated between 100°C and up to 200 °C. The viscoelastic influence is nearly negligible far away below T_G but is much significant at temperatures above T_G . A phenomenological description is given in section II.6.1.

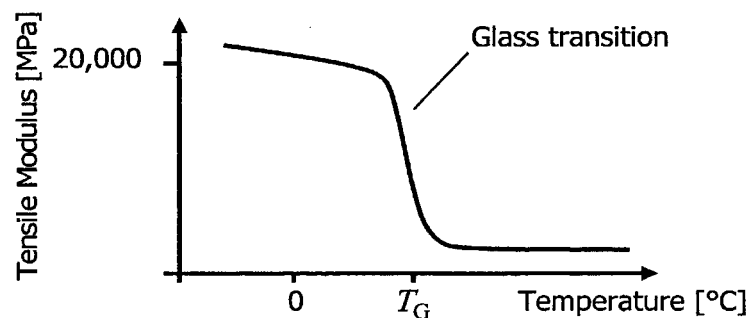


Figure 12: Temperature dependency of molding compounds

The energy release rate at an existing crack tip is affected by the material stiffness change, depending on temperature and strain rate variations. In a simplistic way, G is proportional to a stress multiplied by a deformation. Considering that material stiffness depends on the temperature, the energy release rate also depends on the temperature, especially when approaching T_G ([Liu 2002]).

[Xiong 2000] showed that neglecting viscoelastic effects of EMC could induce important errors in the estimation of the energy release rate and on the estimation of the mode mixity. Moreover, it was shown that temperature drastically affects load conditions at crack tip. More precisely, they found that G_C increases by decreasing temperature or increasing load rate.

[Nishimura 1992] measured the adhesion strength between molding compound and metal allows and observed that it decreases by increasing the temperature.

[Tay 1999] developed a so-called 'Bulge' test setup to explore interfacial toughness between EMC and copper leadframe under mode I loading. They also found that the critical energy release rate dramatically decreases with temperature.

[Hu 2007] showed with end-notched flexure specimens (ENF) EMC/copper that the temperature and loading rate also affect the critical energy release rate. They confirmed as [Xiong 2000] that load at crack tip decreases by increasing the temperature, but found that

the critical energy release rate increases with the temperature. It is in contradiction with former investigations. Their explanation is that strain amount increases with the temperature faster than energy stress reduces, which results to an increase of the strain energy with respect to the temperature.

II.6.1 Phenomenological Description

The time dependent behavior of viscoelastic materials can be characterized using different methods. One is the relaxation test (Figure 13.a), where a specimen is submitted to a constant deformation (within the elastic limit) and load response is measured. The other is the creep test (Figure 13.b), where the sample is submitted to a constant stress and strain response is measured.

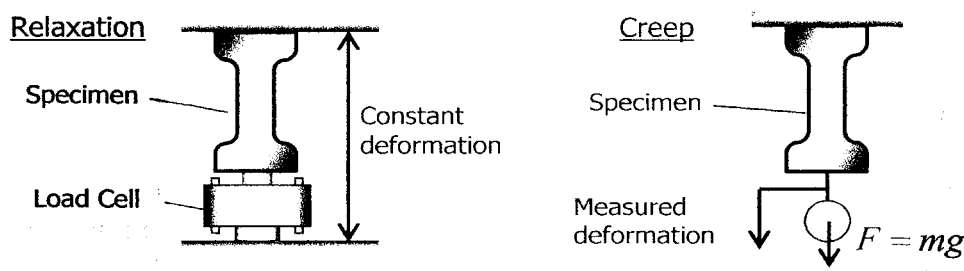


Figure 13: Creep and Relaxation test

Depending on the temperature, the relaxation (or creep) requires days or years to occur entirely. Relaxation occurs faster at higher temperatures ([Schwarzl 1990]). During the relaxation test, polymers firstly show a brittle elastic behavior, given by the strength of the covalent liaison. This is the glassy state. As time advances, strain response first shows small variations (Figure 14), which corresponds to local changes in the molecular structure of the polymer, i.e. conformation change and rotation of small piece of the main polymer chain which brings a first contribution to the material deformability.

The glass-rubber transition follows the glassy state. It occurs as a strong softening of the material, which deformability increases from a factor from 10^2 to 10^4 . This is due to molecule chains reorientation and unknotting under the stress influence. It occurs until all molecules are reordered.

This is then followed by the rubber-elastic plateau, in which deformation stops increasing. This state stays unchanged in the case of a cross-linked polymer, for which ones no viscous flow can occur.

Finally, polymers capable of viscous flow exhibit a further deformation increase after a long time, with a constant strain rate deformation rate corresponding to C_∞ or η_{m+1} (long term compliance, Figure 19) in the generalized Kelvin-Voigt model.

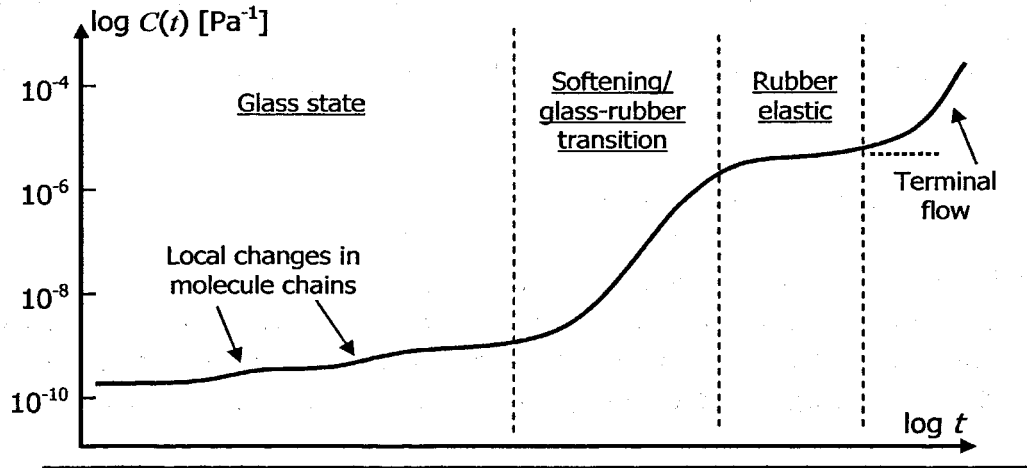


Figure 14: Relaxation Mechanisms

II.6.2 Material Constitutive Laws for Linear Viscoelasticity

A tensile specimen of a polymer with viscoelastic material behavior, subjected to an uniaxial strain exhibits a time-dependent stress response. This stress comes from the superposition of three different contributions (Figure 15):

- a pure elastic contribution
- a time-dependent or retarded elastic contribution
- viscous flow

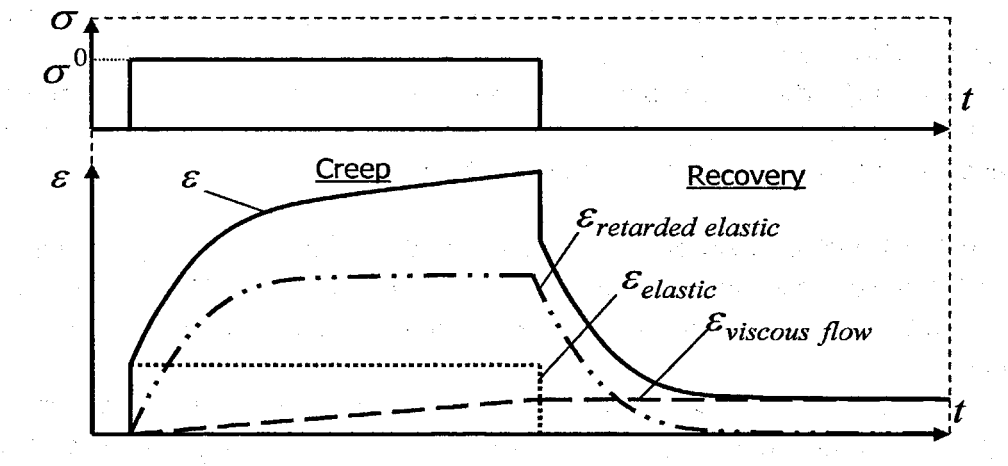


Figure 15: Creep test-response of Polymer

Pure elastic and retarded elastic contribution in the strain response are reversible. The viscous flow contribution is permanent, and corresponds to an irreversible deformation. All polymers are not susceptible to flow. Moreover, viscous flow does not appear by low loading, and can only appear after a very long time.

II.6.2.1 Kelvin-Voigt Spring-dashpot-model

Elementary spring-dashpot model are often used to describe time-dependent compliance of viscoelastic media ([Schwarzl 1990] and [Strobl 1996]). The most well-known are the Kelvin-Voigt and Maxwell models.

The Kelvin-Voigt model is composed of a spring parallelized with a dashpot (Figure 16.a), which permits to describe in a simple way creep deformations. In this model, stress is equal to the sum of spring reaction (pure elastic) and dashpot reaction (viscous reaction).

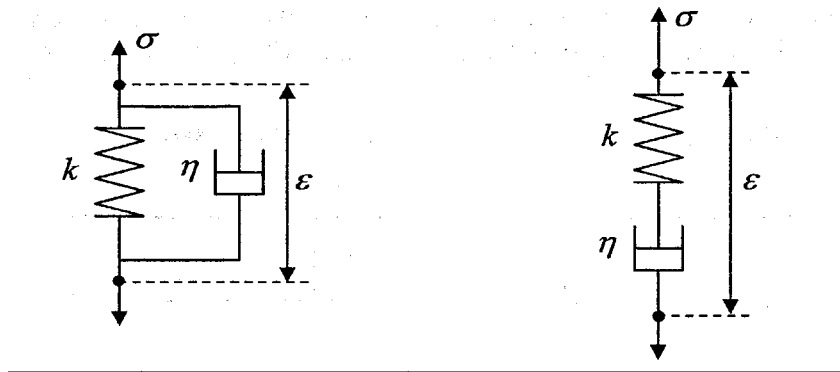


Figure 16.a: Kelvin-Voigt;
b: Maxwell elementary model

Uniaxial stress can consequently be written as $\sigma = k \varepsilon + \eta \dot{\varepsilon}$, corresponding to the sum of both pure elastic and strain rate-dependent (viscous) contributions. It leads to differential equation eq. II-64:

$$\dot{\varepsilon} + \frac{k}{\eta} \varepsilon = \frac{1}{\eta} \sigma. \quad \text{eq. II-64}$$

Initial stress-free condition is considered and a constant load is instantaneously applied at time zero. Solving eq. II-64, neglecting the stress component, furnishes the time-dependent to the strain response (eq. II-65):

$$\varepsilon(t) = \varepsilon_0 + \frac{\eta}{k} \left(1 - \exp\left(\frac{-k}{\eta} t\right) \right). \quad \text{eq. II-65}$$

The strain response to a constant stress solicitation is characterized by an instantaneous strain response, followed by a retarded strain response, decreasing in strain rate until final strain value (Figure 17).

II.6.2.2 Maxwell spring-dashpot-model

The Maxwell spring-dashpot-series model with an initially deformation-free state is now considered. This model permits to illustrate in a simple way the relaxation phenomenon. The differential equation describing this system is defined in eq. II-66:

$$\dot{\varepsilon} = \frac{\sigma}{\eta} + \frac{\dot{\sigma}}{k}. \quad \text{eq. II-66}$$

If initial stress and strain free conditions are observed, stress response of an instantaneous strain solicitation is described by eq. II-67.

$$\sigma(t) = \sigma_0 \exp\left(-\frac{k}{\eta}t\right). \quad \text{eq. II-67}$$

Material behavior under a constant strain echelon is characterized by an instantaneous stress response, followed by a slow stress decrease (Figure 17.b). It corresponds to material relaxation.

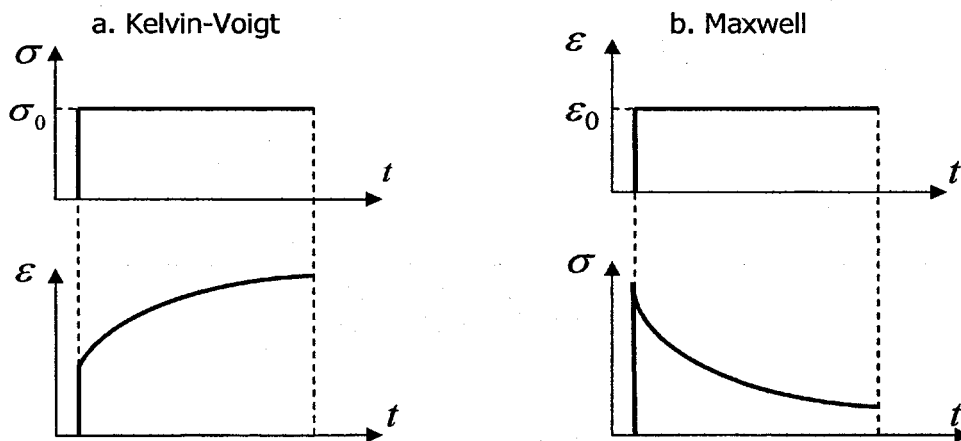


Figure 17.a. Kelvin-Voigt Strain Response to constant Stress Sollicitation
b. Maxwell Stress Response to constant Strain Sollicitation

A better description of linear viscoelasticity requires in any case more sophisticated models. Two models are widely used, the generalized Maxwell model (Figure 18) and the generalized Kelvin-Voigt model (Figure 19). Removing spring $n+1$ in the generalized Maxwell model leads to a model including viscous flow, and removing dashpot $m+1$ in the generalized Kelvin-Voigt model furnishes a model without viscous flow.

II.6.2.3 Generalized Maxwell-model

The model described further in this paragraph permits to establish the so-called Prony series. Generalized Maxwell-model is constituted by several Maxwell elementary models assembled in parallel (Figure 18). Each elementary Maxwell element i constituted of a spring and a dashpot in series is governed by the differential equation eq. II-66.

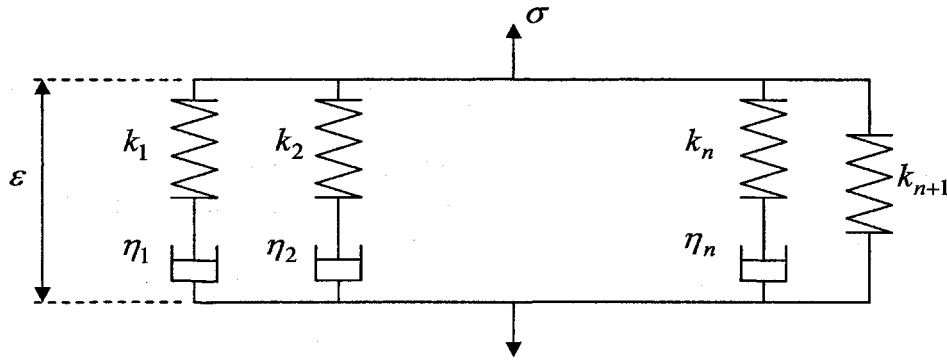


Figure 18: Generalized Maxwell model

Transposed in the Laplace space, each elementary stress contribution is given in eq. II-68, where over-lined expressions denote transposed function in the Laplace space, and p the Laplace variable.

$$p\overline{\sigma}_i + \frac{k_i}{\eta_i}\overline{\sigma}_i = p\overline{\varepsilon} \quad \text{and} \quad \overline{\sigma}_{n+1} = \frac{k_{n+1}}{p}\overline{\varepsilon} . \quad \text{eq. II-68}$$

Total stress is defined by the sum of all elementary stress:

$$\sigma(t) = \sum_{i=1}^n \sigma_i(t) . \quad \text{eq. II-69}$$

A factorization of the eq. II-68 injected into the eq. II-69 permits to establish the eq. II-70.

$$\overline{\sigma} = \frac{k_{n+1}}{p}\overline{\varepsilon} + \left[\sum_{i=1}^n \frac{\eta_i}{1 + p\frac{\eta_i}{k_i}} \right] p\overline{\varepsilon} . \quad \text{eq. II-70}$$

Expression eq. II-70 is then transposed back in the temporal space using inverse-Laplace transformation (eq. II-71):

$$\sigma(t) = k_{n+1} \varepsilon(t) + \left[\sum_{i=1}^n k_i \exp\left(-t\frac{k_i}{\eta_i}\right) \right] \otimes \dot{\varepsilon}(t) , \quad \text{eq. II-71}$$

which leads to the eq. II-72.

$$\sigma(t) = k_{n+1} \varepsilon(t) + \sum_{i=1}^n \left[\int_{-\infty}^t k_i \exp\left(-t'\frac{k_i}{\eta_i}\right) \dot{\varepsilon}(t-t') dt' \right] . \quad \text{eq. II-72}$$

Using the distributive property of the integration permits to include the series into the integral:

$$\sigma(t) = \int_{-\infty}^t E(t-t') \dot{\varepsilon}(t') dt' , \quad \text{eq. II-73}$$

With

$$E(t) = k_{n+1} + \sum_{i=1}^n \left[k_i \exp\left(-\frac{t}{\tau_i}\right) \right] \text{ and } \tau_i = \frac{\eta_i}{k_i}. \quad \text{eq. II-74}$$

The time-dependent tensile modulus $E(t)$ is therefore defined as a finite series also known as the Prony-series. The n couples of parameters $k_i; \eta_i$ are used to describe the viscoelastic material properties. The k_{n+1} term corresponds to the long term tensile modulus E_∞ . In the case of material capable of viscous flow, spring $n+1$ is removed from model and E_∞ vanishes.

II.6.2.4 Generalized Kelvin-Voigt-model

The generalized Kelvin-Voigt model is a further possibility to model the behavior of linear viscoelastic materials (Figure 19). This spring-dashpot model permits to establish the Creep-Compliance function.

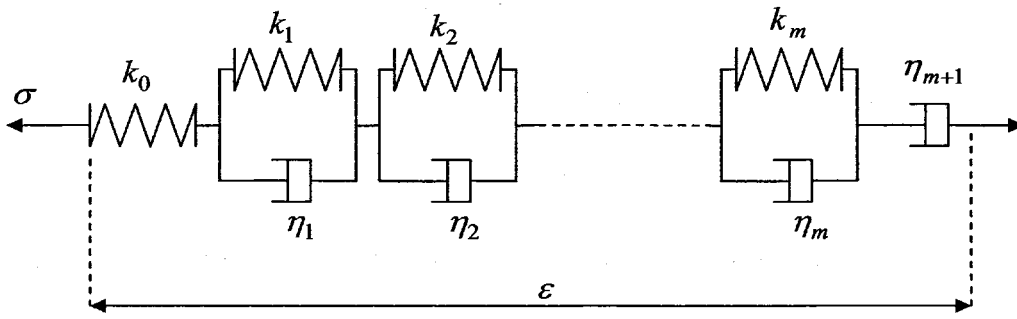


Figure 19: Generalized Kelvin-Voigt model

In the generalized Kelvin-Voigt model (Figure 19), the total strain is given by eq. II-75:

$$\varepsilon(t) = \sum_{i=1}^m \varepsilon_i(t). \quad \text{eq. II-75}$$

Expressed in the Laplace space, eq. II-75 in conjunction with each elementary element differential equation (eq. II-64) leads to:

$$\bar{\varepsilon} = \left[\frac{1}{k_0 p} + \frac{1}{\eta_{m+1} p^2} \right] \bar{\sigma} + \left[\sum_{i=1}^m \frac{\frac{1}{k_i}}{p + \frac{\eta_i}{k_i} p^2} \right] p \bar{\sigma}. \quad \text{eq. II-76}$$

Expression in eq. II-76 expressed back in the temporal space furnishes eq. II-77:

$$\varepsilon(t) = \left[\frac{1}{k_0} + \frac{t}{\eta_{m+1}} \right] \sigma(t) + \sum_{i=1}^m \left[\frac{1}{k_i} \left(1 - \exp\left(-t \frac{k_i}{\eta_i}\right) \right) \right] \otimes \dot{\sigma}(t). \quad \text{eq. II-77}$$

Latter expression finally leads to the resulting strain response to stress solicitation history:

$$\varepsilon(t) = \int_{-\infty}^t C(t-t') \dot{\sigma}(t') dt', \quad \text{eq. II-78}$$

with

$$C(t) = \frac{1}{k_0} + \frac{t}{\eta_{m+1}} + \sum_{i=1}^m \frac{1}{k_i} \left(1 - \exp\left(-\frac{t}{\tau_i}\right) \right) \quad \text{and} \quad \tau_i = \frac{\eta_i}{k_i}. \quad \text{eq. II-79}$$

C is the creep-compliance function. E_0 is defined as the instantaneous tensile modulus, equal to the inverse of the instantaneous compliance C_0 (eq. II-80). C_∞ is defined as the long term material fluidity, $1/C_\infty$ as the long term material viscosity. Material fluidity corresponds to the material flowing-capability and vanishes if the considered material can not flow (dashpot $m+1$ is removed in the generalized Kelvin-Voigt model).

$$C_0 = \frac{1}{E_0} = \frac{1}{k_0} \quad \text{and} \quad C_\infty = \frac{1}{\eta_{m+1}} \quad \text{eq. II-80}$$

Variables $\tau_i = \eta_i/k_i$ are the material retardation times. The corresponding k_i factors for the time-dependent tensile modulus, respectively the $1/k_i$ factors for the creep function correspond to the discrete retardation magnitude. For both the generalized Maxwell and generalized Kelvin-Voigt models, the material time dependency is completely determined by the definition of the k_i and τ_i parameters.

II.6.2.5 Material Response to Sinusoidal Excitations

Due to the retarded stress response, viscoelastic media undergoing sinusoidal strain excitations exhibits stress-strain curves with hysteresis (Figure 20). Response amplitude depends on the temperature and frequency.

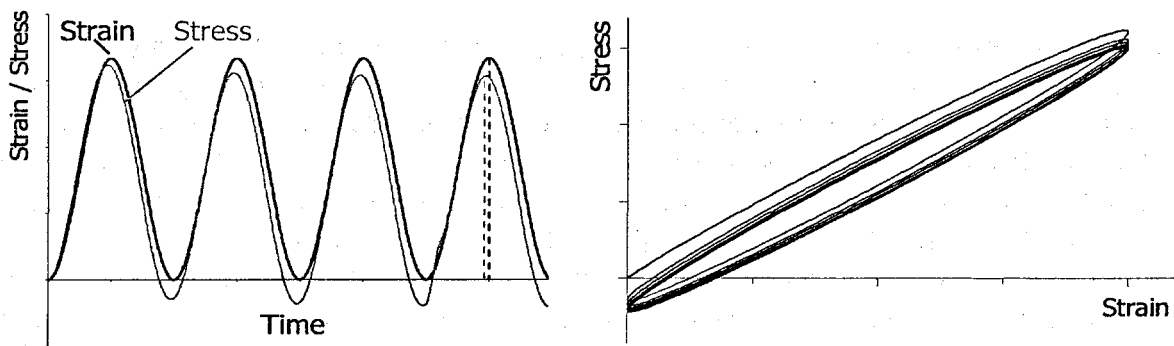


Figure 20: Viscoelastic Response to Sinusoidal Excitation

These observations lead to the idea that viscoelastic materials can be characterized by measuring the dynamical response of a sinusoidal excitation varying in frequency.

A sinusoidal strain excitation of angular frequency ω is considered.

$$\varepsilon(t) = \varepsilon_0 e^{i\omega t}. \quad \text{eq. II-81}$$

The stress response is defined by the generalized Maxwell model (eq. II-73). Combined with the Prony definition of the tensile modulus (eq. II-74), in which strain excitation defined above is injected, the stress response to sinusoidal strain is obtained (eq. II-82).

$$\sigma(t) = \int_{-\infty}^t \left(k_{n+1} + \sum_{i=1}^n k_i \exp\left(-\frac{t-t'}{\tau_i}\right) \right) \cdot (i\omega \varepsilon_0 \exp(i\omega t')) dt'. \quad \text{eq. II-82}$$

Mathematical expanding and separation of eq. II-82 into real and imaginary part leads to eq. II-83.

$$\sigma(t) = (E'(\omega) + iE''(\omega)) \varepsilon_0 \exp(i\omega t). \quad \text{eq. II-83}$$

The complex elastic modulus is given in eq. II-84:

$$\begin{aligned} E(\omega) &= E'(\omega) + iE''(\omega), \\ E'(\omega) &= \sum_{i=1}^n k_i \frac{\omega^2 \tau_i^2}{1 + \omega^2 \tau_i^2}, \\ E''(\omega) &= \sum_{i=1}^n k_i \frac{\omega \tau_i}{1 + \omega^2 \tau_i^2}. \end{aligned} \quad \text{eq. II-84}$$

The real part of the dynamical tensile modulus corresponds to the in-phase (or instantaneous) stiffness and the imaginary part to the out-of-phase (or retarded) stiffness. The former is known as storage modulus and the latter as loss modulus.

In eq. II-84, parameters k_i and τ_i correspond the elementary elastic and retardation constants used in the Prony series (eq. II-74) and in the Creep-Compliance function (eq. II-79).

Storage and loss modules are measured using Dynamical Mechanical Analyses (DMA) with respect to the frequency and temperature. A DMA consists in a classical uniaxial stress test or alternatively in a three points bending test where a sinusoidal strain excitation is applied to the specimen. Frequency is varied over several decades in the log domain. The temperature is also varied over the temperature range desired for the material characterization, classically between -50 °C and 200 °C. Obtained data allows to establish a master-curve of the tensile modulus (or alternatively of the shear modulus). The master curve is used to fit the Prony series and to determine the Prony parameters k_i and τ_i (section II.6.3). For fatigue purpose, nominal strain amplitude given during the test must remain low in order to avoid the appearance of damage phenomenon during the measures.

II.6.3 Time-Temperature Correspondence

II.6.3.1 Time-Temperature Superposition Principle

Polymer deformability shown in Figure 14 is given for a constant temperature. The temperature has an influence on the relaxation process. Increasing the temperature accelerates the relaxation process, and vice versa. Using a logarithmic time scale, changing the temperature leads to a translation of the relaxation curve along the time-axis. The temperature affects neither the form of the curves or the compliance levels. This empirical law is known as the time-temperature superposition principle.

A mathematical formulation of this empirical observation is given by eq. II-85:

$$E(T, \log t + \log a_T(T)) = E(T_0, \log t). \quad \text{eq. II-85}$$

Expressed in a logarithmic coordinates system, eq. II-85 becomes eq. II-86:

$$E(T, t') = E(T_0, t) \quad \text{eq. II-86}$$

with $t' = a_T(T)t$.

In eq. II-86, t' is called 'reduced time'. The time-temperature superposition principle is used to determine the master relaxation curve shown in Figure 14. Relaxation curves are obtained by assembling different curves corresponding to different time-segments, each one obtained by different temperatures. One of these temperatures is chosen to be the reference temperature T_0 (T_G is often taken as reference temperature). Other curves (obtained by different temperatures) are then shifted along the time-axis until they all define together a continuous and smooth curve defining the elastic constant with respect to the temperature (Figure 21). This curve is called the master curve.

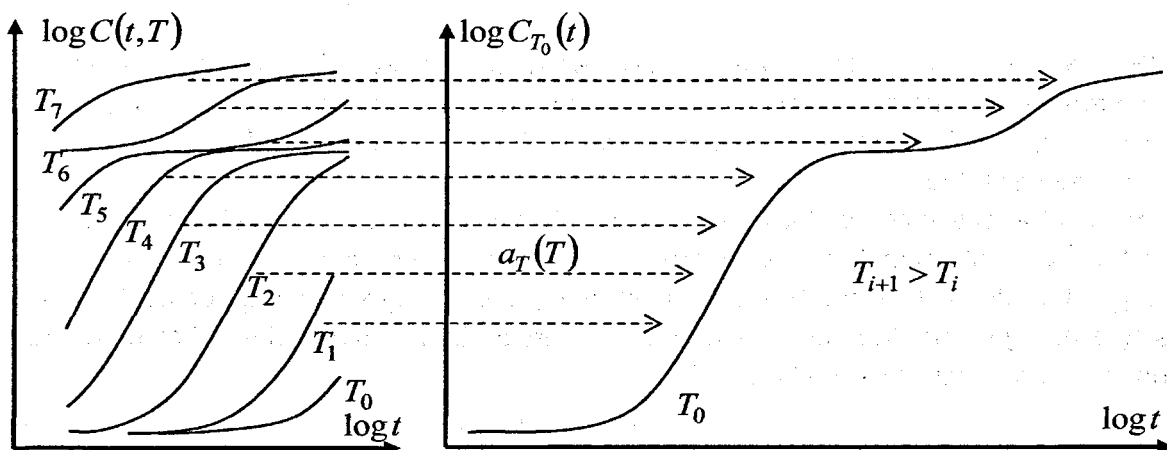


Figure 21: Time-Temperature Superposition: Mastering

II.6.3.2 Shift Function

The master curve defines a material elastic constant by a reference temperature T_0 . To be obtained, all individual parts except the one obtained by T_0 are shifted along the temperature axis. Amount of shifting at each temperature defines a so called shift parameter for the given temperature. All the shift parameters are used to define the shift function $a_T : T \rightarrow a_T(T)$.

With the shift function, the master curve can be expressed at any temperature, i.e. can be shifted at any desired temperature. So, the Prony series describes the rate dependency of the material, and the master curve describes the temperature dependency.

It means that knowing both permits to determine the elastic constant at any time (or frequency) and for any temperature. It constitutes a complete characterization of a viscoelastic constant (tensile modulus, shear modulus, etc.).

A typical form for the shift function for thermosetting polymers is given in Figure 22 below.

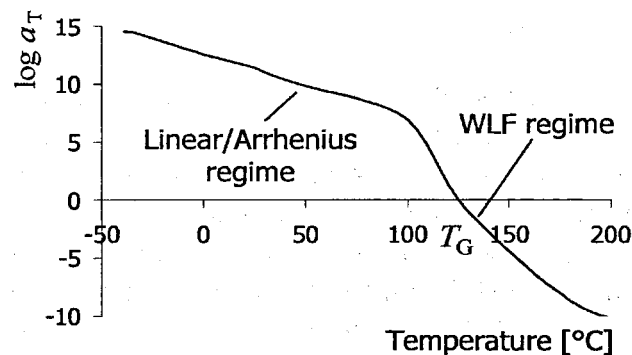


Figure 22: Typical Shift Function for thermosetting Polymers

A DMA, a series of creep tests or a series of relaxation tests at different temperatures deliver the Prony parameters and also the Shift function in a tabular form. For modelization purpose, it may be preferable to define the shift function as a mathematical expression rather than as a table.

Experimental observations have led to empirical mathematical formulation of the shift function. One of them is the WLF-function, from its author names (William, Landell and Ferry). It is defined in eq. II-87. Parameters C_1 and C_2 are material constants obtained using a fitting of the WLF-function with experimental data. This model is suitable around T_G and above, but inappropriate below T_G .

$$\log a_T(T) = \frac{C_1(T - T_0)}{C_2 + (T - T_0)} \quad \text{eq. II-87}$$

Other approximations can be used for the more linear part of the shift function (under T_G), for example the Arrhenius equation based on the chemical reaction kinetic and given in eq. II-88, where E_a is a reaction activation energy and R the gas constant

$$\log a_T(T) = \frac{-E_a}{2.303R} \left[\frac{1}{T} - \frac{1}{T_0} \right]. \quad \text{eq. II-88}$$

II.6.3.3 Poisson's Ratio

A sample submitted to a uniaxial relaxation test in the x -direction is considered. It can be assumed that $\varepsilon_{xx}(t) = \varepsilon_{xx}^0$ is a constant. Consequently, the Poisson ratio can be defined as the eq. II-89:

$$\nu(t) = -\frac{\varepsilon_{yy}(t)}{\varepsilon_{xx}^0}. \quad \text{eq. II-89}$$

[Wunderle 2003] furnishes an estimation of the Poisson ratio for a classical thermosetting polymer. It is performed through the characterization of the tensile and shear modules, and then using eq. II-90:

$$\nu(t) = \frac{E(t)}{2G(t)} - 1. \quad \text{eq. II-90}$$

The obtained Poisson's ratio is displayed in Figure 23. It reveals that the Poisson's ratio exhibits a transition from this nominal value at room temperature to the limit value 0.5 during the glass-rubber transition.

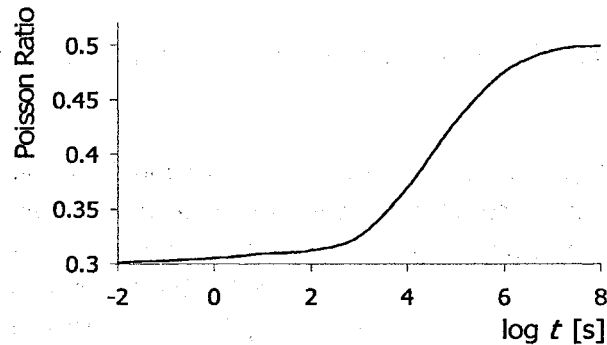


Figure 23: Poisson Ratio for thermosetting Polymers (data from [Wunderle 2003])

This results shows that the Poisson's ratio should not be considered constant in the simulation because obtained results may be very imprecise in the rubber state. It is particularly true for problems where out-of-plane-strain causes mode II loading at crack tip. In this case, considering the Poisson's ratio constant would lead to an underestimation of the mode II amount at crack tip ([Roger 2007]).

II.6.4 Using Linear Elastic Fracture Mechanics with Time-dependent Materials

The fracture concepts discussed until this point come from the linear elastic fracture mechanics (LEFM). Using these concepts with linear viscoelastic materials, which exhibit time dependent properties, poses some questions.

The use of the VCCT as presented in section II.4.2 is only valid in the case of isotherm monotonic loading at crack tip, i.e. at constant temperature and constant strain rate.

For other cases, the Schapery approach ([Schapery 1981], [Wittler 2004]) can be used to estimate the ERR at crack tip even if the material exhibits important elastic change during loading. The Schapery approach is also known as "Correspondence Principle".

II.7 Moisture influence on adhesion strength

One important disadvantage of polymeric molding compound is that they absorb humidity in moist environment ([Shen 1976], [Teverovsky 2002], [Chen 2005]). Moisture absorption causes a degradation of material properties.

As shown by [Dudek 2002] and [Ferguson 2005] moisture causes a decrease of the tensile modulus. [The 2005] showed that moisture also reduces shear strength of epoxy based materials.

[Nishimura 1992] and then [Tay 1999] found that adhesion strength of molding compound/copper interfaces decreases with moisture concentration. [Zhu 2005] and [Dudek 2002] showed that moisture reduces the fracture toughness of molding compounds and confirm former results.

Consequently, depending on the accumulated moisture, fracture toughness of molding compounds should decrease.

According to [Shirangi 2008], moisture diffusion in epoxy molding compounds exposed to humid environment evolves according a two-stage Fickian manner along the time. It means that water is absorbed in two stages. In the first one, water is physically absorbed in the voids of epoxy resin. In this case, absorption increases linearly until saturation is reached. Then in a more long term, water chemically interact with the molding compound and brings a second, slow contribution to water absorption. Increasing the temperature may accelerate humidity absorption, but complete saturation may need several weeks, by high temperature and high humidity concentration storage too.

III. Numerical Background

III.1 VCCT Implementation In Abaqus

III.1.1 General FEM Methodology

According to eq. II-36 and eq. II-37, the energy release rate is estimated using nodal displacement and nodal forces at crack tip. Finite element analyzes provide the nodal reaction forces only where external boundary conditions are applied. The nodal forces can not be directly estimated anywhere in the model. They must be extrapolated subsequently through the estimated nodal displacement and the individual elements stiffness. This approach provides a very imprecise estimation of the nodal forces.

III.1.2 Abaqus 6.8 VCCT Implementation

In Abaqus, another method is chosen to estimate nodal forces at crack tip when using the Abaqus VCCT features. The method consists to model each partner constituting the interface separately and to assemble them using a contact interaction. A contact interaction permits the simulation of contact between two parts in an assembly, i.e. to avoid interpenetration and estimate contact forces.

To solve the overall problem, initial virtual forces – estimated through a boundary condition equilibration - are applied on the nodes constituting the contact interface.

Subiterations are performed in which contact forces on the interfacial nodes are tuned in order to bring the contact interpenetration or contact opening within a certain tolerance.

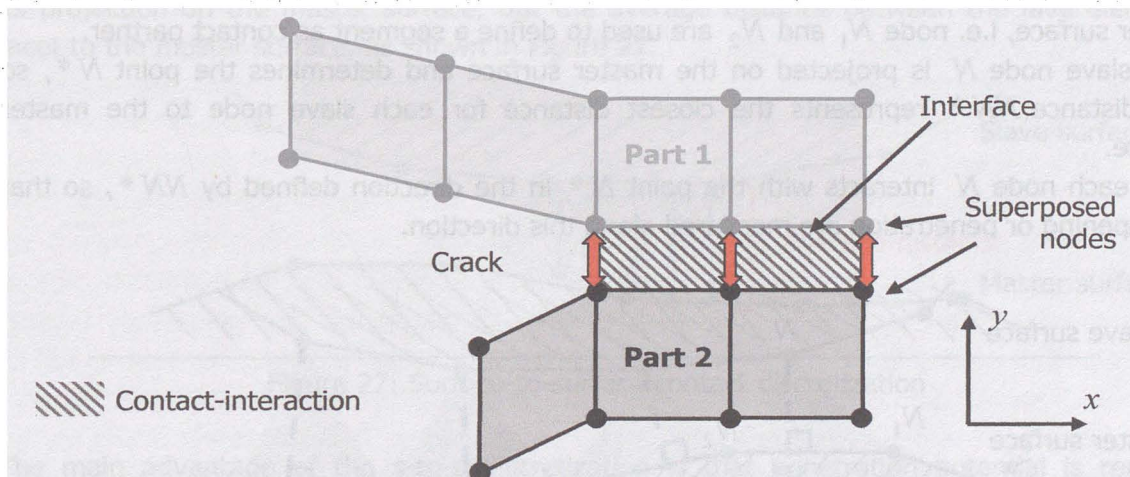


Figure 24: Contact Interaction used for the Abaqus VCCT

In analysis involving the VCCT, a contact interaction is modeled at the material interface. The system uses the contact interaction to maintain the part joined along the undelaminated are, but allows contact separation where the interface is predefined as delaminated (Figure 24).

Virtual forces obtained at the node constituting the delamination front are then used to estimate the energy release rate (eq. II-36 and eq. II-37).

III.1.3 Contact Interaction: Background of VCCT implementation

Algorithmic chosen to solve the contact interaction depends on two main criteria: the choice of contact discretization and choice of contact enforcement ([Abaqus 2] and [Abaqus 3]). The quality of the solution is linked to these two aspects, i.e. the precision of the interfacial forces estimated and applied to the interfacial nodes. It affects consequently directly the precision of the energy release rate estimation.

III.1.3.1 Contact Discretization

Basically, contact interaction acts between two user-defined surfaces; one is the master surface and the other the slave surface. The contact discretization defines how interpenetration or contact opening between contact partners is detected. Depending on the discretization method, only nodes or also surface geometry on one or both surfaces are considered in the interaction. Two discretization methods are proposed in Abaqus, the node to surface discretization method (n-to-s) and the surface to surface method (s-to-s).

- Node to surface discretization method

In a node to surface interaction, nodes of the slave surface and surface constituted from master surface nodes are considered.

A node N is considered on the slave surface (Figure 25). Its two closest neighbors on the master surface, i.e. node N_1 and N_2 are used to define a segment as contact partner.

Each slave node N is projected on the master surface and determines the point N^* , so that distance NN^* represents the closest distance for each slave node to the master surface.

Then each node N interacts with the point N^* in the direction defined by NN^* , so that slip, opening or penetration are measured along this direction.

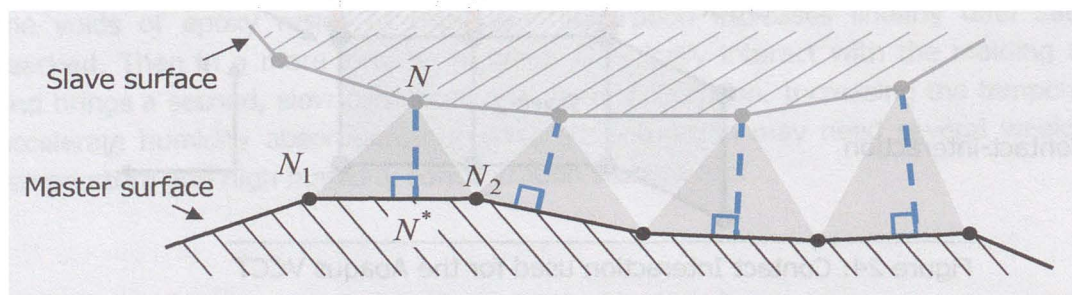


Figure 25: Node-to-surface contact discretization

The n-to-s contact discretization does not take into account the shape of the slave surface. The slave surface is rather considered as a series of nodes. Consequently, if the mesh

refinement over the slave surface is much larger than the mesh refinement over the master surface, master surface can penetrate the slave surface between its nodes, as shown in Figure 26 between nodes N_1 and N_2 .

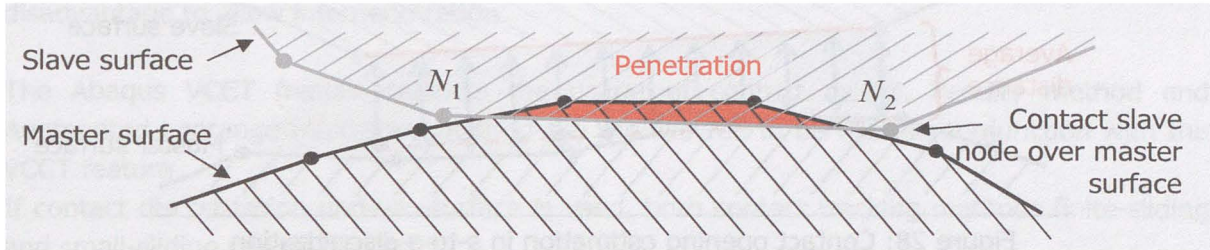


Figure 26: Penetration by node-to-surface discretization

To avoid penetration with n-to-s discretization and to get a better accuracy the most refined surface should be defined as the slave surface. Moreover, the stiffer the master body, the smaller its deformation between nodes N_1 and N_2 , and the smaller the penetration in the slave body. Then, if both bodies have equivalent mesh refinement, master surface should be defined over the stiffer body.

- Surface to surface contact discretization

In the surface-to surface discretization, interaction is not only considered on the nodes of the slave surface but also on element faces defining the slave surface.

The direction taken to measure slip, opening or penetration is the normal to the slave surface (instead of the normal to the master surface is n-to-s).

Then, distance considered between the surfaces is not the distance between slave nodes to its projection on the master surface, but the average distance between the slave elements facet to the master surface, as shown in Figure 27.

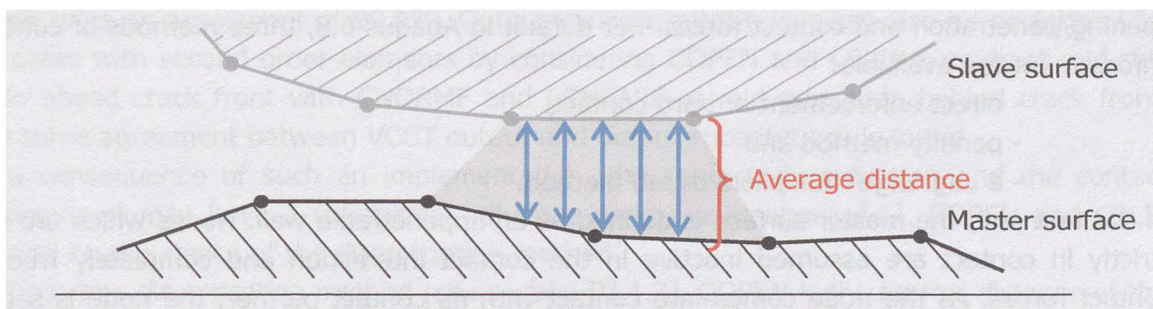


Figure 27: Surface-to-surface contact discretization

The main advantage of the s-to-s discretization is that penetration potential is reduced because both master and slave surfaces are considered. Compared to n-to-s the computation time is higher. In the case of two surfaces with analog mesh refinement, contact distance is estimated using 5 nodal positions (grey area in Figure 27), three on master surface and two on slave surface.

If the master surface is much more refined than the slave surface (Figure 28), distance is averaged with much more nodes (seven in this case), depending on the ratio of node density

of master surface over node density of slave surface. Surface-to-surface can consequently be much more time consuming than node-to-surface discretization.

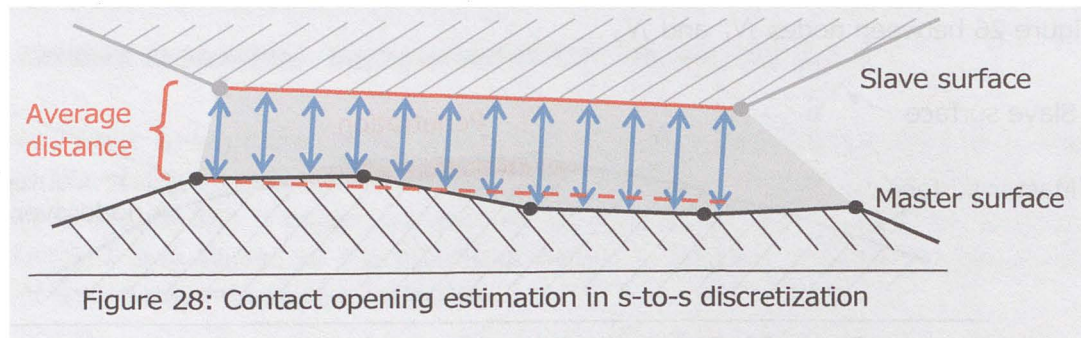


Figure 28: Contact opening estimation in s-to-s discretization

III.1.3.2 Contact Tracking

The finite and small sliding tracking methods define how the master/slave node partners are detected in the contact discretization. Finite sliding is the default method. It allows large motions and rotation between both contact partners. If motion occurs during a step, slave nodes may change of node neighbors on the master surface.

For example for n-to-s discretization (Figure 25), if N_1 moves along the master surface and consequently N^* comes out of M_1M_2 , the new closest master neighbors are redefined as nodes M_1 and M_2 . The small sliding method admits that nodal displacements are small enough and that slave nodes do not change of contact partner on the master surface. The same assumption is also valid for s-to-s discretization.

III.1.3.3 Contact Enforcement

The contact enforcement defines the relation between 'measured' contact opening/penetration and contact forces. Per default in Abaqus 6.8, three methods of contact enforcement are available:

- direct enforcement or hard contact,
- penalty method and
- a Lagrange multipliers based method.

In the first one, the master surface is defined as an impenetrable wall. Nodes which are not strictly in contact are assumed inactive in the contact interaction and completely free of contact forces. As the node comes into contact with its contact partner, the node is set to active and are applied forces to avoid any contact violation. This contact model adds discontinuities in the model and brings convergence difficulties. In many cases, it can not be numerically solved without optional contact stabilization such as small virtual viscous forces on contact nodes. In particular, if contact is initially open everywhere on the model, no forces/no displacements are transmitted in the contact zone and the system may be insufficiently constrained in order to solve the force equilibrium.

The other constraint enforcement methods do not present this inconvenience. Contact nodal forces are given progressively as the node approaches its contact partner. These methods are known as softened methods. These contact enforcement formulations have the disadvantage to allow interpenetration.

The Abaqus VCCT feature restricts the usage of contact model. Penalty method and Augmented Lagrange multipliers method are not allowed to be used in conjunction with the VCCT feature.

If contact discretization node-to-surface is used, both contact tracking methods finite-sliding and small-sliding can be applied.

If the contact discretization surface-to-surface is used, only the small sliding contact tracking method can be applied.

III.1.4 Apparent Implementation of the Abaqus VCCT

Abaqus implementation of VCCT is not described in the documentation and is not clarified by Abaqus support¹. It can be assumed, that the energy release rate is estimated within Abaqus using the existing outputs of the contact interaction. To estimate the energy release rate, the classical formulation (eq. II-36 and the eq. II-37) is used in combination with a variable substitution as given indicatively as follows for a crack propagating in the X-direction, Y and Z directions corresponding respectively to the mode II and mode III directions.

In Table 1, index (i) corresponds to the node situated at crack tip and (i-1) to the first node in front of crack tip, associated either with the slave (S) or master (M) surface.

Estimating the energy release rate through these formulas is shown for a CT-specimen in the following section. The difference between G_1 and G_2 from direct outputs and from formula above gave an agreement of 99.9%. Output variable substitution can also be performed for 2D cases with second order elements by considering COPEN and CSLIP outputs at mid-side node ahead crack front with CNORMF and CSHEARF at mid-side node behind crack front. The same agreement between VCCT output and output substitutions is found.

As a consequence of such an implementation, the contact discretization and the contact enforcement may have a substantial influence on the estimation of G . COPEN and CSLIP depend on the choice of the discretization method.

In the n-to-s discretization method (see section III.1.3), COPEN is the normal distance of the slave node to the master surface, but not the distance between the two nodes ahead crack front as it should be.

In a s-to-s discretization, COPEN and CLIP are related to the AVERAGE distance between slave and master surfaces. In this case, using COPEN and CSLIP constitutes a very inadequate approximation of the crack opening. CNORMF and CSHEARF are the nodal forces

¹ The German Abaqus Online was several times questioned about this topic, but never provided substantial informations and never validated/unvalidated assumption in the table on the following page.

respectively in the normal and tangential direction; their estimation depends on the choice of the contact enforcement.

Original Term	Substitution	Description
$b\Delta a$	$CNAREA^{(i)S}$	Contact Nodal Area at node (i)S (Associated surface with node in the contact interaction)
$u_y^i - u_y^j$	$COPEN^{(i-1)S}$	Contact Opening at node (i-1)S
$u_x^i - u_x^j$	$CSLIP1^{(i-1)S}$	Contact tangential motion in tangential direction 1 at node (i-1)S
$u_z^i - u_z^j$	$CSLIP2^{(i-1)S}$	Contact tangential motion in tangential direction 2 at node (i-1)S
F_x^k	$(CSHEARF:CSF1^{(i)S} + CSHEARF:CSF1^{(i)M})/2$	Average Contact Shear Force vector (taken in the mode II direction) at nodes (i)S and (i)M
F_y^k	$(CNORMF^{(i)S} + CNORMF^{(i)M})/2$	Average Contact Normal Force magnitude at nodes (i)S and (i)M
F_z^k	$(CSHEAR2:CSF3^{(i)S} + CSHEAR2:CSF3^{(i)M})/2$	Average Contact Shear Force vector (taken in the mode III direction) at nodes (i)S and (i)M

Table 1: Variable Substitution with Abaqus VCCT Estimation

III.2 Crack Propagation Analysis with Abaqus

III.2.1 Principle

With Abaqus VCCT, five fracture criteria can be used, inclusively the ERR criterion. Criteria based on stress conditions at crack tip or based on the crack tip opening are also available, but are not the scope of this work since they are not based on fracture mechanical theories.

Independently from the method chosen, the condition for a crack to be extended is given by the failure function f . The failure condition is then defined by:

$$1 - f_{tol} \leq f \leq 1 + f_{tol}. \quad \text{eq. III-1}$$

Parameter f_{tol} is a tolerance per default taken to 0.2 when using the Abaqus VCCT. When the failure condition is met, the interaction maintaining the two nodes at crack tip (the first on the master surface and the second on the slave surface, paragraph III.1.2) are released. The crack is propagated until the next interfacial node pair.

The failure function in the case of the virtual crack closure technique is defined by:

$$f = \frac{G_1 + G_2 + G_3}{G_C}. \quad \text{eq. III-2}$$

In eq. III-2, the parameter G_C refers to an equivalent critical energy release rate estimated depending on the mode mixity at crack tip. Different models of equivalent critical ERR are available in Abaqus.

III.2.2 The BK-Law

The equivalent critical ERR known as BK-Law is proposed in [Benzeggagh 1996]. It defines the critical ERR as function of the ratio of ERR amount related to the pseudo mode II and mode III loading at crack tip on the total ERR:

$$G_{C-BK} = G_{IC} + (G_{2C} - G_{IC}) \left(\frac{G_2 + G_3}{G_1 + G_2 + G_3} \right)^\eta. \quad \text{eq. III-3}$$

As already mentioned, the different G_i terms cannot be directly related to the loading mode I, II and III in case of fracture between dissimilar media. G_{IC} and G_{2C} are the critical ERR in the respective cases of pseudo pure mode I loading and pseudo pure mode II loading.

In this work, mode III is not investigated, for this reason G_3 is taken to zero. The pseudo mode I ratio r_1^G and the mode II ratio r_2^G are then given by

$$r_1^G = \frac{G_1}{G_1 + G_2} \quad \text{and} \quad r_2^G = \frac{G_2}{G_1 + G_2}. \quad \text{eq. III-4}$$

The BK law can then be expressed as:

$$G_{C-BK} = G_{IC} + (G_{2C} - G_{IC}) (r_2^G)^\eta. \quad \text{eq. III-5}$$

As suggested by [Hutchinson 1992], the following hypothesis is admitted so far:

$$\psi = \psi_G + \omega, \quad \text{eq. III-6}$$

in which ψ refers to the real mixed mode angle, ψ_G to the ERR angle defined in eq. II-44 and ω to a constant phase shifting. The validity of such an assumption is further discussed in the numerical part. Combined with eq. II-44, eq. III-6 furnishes the expression of the pseudo ERR ratio as function of the phase angle:

$$\frac{G_2}{G_1} = \tan^2(\psi - \omega). \quad \text{eq. III-7}$$

Using the eq. III-7, the mode II ratio can be expressed as:

$$\frac{G_2}{G_1 + G_2} = \frac{1}{1 + \frac{G_1}{G_2}} = \frac{1}{1 + \frac{1}{\tan^2(\psi - \omega)}} = \sin^2(\psi - \omega). \quad \text{eq. III-8}$$

Finally, the BK-Law is reformulated as eq. III-9, in which the phase angle is considered as absolute value to make the curve symmetric with respect to the ordinate axis:

$$G_{C-BK} = G_{IC} + (G_{2C} - G_{IC}) \sin^{2\eta}(|\psi| - \omega). \quad \text{eq. III-9}$$

The aim of this expression is to be fitted to experimental results, in order to identify the parameters G_{IC} , G_{2C} and η required to define the equivalent critical ERR. Even if the BK-law is not based on the real ERR ratio considering the oscillatory behavior, the latter can be taken indirectly into account with the parameter ω in eq. III-9. The phase shifting simply vanishes in the case of cracking in homogeneous media.

A similar equivalent critical ERR was also proposed by Hutchinson and Suo in [Hutchinson 1992]:

$$G_{C-Hutchinson} = G_{IC} (1 + (\lambda - 1) \sin^2 \psi). \quad \text{eq. III-10}$$

In eq. III-10, G_{IC} is the critical ERR for real mode I loading. If ω is neglected, λ equal to the ratio G_{IIC}/G_{IC} and η equal to unity, expressions in eq. III-9 and eq. III-10 are then the same.

The parameter η in the BK law permits to define how the critical ERR increases with the mode II amount (Figure 29). If η is close to 1, G_C increases linearly with the mode II ratio. Increasing η increases the curvature of the curve. In the case where mode III loading is also considered, the BK law does not consider the critical pure mode III and the same weight is given to modes II and III.

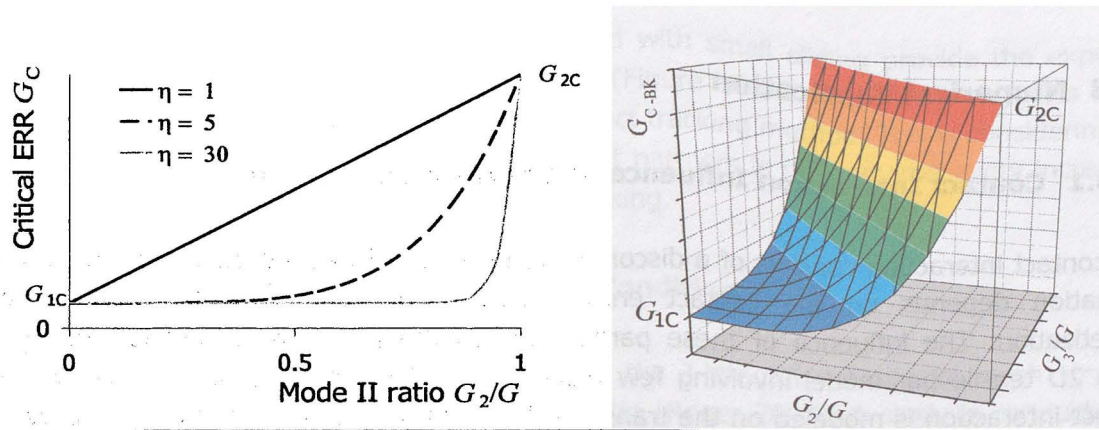


Figure 29: The BK critical Energy Release Rate
 a. Influence of the η Parameter (mode III not considered)
 b. Three-Modi BK Law

III.2.3 Reeder and Power Laws

The Reeder Law is suggested in [Reeder 2002]. It is an extension of the BK-Law which gives a different weight to the mode II and mode III loading. The Reeder equivalent energy release rate is defined on the eq. III-11.

$$G_{C-Reeder} = G_{C-BK} + (G_{3C} - G_{2C}) \left(\frac{G_3}{G_2 + G_3} \right) \left(\frac{G_2 + G_3}{G_1 + G_2 + G_3} \right)^\eta. \quad \text{eq. III-11}$$

Since the mode III loading is not considered in this work, the BK law and the Reeder law provides both the same result. The latter is consequently not longer investigated.

Another delamination propagation criterion, i.e. the Power law, is available in Abaqus (eq. III-12). The condition of crack propagation is defined by eq. III-2 and is met when $f \geq 1$.

With this criterion, the mode mixity is not considered using the ERR ratio but each load mode is considered separately and respectively weighted using the critical ERR for pure mode loading:

$$f = \frac{G}{G_{C \text{ equivalent}}} = \left(\frac{G_1}{G_{1C}} \right)^{am} + \left(\frac{G_2}{G_{2C}} \right)^{an} + \left(\frac{G_3}{G_{3C}} \right)^{ao}. \quad \text{eq. III-12}$$

Since the mode mixity angle does not appear clearly in this model, it is not used in this work.

III.3 Numerical Verification

III.3.1 Contact Interaction Influence on the Near-Stress-Field

The contact interaction consists of a discontinuity in the mesh. At the interface, nodal forces estimation depends on the contact enforcement used, contact tracking and contact discretization. The influence of these parameters on the near stress field is investigated using 2D tensile bar model involving few plane stress elements of 1st order integration. A contact interaction is modeled on the transversal section to the uniaxial loading (Figure 30). The material is defined purely elastic with an elastic module of 1 MPa. Poisson's ratio is set to zero. Vertical forces F of 3N are applied on the upper nodes. The tensile bar width is constituted of three elements at the interface.

From the analytical solution, the tensile bar should exhibit a homogeneous uniaxial stress of 2 MPa. The three possible usable contact formulations in conjunction with the VCCT are tested: Node-to-surface discretization with finite and small sliding tracking and surface-to-surface discretization with only the small sliding tracking.

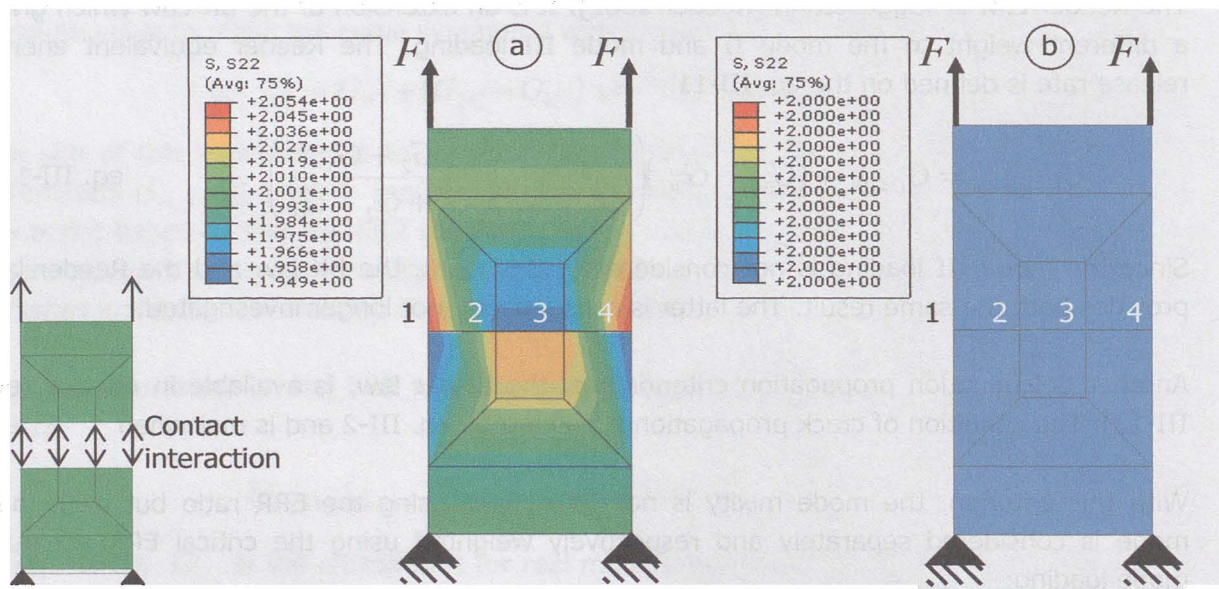


Figure 30: Benchmark Model for Contact Testing
 a. Result with Finite Sliding Tracking and n-to-s
 b. Result with Small Sliding Tracking, identical with n-to-s and s-to-s

The stress solution furnished by the Abaqus default parameters is plotted in Figure 30.a. It corresponds to the node to surface discretization with the finite sliding tracking. The stress oscillates of ± 0.05 MPa along the interface. Nodal forces found on the interfacial nodes are 0.938, 2.044, 2.044 and 0.938 N on the slave side and 1.040, 1.941, 1.941 and 1.040 N on the master side, instead of 1, 2, 2 and 1 N. The equilibrium in the individual node pairs is not respected.

Surface-to-surface and node-to-surface associated with small sliding provide the expected result, a homogeneous uniaxial stress of 2MPa (Figure 30.b). This result suggests using rather the small sliding than the finite sliding contact tracking method. This is considering the CPU time as an advantage since searching contact partners is not required every increment but only on the first one with the small sliding tracking.

III.3.2 Mesh refinement and Convergence Condition

VCCT has the advantage that, in comparison to the J-integral, no special mesh strategy involving collapsed elements is required at crack tip [Roger 2007]. A study is conducted to estimate mesh size influence on the energy release rate estimation with Abaqus VCCT. In the contact interaction, the default Abaqus parameters are used. Compact Tension (CT) specimens are modeled with different mesh sizes and for different load conditions (Figure 31).

The first case presents a CT specimen constituted with a single material under mode I loading. Second case is the same specimen turned by 45° in order to induce mixed-mode loading at crack tip. In the third case, mixed-mode is induced, using dissimilar media on both sides of the crack flanks.

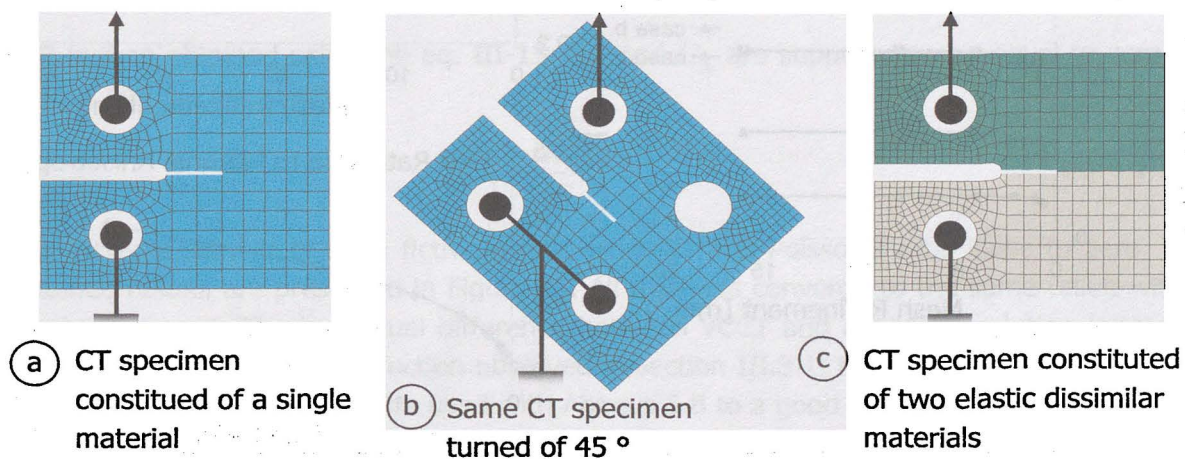


Figure 31: CT specimen for convergence study
 a. Pure mode I loading
 b. Mixed-mode loading due to specimen rotation
 c. Mixed-mode loading due to material anisotropy

As shown in Figure 32.a, the ERR converges to a stable value, as a mesh refinement of 4 mm⁻¹ is reached. It means that a mesh reference length of 0.25 mm at crack tip should be sufficient. The curve b shows that the mixed-mode ratio in isotropic media does not really converge to a stable value, even for a refinement of 33 mm⁻¹, but its value does not vary more that 2% if a refinement of 8 mm⁻¹ is reached. For isotropic crack problems, using elements of length 0.1 mm at crack tip is consequently sufficient to obtain results with acceptable accuracy.

For problems involving delamination between dissimilar media, the ERR ratio never converges to a stable value with the element size reduction. As suggested by [Beuth 1996], the energy ratio G_2/G_1 for crack between dissimilar media does not converge to a stable value because of the stress field nature at crack tip: G_1 and G_2 are estimated using crack tip opening at a distance Δa to the crack front corresponding to the mesh size at crack tip. As suggested by [Williams 1959], crack flanks displacement ratio $\Delta u_x/\Delta u_y$ varies in a logarithmic manner with Δa , so does the energy ratio G_2/G_1 according to Figure 32.c. To conclude about the required mesh refinement at crack tip to get accurate estimation of the energy release rate, it seems reasonable to have an element length smaller than 0.1 mm at crack tip considering a crack length in the order of magnitude of 10 mm. Considering mode mixity estimation for crack between dissimilar media, it should be estimated using other methods. In any case the mode mixity estimation is meaningful associated with the reference length at crack tip.

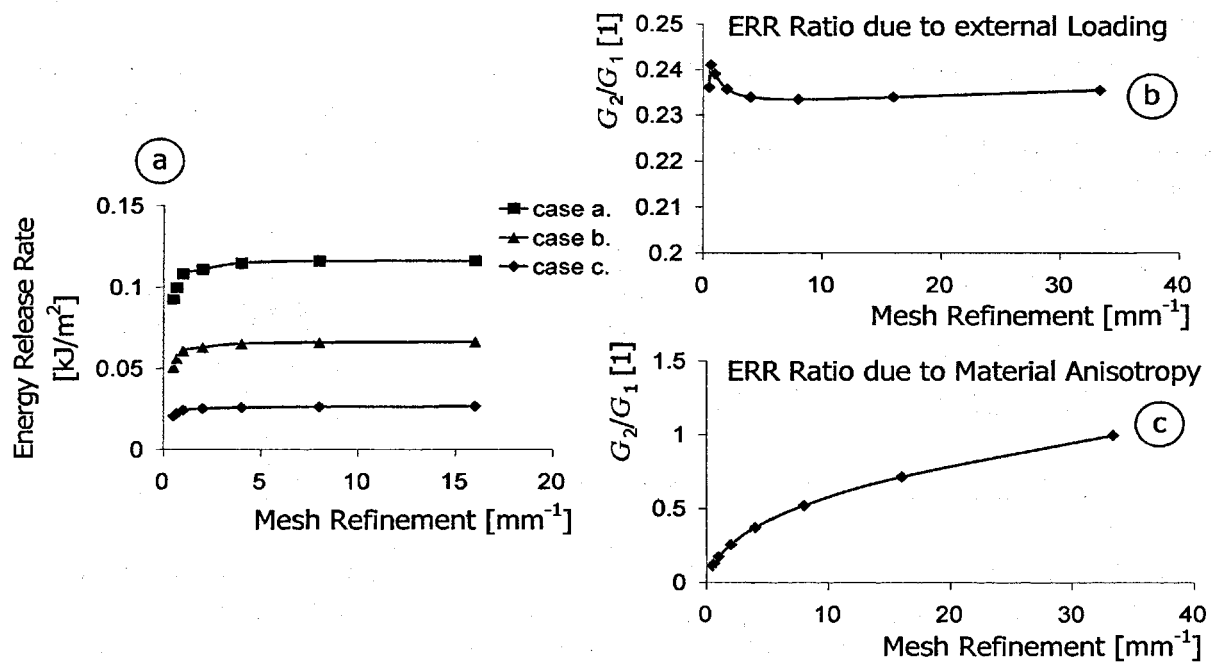


Figure 32: Result convergence by respect with mesh refinement

a. Total ERR

b. Mixed mode ratio in isotropic media

c. ERR ratio in dissimilar media

The model displayed in Figure 31.a is used to investigate the influence of the contact discretization. For all simulated cases, the ERR difference between s-to-s and n-to-s contact discretization varies less than 0.1 %. It suggests that both contact discretizations can be used with VCCT. Since the n-to-s contact discretization is less time consuming (section III.3.1), it should be preferred to s-to-s discretization and used in conjunction with the small sliding contact tracking method (section III.3.2).

III.3.3 VCCT vs. J-Integral and Analytical solution

As further verification, the energy release rate is estimated for a conventional CT specimen (pure mode I loading in isotropic material) for different crack length, using FEM and Virtual Crack Closure Technique, FEM and J-Integral and analytic solution [ASTM E399-90].

According to [Roger 2007], the stress intensity factor for mode I can be estimated using eq. III-13, by respecting some restriction on parameters a , B and W :

$$K_I = \frac{P}{B\sqrt{W}} f_{CT} \left(\frac{a}{W} \right). \quad \text{eq. III-13}$$

In the eq. III-13, B corresponds to the specimen thickness and W to a geometric parameter corresponding to the specimen dimension. f_{CT} is a function only depending on the specimen geometry. It is given by the ASTM standard as:

$$f_{CT}(\alpha) = \frac{2 + \alpha}{(1 - \alpha)^{3/2}} (0.886 + 4.64\alpha - 13.32\alpha^2 + 14.72\alpha^3 - 5.6\alpha^4), \quad \text{eq. III-14}$$

$$\alpha = a/W.$$

ERR is then obtained using the eq. III-15. G_2 and G_3 are supposed to be equal to zero, so that G and G_I are identical.

$$G_I = \frac{K_I^2}{E} \quad \text{eq. III-15}$$

The material used is given a fictive elastic modulus and Poisson's ratio close to zero. The obtained results are presented in Figure 33. All methods converge to the same result with a good agreement. The maximal difference between VCCT and analytical solution is smaller than 1.5%. In spite of imperfection observed in section III.3.1, this suggests that the Virtual Crack Closure Technique can be used with Abaqus 6.8 to a good confidence degree.

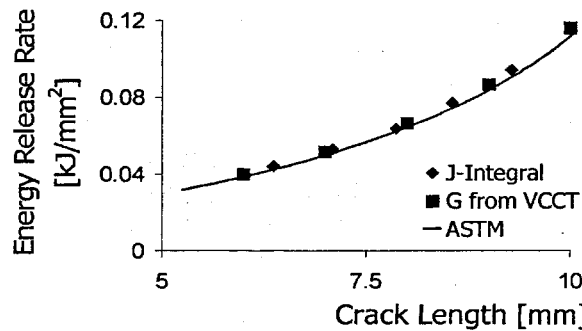


Figure 33: FEM vs. Analytical estimation of ERR

III.3.4 Rendering of linear viscoelastic Properties

The material models implemented in Abaqus for linear viscoelastic materials are those presented in section II.6.2 ([Abaqus 5]). To verify how their stiffness is rendered with Abaqus, a series of numerical tests is performed with simple tensile bar (Figure 35.a) and compared to the experimentally characterized material properties (section IV.5).

The tensile bar is modeled in 2D with 12 plane stress elements with 2nd order integration. A temperature field is defined as initial condition and maintained constant along the simulation time on the overall model.

A sinusoidal uniaxial excitation with a nominal strain ϵ_{22} of 1% is given to the specimen, with a load ratio set to zero. Three sinus periods are simulated. Excitation frequency is varied each decade from 10^{-6} to 10^6 Hz. Simulations are also performed at different temperatures (20 °C, 100 °C, 125 °C, 150 °C and 200 °C) to verify if the applied shifting due to thermal change is correct. The obtained uniaxial elastic modulus is then verified through the stress response S_{22} of the specimen (Figure 34.a). The stress response is not in phase with the strain excitation. The delay of response to the excitation varies, depending on the applied strain frequency and temperature. The rendered material stiffness is estimated at the third stress maximum.

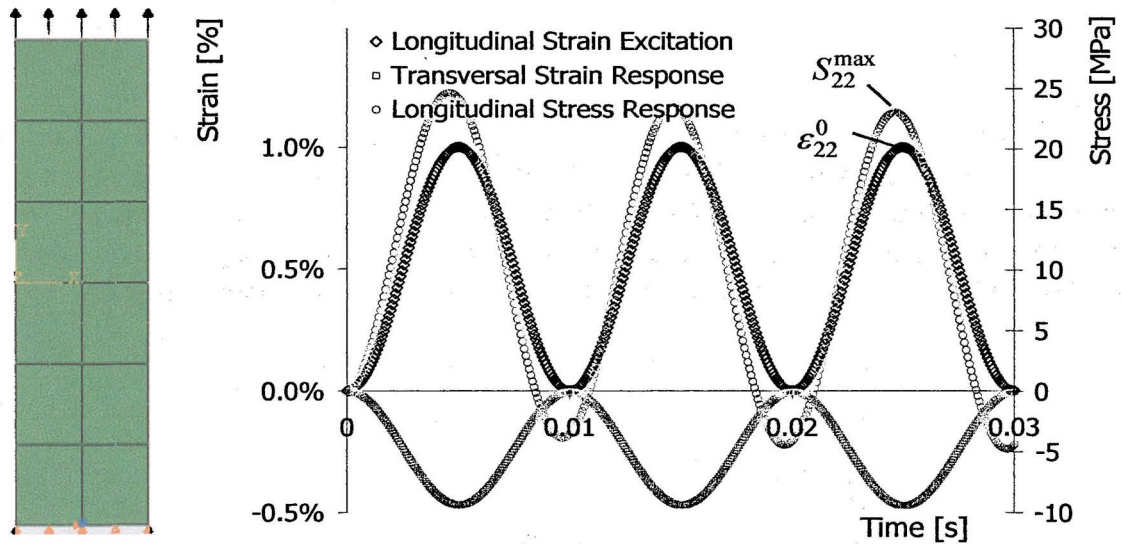


Figure 34: a. Tensile Bar Model Used for the Numerical Benchmark
b. Numerical Results at 150 °C and 100 Hz

The stiffness rendering is then given by eq. III-16:

$$E^{num} = \frac{S_{22}^{max}}{\epsilon_{22}^0} \quad \text{eq. III-16}$$

The obtained elastic modules are expressed as function of the frequency in Figure 35 (black curve). The portion of curve obtained at other temperatures than 125 °C are shifted in the frequency domain using the shift factors from the mastering (section IV.5).

The obtained master curve using the DMA measurement is also displayed in grey in Figure 35 (dashed line). The reproduced master curve using the numerical model fits the one resulting from experimental measurements.

The simulations performed at 125 °C show that the tensile modulus is correctly rendered for frequency varying from 10^{-6} to 10^6 Hz. Simulations performed at the other temperatures show that the frequency shifting as function of the temperature is also correctly applied.

The simulations also exhibit the correct stiffness limits E_0 and E_∞ , for respectively very high and very low load frequencies.

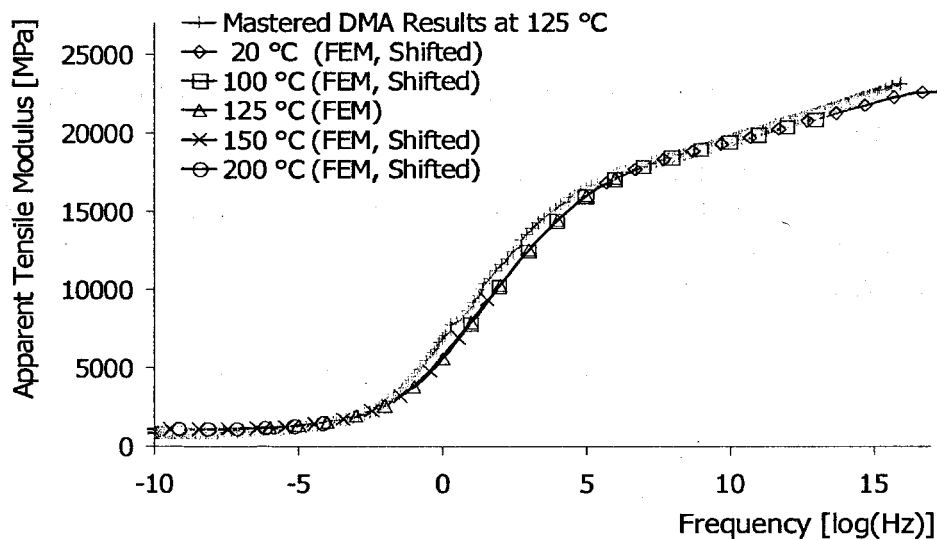


Figure 35: Rendered Tensile Modulus in the Simulation

The same tensile bar (Figure 34) is then taken and simulated with a low monotonic increasing tensile load corresponding to an applied strain rate of $0.1 \text{ \%}\cdot\text{s}^{-1}$ until a longitudinal strain of 1 % is reached to the material. Poisson's ratio in the numerical model is then given by:

$$\nu^{num} = -\frac{\varepsilon_{11}^0}{\varepsilon_{22}^0}, \quad \text{eq. III-17}$$

where ε_{22}^0 is the longitudinal applied strain (1 %), and ε_{11}^0 the corresponding transversal strain. The numerically rendered Poisson's ratio is determined every 5 °C from 50 °C to 200 °C. The results are displayed in Figure 36. Dark points correspond to the experimental estimation of Poisson's ratio through compression tests (section IV.5.2) and the dashed grey line corresponds to the FE rendered Poisson's ratio.

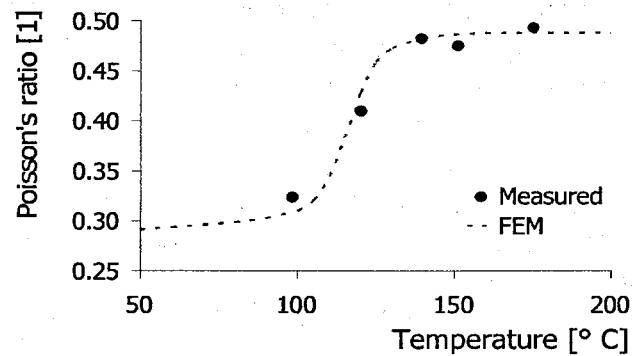


Figure 36: Poisson's Ratio Rendering within FEM

Considering both Poisson's ratio and the tensile modulus, the exhibited material stiffness corresponds by trend to the material properties obtained experimentally. The model used to compare numerical rendering and experimental data, i.e. the rapid frequency/strain rate conversion to express the DMA data in a strain rate must be considered with extreme care. In any case, it permits to valid qualitatively the numerical model implemented for the linear viscoelasticity in Abaqus.

IV. Interfacial Delamination Toughness Characterization

Since the energy release rate is not directly “measurable” during a test, a commonly used method is a correlation between experimental tests and FEM simulations. A specimen containing a preexisting crack is loaded until crack propagates. The test is then reproduced in FEM with identical boundary conditions as the experimental test.

The energy release rate and mixed mode angle are then estimated using the FEM stress and strain results (section II.4.3 and II.5.2).

IV.1 Preexisting Test Setups

Many geometries of specimen exist to determine the delamination toughness of materials interfaces. Most commonly used specimens are represented in Table 2. They are generally bilayer or multi-layer specimens containing an initial delamination. These specimens permit generally to characterize the interfacial crack toughness only for one angle of mode mixity.

The determination of the interfacial crack toughness for a given material combination over the full range of mode mixities requires performing tests with different geometries.

One test setup makes theoretically exception to latter assumption; this is the MMB specimen, which can reach various mixed-mode ratios by varying the lever arm of the jig armature (Table 2). For the realization, the lever arm must be properly fixed or glued to the upper layer, what is in practice very difficult and inadequate in industrial context.

Elsewise, the mode I delamination toughness is given by the DCB specimens (Table 2), whereas the mode II delamination toughness is given by the ENF specimens. The family of four points bending specimen is appropriate for the mixed mode delamination toughness.

In the case of material pairs involving thermosetting polymers, specimens are obtained through transfer molding. A mould (or also a test jig) is required for each specimen type. It involves significant expenditures, wide test and fabrication times. These costs are then multiplied by the number of required test setups.

IV.2 Approach

To avoid cost redundancy using several test setups, an alternative specimen and setup permitting the characterization of the delamination toughness over a full range of mode mixity must be developed. The Triangle Button Shear Specimen fulfills these requirements.

In the following part, the Triangle Button Shear Specimen is presented. Experimental tests are performed. Experimental results can not be evaluated without highlight of the numerical results. For this reason and to help in the comprehension of the experimental results, the numerical results are presented directly after the test concept description and prior to the experimental results.

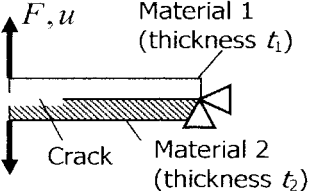
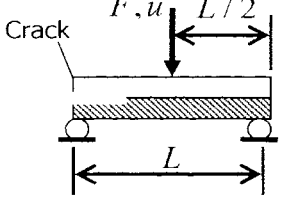
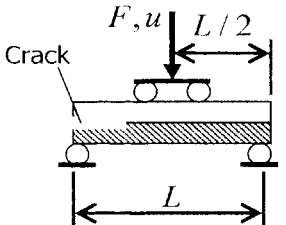
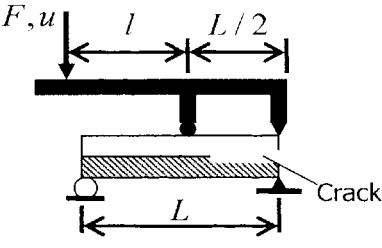
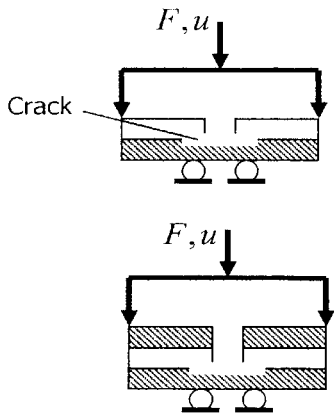
Geometry and Load Conditions	Name	Application
<p>Applied load and displacement</p> 	<p>Symmetric or Asymmetric Double Cantilever Beam (SDCB or ADCB*).</p> <p>(*): symmetric if $t_1 = t_2$</p>	<p>Dominant mode I. Mixed mode ratio constant over crack length, mainly dependent of the thickness of the softest layer.</p>
	<p>Symmetric or Asymmetric End Notched Flexure Specimen (SENF or AENF).</p>	<p>Dominant mode II. Mixed mode ratio variable over crack length.</p>
	<p>Stabilized Symmetric or Asymmetric End Notched Flexure Specimen (SSENF or SAENF).</p>	<p>Dominant mode II loading, with stable crack propagation.</p>
	<p>Mixed Mode Bending Specimen (MMB)</p>	<p>Provides various mixed-mode, depending on the choice of l. Fixing the lever on the specimen makes the realization inappropriate for wide test series.</p>
	<p>Four Points Bending Specimens (FPBS or 4PBS)</p>	<p>Provide various mixed-mode ratios depending on the thickness of the different layers.</p>

Table 2: Selection of Specimens for the Delamination Toughness Characterization

IV.3 The Triangle Button Shear Specimen

IV.3.1 Concept

The specimen is based on the original Button Shear Specimen of [Szeto 2000]. This consists to a round plastic plug molded on a substrate. This specimen does not contain any delamination and therefore fracture mechanics concepts cannot be applied.

Three evolutions of the specimen of Szeto are proposed in this work.

First, an initial delamination is initiated in the front of the specimen before performing the test, which permits to estimate the energy release rate at crack tip. The different manners to initiate a crack at the interface will be discussed further.

Suggested by [Dreßler 2007], the second modification is brought on the test apparatus. The test machinery allows the choice of the shearing-height h , i.e. the distance between the crack plane and the loaded-point on the plastic cone (Figure 37.b). This degree of freedom permits to vary the ratio shearing/tensile load at crack tip, i.e. choosing mode mixity at crack tip. It allows the determination of the critical energy release rate over a wide range of mixed mode ratio, i.e. expected from pure mode I loading to high levels of mode II loading.

Finally, the plastic cone cross section is chosen triangular, that is why this specimen is named as Triangle Button Shear Specimen (TBSS). A consequence of the triangular form of the interfacial section is, that the relative surface to delaminate increases with the crack front advance. As a consequence, the derivative of G with respect to a (crack length) dG/da by constant shear-tool displacement must be negative. The crack is expected to propagate in a stable manner.

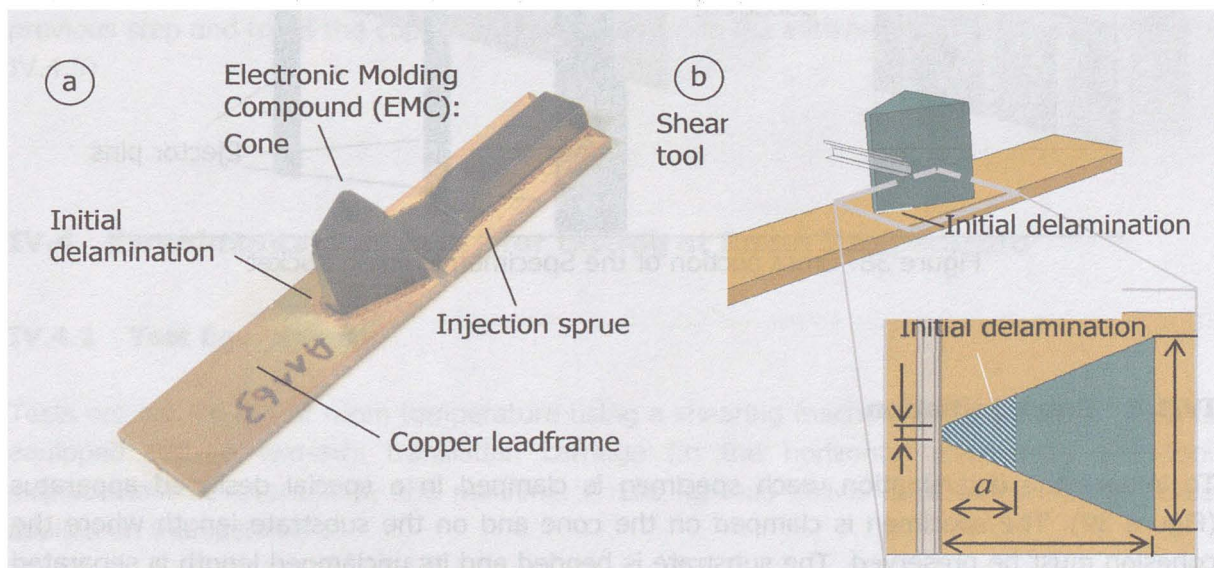


Figure 37: Triangle Button Shear Specimen (TBSS)

IV.3.2 Specimen Fabrication

The specimens are made of an EMC button molded on a copper substrate.

The encapsulating material is one classical epoxy based thermosetting polymer highly filled with micro silicate spheres (about 80%w.). It is molded at 180 °C. At room temperature, this material is brittle elastic, having a tensile modulus 25,000 MPa and Poisson's ratio of about 0.25.

The substrate is a copper plate of dimensions 50 x 10 mm and of thickness 1.5 mm. Copper substrates are cleaned before molding with an Acetone agent in order to dissolve potential grease.

The EMC cone has a symmetrical trapezoidal basis with respect to the loading axis. It has for main base, height and secondary base 8x8x2 mm (refer to Figure 37.b). Cone height is equal to 10 mm.

The plastic cone is slightly angled (about 5°) to ease demolding. After molding, specimens are cured 5 hours at 180°C in dry conditions to finish the chemical hardening of the material. The injection sprue is then sawed to prevent any contribution of the sprue.

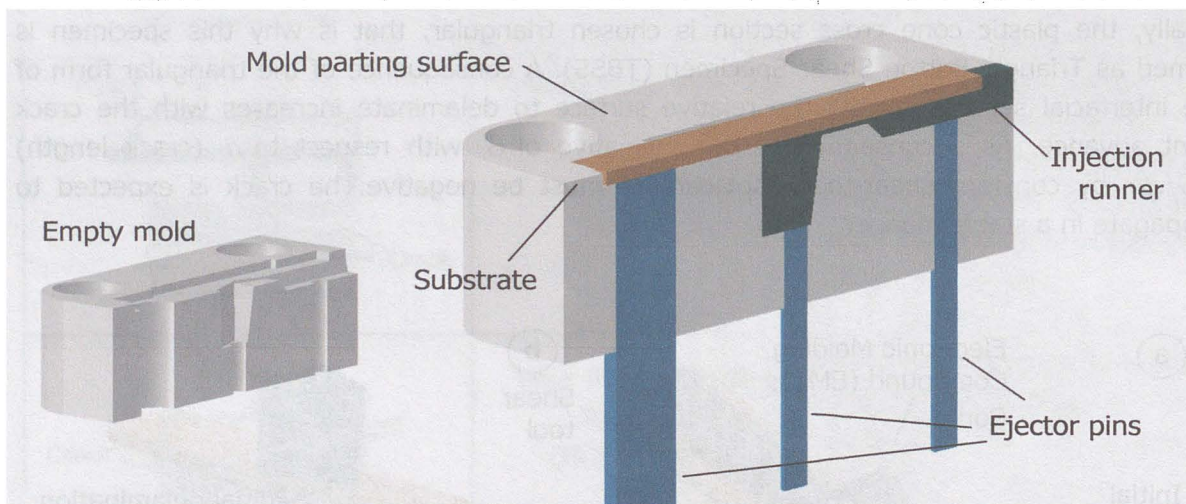


Figure 38: Cross section of the Specimen Molding Socket

IV.3.3 Crack Initiation

To initiate the delamination, each specimen is clamped in a special designed apparatus (Figure 39). The specimen is clamped on the cone and on the substrate length where the cohesion must be preserved. The substrate is bended and its unclamped length is separated from the molding compound.

This apparatus is disposed in a conventional tensile-test machine. To initiate the delamination, a vertical load of 25 N is applied on the copper substrate ahead of the polymer cone. No plastic deformation occurs in the substrate during this step. The initiated delamination length varies from 2 to 4 mm (this topic is further discussed in paragraphs IV.8, IV.9, IV.10).

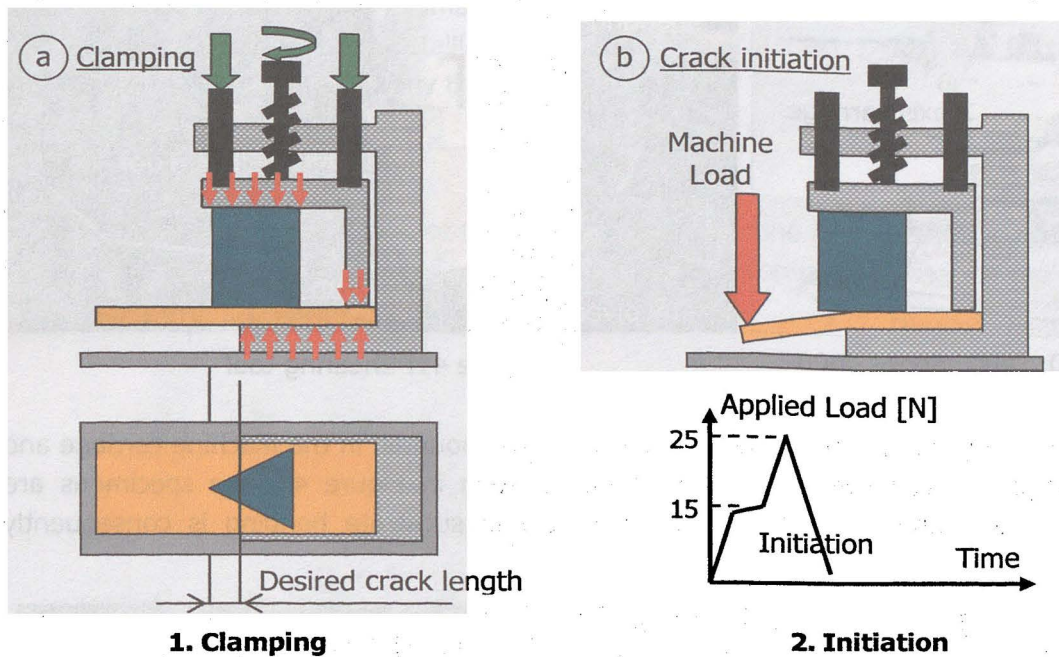


Figure 39: Delamination Initiation into a TBSS

Specimens are then once again 5 hours stored by 180°C to eliminate stress residues from previous step and to let the copper substrate oxidize in the initiated delamination (paragraph IV.4.5).

IV.4 Experimental Procedure for testing at Room Temperature

IV.4.1 Test Equipment

Tests are carried out at room temperature using a shearing machine DAGE series 4000. It is equipped with a two-axis translation carriage (in the horizontal directions). The tool displacement is recorded by the machine. A 100 kg load cell is used to record the force applied on the specimen.

IV.4.2 Clamping and Shearing Tool

A shearing tool made of hardened steel is designed for this test setup. The involved surface to shear the button has a height of 1 mm and thickness of 10 mm (Figure 41).



Figure 40: DAGE Series 4000

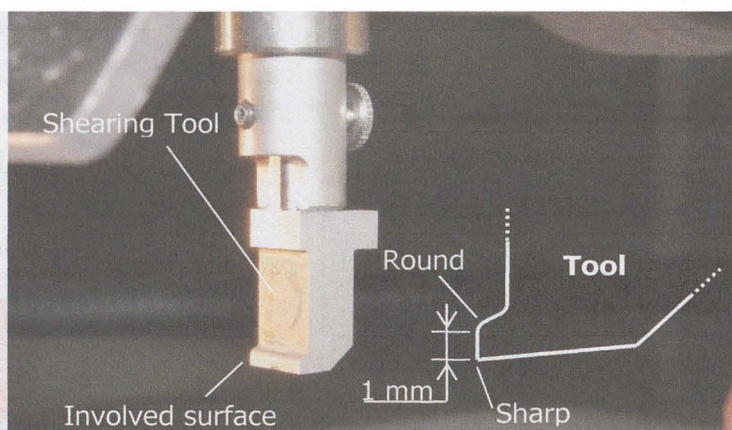


Figure 41: Shearing tool

A clamping bearing is built for this test setup. It can be mounted in the machine carriage and permits clamping seven specimens in parallel. As seen in Figure 42, the specimens are clamped over the long-sides of their substrates. The substrate bending is consequently small.

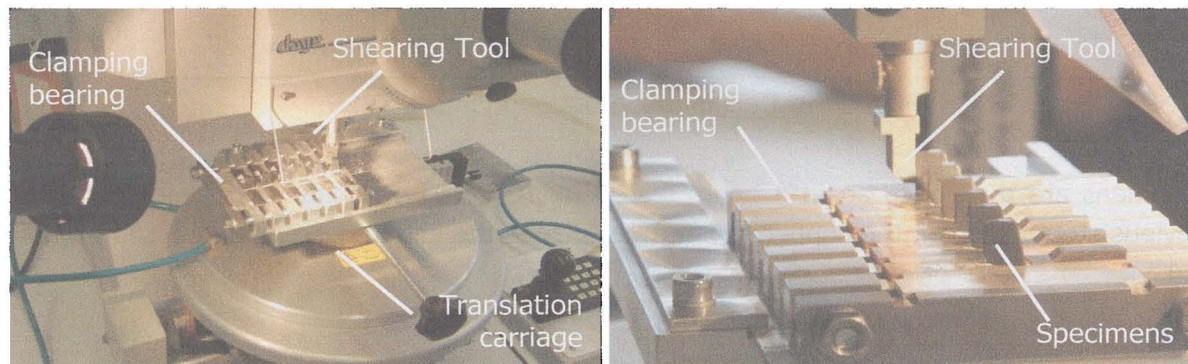


Figure 42: Specimen clamping and clamping bearing

IV.4.3 Shearing tool/Specimen Friction Coefficient

The coefficient of friction between molding compound and shearing tool is also determined. The shearing tool surface is scanned using a standard rheology-meter. The following surface parameters are measured: $R_a=0.9 \mu\text{m}$, $R_{\text{max}}=8.7 \mu\text{m}$ and $R_z=6.1 \mu\text{m}$.

The friction measurements are then performed using a conventional tensile machine and a specific jig, involving a metallic cable, a pulley which is fixed in the tensile machine and a metallic block used as weight (Figure 43). Small discs of EMC are milled from TBSS specimens and disposed in holes drilled in the weight.

A plate made of steel with a R_z equal to $6.5 \mu\text{m}$ is then used. This plate is assumed to have the same rheological properties as the shearing tool.

The steel plate is positioned in a tensile machine. The weight disposed on the EMC discs is positioned on the plates. A horizontal displacement of 120 mm and constant velocity is applied to the weight using the machine traverse, a steel cable and a pulley. The reaction load is measured using the standard 50 kN load cell of the tensile machine.

The coefficient of friction is estimated using Coulomb's law in eq. IV-1. R_N , the normal reaction of the plate on the metallic block is equal to $R_N = mg$. R_f , the friction force is equal to the force F measured by the load cell:

$$f = \frac{R_f}{R_N} = \frac{F}{mg} \quad \text{eq. IV-1}$$

A coefficient of friction of 0.3 is found between the EMC cone and the steel plate. This value is also used as friction coefficient for the contact molding compound/shearing tool.

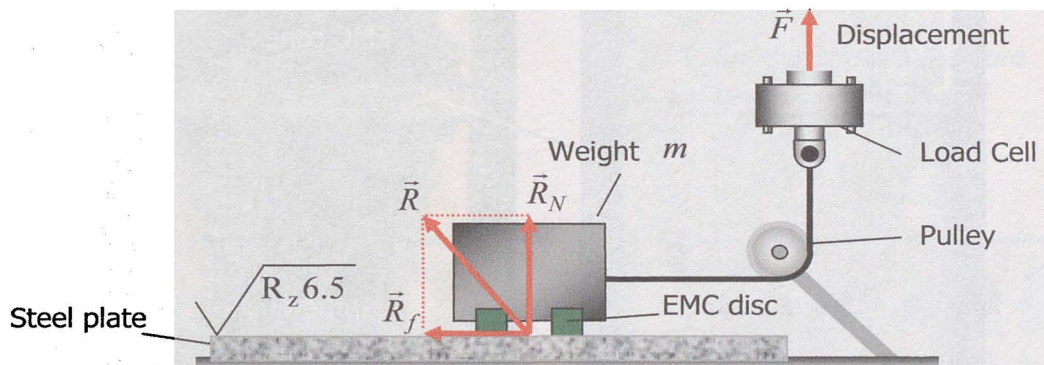


Figure 43: Friction Coefficient Measurement

IV.4.4 Crack Length measurement

After the crack initiation, the specimens are scanned using Scanning Acoustic Microscopy (SAM) to measure the initial delamination state.

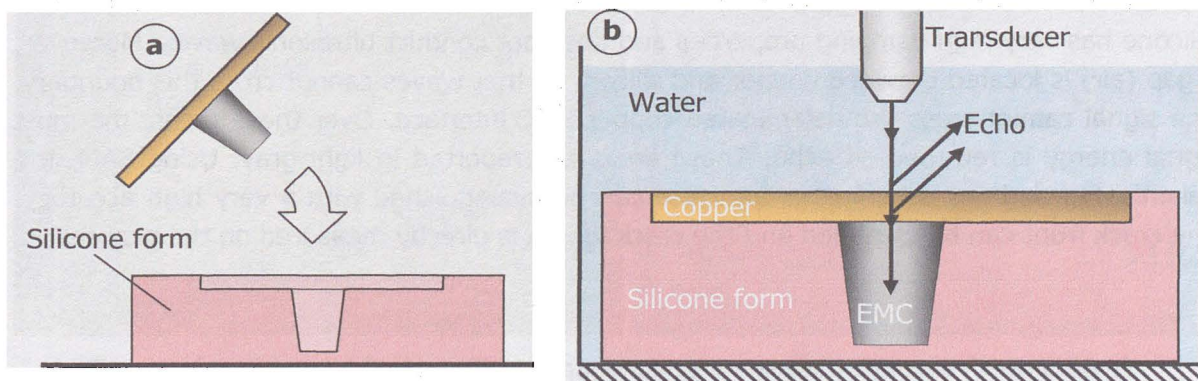


Figure 44: Scanning Acoustic Microscopy

SAM is a non-destructive test which permits to detect cracks, micro cavities, etc. in the volume interiors. The specimen is placed in a silicone form (Figure 44.a). It is completely immersed into water for the wave conduction (Figure 44.b). A transducer emits ultrasonic waves through the copper substrate. A picture is generated using the received echoes (Figure 45.a). The obtained resolution depends on the wave frequency of the transducer. An 80 MHz transducer is used. The obtained resolution is less than 20 μm .

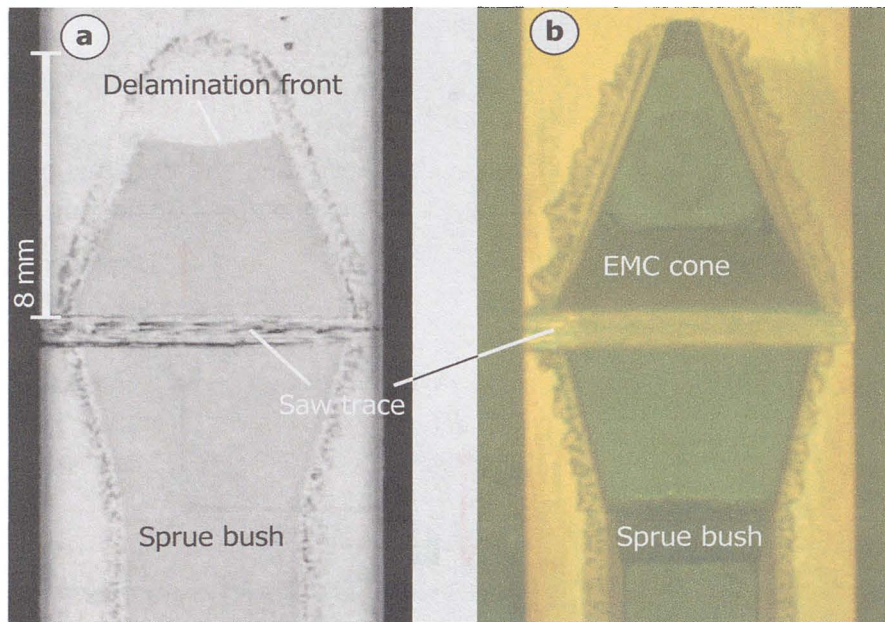


Figure 45: Initial delamination analyze
 a. Ultrasonic scan
 b. Top view on a TBSS

At the copper/EMC interface, the polymer vibrates with the metal. An important fraction of the signal is conducted further in the EMC cone. The rest is returned as echo. These areas are returned in dark-gray (Figure 45.a).

Silicone has very high damping properties and does not conduct ultrasonic waves. Moreover, a gap (air) is located between copper and silicon, so that waves cannot cross this boundary. The signal cannot cross the delaminated copper/EMC interface. Over these areas, the most signal energy is returned as echo. These areas are reported in light-gray. Using SAM, the delaminated and not delaminated interface can be distinguished with a very high accuracy. The crack front can be identified and the crack length is directly measured on the pictures.

IV.4.5 Fracture Pattern Analyze

IV.4.5.1 Verification of the Cohesive Crack Propagation Hypothesis

After the test session, the copper substrates are examined using optical microscopy. The microscope used has a 40x zoom. No EMC rest can be seen on the copper substrates (Figure 46.c). The same analysis on the EMC side does not reveal macroscopic visible copper rest (Figure 47).

The crack propagation is then assumed to occur exclusively at the EMC/copper interface and never kinks in the molding compound. The adhesive crack propagation hypothesis has been verified for all specimens, independently from the shearing heights, crack length, etc.

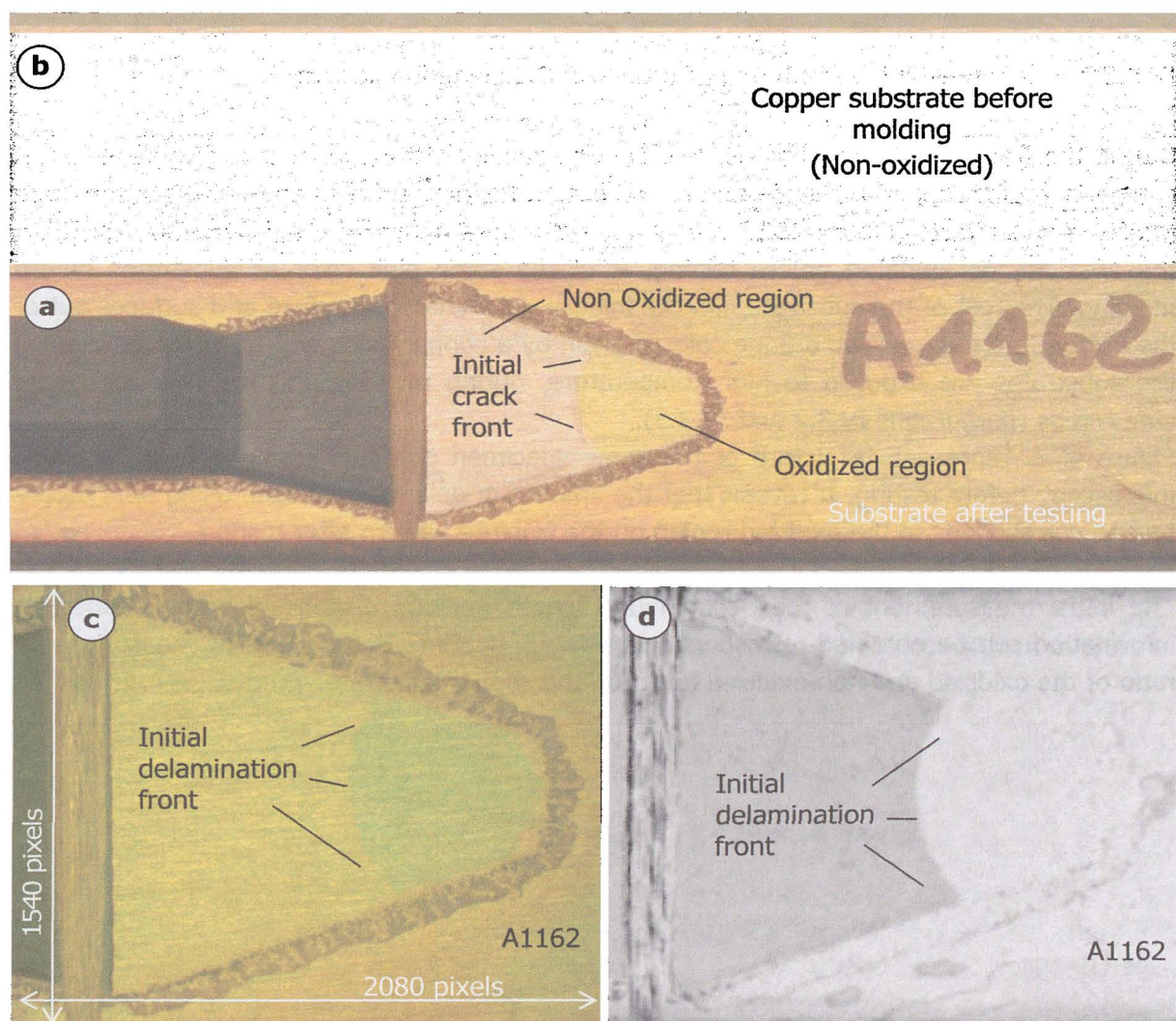


Figure 46.a. Fracture Pattern Photo made using a standard Camera (True Colors)
b. Comparison of a Substrate before modeling (above) and after testing(below)
c. Picture from Light Microscopy (Processed Colors)
d: Picture from Scanning Acoustic Microscopy

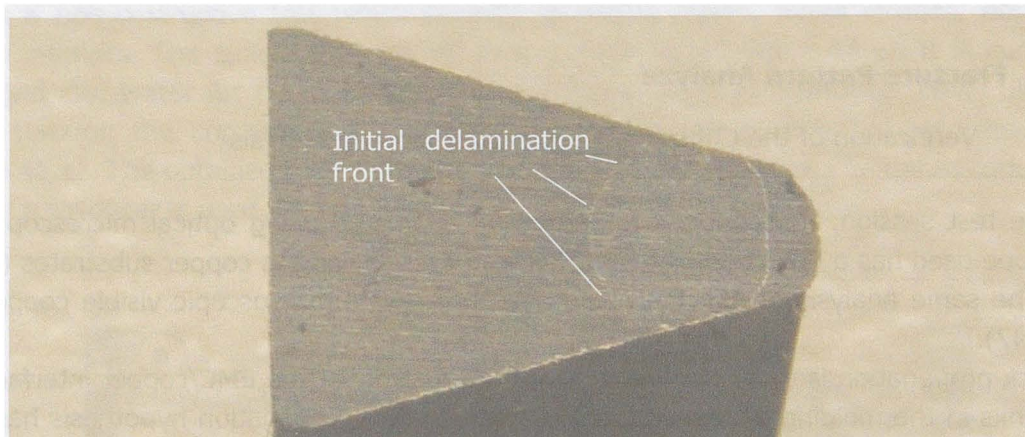


Figure 47: Fracture Pattern on the EMC Cone Side

IV.4.5.2 Afterwards-Measurement of the initial Delamination Length

During the fracture pattern analysis, two colors appear on the copper side (Figure 46.a). A comparison of a copper substrate before the button molding process and a copper substrate after the shear tests (Figure 46.b) reveals that the area behind the delamination front, i.e. the area not delaminated before testing, is of the same pink color as substrates before molding. The rest of the substrate, i.e. the initially delaminated interface and surfaces out of the button, are orange. The orange color is given by a copper oxide which grows, as soon as the substrates are exposed to high temperature, during molding and the two post mold cures steps (paragraphs IV.3.2 and IV.3.3).

Figure 46.c. represents a picture of the same specimen obtained using scanning acoustic microscopy before testing. It reveals that the amount of delamination seen using SAM before testing corresponds to the oxidized region on the fracture pattern after testing.

The initial measurement of the delamination length appears dispensable, since the same information can be obtained retrospectively using optical microscopy and by measuring the ratio of the oxidized and non-oxidized areas on the copper substrate.

IV.5 Material Characterization

IV.5.1 EMC Tensile Modulus

The common molding compound from the market is used for this work. It is characterized using a DMA measurement. The measurements are performed every 5 °C from -40 °C to 250 °C (61 temperatures). For each temperature, nine frequencies are tested (0.5, 0.8, 1.25, 2, 3.15, 5, 8, 12.25 and 25 Hz). The obtained curves showing the storage modulus with respect to the frequency and temperature are reported in Figure 48.

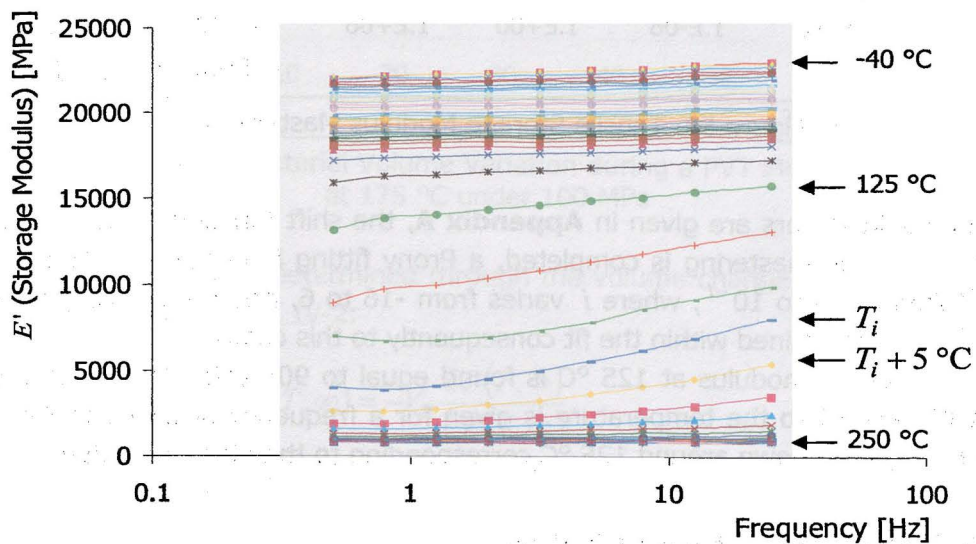


Figure 48: DMA Results for the thermosetting Polymer

The 61 curves are then shifted one by one (mastering) in order to obtain a continuous smooth progression of the tensile modulus with the frequency (Figure 50). The glass transition temperature (125 °C) is taken as reference temperature; the shift function goes to zero at this temperature.

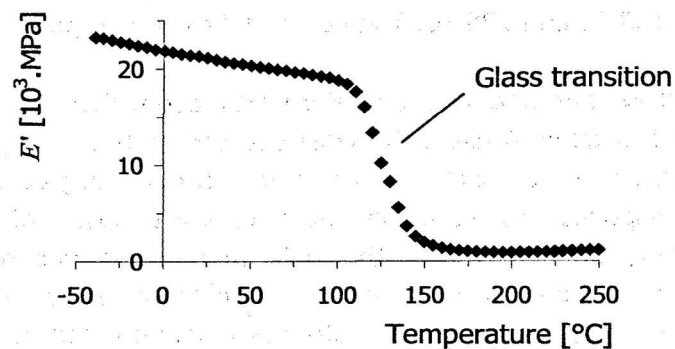


Figure 49: Storage Modulus as function of the Temperature at 25 Hz

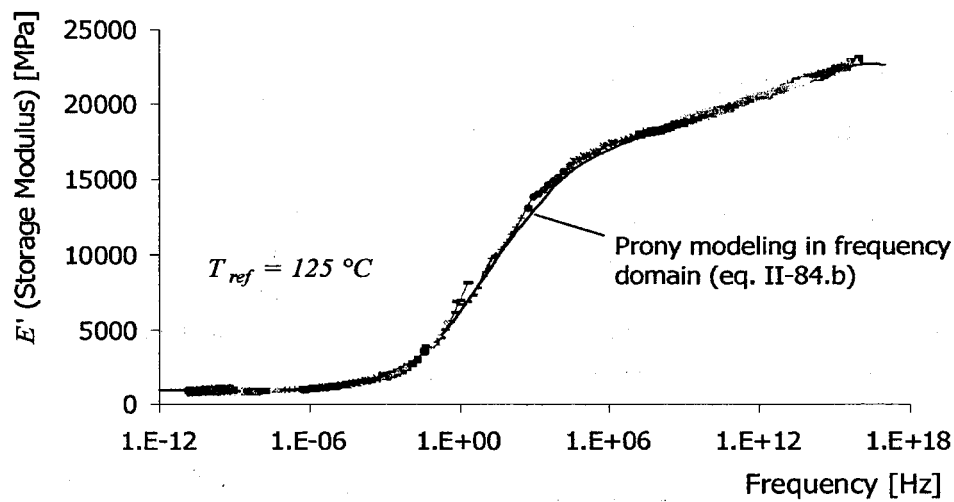


Figure 50: Tensile Storage Modulus Master Curve

The obtained shift factors are given in **Appendix A**, the shift function curve is displayed in Figure 22. When the mastering is completed, a Prony fitting is performed. The retardation times are taken equal to 10^{-i} , where i varies from -16 to 6, and the corresponding elastic constant E_i are determined within the fit consequently to this choice.

The long time tensile modulus at 125 °C is found equal to 905 MPa. The measured tensile modulus with respect to the temperature is given for a frequency of 25 Hz in Figure 49. It exhibits a strong drop down around 125 °C corresponding to the glass transition.

IV.5.2 Poisson's Ratio Characterization

The precise characterization of the Poisson's ratio is not the scope of this paragraph. Since measuring the Poisson's ratio is dynamically difficult, it can be alternatively estimated indirectly through another elastic constant. In this work, the Poisson's ratio is estimated through the bulk modulus. A series of PVT measures (Pressure-Volume-Temperature) are performed at different temperatures to highlight the temperature dependency of the Poisson's ratio. A constant hydrostatic pressure of 100 MPa is given to a small material block of 29.7865 g and volume 14.8943 cm³ at 20 °C. The PVT tests are performed at 60 °C, 100 °C, 120 °C, 140 °C, 150 °C and 175 °C. The result at 175 °C is reported in Figure 51.

The results obtained exhibits strong noises. For that reason, they are fitted to a first order linear model (dashed black line) using the least squares method. This method provides an estimation of the final specific volume variation with a good degree of confidence (a first order model is not supposed to reproduce the temporal behavior of the Poisson's ratio!). Investigating the time dependency of the bulk modulus is not reasonable with such measures. The long term compression modulus is then estimated for each temperature. The obtained compression module, associated with the long term tensile modulus (from DMA measures at 0.5 Hz) is used to estimate the long term Poisson's ratio.

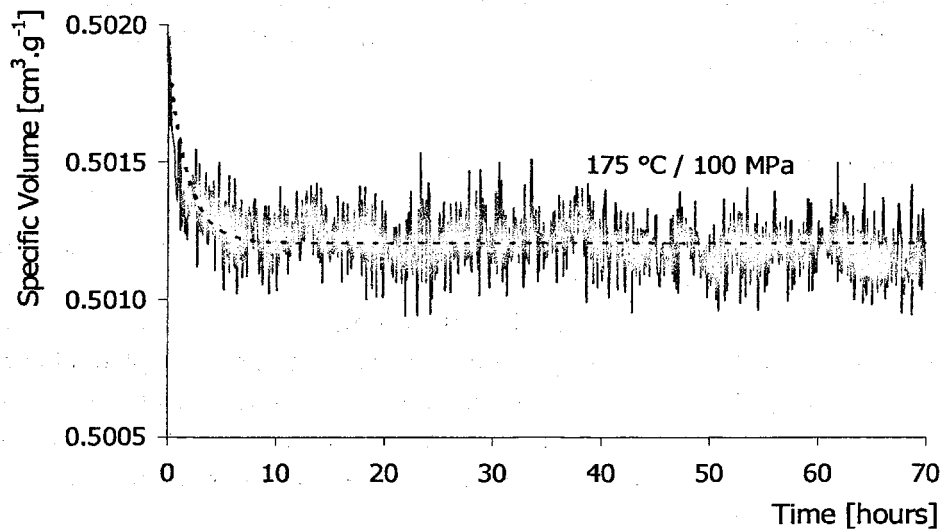


Figure 51: Material Volume Variation during a PVT Measure at 175 °C under 100 MPa

The compression modulus is determined through the volume change of the specimen under pressure using the relation eq. IV-2:

$$K(T, \infty) = -V_0 \frac{\partial P(T, \infty)}{\partial V(T, \infty)} \quad \text{eq. IV-2}$$

The Poisson's ratio is then estimated using eq. IV-3.

$$\nu(T, \infty) = \frac{1}{2} - \frac{E(T, \infty)}{6K(T, \infty)} \quad \text{eq. IV-3}$$

The values found for the Poisson's ratio are displayed in Figure 52 (black points). The general trend is given by the dashed grey line, which goes to the value 0.25 at room temperature (material provider data).

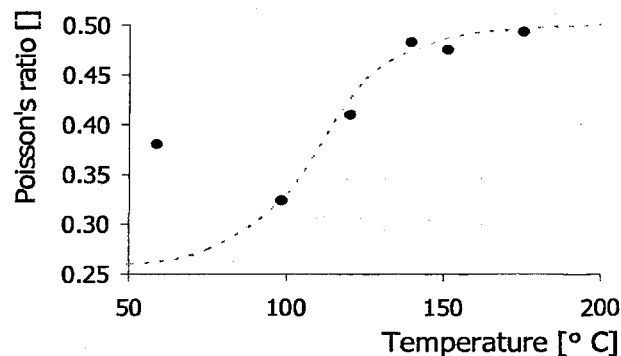


Figure 52: Long Term Poisson's Ratio from Tensile Modulus (DMA Data) and Bulk Modulus (Long Term, Temperature Dependend)

The value found at 60 °C is out of the overall trend, what can be associated to an experimental artifact during the PVT measure. This value is further not considered. A value of 0.25 is admitted at room temperature.

IV.5.3 Copper Leadframe

Copper leadframes are obtained by chemical cutting of copper rolled plates. Its elastic modulus is determined using tensile test.

Tensile test are performed in order to characterize the elastic behavior of the copper substrate. Standard "Dog-Bone" tensile specimens are cut in the copper plates in both rolling and orthogonal to rolling directions, in order to evaluate material anisotropy due to rolling. An elastic modulus of 81000 MPa is found in rolling direction and 83800 MPa in orthogonal direction to rolling. The values of 82000 MPa for the tensile modulus and 0.2 for the Poisson's ratio are assumed.

IV.6 Numerical Modeling

The triangle button shear specimen is modeled within Abaqus CAE 6.8. Modeling is programmed into a Python script, which allows the realization of parametric modeling. Model dimensions, crack length, shearing height, and mesh size at crack tip are parameterized parameters.

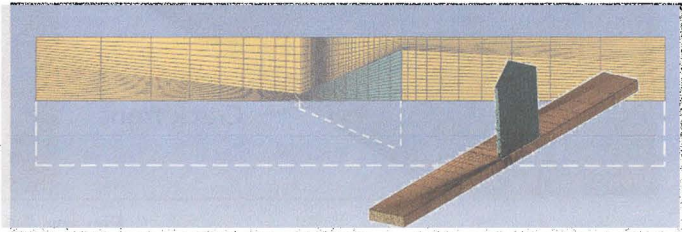


Figure 53: FE Model of the TBSS

IV.6.1 Boundary Conditions

To speed up the computation, just the half is modeled, regarding the longitudinal plane (Figure 53).

The whole system is positioned to obtain crack propagation in the X-direction. The Z-axis is oriented vertically. A symmetry condition is defined on the half-plane according to the X-Z plane.

Nodal degrees of freedom of substrate exterior flank are set to zero in the three directions. It corresponds to the substrate clamping. No pressure is set to reproduce the pressure of the clamping system, considering that the substrate is rigid enough and that clamping does not alter the crack tip field.

IV.6.2 Shearing Tool

The shearing tool is modeled as rigid body. It is constrained to have one degree of freedom: the translation in the X-direction. A hard contact is defined between the shearing tool and the surface loaded on the plastic cone. Friction is also defined in the contact interaction, with a dry friction coefficient of 0.3. A gap of 0.001 mm is initially defined between the specimen and the shearing tool to ease the initial contact resolution. A condition of displacement in the X-direction is given on the shearing tool. Displacement is applied progressively in 10 times increments, until a shear loading superior to the experimental critical shear forces is loaded (depends on the shearing height). It furnishes the ERR with respect to the applied shear loading (10 values from $F = 0$ to $F = F_{\max}$; $F_{\max} > \max(F_C)$, see paragraph V.1).

IV.6.3 Elements

Elements used in the overall model are exclusively cubic C3D8 elements, i.e. 1st order elements with 8 nodes and 8 integration points. Elements with reduced integration allow hourglass deformation on the crack flanks. Therefore, reduced integration is not used.

IV.6.4 Crack modeling

In accordance to Abaqus-VCCT requirements, the molding compound and the copper leadframe are modeled separately in two parts, and a contact interaction VCCT is defined between the components. Each part has exactly the same mesh at the interface, so that each interfacial node of one part forms a pair with a node of the other part.

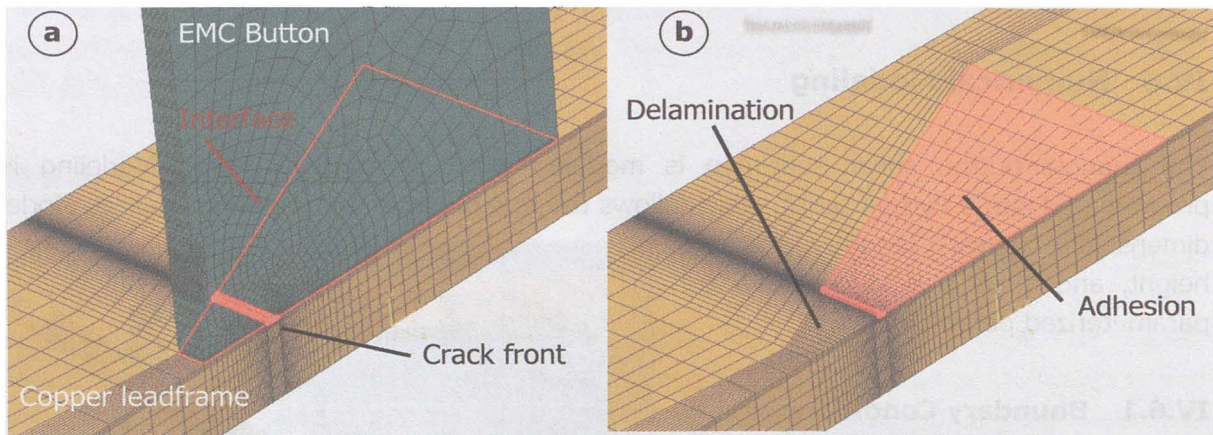


Figure 54:
 a. Model of the bimaterial interface
 b. Model with hidden Molding Compound Cone

In Figure 54, the modeled substrate/EMC interface is shown. Moreover the EMC cone is hidden on Figure 54.b to show the interface section (in red).

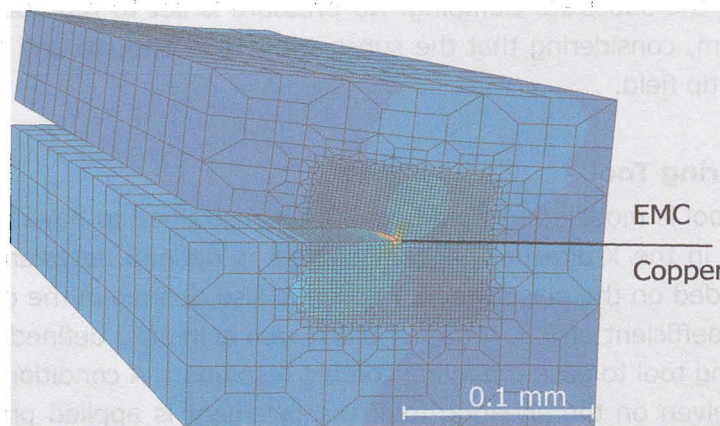


Figure 55: Mesh at crack tip

The delamination front is modeled as a straight line. The red highlighted area in Figure 54.b. corresponds to the area where adhesion between both parts is defined, i.e. all degrees of freedom are transmitted from nodes above to nodes below the interface. The area ahead the red one corresponds to the delaminated domain; nodes in the contact pairs are fully debonded and can move independently. A contact interaction is defined on crack flanks to prevent interpenetration. No friction is defined on the crack flanks.

IV.6.5 Mesh technique

Mesh is refined at crack tip (Figure 55) using a mesh schema only constituted of parallelepiped elements, increasing by 16 the mesh refinement at crack tip without strongly deformed elements. Elements length at crack tip, i.e. the parameter Δa is taken equal

to 0.0025 mm. This length corresponds to approximately 0.1% of the average crack length, which is small enough to fulfill the condition of self similar crack extension hypothesis (the use of the virtual crack closure technique requires that a crack extension Δa does not modify the stress and strain field at crack tip). This is also sufficiently refined to meet the results convergence condition for the estimation of ERR (section III.3.2).

IV.6.6 Material Modeling

Copper is linear elastic and isotropic modeled. Elastic constant from section IV.5.3 are taken. The EMC is modeled isotropic viscoelastic.

The instantaneous elastic module E_0 and Poisson's ratio are defined in the material model. Then, the viscoelastic properties are defined in the time domain with the Prony parameter found with the DMA measure, the time constants τ_i (refer to II.6.2.3, eq. II-74) and the reduced elementary elastic constant e_i defined by:

$$e_i = \frac{k_i}{E_0}. \quad \text{eq. IV-4}$$

The reduced elementary elastic constants are the elementary elastic constant of the Prony series divided by the instantaneous elastic module.

Besides, the shift function is defined as a table giving the shift factors with respect to the temperature, each 5 °C between -40 °C and 260 °C. This table cannot be directly defined in the input file. It is given in a Fortran UTRS subroutine which is compiled prior to the simulation ([Abaqus 6]).

Instantaneous Poisson's ratio of 0.25 is defined. The Poisson's ratio is then locally computed as function of the temperature and strain rate (verified in section III.3.4).

IV.6.7 Residual and thermal Stress Estimation

Residual stresses and thermal stresses are superposed to the mechanical stresses applied to the specimen. Residual stresses results from the mold shrinkage, i.e. from the polymer compression associated to the thermosetting solidification. Thermal stresses come from the incompatible thermal dilatation at the interface. The former is constant, whereas the latter is temperature dependent, assumed null at the post mold cure temperature (180 °C).

A simulation is performed in order to estimate the residual and thermal stresses.

A TBSS specimen is modeled. To simulate the chemical shrinkage of the molding compound, a cooling is applied on the EMC while the copper leadframe is maintained at constant temperature. The temperature variation applied to the EMC is chosen, so that the resulting thermal retraction corresponds to the material shrinkage.

A homogeneous temperature $\Delta T_S + T_M$ is initially given to the EMC button and a homogenous temperature T_M to the copper substrate. T_M corresponds to the molding temperature (180 °C). The material CTE defined in the numerical model are reported in Table 3.

	Copper	EMC	
CTE		$T < T_G$	$T > T_G$
	$16 \cdot 10^{-6}$ ppm/K	$8 \cdot 10^{-6}$ ppm/K	$3 \cdot 10^{-5}$ ppm/K

Table 3: Coefficients of thermal Expansion

The equivalent shrinkage temperature cooling ΔT_s is given by ([Böger 2001]):

$$\Delta T_s = \frac{\Delta V_s}{3\alpha_1} \tag{eq. IV-5}$$

The parameter ΔV_s corresponds to the volume shrinkage of the EMC and α_1 to its CTE at 180 °C. The CTE is given in the EMC datasheet. ΔT is found equal to 21.8 °C.

In reality, the specimen is not delaminated after molding. In the numerical model, the delamination flanks are maintained bounded. In the normal direction to the contact, a contact penalty method is used to maintain the delamination close. In the tangential direction, a 'Rough' property is defined, preventing from any mode II contribution as long as delamination flanks are maintained closed. Using this numerical trick, the modeled delamination is "suppressed".

Hence the chemical shrinkage is simulated; the whole specimen is cooled down till room temperature following a slow temperature ramp (Figure 56.a).

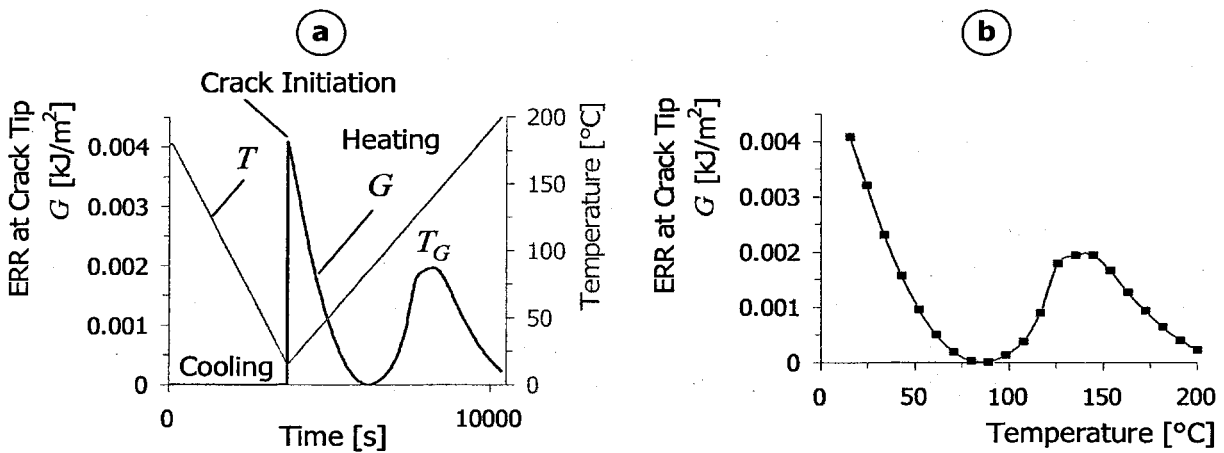


Figure 56: a. Cure Shrinkage and thermal Stress Simulation
 b. Residual and Thermal Stresses with respect to the Temperature

At room temperature, the crack initiation is simulated: the contact interactions maintaining the crack flanks together are suppressed. A delamination of 3 mm is modeled. In the simulation, the specimen is then reheated, following a ramp until 200 °C in order to determine the thermal ERR at delamination front with respect to the temperature. The heating rate is taken in the same order of magnitude as the experimental one (1 °C/min). No mechanical loading is given in this simulation.

The simulated ERR at crack tip, resulting from the sum of residual and thermal stresses, is reported in Figure 56.b.

At 180 °C, a value of 6.4×10^{-4} kJ/m² for the residual ERR at delamination front is found. It corresponds to the load at delamination front due to the EMC cure shrinkage without any thermal stress (no CTE mismatch). At this temperature, copper has a smaller CTE than EMC. By decreasing temperature from 180 °C to 125 °C (EMC glass transition), the copper substrate contracts less than the EMC button. The thermal stress increases as the strain incompatibility increases.

At T_G , the ERR reaches a maximum, with an approximate value of 2×10^{-3} kJ/m².

Under T_G , the CTE mismatch is reversed, i.e. copper has a greater CTE than EMC. By decreasing temperature, copper contracts more than EMC and consequently, the strain mismatch decreases with the temperature. So does the ERR at crack tip.

At 85 °C, materials have thermally retracted in the same magnitude, interfacial strains are hence compatible: a stress-free state appears at this temperature.

By decreasing temperature below 85 °C, copper still contracts more than the EMC. Incompatible interfacial strains appear again. The ERR at delamination front increases as the temperature decreases. At 20 °C, a thermal (and residual) ERR of 4×10^{-3} kJ/m² is found.

Similar simulations with delamination lengths of 2.5 and 3.5 mm exhibit quantitatively identical results.

IV.6.8 Residual and Thermal Stress Implementation

Superposition Principle for linear systems:

"For linear systems, if a forced strain field $\{\varepsilon_A\}$ produces a stress field $\{\sigma_A\}$ and if another forced strain field $\{\varepsilon_B\}$ produces a stress field $\{\sigma_B\}$, then a forced strain field equal to $\{\varepsilon_A\} + \{\varepsilon_B\}$ causes a stress field equal to $\{\sigma_A\} + \{\sigma_B\}$ ".

The mechanical system composed of the overall experimental setup is supposed to be linear and therefore respects the superposition principle.

The sum of the residual and thermal stresses, and the stress induced from the mechanical loading can be estimated separately using two different simulations and summed afterward. The same assumption is made for the strain, displacement and ERR fields.

A separate simulation, as described in paragraph IV.6.7, furnishes the stress and strain fields due to the residual and thermal stresses as function of the temperature, and also the thermal energy release rate G^{TH} . The latter takes the residual and thermal stresses into account. It is considered independent from the delamination length.

Using a mechanical simulation, the mechanically induced ERR G^{ME} is estimated as function of the crack length a , shearing height h and applied loading F , with respect to the elastic properties of the EMC which varies depending on the strain rate and the temperature.

During the post processing, the whole energy release rate G at delamination front is then estimated using the relation:

$$G = G^{\text{TH}}(T) + G^{\text{ME}}(F, a, h, T, \dot{\epsilon}). \quad \text{eq. IV-6}$$

Furthermore, nodal displacements at delamination front and along the delamination flank are obtained from the sum of nodal displacements under mechanical loading and nodal displacement due to thermal strains.

For each node of the delamination flanks, the thermal displacement is noted $u_j^{i-\text{TH}}$, where j denoted the direction x or y and i the node position ahead crack tip (section II.5.2).

The global relative crack flank sliding is then estimated using the eq. IV-8:

$$\frac{\Delta u_x^i}{\Delta u_y^i} = \frac{\left(u_x^{i-\text{TH}} + u_x^{i-\text{ME}}\right)^{\text{EMC}} - \left(u_x^{i-\text{TH}} + u_x^{i-\text{ME}}\right)^{\text{LF}}}{\left(u_y^{i-\text{TH}} + u_y^{i-\text{ME}}\right)^{\text{EMC}} - \left(u_y^{i-\text{TH}} + u_y^{i-\text{ME}}\right)^{\text{LF}}}. \quad \text{eq. IV-7}$$

The phase angle is then estimated as described in section II.5.2.

IV.7 Numerical Results

IV.7.1 Loading Conditions along the Delamination Front

As shown from scanning acoustic microscopy in section IV.4.4, the initial delamination front is curved but is simplified to a straight front in FE modeling.

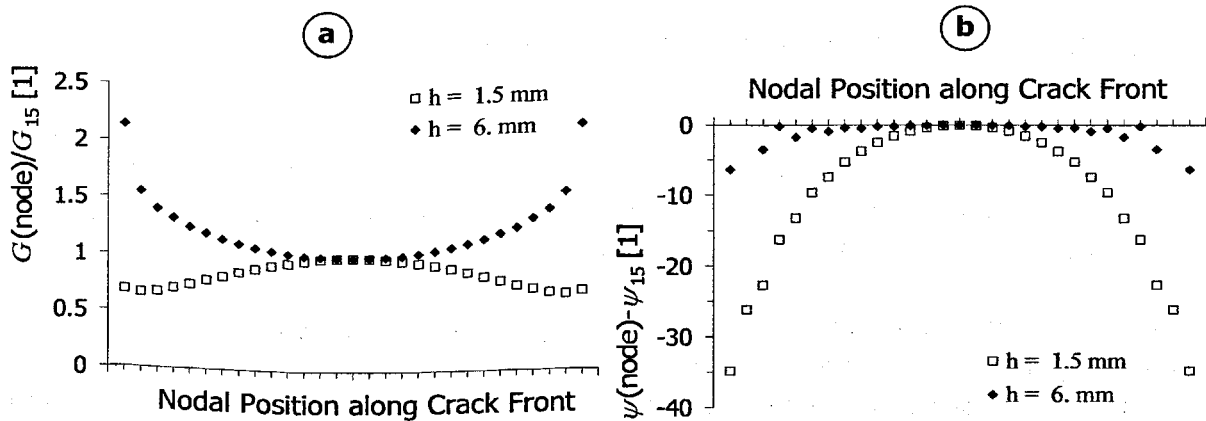


Figure 57: Loading along Delamination Front
a. Normalized ERR
b. Normalized Phase Angle

The Figure 57.a displays the ERR along the delamination front, normalized on the ERR at front midway, i.e. ERR at 15th node: G_{15} . The energy release rate is not constant along the delamination front. For low shearing height, the ERR is maximum at front midway, or minimum at front midway for high shearing height. The ERR can be, respectively two times higher at delamination front midway than at crack boundary, or respectively two times lower at front midway than at crack boundary.

Moreover, the phase angle is also not constant along the delamination front (Figure 57.b). For $h = 1.5$ mm, the phase angle is 35° lower at delamination boundary than at delamination midway. For $h = 6$ mm, the phase angle is only 6° lower at boundaries than at crack midway.

For high shearing height, the energy release rate is higher and the phase angle lower on the crack front boundary. Interfacial toughness is generally lower for phase angle (mode I loading), loading is then supposed to be more critical on crack boundary and supposed to propagate first at this place.

For low shearing height, the ERR and the phase angle are lower at crack boundaries. In this case it is not possible to conclude where the load conditions are more critical, and where delamination firstly propagates.

In the following parts of this work, and for the experimental/numerical correlation, the average ERR over the delamination front is always considered. The three modes ERR are summed in the global ERR. The phase angle is considered at delamination front midway.

IV.7.2 From Shearing Height to Mode Mixity

The simulations are performed for a crack length a varying between 1.5 and 4 mm and shearing heights h between 0.25 and 7 mm. A maximum shearing tool displacement of 0.05 mm is given in the simulations. In a first approach Residual stresses due to the EMC cure shrinkage, cooling down and CTE-mismatch are neglected.

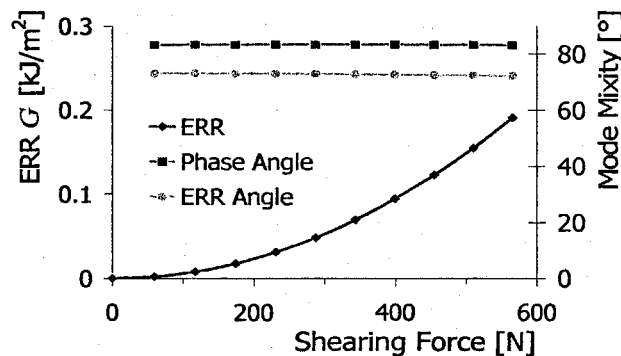


Figure 58: Load Conditions at Crack Tip with respect to the given Shearing Force

The ERR and phase angle variations with respect to the applied shear force are displayed in Figure 58 (for $a = 2.5$ mm and $h = 1.5$ mm). The ERR increases in a quadratic manner with the applied load. Since both stress and strain levels increase linearly with the applied load (linear material model), and considering that the ERR is equivalent to [strain] x [stress] (section II.4.2, eq. II-33 to eq. II-35), this result is the expected one. The phase angle is constant with the applied load.

IV.7.3 Mixed Mode Ratio

IV.7.3.1 General Trend

The phase angle decreases with increasing h , i.e. mode I amount increases as h increases (Figure 59). This trend is no more true if h drops under 1.5 mm. The simulations show that for $h < 1.5$ mm, crack flanks are in contact, which reopens the crack and causes an increase of mode I amount (section IV.7.3.2).

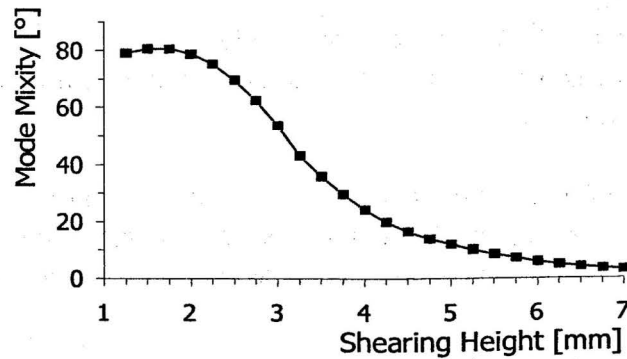


Figure 59: Relationship Shearing Height – Phase Angle at Crack Tip
(Graph obtained for a constant tool displacement of 0.05 mm,
and crack length of 3 mm)

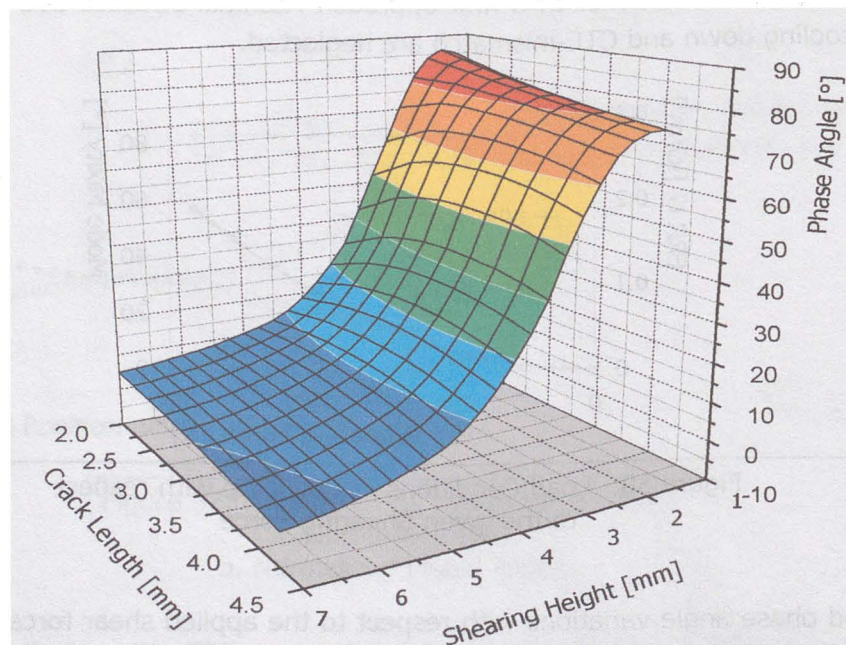


Figure 60: Phase Angle at Delamination Front Midway
(for a tool displacement of 0.05 mm at room temperature)

With shearing heights between 1.5 mm and 7 mm, all phase angle values between -5° and 85° are obtainable (Figure 60). Since the reference length for the phase angle estimation can be arbitrarily varied, the limit values of -5° and 85° are not fixed. In any case,

changing the reference length leads to a vertical shifting of the whole curve. The phase angle trend and the obtainable phase range are unaffected by the reference length.

The delamination length influences the mode mixity at the delamination front, displayed in Figure 60. Depending on the shearing height, the crack length has a low influence on the phase angle at crack tip. This influence remains in an order of magnitude of 10° .

IV.7.3.2 Maximum reachable Mode II Amount

The FEM simulation shows that the maximum mode II amount in this modified button shear specimen is reached by a shearing height of 1.5 mm. The existence of a maximum was unexpected. The phase angle should further increase by diminishing the shearing height. Experimental tests show also that the critical shear force starts to diminish by decreasing the shearing height under 1 to 1.5 millimeters.

This phenomenon is due to the contribution of different factors.

Firstly, reducing shearing height makes the stress concentration at tool contact point closer to the crack flanks, which increases the strain along the crack flanks.

In the area ahead of the shearing tool and along the crack, ε_{xx} approaches $-u/a$ and is negative. The strain in the vertical direction is then given by $\varepsilon_{yy} = -\nu \varepsilon_{xx} > 0$. This provokes a contact zone between the EMC and the substrate ahead of the crack tip in the delaminated area.

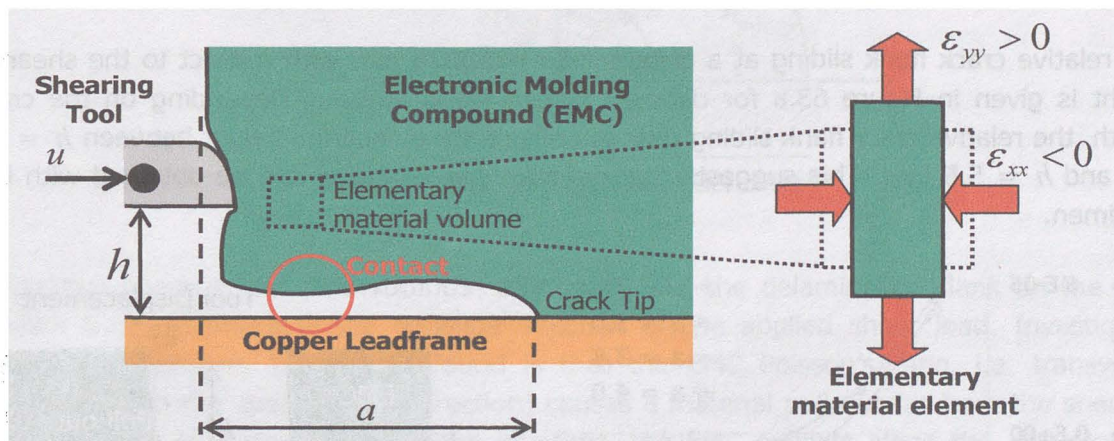


Figure 61: Strain along Crack Flanks by low Shearing Height

This phenomenon can be reproduced in simulation and the effect of this contact zone on the crack opening has been investigated for different shearing heights with a crack length of 1.5 mm.

The curves in Figure 62 are obtained from crack flank nodes displacement. For $h = 1.5$ mm, the crack is nearly closed, which means that the mode II amount is high. For $h = 1.25$, no crack opening occurs; the crack walls glide over each other. It corresponds to the maximum phase angle obtainable. Then, for $h \leq 1.0$, contact over crack flanks begins to induce opening at crack tip. Consequently, the mode II amount decreases and mode I amount

increases. The maximum mixed-mode ratio is obtained for a shearing height of 1.5 mm. Nevertheless this value may vary with the crack length.

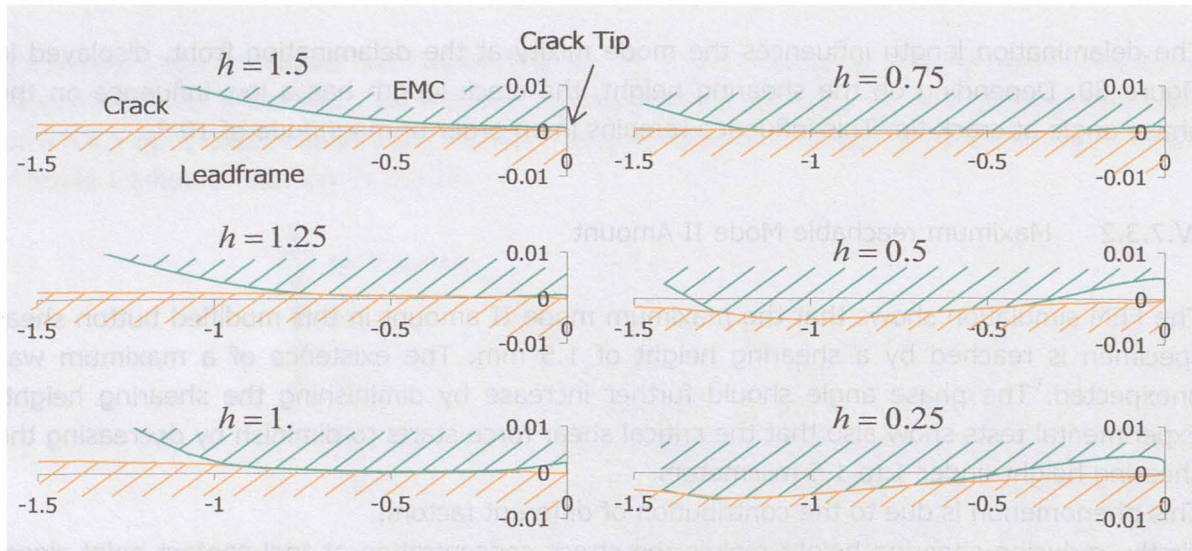


Figure 62: Crack Form by Low Shearing Height (FEM Results)

IV.7.3.3 Negative Mode II Loading

The relative crack flank sliding at a distance $\Delta a = 0.0025$ mm with respect to the shearing height is given in Figure 63.a for different delamination lengths. Depending on the crack length, the relative crack flank sliding changes of sign for a shearing height between $h = 5.0$ mm and $h = 5.5$ mm. This suggests that negative phase angles can be obtained with this specimen.

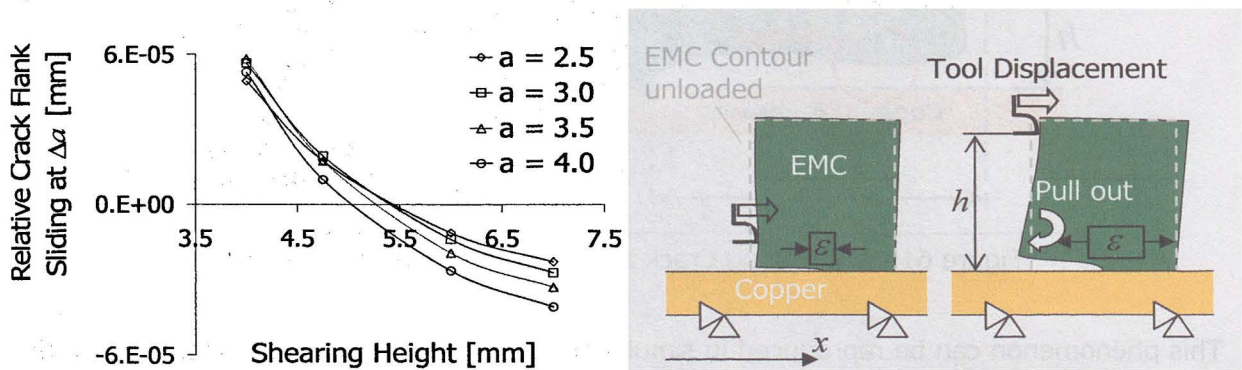


Figure 63: a. Relative Crack Flank Sliding at Δa as function of the Shearing Height
 b. Cone Deformation with respect to the Shearing Height

Anyhow, the relative crack flank sliding is not constant with the distance to the crack tip (due to the oscillatory behavior around the delamination front, refer to section II.3.3). In order to estimate the behavior of the mode mixity at crack tip, the relative sliding must be considered

at a distance infinitely close to the crack tip. In practice, the closest distance possible is the element length at crack tip, namely 0.0025 mm.

The only possible conclusion is that, it exists a shearing height h_0 , for which pure mode I loading appears at delamination front, and above which the mode II amount at delamination front become negative. According to Figure 63.a, h_0 is situated between 4 mm and 5 mm.

The mixed-mode behavior of the TBSS is resumed in Figure 64. The quantity formed by the pair shearing force F and shearing height h can be seen as a rotational vector in a $\{G_{II} \ G_I\}$ referential.

It exists a minimal value $h_{min} = 1.25$ mm, below which crack walls are in contact and the graph is not valid (Figure 62).

It exists a maximal shearing height h_{lim} , above which the mixed mode ratio is not any more affected as suggested by Figure 59 and Figure 60. This limit also corresponds to the button height, i.e. 10 mm. As suggested by Figure 63, it exists a shearing height h_0 for which the mode II amount is zero. The reference length for the phase angle estimation must be chosen, so that $\psi = 0^\circ$ for $h = h_0$.

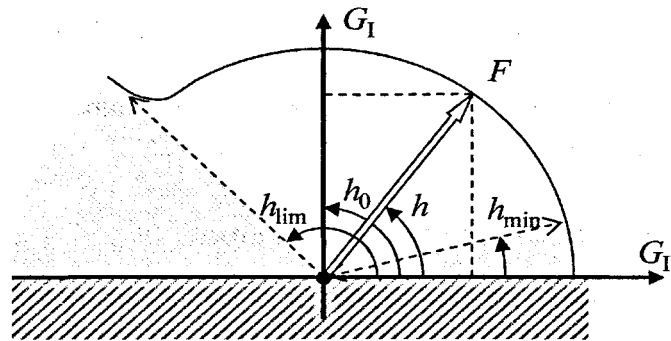


Figure 64: TBSS Mixed-Mode Behavior.

A negative phase angle means for the specimen, that the delamination flank on the EMC exhibits a displacement in the opposite direction of the applied shear load. Investigated using FE simulations, the reason found is that the EMC Poisson's ratio, i.e. transversal deformation (to the applied force direction) causes a material pull out far from the shearing tool. If loading is applied far from the interface, the EMC exhibits along the delamination flanks a positive strain in the horizontal direction. Consequently, the EMC pulls then out in the counter x direction (Figure 63.b).

IV.7.4 Phase Angle (from SIF) and ERR Ratio

The phase angle defined in paragraph II.5.2 is compared in Figure 65 with the so-called ERR Angle (paragraph II.5.3) defined by arctangent of the root of the energy release rate ratio G_2/G_1 . As already mentioned, this angle is inappropriate to describe the mode mixity in the case of interfacial cracking between dissimilar media. More precisely, the ERR ratio is not constant with respect to the distance from crack tip.

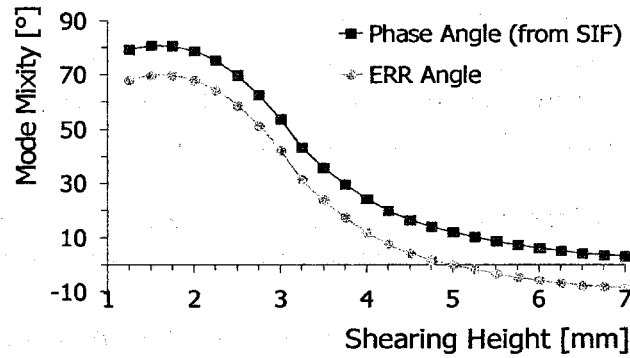


Figure 65: Phase Angle from SIF and ERR Angle (SIF phase angle estimated with an arbitrary reference length of 0.04 mm)

Both angles follow exactly the same trend, with a nearly constant offset of $-11.5^\circ \pm 0.5^\circ$. This confirms the hypothesis admitted in section III.2.2. Thus ω , the difference between both angles takes the value 11.5° . This value depends on the choice of the reference length (which affects ψ) and on the element length at crack tip, which affects the ERR ratio and consequently ψ_G .

Both mode mixity estimation methods lead to the same information, with only a shift factor as difference. This topic is further discussed in paragraph V.2.

IV.7.5 Energy Release Rate at Delamination Front

IV.7.5.1 Expected Behavior

The button is chosen to have a triangular cross section in order to obtain finite crack propagations, i.e. stable crack propagations.

As the delamination propagates at the button/substrate interface, the bonded surface becomes smaller. It leads to an increase of the mean interfacial stress, and an increase of the crack tip loading should be expected.

But due to the triangular section, the elementary area to delaminate dA for elementary crack propagation da increases with the crack length (eq. IV-8)

$$\frac{dA}{da} = 2 + \frac{3a}{4} \quad \text{eq. IV-8}$$

It means, that the energy required to propagate the delamination of da should be higher at $a = a_1$ than at $a = a_1 + da$, since the surface to debond has increased from $dA = da(0.75 a_1 + 2)$ for the same crack advance.

So, due to the triangular cross section, $dG/da < 0$. This is the condition of crack propagation stability, i.e. condition required to obtain finite crack propagations.

IV.7.5.2 Obtained Behavior

The effective obtained variations of the ERR at crack tip with respect to the delamination length are displayed in Figure 66.

As shown in this graph, the ERR does not always decrease with the delamination length. For a shearing height of $h=3$ mm, the ERR increases as the delamination grows.

For other cases, i.e. very low or high shearing heights, the ERR decreases as expected with respect to the delamination length. And even if dG/da is negative in these last cases, G decreases with a low derivative, which means that the condition of stable crack propagation may be hardly reached.

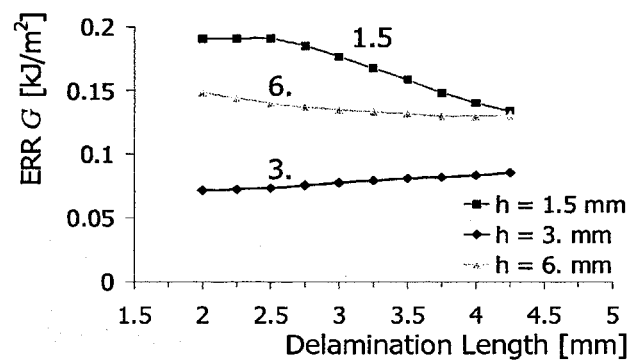


Figure 66: Energy Release Rate with respect to Delamination Length (estimated by constant tool displacement of 0.05 mm)

Moreover, these results are obtained by considering that the delamination propagation occurs at constant tool displacement, and that a part of the shear loading is released at propagation. In the case, where applied shear loading is not released at crack propagation, ERR at delamination front with respect to the delamination length is displayed in Figure 67 and Figure 70. Considering that the applied shearing force is not released at crack propagation, results exhibit a different trend.

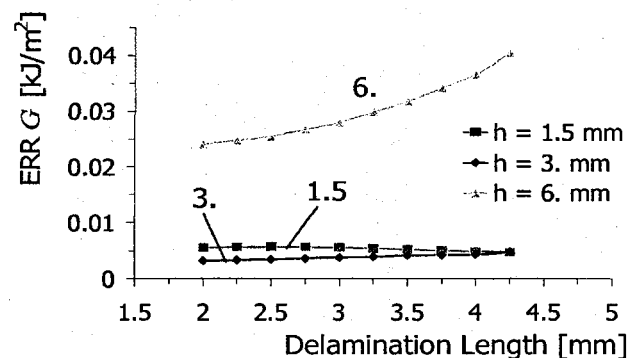


Figure 67: Energy Release Rate with respect to Delamination Length (estimated by constant tool force of 100 N)

For shearing heights lower than 3 mm, the ERR at delamination front is nearly constant with the delamination length. But for higher shearing heights, the ERR increases as the delamination propagates. It means that if the delamination propagation does not release a part of the applied loading, the critical loading is reached; delamination propagates in an unstable manner until the complete button is delaminated.

The influence of the shearing height on the ERR at delamination front is displayed in Figure 68 and Figure 70.

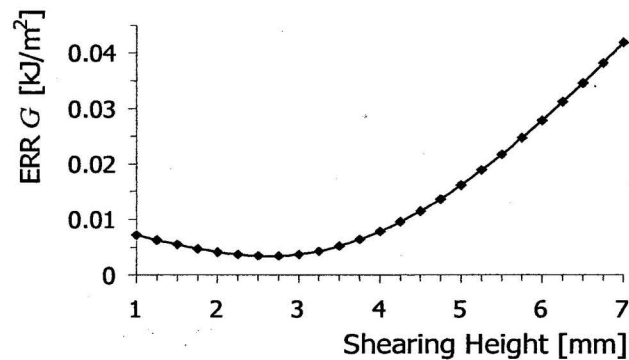


Figure 68: Energy Release Rate with respect to the Shearing Height (Graph obtained for a constant tool force of 100 N, and crack length of 3 mm)

Loading at crack tip varies monotonically with the shearing height. The expected behavior is that the ERR increases (by constant shear loading and crack length) with the shearing height: the shearing height corresponds to a lever arm between the applied force and the delamination plane. Load at crack tip should increase as the lever arm increases.

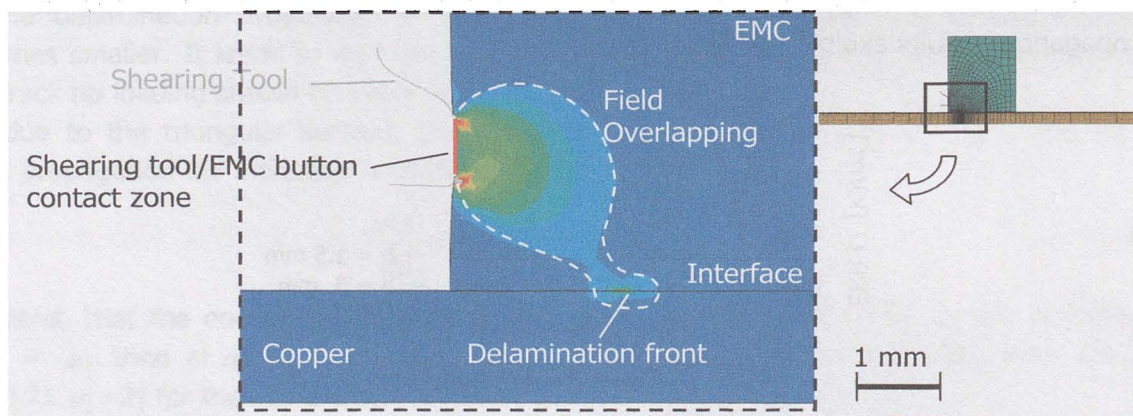


Figure 69: Overlapping Tool Contact Field/Crack Tip Field

The obtained result shows that previous assumption is only true for shearing heights higher than 2.5 mm. If the shearing height is lower than 2.5 mm, the ERR at delamination front is governed by another influence. For a low h , the shearing tool presses the EMC button close to the crack tip field. It brings a secondary stress concentration (the tool contact field) over the crack tip singularity (Figure 69). This influence disappears, as the distance between the crack front and the tool contact zone increases, i.e. as h or also a increases (Figure 70).

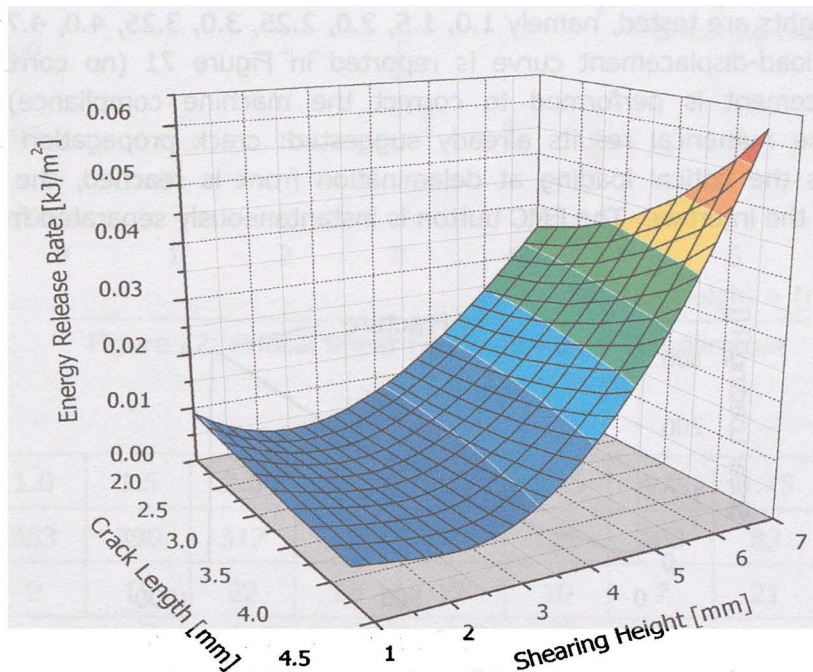


Figure 70: Average Energy Release Rate along Delamination Front
(For an applied tool force of 100 N, at room temperature)

IV.8 Experimental Investigation of the Mode Mixity Influence on the Delamination Strength at Room Temperature

IV.8.1 Experimentally obtained Critical Shear Forces

Nine shearing heights are tested, namely 1.0, 1.5, 2.0, 2.25, 3.0, 3.25, 4.0, 4.75, 6.0 mm. A typical obtained load-displacement curve is reported in Figure 71 (no correction on the measured displacement is performed to correct the machine compliance). This curve confirms what the numerical results already suggested: crack propagation occurs in an unstable way. As the critical loading at delamination front is reached, the delamination propagates along the interface. The EMC button is instantaneously separated from its copper substrate.

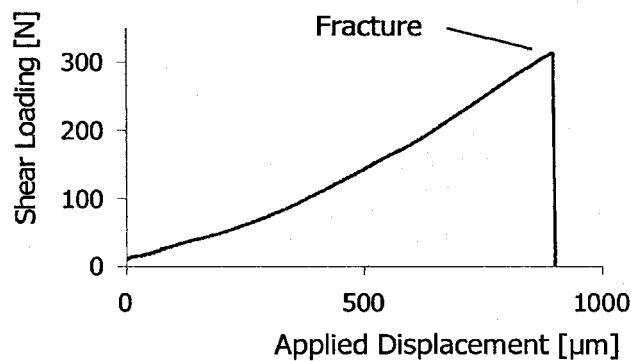


Figure 71: Typical Displacement-Load Curve

Force drop-down is used to identify the crack propagation and is taken as critical shear force. All experimental results are reported in Figure 72, displaying for each specimen the measured critical force with respect to the shearing height. To make the analysis of experimental results easier, a sketch of the numerical results is displayed on the corner up of the same figure: the phase angle and ERR with respect to the shearing height.

The average forces \bar{F} for each shearing height h and the corresponding experimental dispersion σ (standard deviation) are reported in Table 4.

The general trend reveals that the higher the specimens are sheared, the lower the force to propagate the delamination is.

For h varying between 1.5 and 3.5 mm, the critical shear forces exhibit strong variations with h . In the same interval, the ERR at crack tip exhibits a relatively low dependency to the shearing height. On the contrary, the phase angle drops down from about 45°.

Consequently the critical shear forces decrease can be associated with the phase angle variation: the higher the mode I loading amount at crack tip is, the lower the interfacial toughness is.

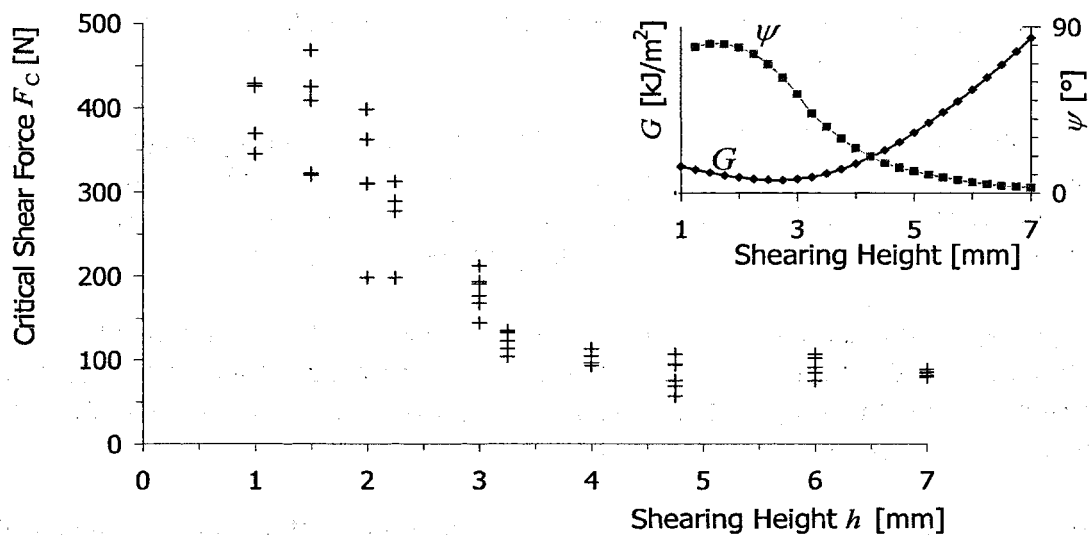


Figure 72: Critical Shear Forces at Room Temperature

h [mm]	1.0	1.5	2.0	2.25	3.0	3.25	4.0	4.75	6.0	7.0
\bar{F} [N]	383	390	317	270	181	122	103	83	92	84
σ [%]	9	15	22	16	12	10	7	21	12	4

Table 4: Shear Forces at Room Temperature

For h varying from 3.5 mm to 7 mm, the critical shear forces are all in the same range of 100 N. The critical shear force appears to be independent of the shearing height. The numerical results show in this range of h that, by constant force, the ERR at crack tip increases as the lever arm also does, i.e. as the mode II amount becomes larger.

The FEM results also show that the phase angle sink further as h becomes lower. As a consequence, for shearing heights between 3.5 and 7 mm, the mode I amount is expected to gain weight and the interfacial toughness increases. This unexpected result can be better investigated after the experimental/numerical correlation, the necessary procedure to determine the critical energy release rate, i.e. quantitative information about the interfacial toughness.

Finally, for $h = 1$ mm, the critical shear forces are lower than for $h = 1.5$ mm. As explained in part IV.7.5, for shearing heights below 1.5 mm, the crack flanks are in contact and the mode I loading increases at crack tip, what explains why the shear forces decreases again by very low shearing height.

IV.8.2 Experimental Dispersion

A relatively large dispersion can be observed in Table 4 and Figure 72. Specimens have different crack lengths. It results from the crack initiation process, during which the initial

delamination length is not precisely controlled. The initial crack length may have an influence on the loading at crack tip (Figure 66, Figure 67 and Figure 70), and consequently impacts the obtained critical shear forces.

The initial delamination length is investigated and measured on each specimen. In Figure 73, specimens are distributed in 30 fuzzy classes with respect to their initial delamination length. The first class, i.e. the first bar, corresponds to the smallest delamination length measured for the test session and the last bar to the longest delamination length.

The belonging to a class is one if the specimen delamination length is perfectly equal to the central value of the class and drop to zero as the delamination length is further away from the center value of the adjacent classes. The number of specimens in a class of delamination can be a decimal quantity.

The specimen repartition approaches a Gaussian repartition centered on the value 3.64 mm. The 80% specimen majority is considered: 80% of the specimens have an initial delamination length between 2.63 and 5.12 mm, which means that the initial delamination of most specimens varies till 2.5 mm. The average expected crack length variation is equal to 1.12 mm (estimated standard deviation).

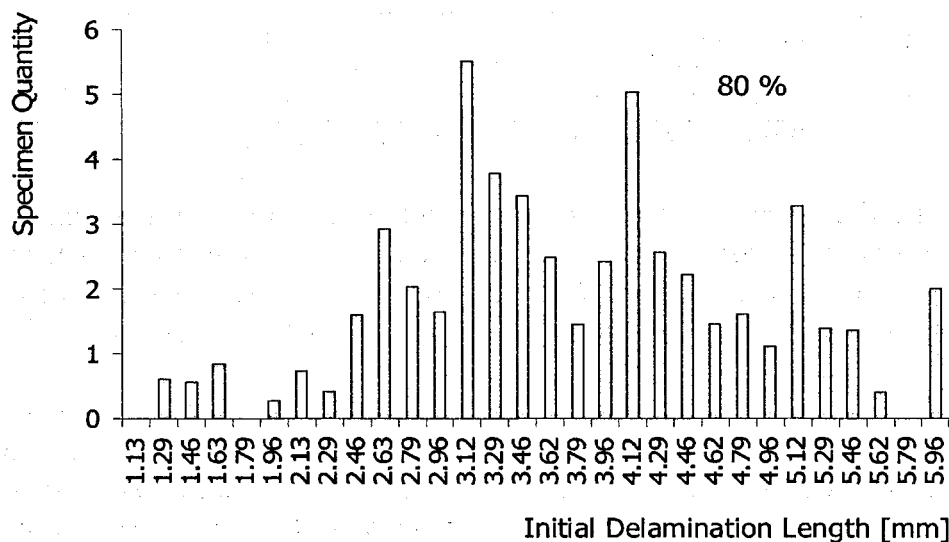


Figure 73: Specimens Repartition with respect to the initial Delamination Length

The initiated delamination length exhibits a large dispersion. It may explain the magnitude of the shear forces dispersion. The initial delamination length is taken into account in the experimental/numerical correlation (section V.1), so a lower dispersion is consequently expected for the estimation of the critical energy release rate.

IV.9 Experimental Investigation of the Temperature Influence on the Delamination Toughness

IV.9.1 Test Set-Up

The tests at higher temperatures than room temperature are carried out in a conventional Zwick/Roell tensile machine equipped with a temperature chamber. An adaptation of an existing button shear test jig is used in this test session (Figure 74

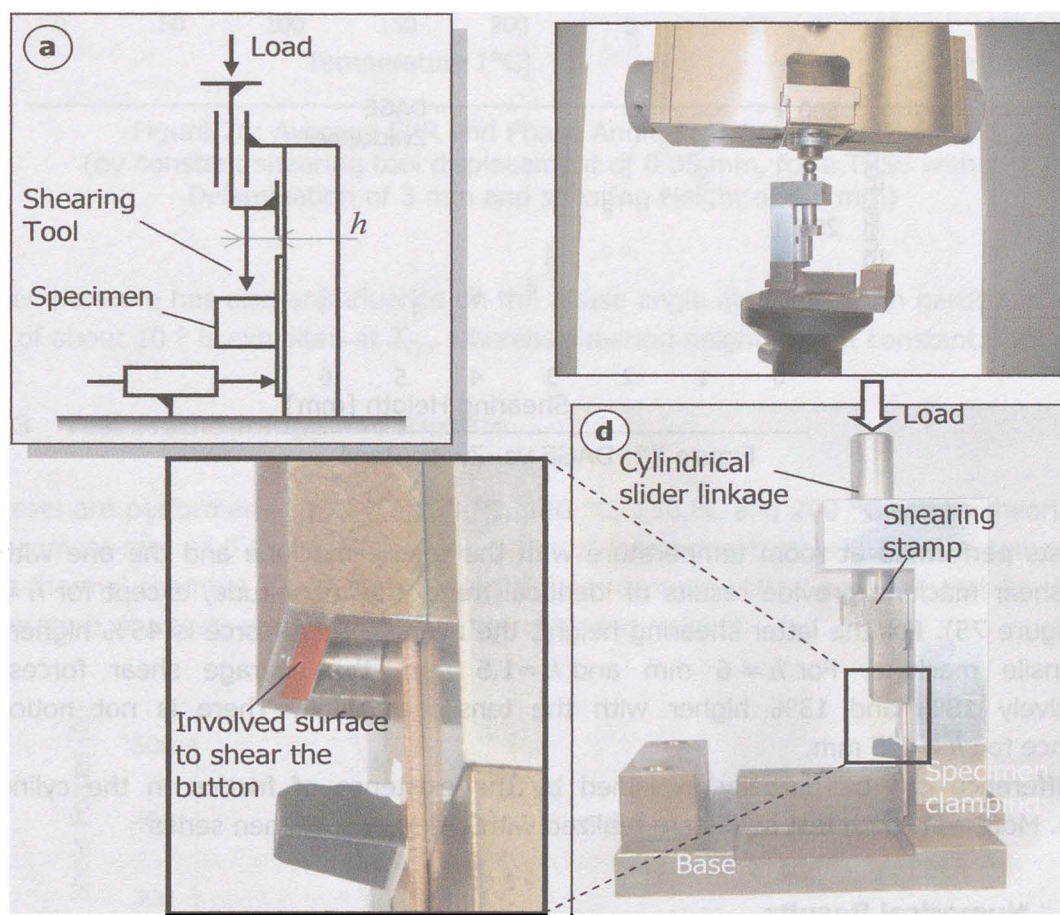


Figure 74: a. Test Jig Cinematic Description for Shear Test in a Tensile Machine
 b. Montage in the Machine
 c. Shearing Height
 d. Test Jig

The specimens are disposed vertically in the test jig chassis. They are not clamped on the substrate sides, but glided in a cleavage corresponding to the substrate thickness (Figure 74.b). A stamp glides vertically against the specimen to shear the EMC button (Figure 74.a). The stamp is guided vertically thanks to a cylindrical linkage. A rectangular cavity is milled in the stamp, so that the part of substrate situated forward to the button goes in the stamp as

the latter advances over the specimen (Figure 74.c). This permits to maintain the specimen in position. The stamp is also milled so that the attack point on the button is situated at the desired shearing height.

All mechanical linkages between stamp and structure are lubricated with a oil to avoid friction and parasite forces.

With this equipment, the shearing height depends on the stamp geometry and can not be chosen, excepting by changing the stamp. Four stamps are built to furnish the following shearing heights: 1.5, 2.5, 3.25 and 6 mm. This equipment can be used in a temperature chamber.

Tests are firstly performed at room temperature, in order to compare the obtained results with the ones from the test session with the DAGE Shear Machine (Figure 75).

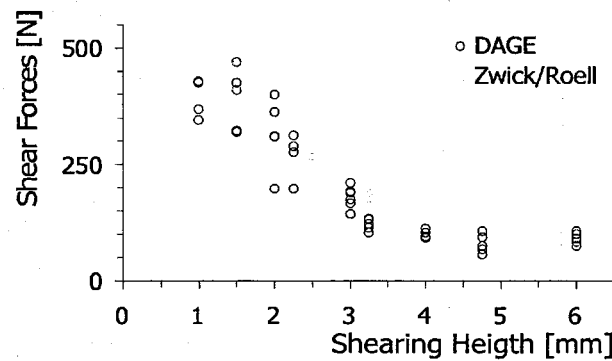


Figure 75: DAGE vs. Zwick/Roell

The tests performed at room temperature with the tensile machine and the one with the DAGE shear machine provide results of identical trend and magnitude, except for $h=3.25$ mm (Figure 75). For the latter shearing height, the average shear force is 45% higher with the tensile machine. For $h=6$ mm and $h=1.5$ mm, the average shear forces are respectively 18% and 13% higher with the tensile machine. There is not noticeable difference for $h=2.5$ mm.

This difference can be partially explained by the existence of friction in the cylindrical linkage. Moreover, both test series are realized with different specimen series

IV.9.2 Numerical Results

For this test session, the seven crack lengths (cf. section IV.7.2) and the four shearing heights tested (1.5 mm, 2.5 mm, 3.25 mm and 6 mm) are simulated.

All the 28 possible configurations with these parameters are simulated at the tested temperatures: 20 °C, 100 °C, 120 °C, 130 °C, 150 °C and 200 °C. A tool displacement rate of 0.1 mm/min is considered. Additionally to the numerical results, described in section IV.7, the numerical results obtained at higher temperatures reveal that the energy release rate at delamination front obtained with a constant shearing tool displacement decrease in the same

manner as the EMC elastic constants with respect to the temperature (Figure 76). The ERR monotonically decreases with the temperature; a strong drop is visible at T_G .

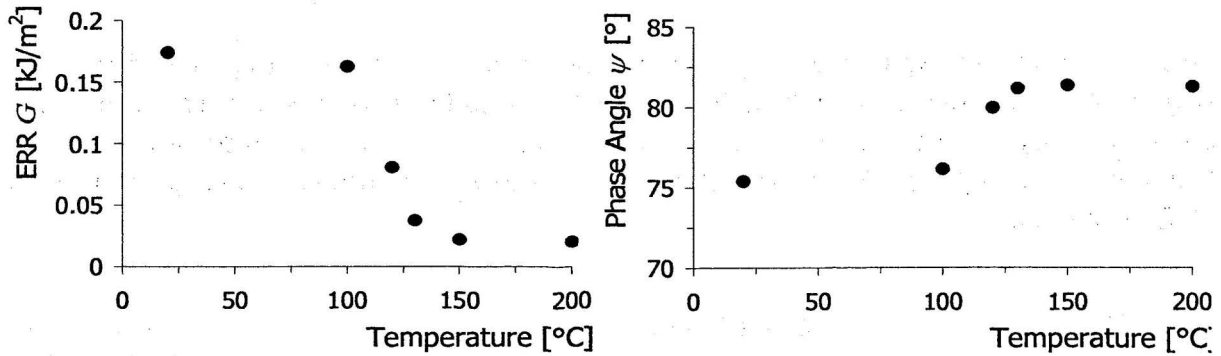


Figure 76: Average ERR and Phase Angle at Delamination Front (by constant shearing tool displacement of 0.05 mm, for a TBSS with a Delamination of 3 mm and shearing Height of 1.5 mm)

The temperature has also an influence on the phase angle at crack tip; in particular a phase jump of about 10 ° is exhibited at T_G , whereas shearing height is kept constant.

IV.9.3 Test Methodology and Results

The tests are performed at 100 °C, 120 °C, 130 °C, 150 °C and 200 °C with a shearing tool displacement-rate of 0.1 mm/min, in the order of increasing temperature. The temperature in the thermal chamber is monitored using a thermocouple placed near the test jig. At each temperature, the tests are performed at four shearing heights.

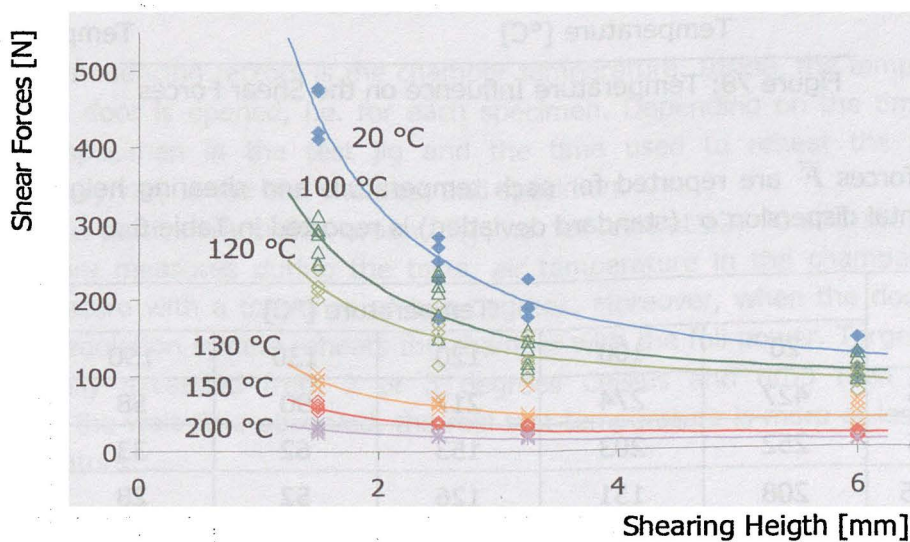


Figure 77: Shear Forces as function of the Temperature

A total of 120 specimens are used in this investigation (including tests at room temperature). The measured critical shear forces are displayed in Figure 77.

The lower the shearing height is; the higher the critical shear force is. This is observed at each temperature. The lower the mode I amount, the higher the interfacial toughness.

This test session shows that the higher the temperature is, the lower the shear forces are (Figure 78). The numerical results reveal that the stiffness of the molding compound decreases by temperature, what corresponds to analyses reported in the literature (section II.6). The critical shear forces show in particular a strong drop down at T_G (125 °C).

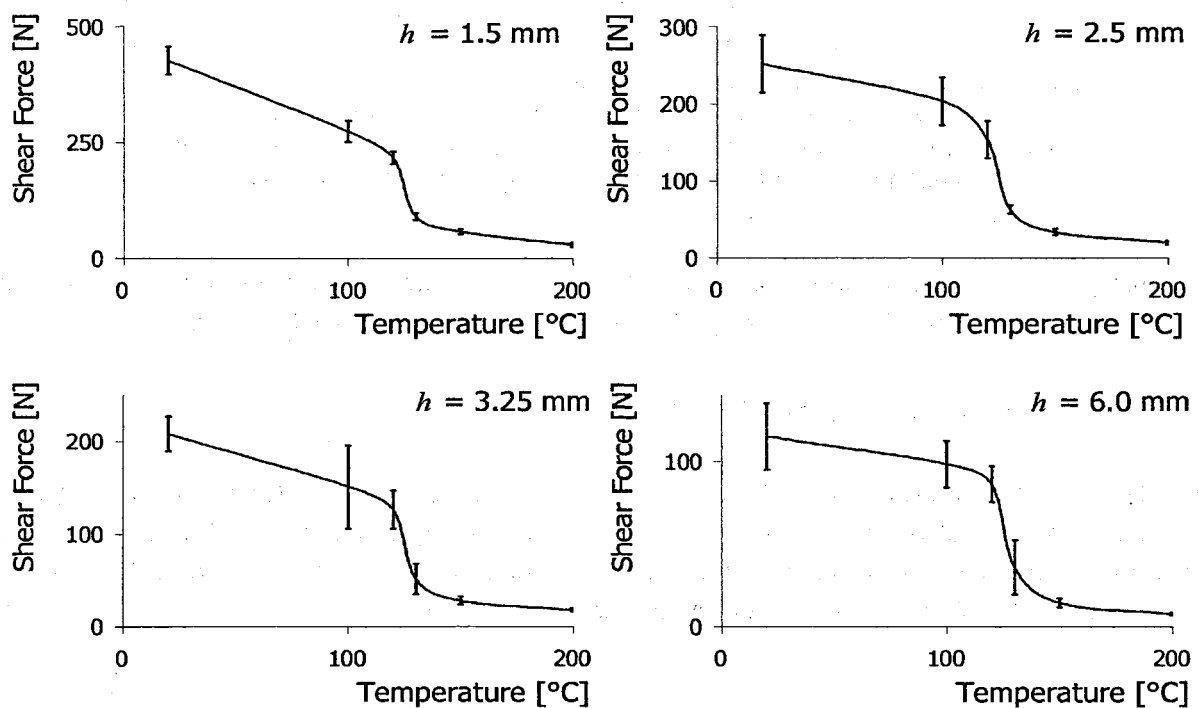


Figure 78: Temperature Influence on the Shear Forces

The average forces \bar{F} are reported for each temperature and shearing height in Table 5. The experimental dispersion σ (standard deviation) is reported in Table 6

\bar{F} [N]		Temperature [°C]					
		20	100	120	130	150	200
h [mm]	1.5	427	274	217	90	58	29
	2.5	252	203	153	62	33	20
	3.25	208	151	126	52	28	18
	6	115	98	86	36	14	8

Table 5: Temperature Influence: Average shear Forces

σ [%]		Temperature [°C]					
		20	100	120	130	150	200
h [mm]	1.5	7.0	8.5	6.4	8.1	9.4	15.6
	2.5	14.9	15.2	15.6	8.9	12.3	12.6
	3.25	9.1	29.60	16.2	31.0	15.7	11.7
	6	17.5	14.4	12.5	45.9	18.9	8.3

Table 6: Temperature Influence: experimental Scatter

IV.9.4 Experimental Dispersion

The experimental results for this test session exhibit more experimental dispersion than the results obtained with the DAGE machine (Table 4 and Table 6). There are exceptions in some cases – as for example at 100 °C with $h = 3.25$ mm and 130 °C with $h = 3.25$ and 6 mm – where the experimental dispersion reaches 30%. As in the previous test session, the initial delamination length varies and influences the crack tip stress and strain fields.

A statistical study is realized on the measured initial delamination length. The specimens are distributed in 30 classes (Figure 79). A Gaussian-like repartition centered on 3.2 mm and a standard deviation of 0.59 mm is found. The 80% majority is considered: most of the specimens have an initial delamination length between 2.53 and 3.81 mm. For most specimens, the initial delamination varies in a range of 1.28 mm.

Even if the initial delamination length dispersion has been reduced by a factor 2 in this session in comparison to the previous one, the experimental dispersion does not. It leads to the assumption that experimental dispersion is due to other influencing factors.

One of these influencing factors is the chamber temperature. Inside, the temperature drops each time the door is opened, i.e. for each specimen. Depending on the time required to position the specimen in the test jig and the time used to reheat the chamber, the temperature may vary in the test chamber and specimen.

This influence is particularly critical around T_G , i.e. for tests at 120 °C and 130 °C. According the temperature measures during the tests, air temperature in the chamber reaches the target temperature with a tolerance of two degrees. Moreover, when the door is reclosed, temperature regulation system reheats the chamber with the full power. Target temperature is systematically exceeded from 2 or 3 degrees Celsius and drop then slowly down. Depending on the wait-time observed, the real test temperature is more or less close to the target temperature.

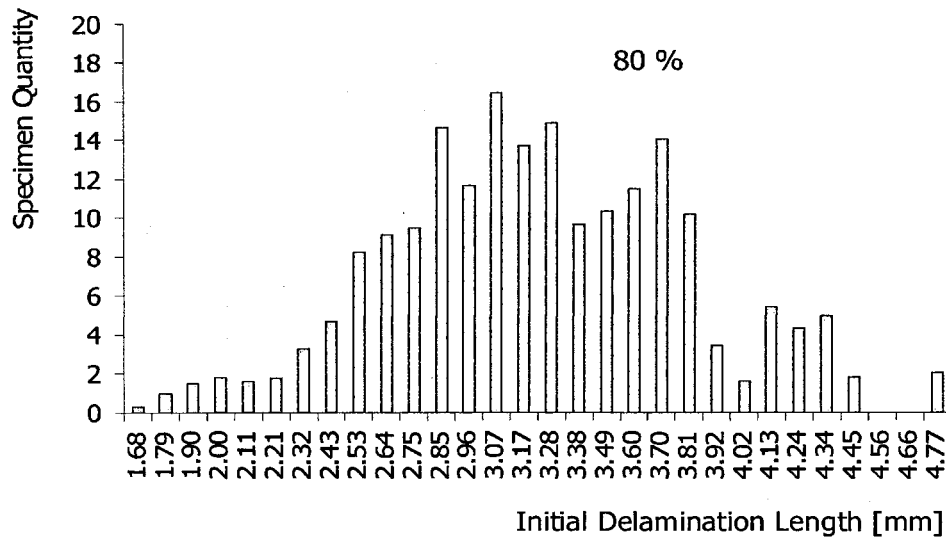


Figure 79: Specimens Repartition with respect to the initial Delamination Length

A potential influence is the variation of the shearing height due to the tolerance in the cylindrical linkage and the thermal expansion.

The cylindrical linkage between the stamp and the jig structure (Figure 74.a) leads to variation of the actual shearing height.

The thermal expansion of all parts of the test jig causes a deformation of the test apparatus. The shearing height for each stamp is given at room temperature at which the jig was manufactured. The variations of the shearing height involve variations of the mode mixity at crack tip and consequently different a delamination toughness.

Finally, there is also a perceptible friction in the sliding linkage between the stamp and the jig guiding part. It leads to random variations in the measured shear force. The contribution of these variations cannot be quantitatively estimated, but there existence can explain why critical shear forces are a higher with this test equipment than with the DAGE test machine (Figure 75).

IV.10 Experimental Investigation of the Load-rate Influence on the Delamination Strength

Further tests are carried out at high temperature using a Zwick/Roell tensile machine. The purpose of this test session consists in highlighting an expected rate dependency of the adhesion strength of thermosetting polymers.

IV.10.1 Test Set-Up

Another test jig is designed in order to improve the test results quality, i.e. to reduce experimental dispersion and improve test reproducibility (Figure 80).

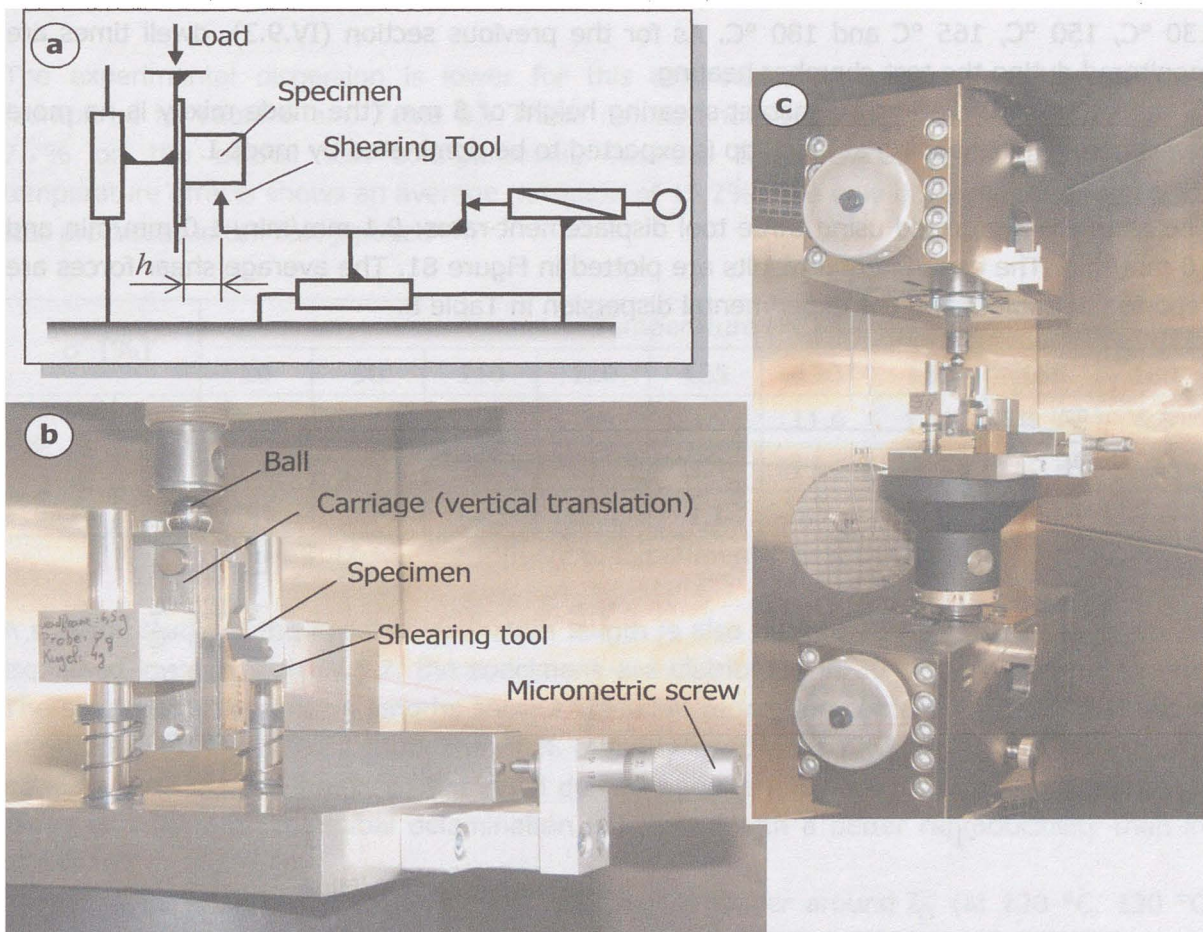


Figure 80: a. Jig Cinematic Description
 b. Shear Test Jig
 c. Montage in the Tensile Machine

The test jig functionality is enhanced to allow the choice of any shearing height between 0 and 10 mm thanks to a micrometric screw (Figure 80). A tool seat has been designed to accept the shearing tool initially used with the DAGE machine (tests at room temperature). The specimen is clamped in a carriage moving vertically. Hence the shearing height is chosen, the shearing tool is blocked and the specimen is pulled against the shearing tool in order to shear the button.

The sliding linkage between specimen carriage and jig guiding is realized with a double cylindrical linkage of 14 mm diameter.

The specimen and its carriage have a total weight of 355 g. It produces a force of 3.5 N superposed to the machine loading.

IV.10.2 Test Methodology and Results

The tests are performed at nine temperatures: 20 °C, 90 °C, 110 °C, 120 °C, 125 °C, 130 °C, 150 °C, 165 °C and 180 °C. As for the previous section (IV.9.3), dwell times are monitored during the test chamber heating.

All tests are performed at a constant shearing height of 5 mm (the mode mixity is no more investigated). The loading at crack tip is expected to be dominated by mode I.

The tests are performed using three tool displacement-rates: 0.1 mm/min, 1.0 mm/min and 10 mm/min. The experimental results are plotted in Figure 81. The average shear forces are reported in Table 7 and the experimental dispersion in Table 8.

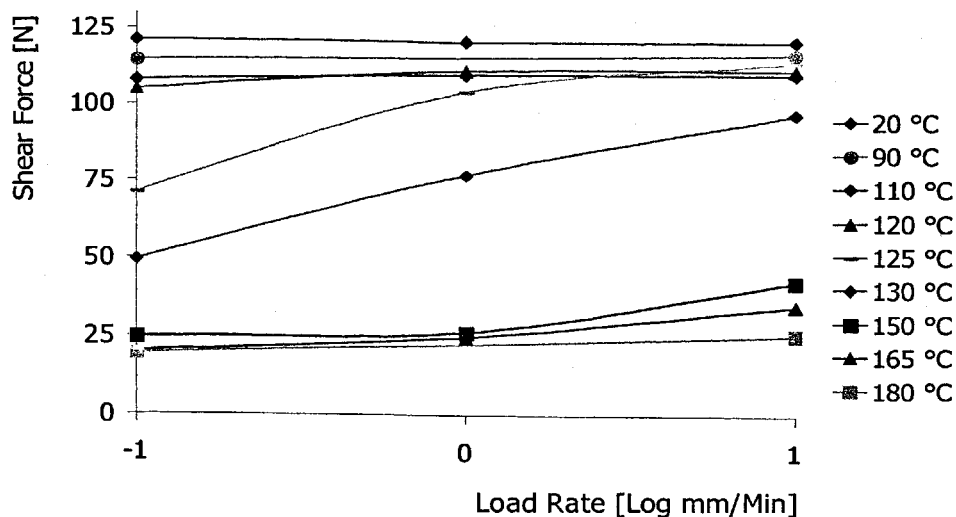


Figure 81: Experimental Result: Load Rate Effect on the Delamination Strength

These test results confirm the ones obtained in section IV.9: the higher the temperature, the lower the force required to shear the button.

Around the glass transition temperature, a significant influence of the load-rate can be observed: The higher the load rate is, the higher the critical shear force is. At 120 °C and

130 °C, the average shear force is respectively 1.6 and 2 times higher at 10 mm/min than at 0.1 mm/min. This influence decreases for test temperatures far from T_G , and has nearly no influence at room temperature or at 180 °C.

\bar{F} [N]		Temperature [°C]								
		20	90	110	120	125	130	150	165	180
dv/dt [mm/min]	0.1	121	114	108	105	71	49	25	20	19
	1	121	NA.	111	112	105	78	27	25	NA.
	10	122	118	111	113	115	99	44	36	27

Table 7: Average critical shear Forces for the Load-Rate Investigation

IV.10.3 Experimental Dispersion

The experimental dispersion is lower for this test session than for the previous ones (compared to Table 6 and Table 8). These results show an overall standard deviation of 7.7% on the overall test configurations, whereas the previous investigation of the temperature effects shows an average deviation of 15.2%. The only difference between both test processes is the test jig used

σ [%]		Temperature [°C]								
		20	90	110	120	125	130	150	165	180
dv/dt [mm/min]	0.1	3.9	5.0	2.9	9.6	3.5	11.6	12.7	4.3	6.3
	1	7.6	NA.	1.2	10.1	3.8	11.4	8.9	12.4	NA.
	10	8.1	10.6	NA.	17.1	3.1	8.4	11.3	6.4	3.5

Table 8: Load Rate Influence: Experimental Test Dispersion

A statistic study of the initial delamination length is also performed for this test session. As explained in paragraph IV.8.2, the specimens are distributed in 30 classes of crack length. The specimen delamination lengths show a Gaussian repartition centered in 3.63 mm with a standard deviation of 0.52 mm. The 80% majority specimens have an initial delamination between 3.07 and 4.13 mm, so the initial delamination length vary for most specimens in a range of 1.06 mm. The initial delamination is initiated with a better reproducibility than in others test sessions.

According to Table 8, the experimental dispersion is higher around T_G (at 120 °C, 130 °C and 150 °C). Around the glass transition temperature, a variation of 1 °C implies important changes in the material behavior. As explained in section IV.9.4, the temperature field in the test chamber is not homogeneous and can vary from the target temperature. This is probably a factor responsible for the higher experimental dispersion around 125 °C.

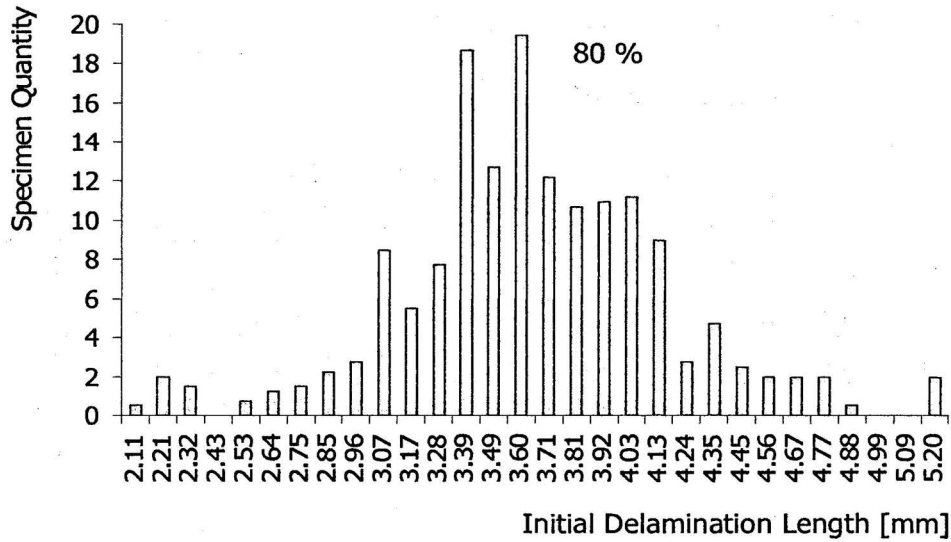


Figure 82: Specimen Repartition with respect to the initial Delamination Length

In Table 7 and Table 8, the cells for 1 mm/min at 90 °C and 1 mm/min at 180 °C are not filled. These test configurations are not investigated. Only one specimen is used for the test at 10 mm/min at 110 °C; that is why the standard deviation is not given for this case.

IV.10.4 Applying the Time Temperature Superposition to the Interfacial Toughness

Considering the combined temperature and load-rate dependency, the time-temperature superposition principle can be also be applied for the interfacial toughness of the EMC/copper interface. A mastering is performed (Figure 83) with the obtained critical shear forces.

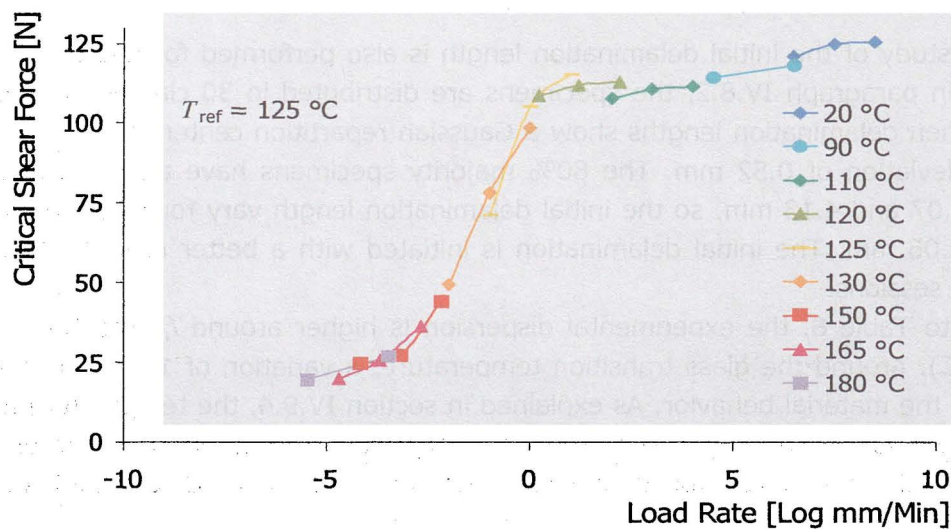


Figure 83: Mastered Shear Forces

Below the glass transition temperature, only few temperatures are tested so that segments do not intersect themselves. The shifting is performed with the assumption that the critical forces vary linearly with respect to the logarithmic load-rate. The obtained trend is similar to the storage modulus variation with respect to the excitation frequency (DMA, figure 25). In any case, the shift factors estimated with the shear force required to shear the button are lower than the shift factors defining the elastic properties of the EMC. The time-temperature superposition can obviously be defined for the interfacial toughness, but the time-temperature or rate-temperature correspondence is not the same as the one for the elastic properties. The interfacial toughness has its own shift factors, consequently its own Prony definition. The topic is further investigated in section V.4.2.

IV.11 Investigation of the Moisture Influence

IV.11.1 Test Preparation

The purpose of this investigation is to prove that the developed test set-up can be used to characterize the delamination toughness with respect to other influences, as for example water or petrol based media such as oil, gas, etc.

A series of 80 triangle button shear specimens is prepared as described in capital IV.4. Seven specimens are selected and weighted dry with a microgram balance directly after curing. The latter specimens and the 73 others are stored in a climatic chamber at 85 °C and 85 % air saturated with water. The EMC buttons are supposed to absorb humidity (swelling). The seven originally weighted specimens are then regularly weighted until moisture saturation is detected, i.e. until their weights do not increase anymore (Figure 84).

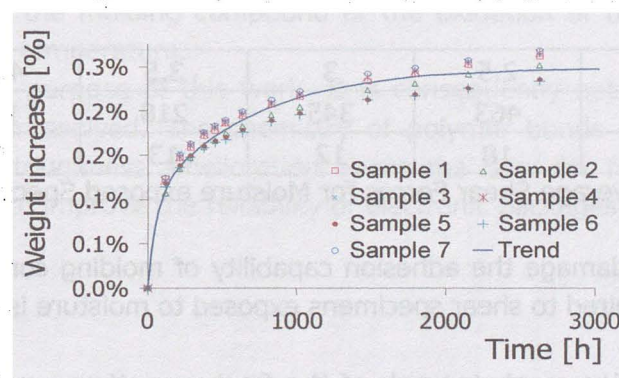


Figure 84: Moisture Absorption of Molding Compound

The moisture concentration in the EMC buttons reaches saturation after 3000 hours. An average maximal absorption level of 0.26% of the EMC weight is found. It corresponds to the value furnished in the material datasheet. The specimens are then stored at dry condition at 90 °C during 3000 hours. After this time, the molding compound is assumed completely dry and its original elastic properties are recovered. Hygroscopic material characterization is not performed.

IV.11.2 Test Results

The shear tests are performed at room temperature using a DAGE shear machine and the same test jig as in section IV.4. Six shearing heights are tested: 1.5, 2.5, 3, 3.5, 4.25 and

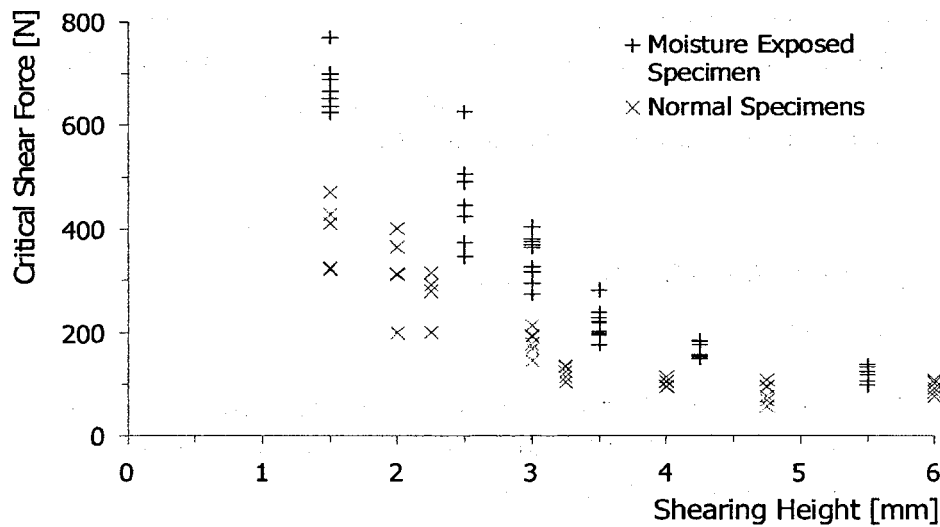


Figure 85: Critical Shear Forces for Moisture exposed Specimens

5.5 mm. The shearing tool is given a displacement rate of 0.1 mm/min. The obtained critical shear forces are displayed with straight crosses in Figure 85. The average forces and standard deviations are given in Table 9. The critical shear forces with normal specimens (section IV.8) are reported using oblique oblique crosses.

h [mm]	1.5	2.5	3	3.5	4.25	5.5
\bar{F} [N]	676	463	345	218	164	122
σ [%]	7	18	12	13	9	11

Table 9: Average Shear Forces for Moisture exposed Specimens

Moisture is supposed to damage the adhesion capability of molding compounds (paragraph II.7). Here, the force required to shear specimens exposed to moisture is 60 % higher.

For a better comprehension, a photograph of the fracture pattern, realized with a optical microscopy is reported in Figure 86. This picture is obtained using a zoom factor of 40. The fracture pattern exhibits on the back of the button a large area where the crack leaves the interface and kinks into the molding compound. Moreover, some micro-zones of non cohesive crack propagation are also visible.

The crack toughness at the interface is obviously becomed as good as the crack toughness inside the polymer.

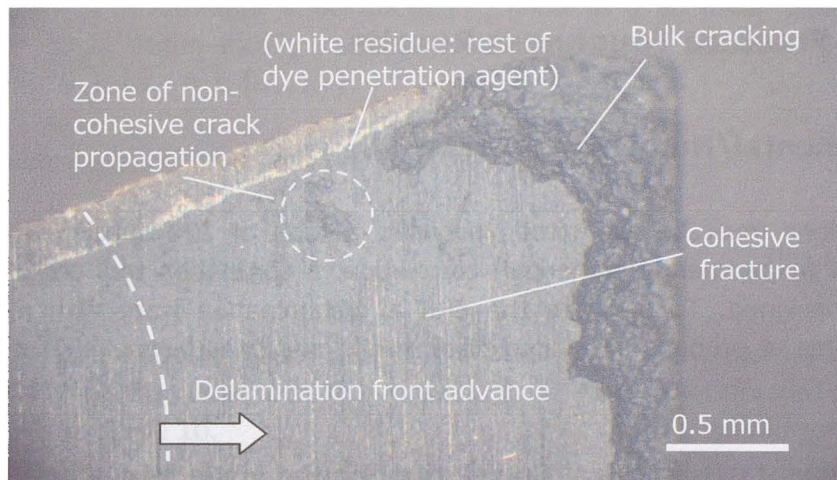


Figure 86: Fracture Pattern on Moisture exposed Specimens

As supposed that mode II amount considered in the interfacial direction increases as the crack propagates, then mode I amount increases for crack propagating in the normal direction to the interface. It means that crack propagates under increasing mode II amount along the interface, but would propagate under higher mode I amount in a transversal direction to the interface. Consequently, as supposed that crack toughness is the same order of magnitude along the interface as in the molding compound, a critical delamination length exists, from which crack easier propagates in the EMC button than along the interface.

However the reason why the interfacial crack toughness should increase is unknown. The specimens are not only 3 months stored in a moist environment, but also at 95 °C. An accelerated aging of the molding compound or the oxidation of the copper substrate may occur because of the temperature.

This topic is not the purpose of this work. It is consequently not further investigated and stays in this work unresolved. The chemistry of polymer bonds is a full topic itself. The observed interfacial toughness amelioration opens the door for further investigations and may be a key factor to improve the reliability of electronic packages.

V. Interfacial Fracture Toughness Results

V.1 Experimental/Numerical Correlation

Three test sessions must be evaluated, involving a total of 320 specimens. In order to perform the E/N (experimental/numerical) correlation, a correlation tool programmed in an excel sheet is designed. To estimate the ERR at delamination front with respect to the applied shear force at propagation, initial crack length and shearing height, an interpolation method is used.

V.1.1 Experimental/Numerical Correlation for the Mode Mixture Investigation at Room Temperature

The measures performed on the copper substrate to determine the initial delamination length reveals that for 80 % of the specimens, the initial crack length is situated between 2.5 and 5.1 mm. The finite element models are realized with a delamination length varying every 0.25 mm from 2 mm to 4.25 mm in 0.25 mm increments. Each model is simulated with nine shearing heights: every 0.25 mm, from $h = 1.25$ mm to 4.75 mm, and also $h = 6$ mm and $h = 7$ mm. It represents a job matrix of 81 simulation cases at room temperature.

In each case, the shear loading is given using a displacement of 0.05 mm, which produces resultant shear forces in the same order of magnitude as (or higher) than the experimental shear forces.

A post processing routine extracts the necessary results from the Abaqus result files and stores the information for each of the 81 simulations in a text file, as presented in Table 10.

Tool Disp. [mm]	Shear Force [N]	Mean ERR [kJ/m ²]	Crack Length [mm]	Shear. Height [mm]	Phase Angle [°]
0.00	0.0	0.0000	2.25	1.5	0.0
0.01	61.9	0.0019	2.25	1.5	79.1
0.01	123.6	0.0078	2.25	1.5	79.6
0.02	185.1	0.0175	2.25	1.5	79.7
0.02	246.9	0.0310	2.25	1.5	79.7
0.03	308.9	0.0484	2.25	1.5	79.6
0.03	370.7	0.0696	2.25	1.5	79.6
0.04	432.6	0.0946	2.25	1.5	79.5
0.04	494.4	0.1232	2.25	1.5	79.4
0.05	556.3	0.1556	2.25	1.5	79.3
0.05	618.3	0.1918	2.25	1.5	79.2

Table 10: Treatment of FEA Result for the E/N Correlation

The 81 tables are then copied in an interpolation tool which picks in the corresponding result. For example, to estimate the critical ERR corresponding to a specimen sheared with a

shearing height h_{exp} and critical shear force F_C , containing an initial delamination length of a_{exp} , the tool automatically selects four numerical models with parameter set $(a_1, h_1), (a_1, h_2), (a_2, h_1), (a_2, h_2)$.

The four numerical models are chosen so that

$$\begin{aligned} a_1 &\leq a_{\text{exp}} < a_2, \\ h_1 &\leq h_{\text{exp}} < h_2. \end{aligned} \quad \text{eq. V-1}$$

For each of the four models, a polynomial interpolation of the mean energy release rate along the crack tip with respect to the applied shear force is performed (eq. V-2) using tables analogous to Table 10.

$$G|_{a_i, h_j} = mF^2 + nF + p. \quad \text{eq. V-2}$$

The parameters m , n and p are given by (G_i , F_i refer to Figure 87.a)

$$m = \frac{(G_1 - G_3)(F_1 - F_2) - (G_1 - G_2)(F_1 - F_3)}{(F_1^2 - F_3^2)(F_1 - F_2) - (F_1^2 - F_2^2)(F_1 - F_3)}, \quad \text{eq. V-3}$$

$$n = \frac{(G_1 - G_2) - m(F_1^2 - F_2^2)}{(F_1 - F_2)} \quad \text{eq. V-4}$$

and

$$p = G_1 - mF_1^2 - nF_1. \quad \text{eq. V-5}$$

For each case, the critical ERR corresponding to the experimental shear force at failure F_C is determined:

$$\begin{aligned} &G|_{a_1, h_1}(F_C), \\ &G|_{a_1, h_2}(F_C), \\ &G|_{a_2, h_1}(F_C) \text{ and} \\ &G|_{a_2, h_2}(F_C). \end{aligned} \quad \text{eq. V-6}$$

A bi-linear interpolation is then performed using the four obtained critical energy release rates of the eq. V-6 (Figure 87.b). The interpolated critical energy release rate for the considered specimen is finally given by:

$$G_C = \frac{h_{\text{exp}} - h_1}{h_2 - h_1} (G|_{h_2} - G|_{h_1}) + G|_{h_1}, \quad \text{eq. V-7}$$

with

$$G|_{h_1} = \frac{a_{\text{exp}} - a_1}{a_2 - a_1} (G|_{a_2, h_1} - G|_{a_1, h_1}) + G|_{a_1, h_1} \quad \text{eq. V-8}$$

and

$$G|_{h_2} = \frac{a_{\text{exp}} - a_1}{a_2 - a_1} (G|_{a_2, h_2} - G|_{a_1, h_2}) + G|_{a_1, h_2}. \quad \text{eq. V-9}$$

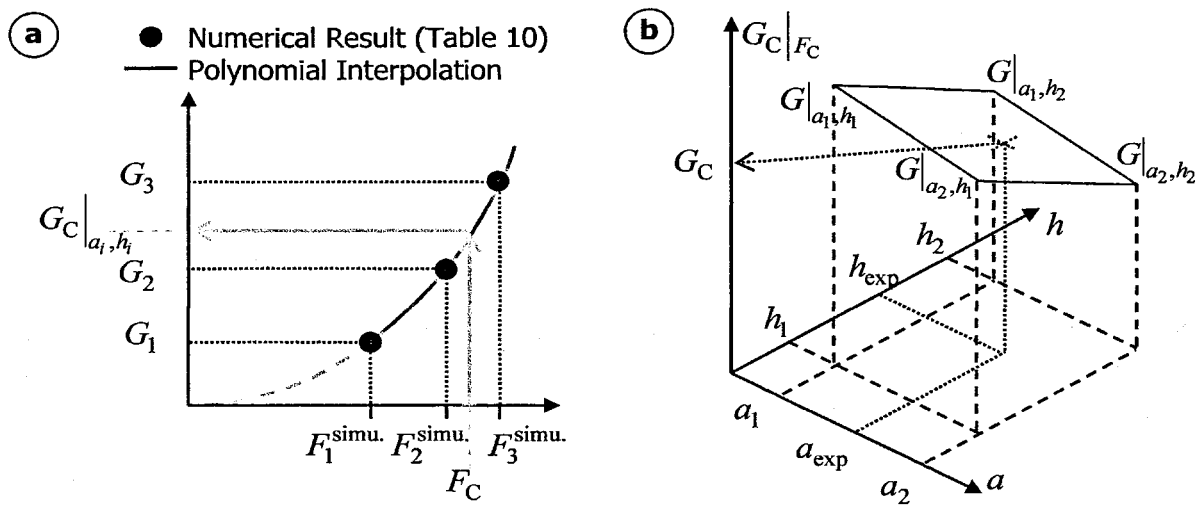


Figure 87: Numerical/Experimental Correlation
 a. Quadratic Interpolation of the elementary ERRs
 b. Bi-linear Interpolation of the Critical ERR

This method provides the obtained critical energy release rate corresponding to the critical shear force (force at failure) for each specimen. It permits to realize the numerical/experimental correlation with a reduced number of simulations. However the critical ERR is approximated. The ERR and phase angle at TBSS crack tip do not vary linearly with respect to the applied shear force (Figure 60 and Figure 70).

The quality of the interpolation depends on the quantity of simulated cases. The merrier the interpolation tool has information at disposal, the better is the interpolated critical ERR. In practice, all tested shearing heights are simulated.

V.1.2 Correlation for Tests at higher Temperatures than Room Temperature

The same methodology is used for tests at higher temperature. For the temperature investigation (paragraph IV.9), the four tested shearing heights (1.5 mm, 2.5 mm, 3.25 mm and 6 mm) are simulated at five different temperatures: 100 °C, 120 °C, 130 °C, 150 °C and 200 °C. Identically to the previous sessions, all configurations are simulated in nine crack length configurations (from 2 mm to 4.25 mm).

For the load rate investigation (paragraph IV.10), just one shearing height is simulated (5 mm) with the nine tested temperatures.

V.2 Mode Mixity Effect at Room Temperature

V.2.1 Experimental/Numerical Correlation

The critical energy release rate and phase angle obtained at crack propagation for each individual specimen are plotted in Figure 88.

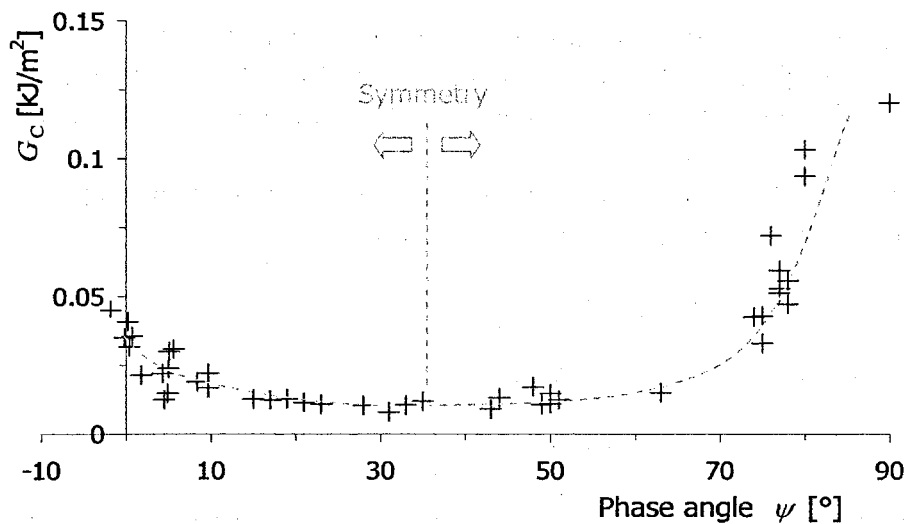


Figure 88: Critical ERR for Mixed Mode Ratio at Room Temperature

The general trend describes a bathtub formed curve. The curve seems symmetric around the mixed angle value of 35° where a minimum is met.

On the right side of this symmetry axis, the higher the phase angle, the higher the delamination toughness, i.e. the lower the mode I loading amount at crack tip, and the higher the delamination toughness.

By extrapolating in 90°, G_{2C} appears to be ten times higher than G_{1C} . It confirms that mode I loading at crack tip is much more critical than mode II loading.

This side of the curve can be split into two parts. Between 35° and 70°, the interfacial toughness increases slowly with the phase angle ($4 \times 10^{-5} \text{ kJ/m}^2/\text{°}$). At 70°, a strong change of derivative occurs. The interfacial toughness increases then from about $6 \times 10^{-3} \text{ kJ/m}^2/\text{°}$.

As suggested by [Mantič 2008], the fracture toughness curve is expected to be symmetric with respect to the ordinate (phase angle value 0°). Nevertheless this assumption is valid as long as the fracture phenomena are identical for positive and negative phase angles. More precisely, if fracture mechanisms are the same for negative and positive phase angles, the same level of energy is released at crack propagation.

The fact that the delamination toughness curve is not centered on $\psi = 0^\circ$ reveals that the reference length L used in the phase angle estimation (eq. II-42, paragraph II.5.1) is not correctly chosen.

V.2.2 Reference Length Determination

Considering eq. II-42 in section II.5, the reference length L generates a constant phase shifting ϕ_0 defined as:

$$\psi_0 = \arctan \frac{\Delta u_x}{\Delta u_y} + \arctan(2\varepsilon) - \varepsilon \ln(\Delta a) + \phi_0, \quad \text{eq. V-10}$$

with:

$$\phi_0 = \varepsilon \ln L. \quad \text{eq. V-11}$$

The previously chosen reference length of 0.04 is further noted as L_0 , the resulting phase shifting is noted as ϕ_0 (eq. V-11). The obtained interfacial toughness curve (Figure 88) reveals that the phase angle estimation is about 35 ° too high. A correction of $\phi_C = -35^\circ$ is required.

The new reference length determined with this investigation at room temperature is noted as L_{20} . This new reference length is given by the relation:

$$\varepsilon \ln \frac{\Delta a}{L_{20}} = \varepsilon \ln \frac{\Delta a}{L_0} + \phi_C. \quad \text{eq. V-12}$$

The reference length L_{20} is consequently defined by:

$$L_{20} = L_0 \exp\left(\frac{\phi_C}{\varepsilon}\right). \quad \text{eq. V-13}$$

The numerical application furnishes a value for L_{20} in the range of 10^{-6} mm. The phase angle estimated with the reference length L_{20} is further noted as ψ_{20} .

To find more precisely the position of the axis of symmetry in Figure 88, the points of the latter curve must be fitted to a mathematical model describing the critical energy release rate with respect to the phase angle. This model must be by definition symmetric with respect to the ordinate.

The equivalent critical ERR of [Benzeggagh 1996] is chosen and adapted in order to relate the critical ERR to the phase angle. From eq. III-9, the equivalent critical ERR at 20 °C is given by:

$$G_{C-20} = G_{IC} + (G_{IIC} - G_{IC}) \sin^{2\eta} \psi_{20}. \quad \text{eq. V-14}$$

ψ_{20} is the phase angle estimated using the reference length L_{20} which is not yet precisely known. G_{IC} , G_{IIC} are respectively the critical ERR for pure mode I loading and pure mode II loading. This function and the experimental results are fitted using the mean squares method. The reference length and the parameters G_{IC} , G_{IIC} and η are adjusted until the sum of the square differences reaches a minimal value. The estimated parameters are reported in Table 11.

G_{IC} [kJ/m ²]	G_{IIC} [kJ/m ²]	η [1]	L_{20} [mm]
0.0115	0.161	6.13	5.5×10^{-6}

Table 11: Interfacial Fracture Toughness at Room Temperature

V.2.3 Result Implementation

The fit performed in the last paragraph provides the interfacial fracture parameters required to define the equivalent energy release rate of [Benzeggagh 1996].

However these results can not be directly used with Abaqus since Abaqus only consider the mode mixity using the ERR angle ψ_G (eq. II-44) but not the real mode mixity at crack tip as in eq. V-14.

As highlighted by the numerical results (Figure 65), a relation between ERR angle and phase angle can be reasonably approximated with eq. V-15 where ω_0 is approached with 11.5° (for a crack tip element length of 0.0025 mm).

$$\psi_0 = \psi_G + \omega_0. \tag{eq. V-15}$$

With the reference length L_{20} , the eq. V-15 becomes $\psi_{20} = \psi_G - \omega_{20}$; ω_1 is given by:

$$\omega_{20} = \omega_0 - \phi_C = \omega_0 - \varepsilon \ln \frac{L_0}{L_{20}}. \tag{eq. V-16}$$

$\omega_1 = -21.3^\circ$ is found at room temperature. Thus the equivalent critical ERR of Benzeggagh is reformulated as:

$$G_{C-BK} = G_{IC} + (G_{2C} - G_{1C}) \sin^{2\eta}(\psi_G + \omega_{20}). \tag{eq. V-17}$$

As in the previous paragraph, the function in the eq. V-17 is fitted with the experimental results (Figure 89) re-estimated with the reference length L_{20} and thus symmetric with respect to ordinal axis.

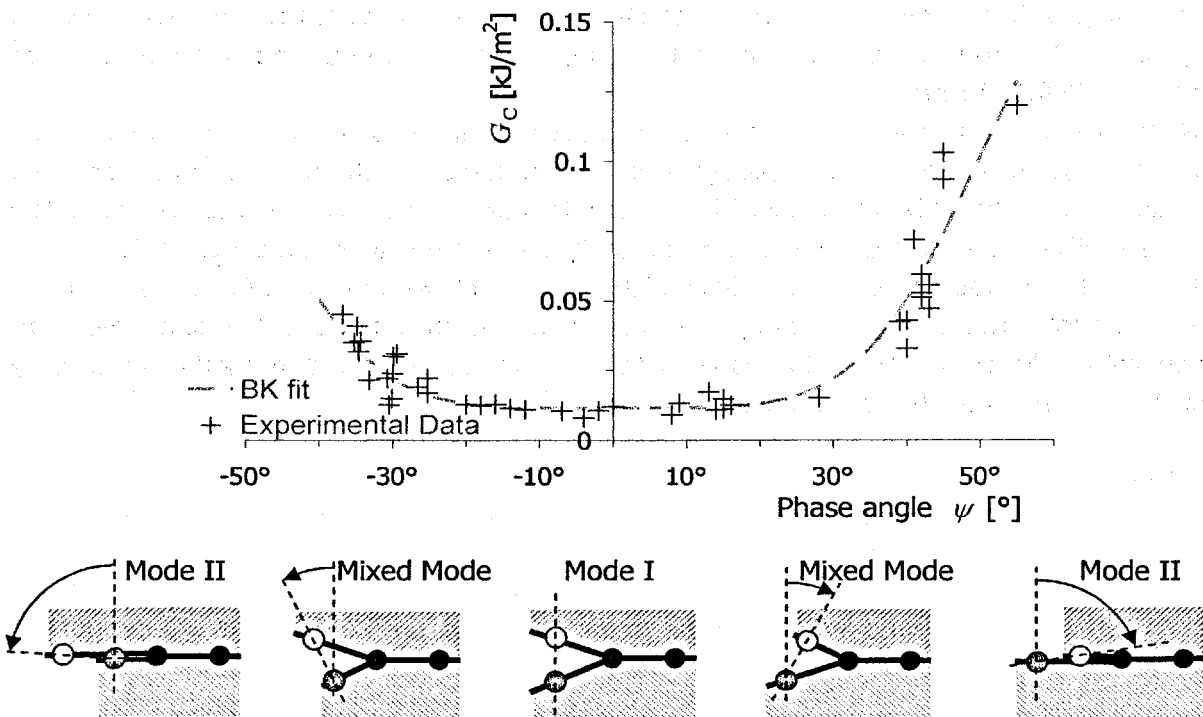


Figure 89: Numerical Implementation of the Interfacial Toughness at Room Temperature

The parameters are once again estimated using the mean square method (Table 12). This parameter set can be used to implement the interfacial toughness as a BK law in Abaqus.

G_{1C} [kJ/m ²]	G_{2C} [kJ/m ²]	η
0.0115	0.161	6.13

Table 12: Parameters for the BK implementation at Room Temperature

Since the ERR ratio G_2/G_1 at the crack tip estimated with the FEM varies with the element length at the crack tip Δa , the values given in Table 12 are only valid for models having the same mesh refinement as in simulations performed in this investigation, i.e. mesh length of 0.0025 mm at the crack tip.

V.2.4 General Comments

Similar results are reported in [Hutchinson 1992] for the delamination toughness of the Plexiglas/epoxy interface, investigated with a Brazil-Nut sandwich specimen. In the latter work, G_C slowly increases with the phase angle until 50°. At 50°, the curve describing G_C with respect to the phase angle exhibits a strong derivative change, and then the delamination toughness of the plexiglas/epoxy interface strongly increases with the phase angle. Hutchinson succeeds to characterize the latter mentioned interface at higher mixed mode angles. These results are in the same order of magnitude as the results shown in Figure 88. For the plexiglas/epoxy interface, G_{1C} is approximately equal to 0.03 kJ/m² and G_{IIC} to 0.13 kJ/m².

[Wang 1990] also investigated the delamination toughness of the aluminum/epoxy, brass/epoxy, steel/epoxy and plexiglas/epoxy interfaces with a Brazil-nut sandwich specimen. For the four interfaces, "2-segment toughness curves" are also found. A low increase of G_C is exhibited between 0° and 55°, and a strong increase above 55°.

This trend was also confirmed by [Shih 1991] for the glass/epoxy interface. [Benzeggagh 1996] investigated the glass/epoxy interface with the mixed mode bending specimen. Identical results are published in this work (the results are presented in another form; they must be reformulated to be compared).

V.3 Temperature Influence on the Delamination Toughness

V.3.1 Reference Length Estimation

Four shearing heights are tested to investigate the temperature influence of the delamination toughness. For this reason, the obtained curves giving the critical ERR with respect to the phase angle are not determined using many experimental points as in the previous paragraph.

The correct reference length for the mixed mode separation is obtained when the resulting phase angle shifting makes the toughness curve symmetrical with respect to the ordinal axis. As schematically displayed in Figure 90, each shearing height provides a set of points and lets the graph blank in between. The position of the symmetry axis is consequently difficult to estimate. To make it easier, every points found with a negative phase angle are mirrored in the positive side (Figure 90). The reference length is then adapted until the trend described by the mirrored points fit to the other points, so that all sets of points describe a smooth monotonic increasing toughness curve.

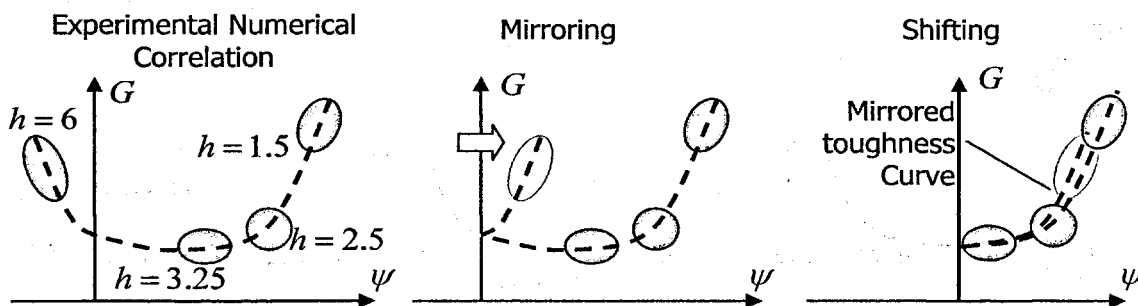


Figure 90: Reference Length Determination

V.3.2 Experimental Numerical Correlation

The critical shear forces obtained for the individual specimens at the six tested temperatures are correlated with the numerical results.

The corresponding critical energy release rates with respect to the estimated phase angle are displayed in Figure 91. Each point corresponds to a tested specimen. As explained previously, the points resulting from specimens in whom the phase angle at the crack propagation is found negative are mirrored on the right side of the curve. These points are represented using grey quad points.

The experimental results at each temperature are fitted with a BK equivalent ERR as in section V.2.2 (dashed grey lines). The parameters estimated for the BK laws and the reference lengths are estimated using the least squares method.

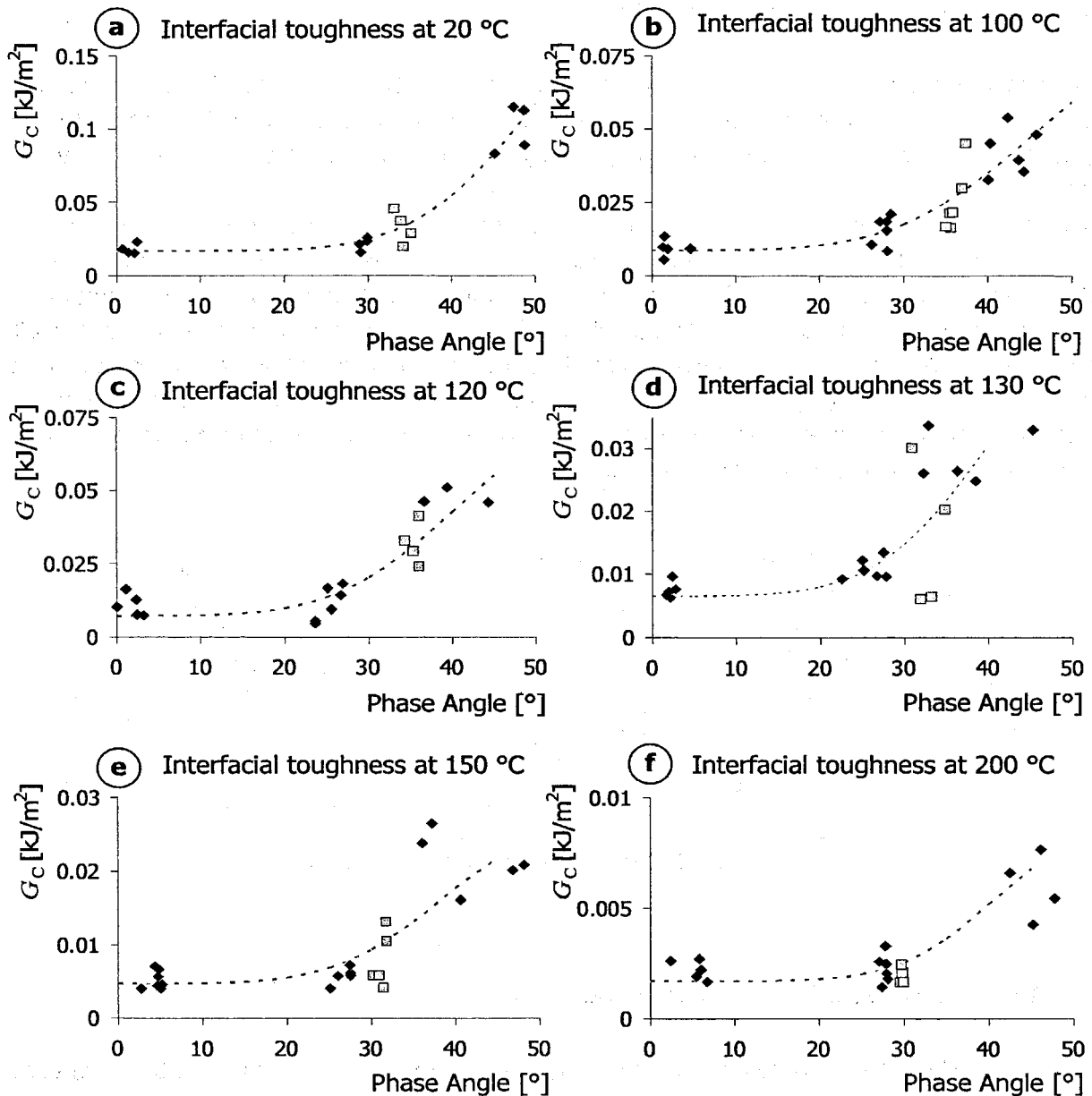


Figure 91: Individual Interfacial Toughness Curves

The obtained results exhibit a large dispersion. This is explained by the large experimental dispersion already exhibited by the critical shear forces as discussed in the section IV.9.4. Consequently there is a large degree of uncertainty by performing the BK fit and by determining the reference length.

As observed for individual toughness curves in Figure 91, the higher the phase angle, the higher the interfacial toughness. The trend is the same for all temperatures, but in lower ranges of magnitude as the temperature increases. The interfacial toughness is nearly constant from 0 ° (pure mode I loading) to 30 °. A strong derivative increase appears by 30 °. Then, the interfacial toughness is approximately doubled every 10 ° of phase. This kind of two-segment toughness is identical as the toughness curve characterized at room temperature with the DAGE machine.

At that time, we are not aware of similar results published which can be used in comparison.

All BK fit are displayed together in Figure 92, where the individual points are removed to ameliorate the readability of the graphic.

With exception to the curve obtained at 120 °C (which is dashed), the higher the temperature; the lower the interfacial toughness. It remains true independently from the phase angle.

The characterized interfacial toughness at 120 °C does not follow this ranking. Figure 91.b (correlation at 100 °C) and Figure 91.c (correlation at 120 °C) are plotted using the same axis scale. The interfacial toughness is clearly higher at 120 °C than at 100 °C. It is for mode II even higher at 120 °C than at 20 °C.

However the ranking of the temperature is also seen when considering the variation of the critical shear forces with respect to the temperature (Figure 77), even if shear forces are rather in the same order of magnitude at 100 °C and 120 °C.

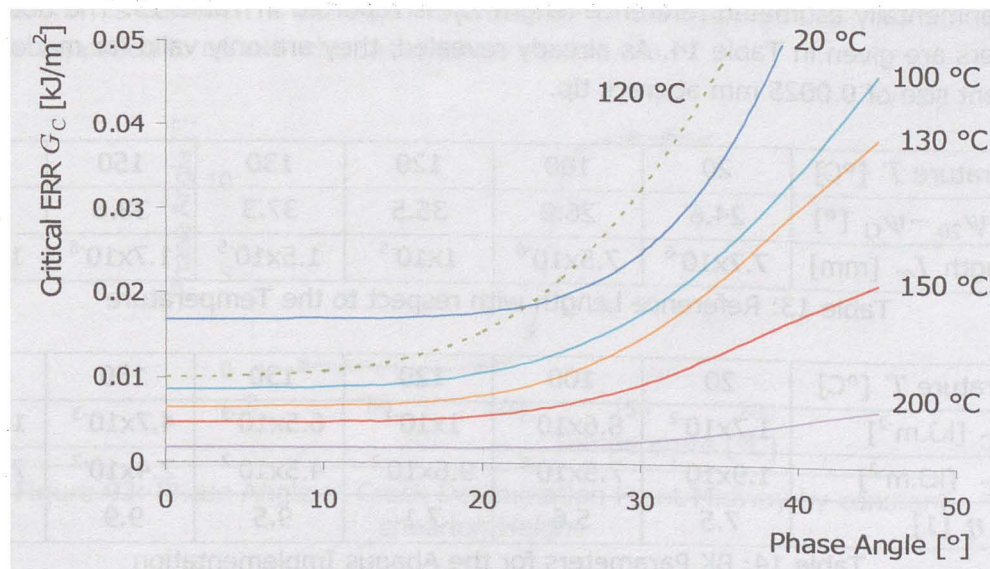


Figure 92: Equivalent Critical Energy Release Rate of Benzeggagh with respect to the Temperature

The difficulty to maintain the test temperature is an explanation to this inconsistency. If the test temperature is in the reality lower than 120 °C, the critical shear forces are obtained much higher than expected. 120 °C is also near the glass transition. The temperature variations have a significant influence on the material behavior at that temperature. Anyway,

numerical simulations are performed at 120 °C, where the molding compound exhibits a high deformability. In this case, the ERR estimation would involve the product of stresses with higher strain levels than what real state exhibits. The critical energy release rate is then found much higher than the expected one.

Furthermore, [Wunderle 2003] and [Wittler 2004] reported that the viscoelastic characterization of polymers may strongly depend on the test method. In particular, DMA and relaxation results exhibit large divergence around the glass transition. It means that the measured polymer properties around T_G may be imprecise and that the material behavior is not accurately well reproduced around T_G .

The characterized interfacial toughness at 120 °C must be unfortunately invalidated considering suspicions about the plausibility of such a result.

V.3.3 Result Implementation

Hence the BK fit is performed; the interfacial toughness data can be implemented in Abaqus. Since Abaqus does not estimate the mode mixity from the oscillatory SIF but from the ERR ratio, the parameters G_{1C} and G_{2C} (critical ERR for the apparent pure mode I and pure mode II loading) are defined in the numerical model instead of G_{IC} and G_{IIC} (critical ERR for real pure mode I and pure mode II loading). The method to determine these parameters is explained in sections V.2.2 and V.2.3.

The experimentally estimated reference length L_T is reported in Table 13. The obtained BK parameters are given in Table 14. As already revealed, they are only valid for models having an element size of 0.0025 mm at crack tip.

Temperature T [°C]	20	100	120	130	150	200
$\omega_{20} = \psi_{20} - \psi_G$ [°]	24.6	26.9	35.5	37.3	38.6	38.4
Ref. length L_T [mm]	7.7×10^{-6}	7.5×10^{-6}	1×10^{-5}	1.5×10^{-5}	1.7×10^{-5}	1.8×10^{-5}

Table 13: Reference Length with respect to the Temperature

Temperature T [°C]	20	100	120	130	150	200
G_{1C} [kJ.m ⁻²]	1.7×10^{-2}	8.6×10^{-3}	1×10^{-2}	6.5×10^{-3}	4.7×10^{-3}	1.7×10^{-3}
G_{2C} [kJ.m ⁻²]	1.9×10^{-1}	7.5×10^{-2}	9.6×10^{-2}	4.5×10^{-2}	2.4×10^{-2}	7.8×10^{-3}
η [1]	7.5	5.6	7.1	9.5	9.9	13.5

Table 14: BK Parameters for the Abaqus Implementation

The implementation in an Abaqus input file can then be performed with the following keywords placed after the step definition ([Abaqus 4]). With this data, the simulation of the delamination propagation can be simulated in any part involving this interface.

V.4 Strain Rate Effect

V.4.1 Experimental/Numerical Correlation

As suggested by the experimental results in section IV.10, the interfacial toughness of molding compounds exhibits strain rate and temperature dependencies. As discussed in the theoretical parts (sections IV.5 and II.6), elastic constants of viscoelastic polymers vary with temperature, load frequency, strain rate and time.

In order to highlight the time/temperature superposition principle for the interfacial toughness, it would be more judicious to work with a fracture criterion varying linearly with the stress and strain components. For this reason, the modulus of the complex stress intensity factor is used instead of the energy release rate in this section. It is determined in FEA using nodal displacements at delamination front (eq. II-22).

All tests are performed at a shearing height of 5 mm. The numerical investigation shows that the phase angle varies with the temperature even if h is constant.

The phase angle at delamination front midway estimated with a reference length of 0.004 mm is displayed in Figure 93. The phase angle found at the crack propagation is effectively not constant with the temperature. It shows a jump of about 12 ° at the EMC glass transition temperature. This variation is admitted low enough to be neglected. In the next part, all results are supposed to be with the same mixed mode ratio.

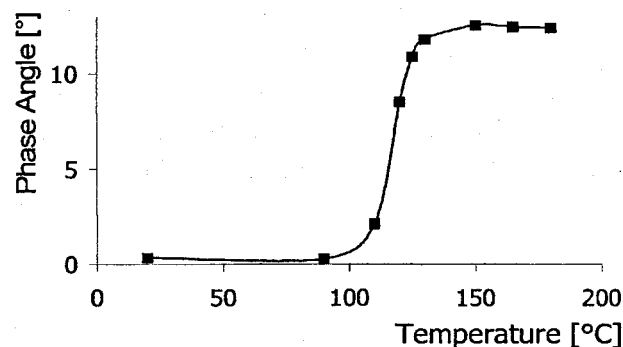


Figure 93: Phase Angle at Crack Delamination Front Midway by constant shearing Height

The critical shear forces obtained by shearing the buttons (Figure 81) are correlated with the numerical results. The results furnish the corresponding SIF at crack propagation (Figure 94), i.e. the critical stress intensity factor for the copper/EMC interface with respect to the tensile machine displacement-rate and temperature (correlation performed identically with the SIF as with the ERR).

The estimated average critical SIF with respect to the applied load-rate and test temperature is displayed in Figure 94.

As expected, the interfacial toughness decreases as the temperature increases. It corresponds to the results of the paragraph V.3.2.

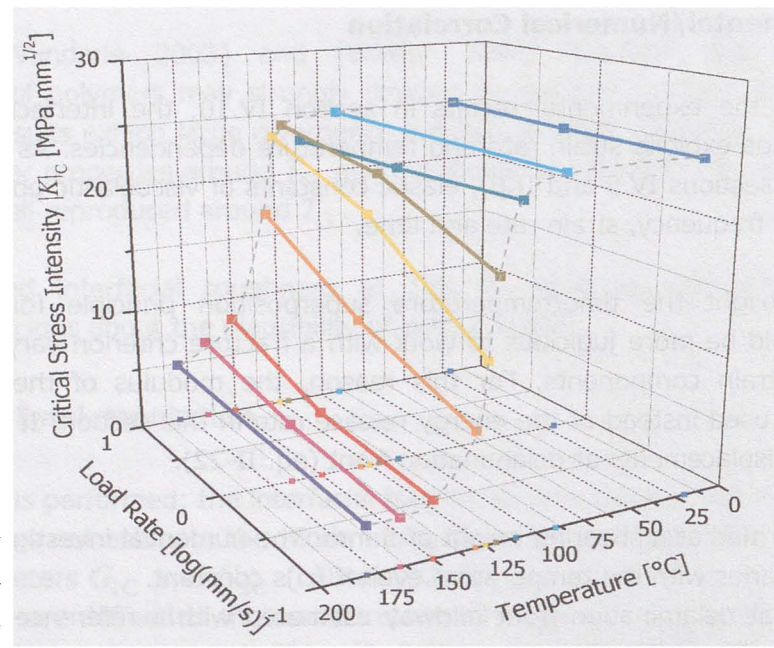


Figure 94: Critical Stress Intensity Factor as function of the Temperature and Load Rate

As for the polymer's elastic constants, the critical SIF exhibits a strong drop at the glass transition temperature. Depending on the temperature, the fracture toughness is also sensitive to the applied load rate. The latter has a significant influence near the glass transition temperature. This influence declines as the temperature is becoming far from T_G . At room temperature and 180 °C, the interfacial toughness is not influenced by the load rate. The interfacial toughness seems to be more governed by the EMC material properties than by the copper ones. As all elastic constants of the EMC, the interfacial toughness shows a transition at T_G .

V.4.2 Strain Rate/Temperature Superposition

Using the simulation results, the critical SIF are expressed as function of the average strain rate at crack tip instead of the applied shearing tool displacement rate. The individual curves are then shifted and fitted to obtain a unique curve (Figure 95). 125 °C is taken as the reference temperature. The dispersion bars are displayed in black. A large dispersion of the determination of the critical SIF can be seen for temperatures below T_G . Moreover, the values obtained at 110 °C are slightly out of the overall trend. The mastering is relative subjective for segments corresponding to test temperatures 20 °C, 90 °C and 110 °C since

these individual segments do not cross each other. In any case, this condition is met for other curves and the mastering can be performed with a good confidence level.

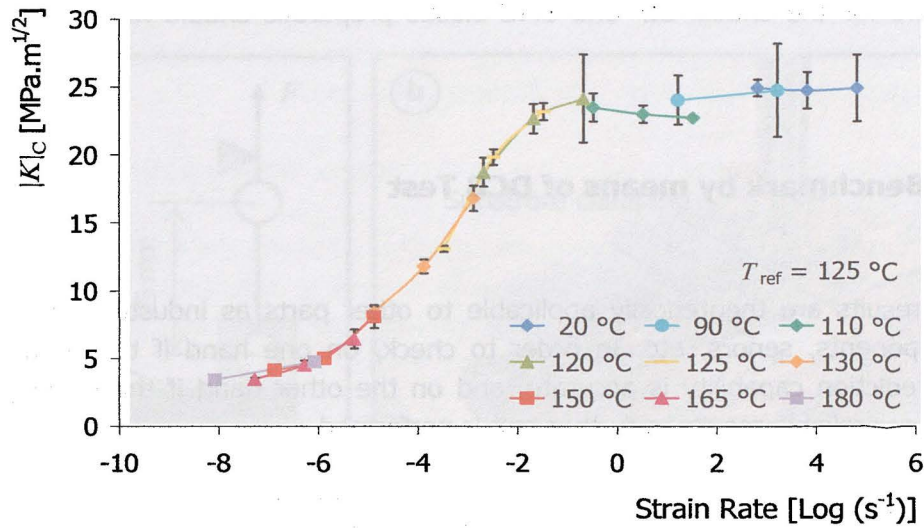


Figure 95: Interfacial Fracture Toughness Master Curve

Temperature [°C]	20	90	110	120	125	130	150	165	180
Log a_T^{SIF}	6.3	4.7	3.0	0.8	0	-1.4	-3.4	-3.8	-4.6

Table 15: Shift Factors for the Critical Interfacial SIF

The obtained shift factors (Table 15) are superposed to those from EMC material properties in Figure 96. The points represent the shift factors relative to the delamination toughness and the dashed line represents the EMC material ones. Both series of shift factors follow the same trend. Ones are obtained using data expressed in the frequency domain, whereas others are obtained using data in the strain rate domain.

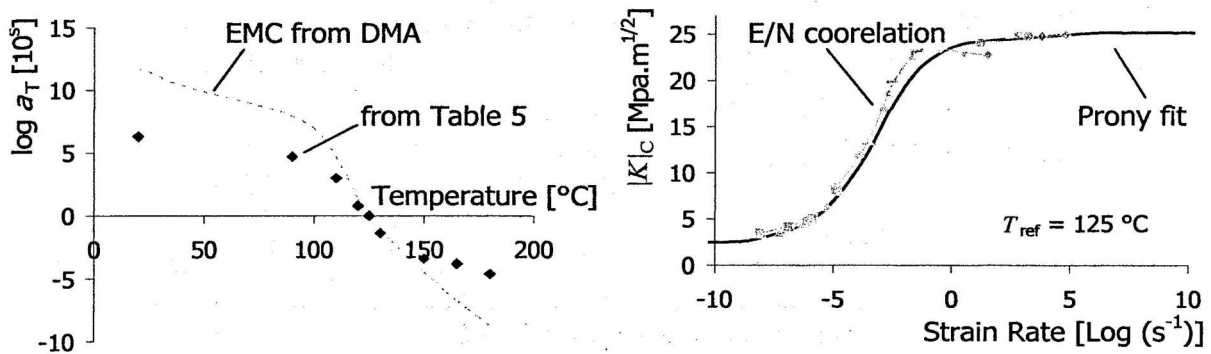


Figure 96: a. Critical SIF Shift Factors – EMC own Shift Factors
 b. Prony Fit with the Critical SIF

The fact that the interfacial toughness and the EMC elastic do not exhibit the same temperature shifting is not surprising. The interfacial toughness is expected to be governed by both material partners, i.e. by thermosetting molding compound and copper properties. The shift factors for the critical SIF and EMC elastic properties should not be exactly the same.

V.5 Final Benchmark by means of DCB Test

The obtained results are theoretically applicable to other parts as industrial products like electronic components, sensors, etc. In order to check, on one hand if the Abaqus crack propagation prediction capability is accurate, and on the other hand if the developed test procedure delivers reliable results, a further test is performed.

V.5.1 Experimental Procedure

Modified double cantilever beams (MDCB) are fabricated using the same copper substrate as for the triangle button shear specimen, i.e. copper plates of 50x10 mm, with a thickness of 1.5 mm. The test set-up is called modified DCB because on the contrary to normal DCB tests, the boundary and load conditions are not symmetric with respect to the crack plane. The substrates are cleaned with an Aceton agent before molding. A thin PTFE film of 100 μm is disposed on the front end of the copper substrate to ease the crack initiation.

A layer of 2 mm of the already used polymeric molding compound is then molded on the copper layer (Figure 97).

In order to apply a tensile load on the EMC layer, a drilled steel cube of dimensions 10x10x10 mm³ is glued on the EMC layer using an epoxy glue.

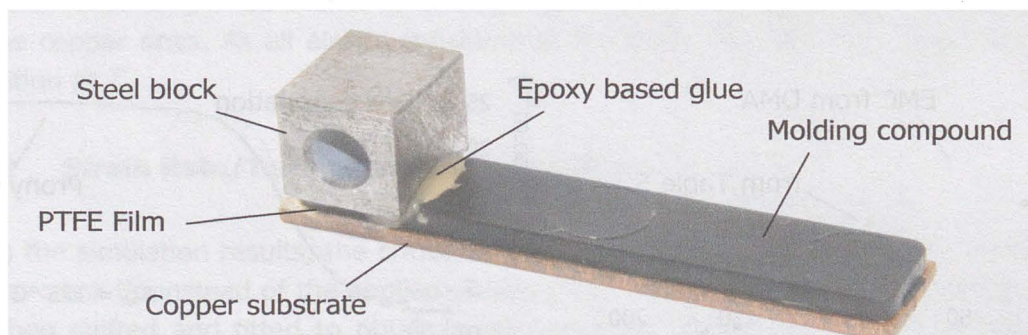


Figure 97: Modified DCB Test Sample

The tests are performed using a tensile machine equipped with 25 kN load cell. A vertical load is applied on the EMC layer through the attached steel block. The loaded point on the

specimen is free of horizontal displacement since a system of rods is used to load the specimen (Figure 98.a).

The copper substrate is clamped between flanks over its overall length (Figure 98.b).

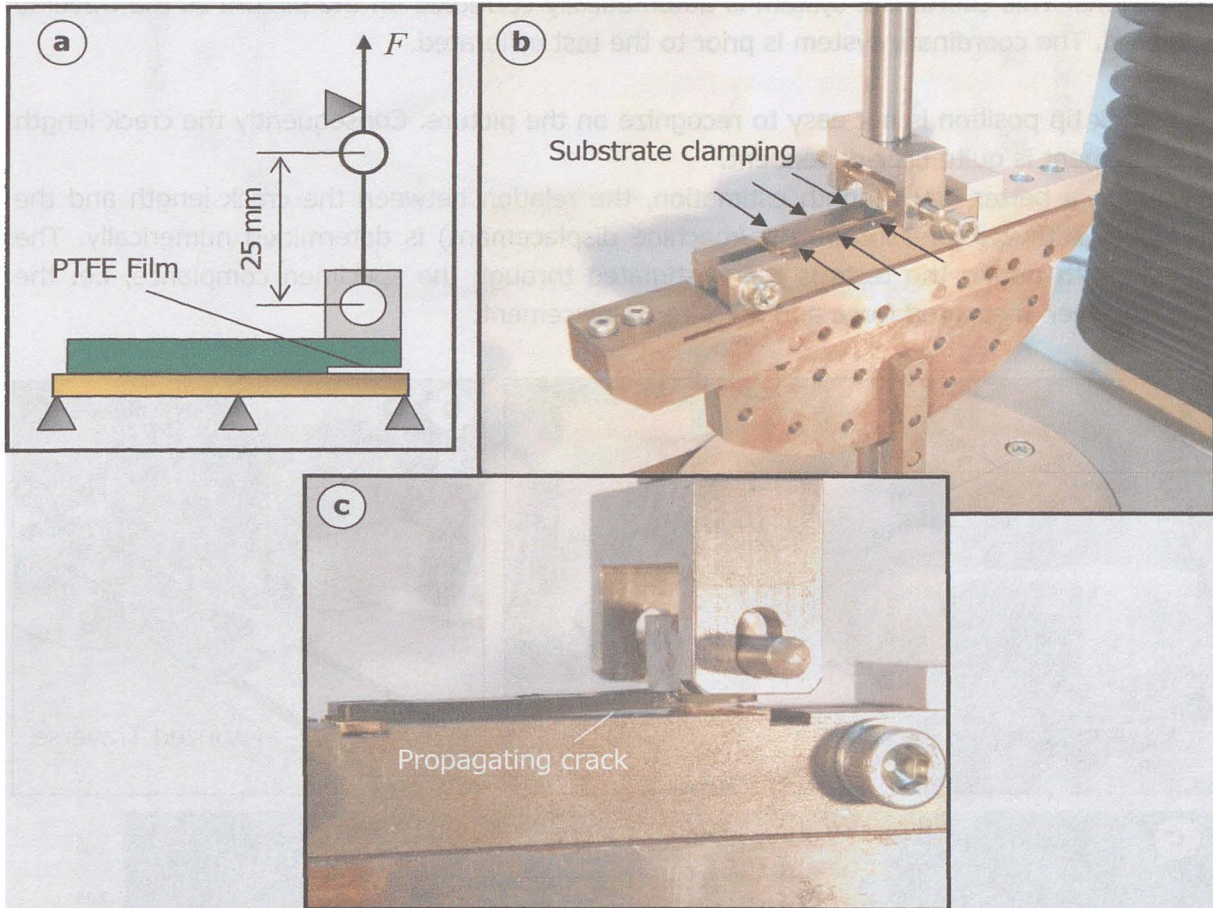


Figure 98: Modified DCB Test Set-up

The machine is given a constant displacement rate of 0.1 mm/min. The resulting force is recorded. The force linearly increases as the machine displacement increases, until a critical loading is met. Thus the crack starts to propagate. The crack progressively propagates and in a stable manner as the machine displacement increases. It means that the crack tip loading diminishes as the crack propagates. The specimen compliance also diminishes, so that the measured force decreases along the test.

As the crack length approximately reaches the half of the specimen, the crack starts to propagate stepwise. Finally, as about 5 mm of the specimen length remains, the delamination propagates in the rest of the interface, so that the two layers are completely separated after the test.

The crack length is measured during the test using an imaging system, involving a CCD camera and an optical objective mounted on a motorized carriage (Figure 99.a and b). The optical system focuses on an area of $5 \times 5 \text{ mm}^2$ on the specimen flank. The camera is initially

positioned on the notch end. The optical system is then translated as the crack propagates in order to maintain the crack tip in the focus of the camera. This system provides pictures of the specimen flank, where the crack tip can be observed (Figure 99.c). After calibration, the software integrates a coordinates system in the pictures, reporting the real spatial dimensions. This coordinate system is automatically corrected on the picture as the traverse is shifted. The coordinate system is prior to the test calibrated.

The crack tip position is not easy to recognize on the picture. Consequently the crack length measurement is quite user-dependent.

To obtain a better crack length estimation, the relation between the crack length and the specimen stiffness (measured force/machine displacement) is determined numerically. The crack length during the tests is then estimated through the specimen compliance, i.e. the ratio between measured force and machine displacement.

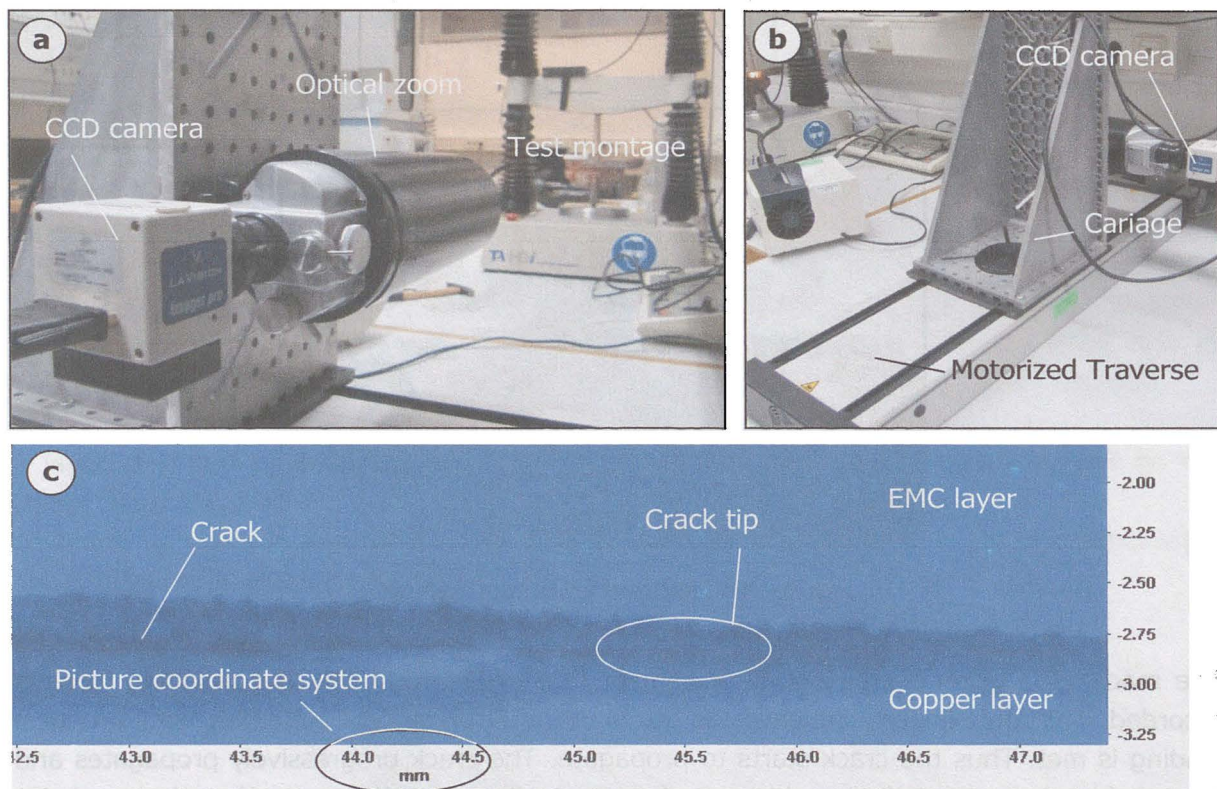


Figure 99: Optical System for the Crack Length Measurement (above)
Typical obtained Picture from Crack Length Measurement Procedure (below)

The delamination length is then estimated numerically through the specimen compliance during the test. Obtained delamination length corresponds to the measured length.

This DCB test is performed three times with a sufficient reproducibility. Obtained results for three specimens are plotted in Figure 100.

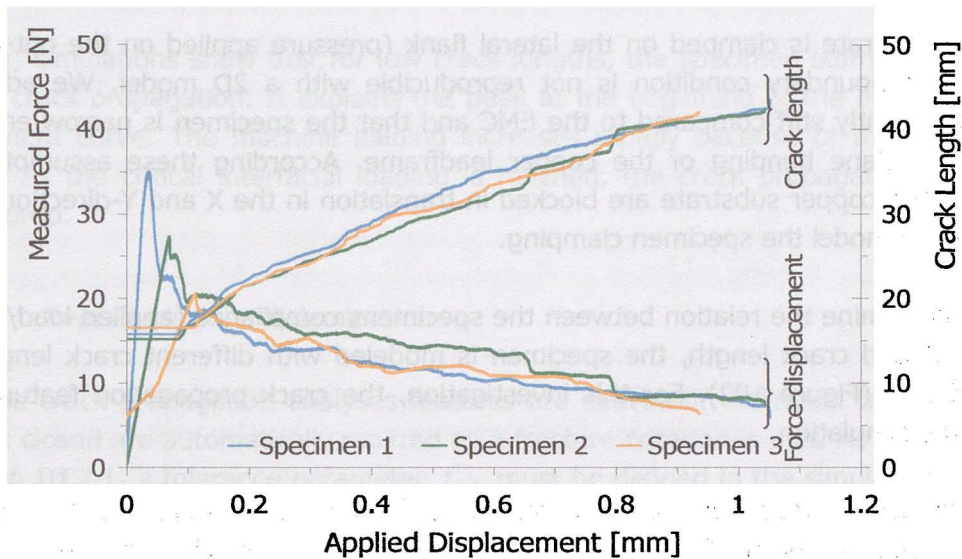


Figure 100: DCB Test Results

V.5.2 Numerical Model

The DCB specimen is modeled in 2D with Abaqus 6.8. As in section IV.6, EMC the layer and copper substrate are modeled in two Abaqus parts, and bounded using a VCCT interaction. Copper is defined linear elastic and the molding compound linear viscoelastic.

The layer of epoxy glue and the iron bloc are also modeled. The glue layer is assumed to be 0.2 mm thick. This material is also linear viscoelastic. A DMA (Dynamical Mechanical Analyze) is performed. The glue has its glass transition at 150 °C. Since the DCB test is performed at room temperature, viscoelastic effects are negligible. This material is assumed linear elastic, with a tensile modulus of 6 MPa and Poisson's ratio of 0.35.

The iron block is much stiffer as the other material. Considering the load level during the tests (< 50 N), the material properties of the block glued on the EMC layer have little influences. It is assumed linear elastic, with a tensile modulus of 200 GPa and a Poisson's ratio of 0.3. The hole in the middle of the block is not modeled (Figure 101). The node on the middle of the block (crossing of both diagonals) is used to apply a vertical force.

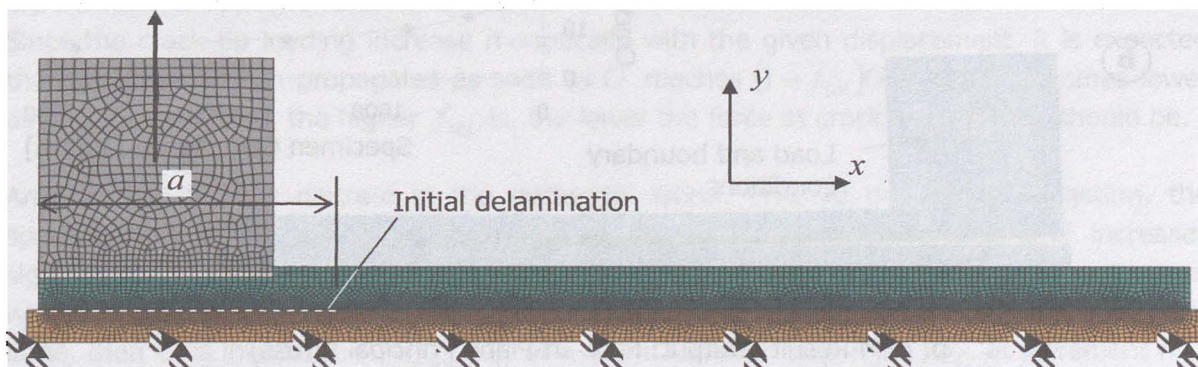


Figure 101: Finite Element Model of the DCB Specimen

The copper substrate is clamped on the lateral flank (pressure applied on the out-of-plane direction). This boundary condition is not reproducible with a 2D model. We admit that copper is sufficiently stiff compared to the EMC and that the specimen is narrow enough to prevent out-of-plane bending of the copper leadframe. According these assumptions, all nodes under the copper substrate are blocked in translation in the X and Y-direction (Figure 101) in order to model the specimen clamping.

In order to determine the relation between the specimens compliance (applied load/machine displacement) and crack length, the specimen is modeled with different crack length from 6 mm to 40 mm (Figure 102). For this investigation, the crack propagation feature is not enabled in the simulation.

To benchmark the Abaqus crack propagation analyze feature, the specimen is then modeled with an initial crack length of 13 mm. The interfacial parameters characterized in Section V.3.3 are defined in the Abaqus model input file as reported in **Appendix C**. The crack propagation capability is activated. The specimen is monotonically loaded with a displacement rate of 0.1 mm/min.

V.5.3 Numerical Results

V.5.3.1 Specimen Compliance-Crack Length Relation

The determined crack length-specimen compliance relationship is plotted in Figure 102.a. The stress field after a crack propagation of 19 mm, i.e. for a crack length of 30 mm is displayed in Figure 102.b. It can be observed that the specimen compliance is proportionally inverse to the crack length, i.e. the higher the crack length, the lower the specimen stiffness. It corresponds to the experimental results, which show that the applied load on the specimen decreases as the crack propagates at the copper-EMC interface.

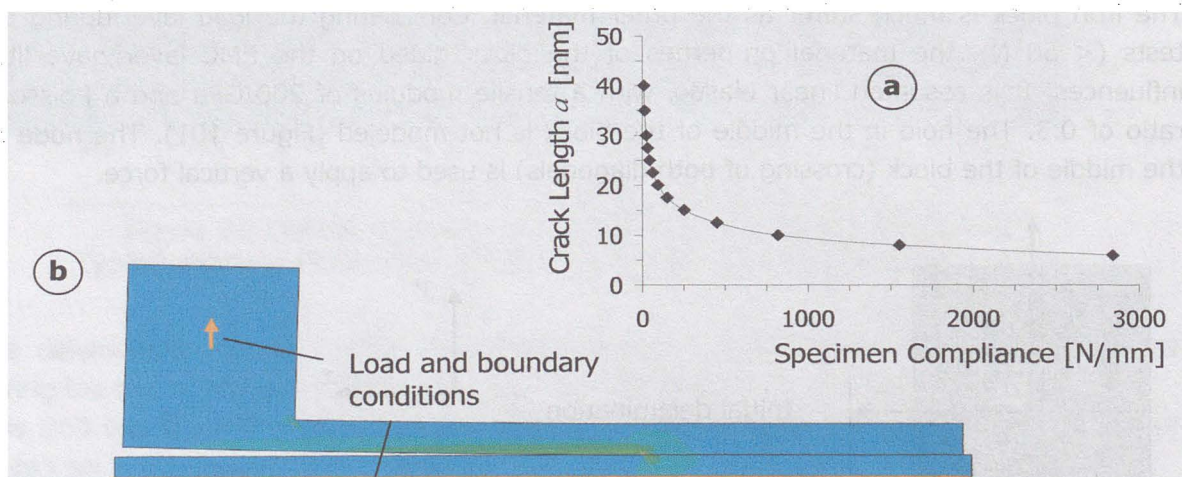


Figure 102.a: Relation Crack Length – Compliance for the testes DCB
b. FEM Result (Output: Max. In-Plane Principal Stress)

Moreover, simulations show that for low crack lengths, the specimen stiffness rapidly drops with the crack propagation. It explains the peak at the beginning of the experimental load-displacement curve. The machine loading increases rapidly because of the high specimen stiffness. As the critical interfacial loading is reached, the crack propagates and the force rapidly drop.

V.5.3.2 Reproducing the Delamination

Hence the crack propagation analyses features are activated, the nodal forces maintaining the crack closed are automatically realized as a fracture criterion is met. As mentioned in the paragraph III.2.1, a tolerance parameter f_{tol} must be defined in the simulation, so that the fracture criterion f_{BK} is met if $f_{BK} \in [1 - f_{tol}, 1 + f_{tol}]$, where f_{BK} is equal to G/G_C . In other words, the numerical fracture criterion is met if $G \in [(1 - f_{tol})G_C, (1 + f_{tol})G_C]$. The choice of f_{tol} has consequently a substantial influence on the numerical results.

Simulating the delamination with the DCB specimen is performed with several values for the parameter f_{tol} (Figure 103).

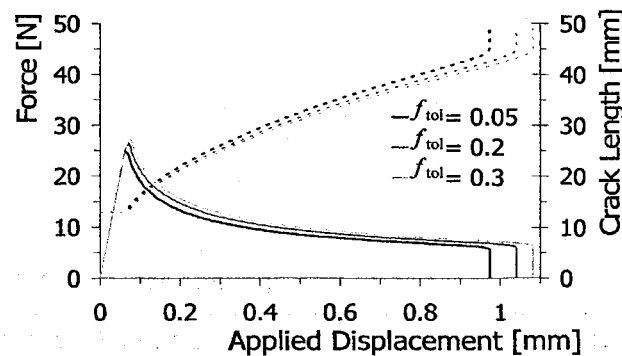


Figure 103: Propagating the Delamination in FEA, Influence of the f_{tol} Parameter

The force required to propagate the delamination increases as the f_{tol} parameter is increased. The opposite result is expected.

Since the crack tip loading increase monotonically with the given displacement, it is expected that the delamination propagates as soon as G reaches $(1 - f_{tol})G_C$. Latter becomes lower as f_{tol} increases, so, the higher f_{tol} is, the lower the force at crack propagation should be.

Anyway, the time is discrete in the numerical world. Prior to the first propagation, the specimen is maximal stiff. Between each time increment, the crack tip loading G increases significantly, in a quadratic manner with the displacement. The simulation time increment, at which the delamination propagates, is denoted as n . If the increment of time is sufficiently large, then G is inferior to $(1 - f_{tol})G_C$ at $n-1$ and superior to $(1 + f_{tol})G_C$ at increment n .

Increment n is then re-iterated and reduced until G finally meet a value below $(1 + f_{tol})G_C$. To conclude, if the increments of time are large, the fracture criterion in Abaqus is often met by $G = (1 + f_{tol})G_C$. Consequently, the higher f_{tol} , the higher the force at crack propagation. This behavior is nevertheless influenced from the numerical time incrementation.

Obtained numerical results are similar to the experimental ones: the load-displacement curve firstly exhibits a peak before the first crack propagation occurs. Then, applied load rapidly drop as the crack propagates. The crack propagation is in the simulation a continuous phenomenon, whereas experimentation shows that the delamination propagates step by step in the reality. The numerical results obtained with the Abaqus default value of f_{tol} (0.2) is plotted in Figure 104 together with the experimental results obtained with the first DCB specimen.

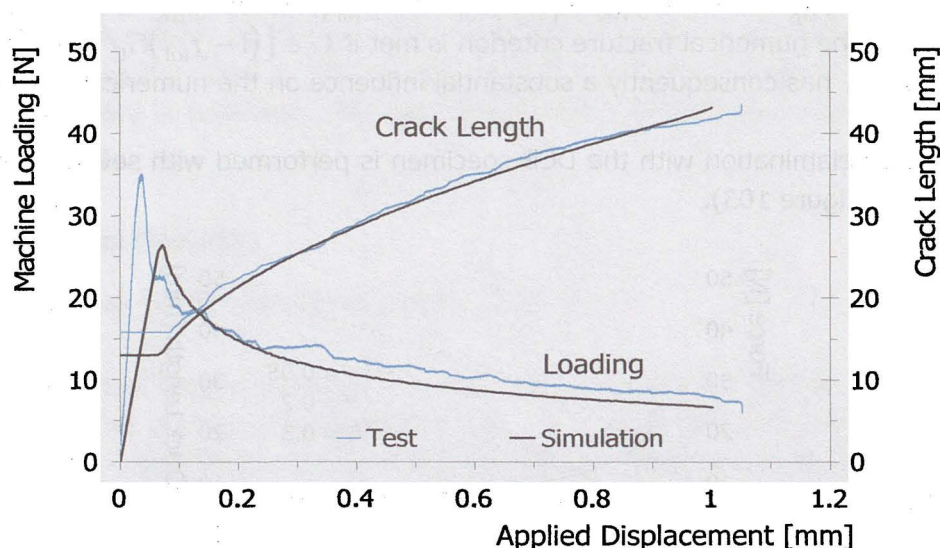


Figure 104: Comparison Numerical Prediction/Test Result

As shown in Figure 100, the value of the peak reached by the measured force and the slope before to the first propagation strongly depends on the original delamination length. This delamination length is not exactly reproduced in the simulation, but the range of magnitude exhibited from the simulation is in agreement with the experimental results. As the delamination propagates, experimentation and simulation let appear small differences.

V.6 Conclusion

The thermosetting polymeric molding compound/copper interface has shown complex behavior with respect to temperature and strain rate conditions. It would be interesting to investigate the bounding nature of this interface to understand how the temperature and strain rate affect the chemical liaison between molding compound and copper.

This test setup successfully permits to characterize the interfacial toughness with respect to different influences as the mode mixity, the temperature and strain rate. It is also appropriate to investigate further influences, as the moisture concentration, fuel or petrol derivative agent influence, or also aging.

This test and its associated results evaluation process have the advantage to furnish implementable values in the FEM. It allows the numerical simulation of electronic parts to verify their operational integrity. Some enhancements would be welcomed in Abaqus in order to define the interfacial toughness with a Prony series and shift factors, as it describes its own viscoelastic behavior. The actual state used with some tricks however allows simulating most interfacial load cases.

VI. Fatigue and Life Time Assessment

VI.1 Thermal loaded two-layer Quad Specimen

VI.1.1 Test Concept

To assess the life time of electronic packaging, i.e. to estimate the delamination growth rate at the molding compound-copper interface, another test setup has to be used. To approach the test conditions from real electronic package life conditions, the tests are carried out using a thermal shock chamber.

Specimens are made of two different material layers, the first one is a copper substrate of dimensions $46 \times 46 \text{ mm}^2$ with a thickness of 0.4 mm, the other one is a molding compound layer of $43 \times 43 \text{ mm}^2$ with thickness 1 mm molded on the copper substrate (figure 105). Both materials are identical to the ones used in section IV.

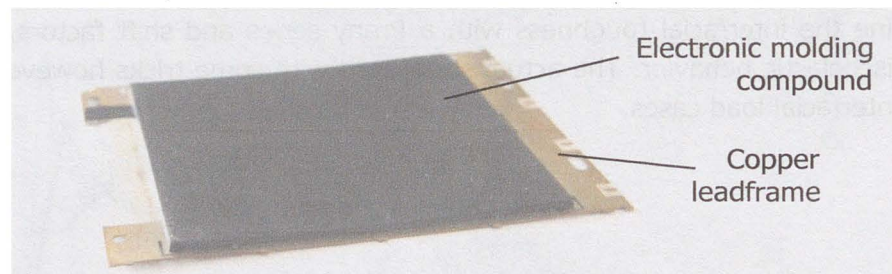


figure 105: Two-layer Specimen

The test principle consists in fatiguing the interface using cyclic stress induced through the incompatible interface strains (CTE-mismatch) and thermal shocks.

VI.1.2 Specimen Preparation and Test Method

Before molding, the copper substrates are cleaned using an acetone agent. The specimens are molded as described in section IV.3.2, and then stored four hours at 180 °C to finish the chemical hardening.

The specimens are submitted to thermal shocks varying alternatively from 150 °C to -40 °C using an Espec TSA three-zone thermal shock chamber. The shock chamber is composed of three levels (Figure 106). The specimens are disposed in a cage in the middle of the second level. The first level contains a cooling system able to reach temperatures down to -70 °C (cold chamber). The third floor contains a heating equipment able to reach temperatures up to 180 °C (hot chamber). A system of multiple fans and gates let air circulates between the test chamber and either the cold or hot chamber. The cold chamber doors are closed when the hot chamber doors are opened and inversely. To generate thermal shocks, the

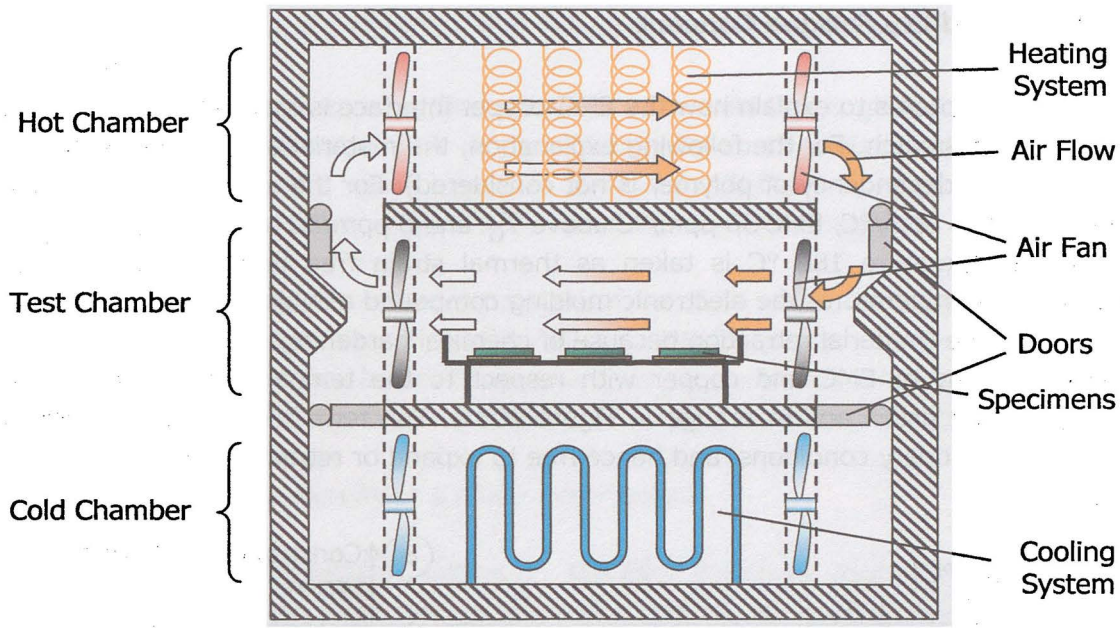


Figure 106: Structure of the thermal Shock Chamber

The heating-cooling periods are set to 20 minutes, so that one heating-cooling cycle takes 40 minutes. This time is sufficient, so that all specimens reach the targeted temperatures, to go either from $-40\text{ }^{\circ}\text{C}$ to $150\text{ }^{\circ}\text{C}$ or from $150\text{ }^{\circ}\text{C}$ to $-40\text{ }^{\circ}\text{C}$. A series of temperature measurements are performed in the chamber to obtain the air temperature profile with respect to time (figure 107). The temperature field is admitted homogeneous in the space directly around the tested specimens.

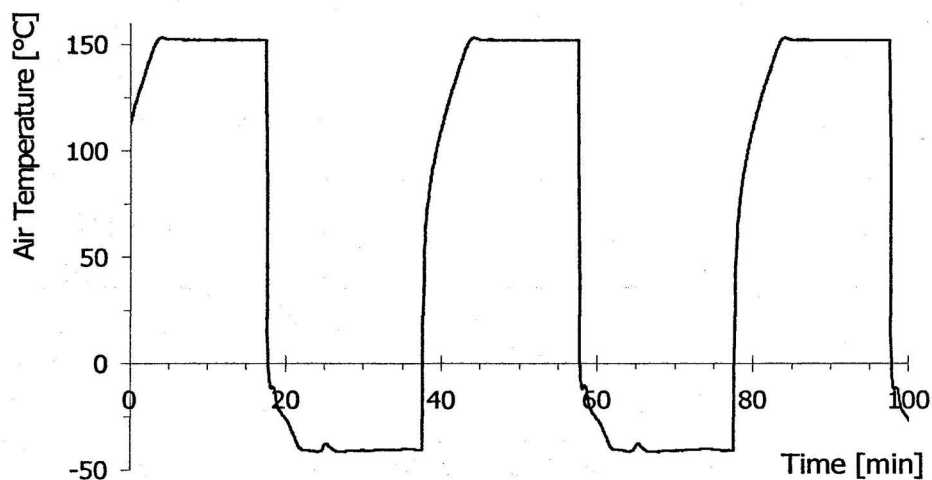


figure 107: Temperature Profile in the thermal Shock Chamber

For simulation purposes, the forced convection coefficient in the chamber is estimated (**Appendix B**). An average value of $30\text{ W}\cdot\text{m}^{-2}\cdot\text{K}^{-1}$ is found.

VI.1.3 Smile and Cry Fatigue Concept

The aim of this chapter is to explain how the EMC-copper interface is fatigued under thermal shocks and CTE-mismatch. For the following explanation, the material are considered purely linear elastic (time dependency of polymer is not considered). For the copper, it is assumed to have a CTE of 16 ppm/°C, EMC 30 ppm/°C above T_G and 8 ppm/°C below T_G (Table 3). The molding temperature 180 °C is taken as thermal strain free temperature for both materials. At this temperature, the electronic molding compound exhibits only strains due to mold cure shrinkage (material retraction because of chemical hardening). Free thermal strains of EMC and copper with respect to the temperature are displayed respectively in dark green and in orange in Figure 108.a. The term "Free" means material element free of boundary conditions, and hence free to expand or retract as the temperature varies.

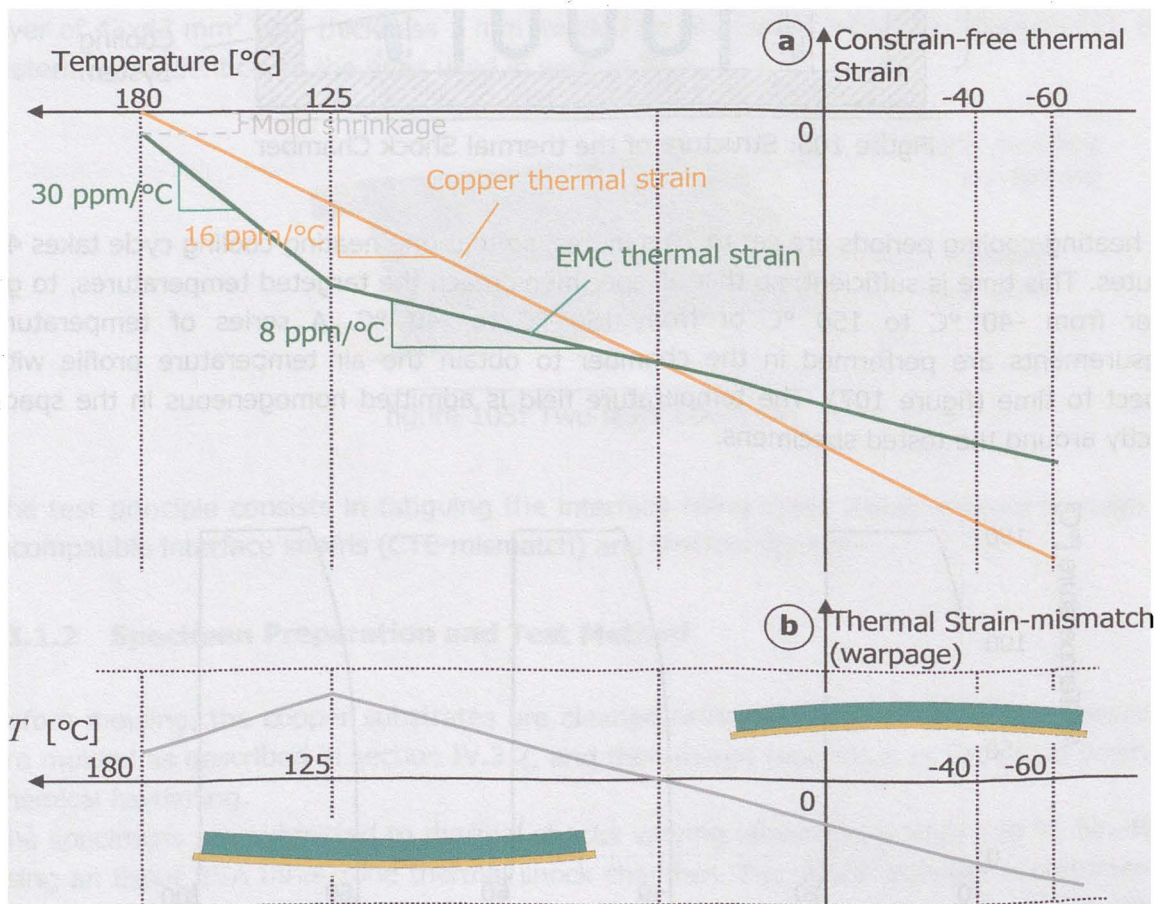


Figure 108: Smile and Cry Fatigue
 a. Copper and EMC constrain-free thermal Strains
 b. Resulting thermal Strain Mismatch

The derivative of the thermal strain curves is given by the respective material CTE. For the EMC, the CTE drops at T_G (125 °C), that is why EMC's thermal stress curve exhibits a kink at this temperature.

The thermal strain-mismatch or thermal strain incompatibility is given by the difference of the constrain-free thermal strains (Figure 108.b). By cooling down a 2-layer EMC/copper specimen (EMC as upper layer) from 180 °C to 125 °C, the EMC retracts itself more than copper. In this temperature range, the 2-layer specimen reproduces a smile, more and more pronounced until T_G is reached.

At T_G , the coefficient of thermal expansion of the EMC drops to 8 ppm/°C. The thermal strain-incompatibility reaches a maximum at 125 °C and decreases until a thermal strain-free temperature T_S is reached. In this temperature range, the smile becomes less pronounced to disappear completely at T_S , where the specimen is completely free of strain.

In this temperature range 180 °C - T_S , thermal strains lead to the delamination opening, hence load at delamination front is mode I dominated.

By decreasing the temperature below T_S , the EMC continues retracting less than copper. Below T_S , the specimen reproduces a cry-formed mouth, more and more pronounced as the temperature sinks. Below T_S , the delamination flanks remain in contact, the load at delamination front is mode II dominated.

Two-layer specimens undergoing the thermal cycles crossing the temperature T_S reproduce alternatively smiles and cries. This phenomenon appears because T_G is situated in the tested temperature range. For other molding compounds, which have a glass transition situated above 180 °C (or hypothetically below -40 °C), the thermal strain-mismatch increases linearly with the temperature variation.

VI.1.4 Delamination Area Measurement

As for the triangle button shear specimen, the delamination state is measured using scanning acoustic microscopy (SAM). For scanning, the specimen is disposed in a silicone form to prevent water penetration in the molding compound or along the interface (Figure 109.a).

The SAM measurements furnish grey-scaled pictures (Figure 110.a). The black areas correspond to scanned surfaces where no echo is returned. This corresponds to the area out of the specimen, where waves meet the silicone form and die because of the damping properties of silicone, or in the specimen, where the EMC-copper interface is not delaminated, where waves cross the interface and are dispersed in the EMC because of the high amount of silicate filler (filler particles disperse waves).

All grey areas correspond to surfaces where emitted ultrasonic waves are reflected. It corresponds to areas where the EMC-copper is delaminated. Waves do not cross the interface and are reflected by the copper behind surfaces. It also corresponds to the copper areas out of the EMC quad, i.e. the copper frame not covered with the EMC layer. On this original picture, the EMC-layer contour is not visible.

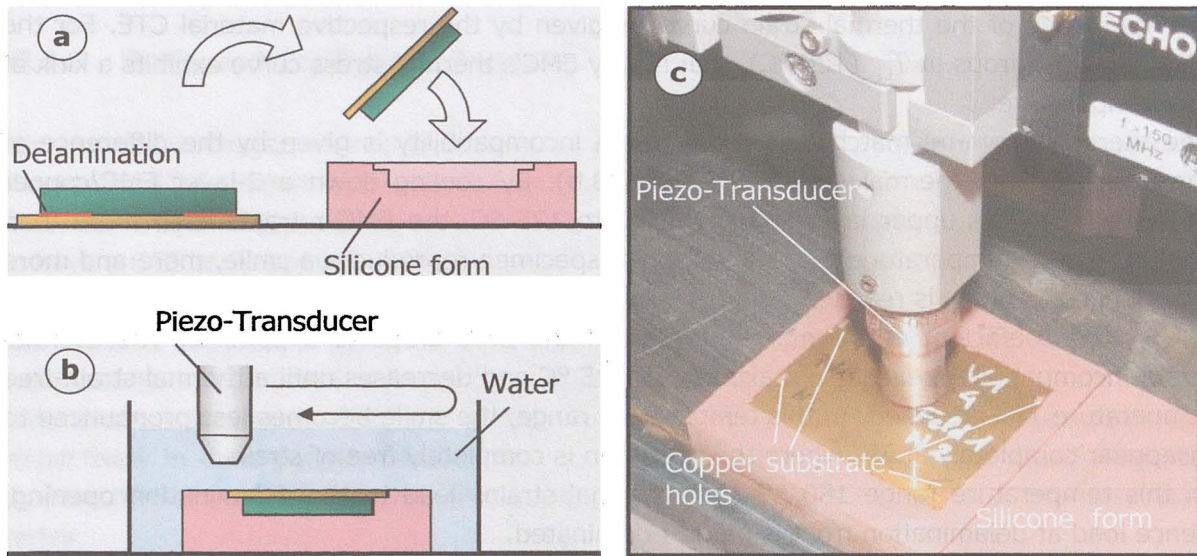


Figure 109: Scanning Acoustic Microscopy of Quad Specimens
 a. Positioning Specimen in the silicon Seat
 b. Scanning Specimen using SAM
 c. Picture of a scanned Specimen

Then the pictures are processed using a python routine (Figure 110.b). For the picture treatment, Python 2.5 with the Python Imaging Library PIL 1.1.3 is used.

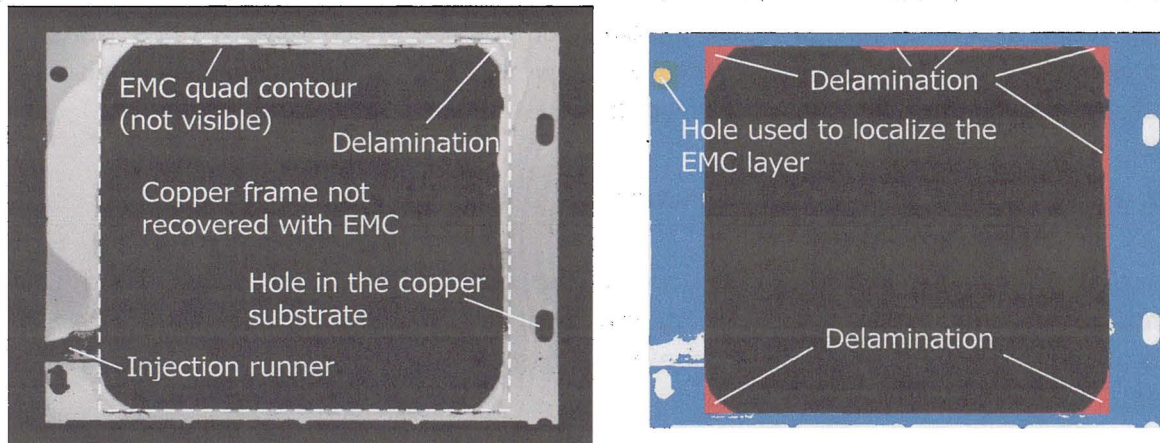


Figure 110.a: Interfacial Scanning from SAM
 b. Picture furnished by the Post-Processing Routine

During the picture processing, the pictures are firstly converted into binary pictures. The originally black areas are given the value zero; all other areas take the value one. Then the pictures are filtered to eliminate isolated single pixels.

The next step consists in localizing the EMC layer on the picture. The copper substrates are precisely positioned in the mold during transfer molding using four holes (Figure 110). Consequently these holes indicate the position to the EMC layer.

The hole on the left upper side in the copper frame is then used to localize the EMC layer and to define the working area. The position of the EMC layer with respect to this hole is measured and defined in the Python script.

Out of the working area, i.e. out from the EMC layer, the pixels with value 0 are rendered in white, the pixels with value 1 (copper leadframe) are rendered in blue (Figure 110.b).

In the working area, i.e. where the copper leadframe is covered by the EMC layer, non-delaminated areas (pixels of value 0) are rendered in black. The delaminated domains (pixels of value 1) are rendered in red.

In the working area, the non-delaminated and delaminated surfaces are separated. The non-delaminated areas are displayed in black and the delaminated one in red. The ratio of black pixels and violet pixels in the work area is used to determine the delamination ratio in the specimen.

VI.1.5 Experimental Results

Ten specimens are exposed to cyclic thermal shocks. An initial delamination is present in the specimen corners because of small air quantity trapped in the corner during molding.

All specimens are examined every 300 cycles using SAM to determine the delamination growth rate. The test session is stopped after 2150 cycles.

After 2150 cycles, the delamination ratio in the ten specimens exhibits a low increase (results of five specimens are displayed in Figure 111).

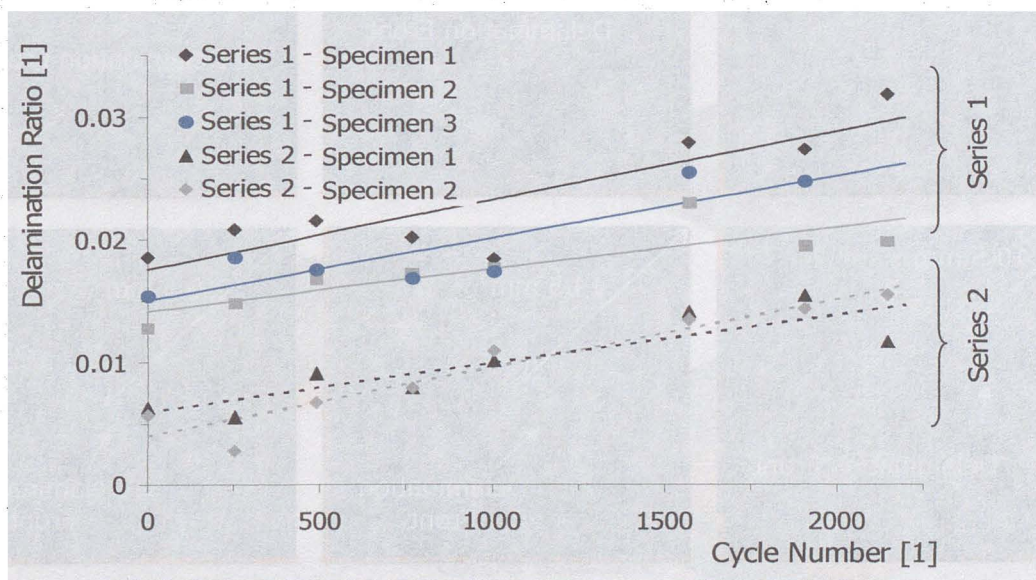


Figure 111: Delamination Ratio in the 2-layer Quad Specimens

A linear trend is estimated for each specimen using the least squares method. It furnishes the delamination ratio increase per cycle and then the delamination growth per cycle (Table 16).

Specimen	Series 1 (acetone clean.)			Series 2 (plasma clean.)	
	Spe. 1	Spe. 2	Spe. 3	Spe. 1	Spe. 2
Delam. ratio increase per cycle [1/cycle]	5.59×10^{-6}	3.39×10^{-6}	5.04×10^{-6}	3.92×10^{-6}	5.53×10^{-6}
Delamination Growth Rate [mm^2/cycle]	1.03×10^{-2}	6.26×10^{-3}	9.31×10^{-3}	7.26×10^{-3}	1.02×10^{-2}

Table 16: Delamination Growth Rate in 2-layer Quad Specimens

VI.1.6 Numerical Modeling

The specimens are modeled with FEM using Abaqus. A quarter of the specimen is modeled and symmetry-conditions are applied on the boundaries. Eight nodes brick elements without reduced integration are used to model the specimen in the regions near the delamination front, and also six nodes wedge elements in remote regions to simplify the mesh generation. As the form of the delamination front involve complex mesh schemes, it is not possible to reach mesh refinement in the same order of magnitude as the model used in parts IV and V. The element length at delamination front is in the order of 0.1 mm.

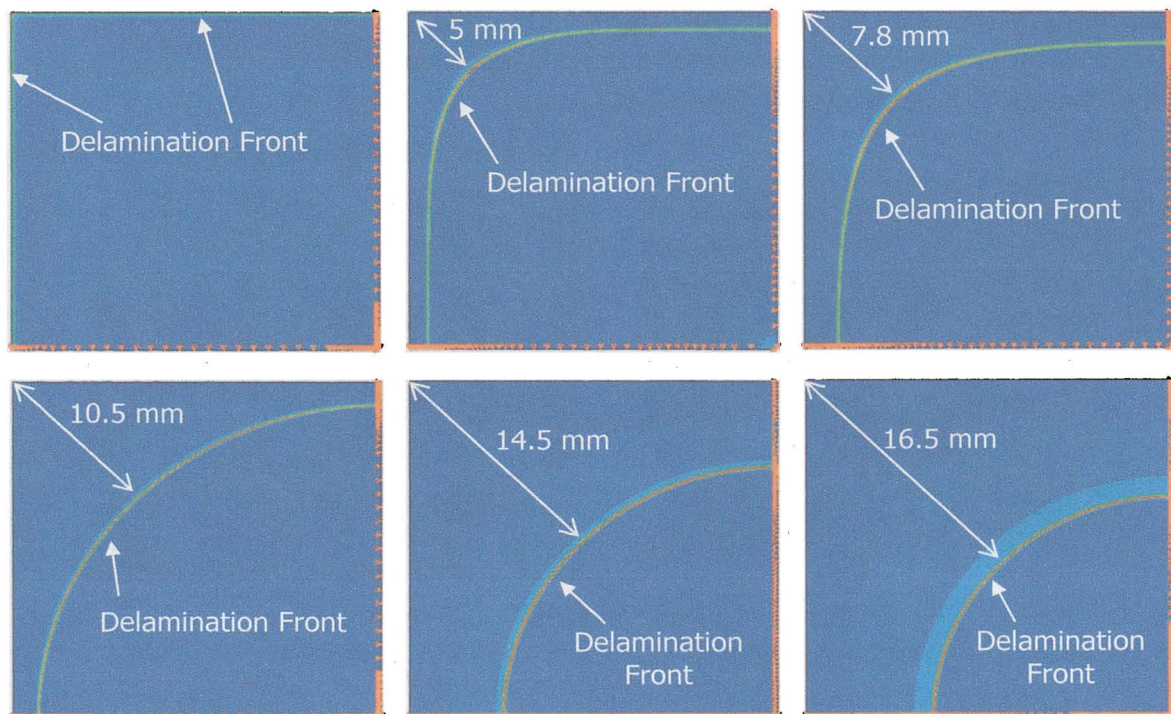


Figure 112: Simulated Configuration of Delamination

Six configurations are modeled with different amount of delamination (Figure 112). These models are distinguished by their respective delamination length measured on the diagonal (shorter distance from the angle to the delamination front). The six models have

delamination length 0.77, 5.0, 7.8, 10.5, 14.5 and 16.5 mm. It corresponds to delamination ratios of respectively 4.5 %, 15 %, 25 %, 32 %, 56 % and 66 %.

VI.1.7 Numerical Results

For each configuration, a thermal simulation is performed in order to estimate the temperature field in the specimen during a cooling phase. An Abaqus film condition interaction is defined on the above surface of the specimen, corresponding to the thermal shock chamber forced convection (**Appendix B**). The air temperature in the chamber is defined as a table corresponding to the measured temperature profile (figure 107). The elements chosen are Abaqus DC3D6 elements (6 nodes wedges) and DCC3D8 elements (8 nodes brick with convection control) are used.

For these simulations, the heat conductivity and the specific heat must be defined for both materials. The heat conductivity is obtained using Xenon-Flash measures performed with a Netzsch LFA 447 equipment. The specific heat is measured using differential scanning calorimetry (DSC).

Then an Abaqus “restart” simulation is performed using the computed temperature field to estimate the stress and strain fields induced by the CTE mismatch. The materials CTE are taken from the respective material datasheets. The previous thermal model is adapted: the mesh stays unchanged but the elements are replaced by normal 3D stress elements (Abaqus C3D6 and C3D8).

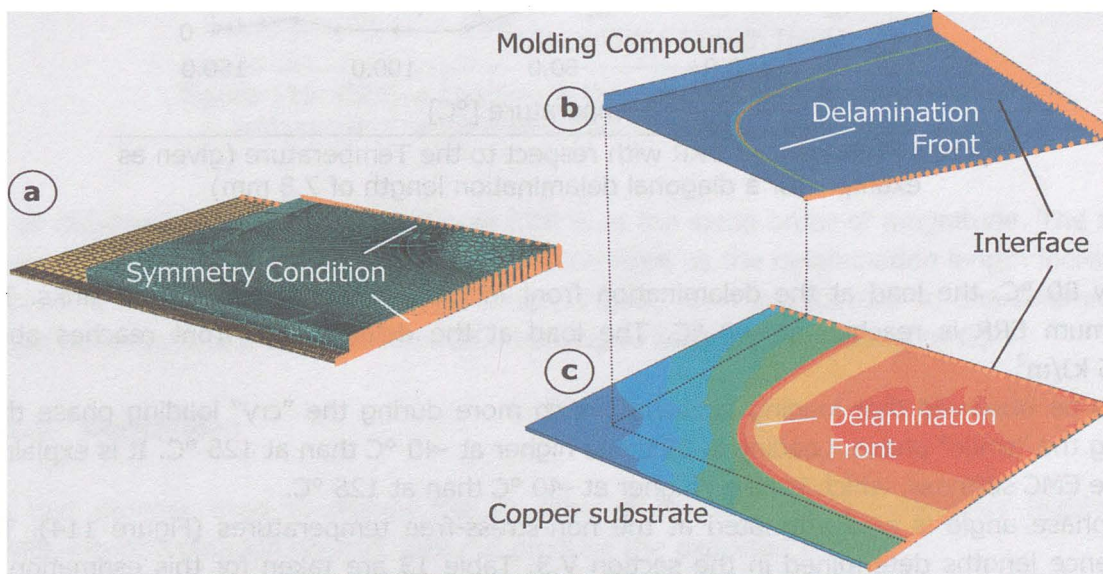


Figure 113.a: 2-layer Quad Specimen Modeling
 b: Interfacial EMC Stress Field (max. principal)
 c: Interfacial Substrate Stress Field (max. principal)

The energy release rate and the phase angle are estimated along the delamination front. The position of maximum energy release rate is considered on the delamination front. It corresponds to a diagonal position. At this point, a delamination length of reference is considered: the shortest distance from the corner to the delamination front (Figure 112).

The simulations show that the ERR reaches a maximum value at the lowest temperature (Figure 114), i.e. at $-40\text{ }^{\circ}\text{C}$. As expected, two phases of loading can be observed along the cooling (paragraph VI.1.3). The "smile" loading occurs between $150\text{ }^{\circ}\text{C}$ and $80\text{ }^{\circ}\text{C}$. The energy release rate at the delamination front reaches a maximum at the EMC glass transition temperature, i.e. $125\text{ }^{\circ}\text{C}$ and decreases then till a stress free temperature, i.e. $90\text{ }^{\circ}\text{C}$. The stress free temperature is approximated since few temperature increments are computed around $90\text{ }^{\circ}\text{C}$.

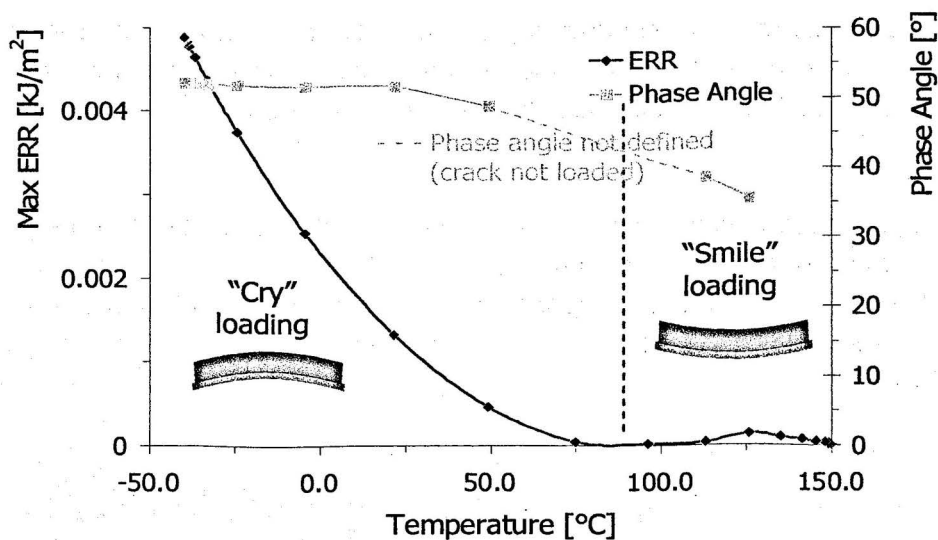


Figure 114: Maximum ERR with respect to the Temperature (given as example for a diagonal delamination length of 7.8 mm)

Below $80\text{ }^{\circ}\text{C}$, the load at the delamination front increases as the temperature sinks. The maximum ERR is reached at $-40\text{ }^{\circ}\text{C}$. The load at the delamination front reaches about 0.005 kJ/m^2 .

It can be observed that loading increases much more during the "cry" loading phase than during the "smile" phase. Loading is 35 times higher at $-40\text{ }^{\circ}\text{C}$ than at $125\text{ }^{\circ}\text{C}$. It is explained by the EMC stiffness, which is much higher at $-40\text{ }^{\circ}\text{C}$ than at $125\text{ }^{\circ}\text{C}$.

The phase angle is also estimated at the non-stress-free temperatures (Figure 114). The reference lengths determined in the section V.3, Table 13 are taken for this estimation. It reveals that loading at crack tip is mode II dominated. The phase angle varies between $35\text{ }^{\circ}\text{C}$ and 40 ° during the "smile" loading and is about 52 ° during the "cry" loading at the lowest temperatures. The load conditions at the delamination front and corresponding interfacial toughness found in paragraph V.3 are summarized in Table 17.

Temperature [°C]	125	-40
ERR G [kJ/m ²]	1.4×10^{-4}	4.8×10^{-3}
Phase Angle [°]	35	52
Interfacial Toughness G_C [kJ/m ²]	1.3×10^{-2}	1.2×10^{-1}
G/G_C [%]	1.1	4

Table 17: Smile and Cry Loading in the 2-layer Quad Specimen with a diagonal delamination length of 7.8 mm

During the “smile” loading, the interface is loaded with about 1 % of its admissible loading and 4 % during the “cry” loading. Interfacial fatigue loading induced through CTE mismatch is much lower than the interfacial toughness; it is probably the reason why nearly no crack propagation has occurred during the 2150 cycles.

The energy release rates determined on the specimen diagonal (Figure 112) is given for the five other delamination lengths at -40 °C (Figure 115).

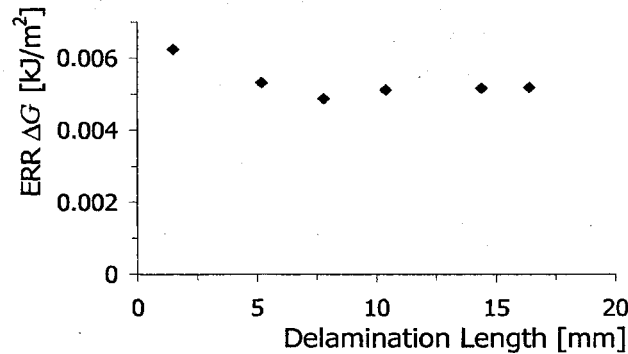


Figure 115: Fatigue Loading in the 2-layer Quad Specimens with respect to the Delamination Length (diagonal)

For all delamination ratios, the maximum ERR is in the same order of magnitude. The trend shows a decrease of the load at the delamination front as the delamination length increases. However it does not describe a large range of ERR, as it is expected to characterize the fatigue behavior of the interface from ΔG tending to zero to ΔG tending to G_C .

VI.1.8 Conclusion

The test process used to assess the life-time of molding compound-copper assemblies considering delamination growth does not produce the expected result.

It was expected that the delamination propagates until a high delamination ratio is reached; in order to determine an experimental curve giving the crack growth rate with respect to the delamination ratio or delamination length a measured on the specimen diagonal:

$$\frac{dA}{dN} = f(a). \tag{eq. VI-1}$$

Then, admitting that the fatigue energy release rate per cycle at the delamination front ΔG varies with the delamination length a , the numerical simulations furnish the relation:

$$\Delta G = g(a, \Delta T). \quad \text{eq. VI-2}$$

Using the experimental and numerical results, a fatigue law for the molding compound-copper interface can be determined:

$$\frac{dA}{dN} = f[g^{-1}(\Delta G)]. \quad \text{eq. VI-3}$$

In a continuous test session over 2150 cycles, the crack growth rate is too low to furnish the experimental function f of eq. VI-1. Moreover, the numerical results show that loading at the crack tip varies sparsely with the delamination length.

This test was also conducted with thermal shocks from 150 °C to -60 °C but did not provide a higher delamination rate.

This specimen appears then to be inappropriate to assess the fatigue strength of the investigated interface. Another specimen geometry, where the induced loading at the crack tip produced by thermal shocks is much higher, could solve this problematic.

This test setup should also be investigated with molding compound having the glass transition temperature above 180 °C. It would provide an increasing CTE mismatch from 180 °C to -40 °C, and consequently, higher interfacial stresses would be induced at -40 °C.

VII. Outlook

Electronic integrated circuits (IC) are required for a very wide range of products in the automotive industry. For example, the constant restriction of allowed CO₂ emissions in Europe, America and now Asia requires engines with electronic controlled fuel injection and ignition systems. Electronic devices play a major role in such applications. In this case, a failure of the electronic directly shuts the vehicle engine down, which is absolutely not conceivable.

Even more critical to consider is the integration of electronic controllers in security systems such as ABS and ESP brake systems, or also airbags, speed control and electrical steering wheels.

The delamination is a significant cause of failure in the electronic. It is driven by harsh environments such as high or low temperatures, rapid temperature variations, vibrations, humidity and hazarding liquids. In particular, temperature variations force incompatible strains at the interface of polymeric encapsulations and other materials they are supposed to protect, leading to the interfacial delamination, the cracking in the encapsulant and finally failure. This phenomenon takes place after a long time, after several duty cycles and is for this reason particularly difficult to predict precisely.

Lifetime assessment requires a precise comprehension of the delamination process and the development of models and methods. Experimental methods are required to characterize the materials. Since the delamination propagated in automotive applications because of temperature loading, a test process permitting to identify the temperature influence on the delamination toughness is required.

Hence the delamination toughness is properly characterized with respect to the mode mixity and temperature, the delamination under thermal cyclic loading must be issued, since it corresponds more to the real component life.

Determining the delamination growth rate as function of the thermal loading is required to identify the Paris or fatigue law governing the fatigue delamination of the interface. Life time of electronic devices can then be assessed using the Paris law determined using specimens.

Fracture mechanics uses non-measurable parameters such as the energy release rate. Those parameters must be determined indirectly through other quantities such as external forces or deformations and using complex calculations. Using finite elements computation is the good way to determine the quantities governing the delamination. For this reason, numerical tools are also required to predict the interfacial crack propagation.

This work focuses on the interfacial delamination between thermosetting polymers and copper. One is used to encapsulate electronic devices; the other constitutes lead frames in ICs.

The theoretical backgrounds required to understand the delamination between dissimilar materials are reviewed in the section II of this work. Different fracture criteria for the

interfacial delamination are presented. Since crack propagation strongly depends on the mixed angle defining the amount of mode I loading and mode II loading (tensile vs. shear loading) at crack tip, different methods are investigated to estimate the mode mixity. Finally, the energy release rate (ERR) estimated by means of the virtual crack closure technique (VCCT) is adopted to characterize the load level at crack tip and an extended version of the oscillatory stress intensity factors is used to determine the mode mixity at crack tip. Since thermosetting polymers are generally linear viscoelastic, backgrounds of linear viscoelasticity are presented.

Features permitting VCCT computations are released with the 2007 version of Abaqus, as this work began. The implementation in Abaqus of the VCCT is widely investigated and verified in the section III of this work. It appears that the contact formulation taken to estimate nodal forces within the VCCT affects the estimation of the energy release rate. Different contact formulations are tested and the one giving the more logical results considering strain perturbations because of the contact formulation (paragraph III.3.1) or comparison with the J-integral and analytical solutions for simple cases (III.3.3) is adopted.

The methods to estimate the mode mixity at not crack tip are not available in Abaqus. The chosen method is programmed as a python script and is always executed as post processing; hence the finite element computation is performed.

To characterize the delamination toughness of the molding compound/copper interface under critical loading, a new specimen and new test set-up is proposed in this work. It permits characterizing the delamination toughness over a wide range of mode mixity, which constitutes an important advantage in comparison with existing test set-ups.

Moreover, the constructed test jig can be used in combination with a conventional tensile machine and with a thermal test chamber. It enables the investigation of the temperature effects on the delamination toughness.

The developed test process is used to characterize the delamination toughness of a standard molding compound with copper. Firstly the mixed mode influence is investigated at room temperature. As expected, this work verified that mode I loading at crack tip is more critical than mode II loading. The interfacial toughness is then characterized at five higher temperatures. At each temperature, the mode II loading remains less critical compared to the mode I. The test series reveals that the adhesion toughness of the molding compound decreases with the temperature, in particular around the glass transition temperature. The load rate effect on the delamination is investigated at constant mixed mode. Three rates are tested at several temperatures. It reveals that the time-temperature superposition principle which governs elastic properties of linear viscoelastic materials can also be applied for the delamination toughness.

A numerical test is then proposed to validate the G_c -Values obtained previously. A modified DCB (double cantilever beam) test is virtually (numerically) performed at room temperature in Abaqus and the delamination propagation is simulated. The same test is parallelly

performed experimentally. Both the numerical and experimental DCB tests provide the crack length with respect to the applied loading with a good agreement.

The interfacial crack propagation can therefore be simulated for any component using finite elements analysis; hence the interface is characterized with the triangle button shear specimen. This process constitutes the first step to investigate the delamination in integrated circuits exposed to heavy thermal loadings.

Finally, delamination under thermal fatigue loading is addressed. A new test process is presented. A bilayer specimen constituted of one layer of thermosetting polymer (molding compound) molded over a thin copper plate is stored in a thermal shock chamber. The specimen is exposed to 150 °C/-40 °C cycles and regularly observed using scanning acoustic microscopy (non-destructive measurement) in order to determine the delamination growth. The delamination rate for the investigated interface under this thermal loading is determined successfully.

However, interfacial crack growth is much slower as expected and the process requires a very long time. The presented specimen geometry requires improvements in order to induce higher loading at crack tip and allows characterizing the crack growth rates for heavier fatigue thermal loadings. This improvement is essential and would permit characterizing the Paris' fatigue law for the investigated interface. Such a fatigue law is the key to assess the lifetime of interfaces in integrated circuits.

The total time required to characterize the interface is another potential improvement of this test set-up. To be transferable in industrial contexts, the triangle button shear test should be performable by a technician within a reasonable time. The experimental dispersion with the triangle button shear specimen is highly sensitive in the preparation, in particular in the crack initiation process. In the case of large experimental dispersion, results may be difficult to analyze and to interpret. For this reason tests must be performed with particular care. Improving the crack initiation process in order to make it easier and faster to perform is an important perspective for the future.

Besides in the field of interfacial fracture mechanics, the estimation of the mode mixity at crack tip is still problematic. As seen in this work, this estimation depends on an interface specific reference length which is undetermined.

In this work, this problem is solved by re-establishing the symmetry of the G_C -curve with respect to the phase angle. However the assumption that the G_C -curve must be symmetric is still questioned in the community. Solving the question of the reference length is essential for the interfacial fracture mechanics.

VIII. Appendix

Appendix A: EMC Material Data

Shift factors with reference temperature of 125 °C:

T [°C]	a_T [log s]
-40	15.54
-35	14.51
-30	14.27
-25	14.00
-20	13.73
-15	13.42
-10	13.15
-5	12.88
0	12.57
5	12.40
10	12.17
15	11.93
20	11.69
25	11.45
30	11.04
35	10.67

40	10.40
45	10.13
50	9.89
55	9.65
60	9.45
65	9.24
70	9.01
75	8.77
80	8.53
85	8.29
90	7.95
95	7.54
100	6.97
105	6.05
110	4.69
115	3.024
120	1.36

125	0.0
130	-1.09
135	-1.97
140	-2.82
145	-3.60
150	4.45
155	-5.20
160	-6.01
165	-6.73
170	-7.41
175	-8.02
180	8.70
185	-9.21
190	-9.65
195	-9.96
200	-10.16

Prony Parameters at 125 °C:

k_i [MPa]	τ_i [log s]
84.94	6
134.88	5
218.92	4
359.29	3
585.55	2
1131.35	1
2188.6	0

2221.75	-1
2622.23	-2
1961.14	-3
2118.11	-4
1418.76	-5
865.86	-6
743.4	-7
570.69	-8

500.4	-9
529.63	-10
563.38	-11
573.65	-12
566.07	-13
592.38	-14
617.46	-15
709.46	-16

Appendix B: Characterization of Heat Transfer Coefficient

- Thermodynamical Analyzis

Heat energy received from an element of volume dV per convection through a surface dS during an elementary time interval dt can be described using

$$\delta^2 Q = d\phi . dt , \quad \text{eq. VIII-1}$$

where $d\phi$ is the elementary heat flow, defined as

$$d\phi = j_{\text{conv}} . dS . \quad \text{eq. VIII-2}$$

The quantity refers to the density of thermal flow, which is defined as

$$j_{\text{conv}} = -h (T_S - T_{\text{air}}) \quad \text{eq. VIII-3}$$

for convection. h is the convection coefficient, T_S is the temperature of the surface element dS and T_{air} the air temperature.

The thermal heat flow per unit of area is consequently given by

$$d\phi = -h(T_S - T_{\text{air}}) . dS , \quad \text{eq. VIII-4}$$

and the total heat flow received by a material body of total surface S is given by

$$\phi = \int_S d\phi = - \int_S h(T_S - T_{\text{air}}) . dS \quad \text{eq. VIII-5}$$

if a uniform coefficient of convection and same surface temperature is admitted over the whole body surface.

Consequently, the total heat energy δQ received by the body of volume V during dt corresponds to

$$\delta Q = \phi . dt = h(T_{\text{air}} - T_S) . dt , \quad \text{eq. VIII-6}$$

whereas T_{air} and T_S are time dependent quantities. h is supposed constant.

The thermodynamical equilibrium of this body of elementary volume dV is considered. The body is supposed to have a homogenous density ρ . The elementary internal energy increase for a body temperature augmentation dT corresponds to

$$d^2 U = \rho c_p dV dT , \quad \text{eq. VIII-7}$$

where C_p is the thermal capacity per unit of volume of the material.

If it is assumed that the material heat conductivity is high enough and the temperature variations are slow enough to keep the body temperature field homogenous in the body, the internal energy variation for the whole body can be expressed as

$$dU = \rho V c_p dT . \quad \text{eq. VIII-8}$$

This can be assumed for small bodies, thin plates or films, since the distance from external surface to body core is small and does not allow significant ΔT between surface temperature and body core.

The first principle of the thermodynamics can then be applied for the body of volume V :

$$\delta W = dU . \quad \text{eq. VIII-9}$$

Combining the first principle of the thermodynamics with the previous expressions, the thermal convection can be related to the derivative of the body temperature T , assumed uniform in the volume:

$$h(t) = - \frac{\rho V c_p}{S} \frac{1}{T(t) - T_{\text{air}}(t)} \frac{dT}{dt}(t). \quad \text{eq. VIII-10}$$

- Determining the Convection Coefficient

The principle is that the convection in the thermal shock chamber can be determined through temperature measurement. Using thin plates, if the air temperature and the temperature inside the plate are monitored along a thermal cycle, the convection coefficient can be estimated through eq. VIII-10.

A series of temperature measurements are performed in the thermal shock chamber using thermocouples embedded in plastic plates of dimensions $180 \times 50 \times 4 \text{ mm}^3$ (Figure 116). The material is an epoxy based encapsulating compound. Thermocouples are also disposed in the chamber in order to measure the air temperature.

The thermal capacity of the plastic material is determined using differential scanning calorimetry (DCS) from $-40 \text{ }^\circ\text{C}$ to $200 \text{ }^\circ\text{C}$, every $30 \text{ }^\circ\text{C}$.

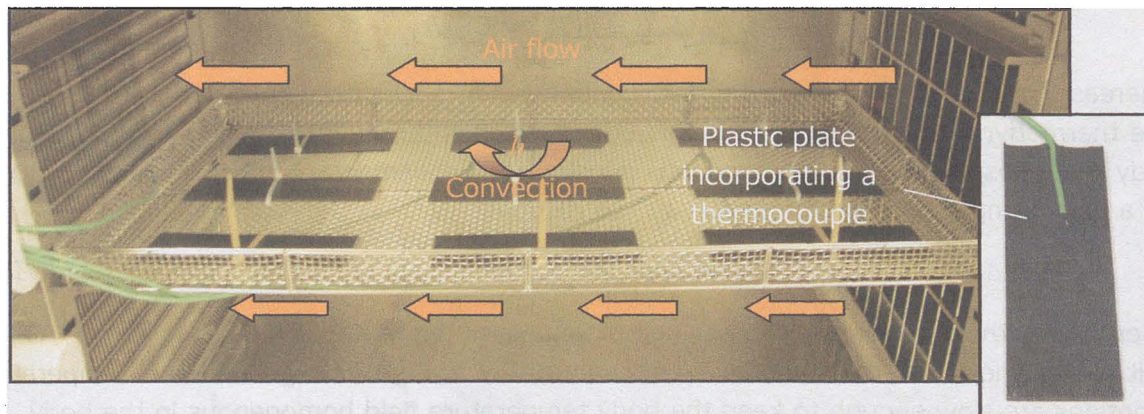


Figure 116: Temperature Measurement in the thermal Shock Chamber

Temperature measurements are performed during the cooling and heating phases. A measurement is reported in Figure 117.a. Measures are performed during 1000 seconds with a sampling time of 2 seconds. To estimate the convection coefficient, eq. VIII-10 is converted in a discrete form as eq. VIII-11:

$$h[N] = -\frac{\rho V c_p}{S t_s} \frac{T[N] - T[N-1]}{T[N] - T_{\text{air}}[N]} \quad \text{eq. VIII-11}$$

Since the first seconds of the cooling phase exhibits strong variations in a short time, the sampling time of 2 seconds does not allow a good estimation of the derivative. The convection coefficient is consequently not estimated from 60 °C to 150 °C.

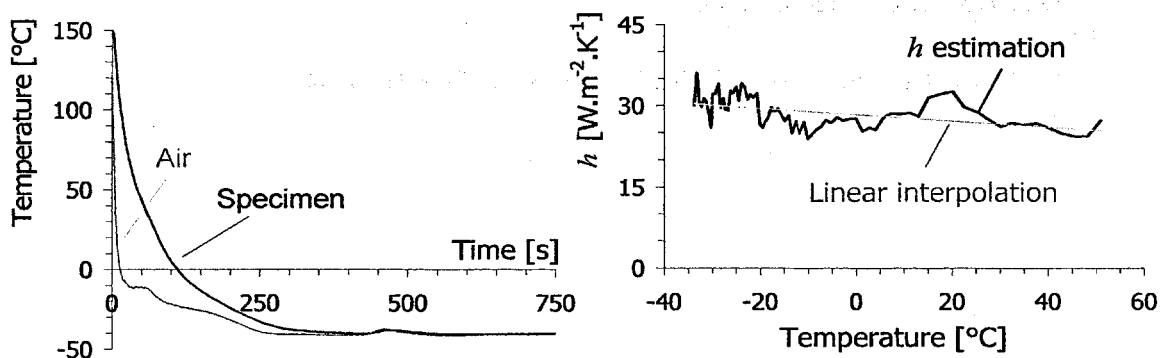


Figure 117: a. Temperature Measures for a cooling Phase
b. Estimated Convection Coefficient during the cooling Phase

The obtained results are displayed in Figure 117.b. the obtained results are noisy because of the limited accuracy of the measurement device. The curve is linear interpolated using the mean squares method. A fix value of $30 \text{ W.m}^{-2}.\text{K}^{-1}$ is assumed in the thermal shock chamber during the cooling phase, from 150 °C to -40 °C.

The same procedure is applied to determine the convection coefficient during the heating phase. As displayed in Figure 116, the convection coefficient is determined on 9 different positions in the chamber.

Appendix C: Abaqus Keywords to define the Interfacial Toughness

***** ABAQUS INTERFACIAL TOUGHNESS DEFINITION

**

*DEBOND, slave=slave_surface, master=master_surface

*FRACTURE CRITERION, type=VCCT, mixed mode behavior=BK

1.7e-2, 1.9e-1, 0.0, 7.50, 20.0

8.6e-3, 7.5e-2, 0.0, 5.60, 100.0

6.5e-3, 4.5e-2, 0.0, 9.50, 130.0

4.7e-3, 2.4e-2, 0.0, 9.90, 150.0

1.7e-3, 7.8e-3, 0.0, 13.5, 200.0

**

***** END OF THE INTERFACIAL TOUGHNESS DEFINITION

Other Communication from the Author

5th International Conference On Fracture Of Polymers, Composites And Adhesives. 5th ESIS TC4 CONFERENCE. 7-11 September 2008, Les Diablerets, Switzerland.

On the Development of a modified Button Shear Specimen to characterize the mixed mode Delamination Toughness. Engineering Fracture Mechanics, Elsevier (in reviewing).

References

- [Abaqus 1] Abaqus 6.8 Documentation, Abaqus Theory Manual/Elements/Continuum Elements/Solid isoperimetric quadrilaterals and hexahedra
- [Abaqus 2] Abaqus 6.8 Documentation, Abaqus Analysis User's Manual, Part IX, Chapter 30.2.2 Contact formulations in Abaqus
- [Abaqus 3] Abaqus 6.8 Documentation, Abaqus Theory Manual, 5 Interface modeling, 5.1.1 and 5.1.2 Contact modeling
- [Abaqus 4] Abaqus 6.8 Documentation, Abaqus Analysis User's Manual, Part IV, Chapter 11, 11.4.3. Crack Propagation Analysis
- [Abaqus 5] Abaqus 6.8 Documentation, Abaqus Analysis User's Manual, Part V, Chapter 18, 18.7. Viscoelasticity
- [Abaqus 6] Abaqus 6.8 Documentation, Abaqus User Subroutines Reference Manual, 1.1.46. UTRS
- [Agrawal 2006] A. Agrawal, A.M. Karlson, *Obtaining mode mixity for a bimaterial interface crack using the virtual crack closure technique*. International Journal of Fracture, vol. 141, pp. 75-98, 2006
- [Agrawal 2007] A. Agrawal, A.M. Karlson, *On the Reference Length and Mode Mixity for a Bimaterial Interface*. Transaction of the ASME, Journal of Engin. Mat. And Tech., vol. 129, pp. 580-587, 2007
- [Andresen 2005] H.W. Andresen, A.T. Echtermeyer, *Critical Energy Release Rate for a CSM reinforced Carbon Fibre Composite/Steel bonding*. In Composites, Part A: applied science and manufacturing, Elsevier, 2005
- [ASTM E399-90] ASTM Standard E399-90, Standard Test Methods for Plane-Strain Fracture Toughness of Metallic Materials, 1997

- [Benzeggagh 1996] M.L. Benzeggagh, M. Kenane, *Measurement of Mixed-Mode Delamination Fracture Toughness of Unidirectional Glass/Epoxy Composites with Mixed-Mode Bending Apparatus*. Composites Science and Technology, vol. 56, pp. 439-449, 1996
- [Beuth 1996] Jack L. Beuth, *Separation of crack extension modes in orthotropic delamination models*. International Journal of Fracture, vol. 77, pp. 305-321, 1996
- [Böger 2001] T. Böger, K. Dilger, G. Schmöller, *FE-Simulation der Klebstoff-Schwindung während des Aushärtevorgangs*. Sonderdruck aus Adhäsion Kleben und Dichten, vol. 10.01, 2001
- [Charalamb. 1989] P.G. Charalambides, J. Lund, A.G. Evans, R.M. McMeeking, *A Test Specimen for Determining the Fracture Resistance of Bimaterial Interfaces*. Journal of Applied Mechanics, vol. 56, pp. 77-82, 1989
- [Cherepanov 1962] G.P. Cherepanov, *The Stress State in a heterogeneous Plate with slits*. Izvestia AN SSSR, OTN, Mekhan. i Mashin. 1, pp. 131-137, 1962
- [Cherepanov 1979] G.P. Cherepanov, *Mechanics of Brittle Materials*. McGraw-Hill, New York, 1979
- [Chen 2005] X. Chen, S. Zhao, *Moisture Absorption and Diffusion Characterization of Molding Compound*. Journal of Electronic Packaging, vol. 127, pp. 460-465, 2005
- [Dreßler 2007] M. Dreßler, K.F. Becker, B. Wunderle, J. Auersperg and H. Reichl, *Application of Interfacial Fracture Mechanics Approach for Obtaining Design Rules for Flip Chip Interconnections*. 1st Internat. Congress Microreliability and Nanoreliability in Key Technology Applications, Berlin, 2007
- [Dudek 2002] R. Dudek, H. Walter, B. Michel, *Studies on Moisture Diffusion and Popcorn Cracking*, IEEE proc. 3rd EuroSime, pp. 225-232, 2002
- [Dugdale 1960] D. Dugdale, *Yielding of Steel Sheets containing slits*. Journal of the Mechanics and Physics of Solids, vol. 8, pp. 100-108, 1960
- [Dundurs 1969] J. Dundurs, *Edge-Bonded Dissimilar Orthogonal Elastic Wedges*. Journal of Applied Mechanics, vol. 36, pp. 650-652, 1969
- [England 1965] A.H. England, *A Crack Between Dissimilar Media*. Journal of Applied Mechanics, vol. 32, pp. 400-402, 1965

- [Erdogan 1963] F. Erdogan, *Stress Distribution in a Nonhomogeneous Elastic Plane with Cracks*. Journal of Applied Mechanics, vol. 30, pp. 232-237, 1963
- [Erdogan 1965] F. Erdogan, *Stress Distribution in Bonded Dissimilar Materials with Cracks*. Journal of Applied Mechanics, vol. 32, pp. 403-410, 1965
- [Ferguson 2005] T. Ferguson and J. Qu, *Elastic Modulus Variation due to Moisture Absorption and Permanent Changes Upon Redrying in a Epoxy Based Underfill*, IEEE Trans. Comp. Package. Technologie, 2005
- [Griffith 1921] A.A. Griffith, *The Phenomena of Rupture and Flow in Solids*. Philosophical Transactions of the Royal Society London, A 221, pp. 163-197, 1921
- [Hu 2006] G. Hu, A.A.O. Tay, Y. Zhang, W. Zhu, S. Chew, *Characterization of Viscoelastic Behavior of a Molding Compound with Application to Delamination Analysis in IC Packages*. Electronics Packaging Technology Conference, IEEE, 2006
- [Hu 2007] G. Hu, A.A.O. Tay, Y. Zhang, S. Chew, *Experimental and Numerical Study of the Effect of Viscoelasticity on Delamination in a Plastic IC Package*. Electronic Components and Technology Conference, IEEE, 2007
- [Hutchinson 1987] J.W. Hutchinson, M.E. Mear, J.R. Rice, *Crack Paralleling an Interface Between Dissimilar Materials*. Journal of Applied Mechanics, vol. 54, pp. 828-832, 1987
- [Hutchinson 1992] J.W. Hutchinson, Z. Suo, *Mixed Mode Cracking in Layered Materials*, Advances in Applied Mechanics, vol. 29, pp. 63-191, 1992
- [Jansen 2007] K. Jansen, *Thermomechanical Modeling and Characterization of Polymers*. Faculty 3mE, Mechanical Engineering, TU Delft, 2007
- [Kaninen 1985] M.F. Kanninen, C.H. Popelar, *Advanced Fracture Mechanics*, Oxford University Press, New York, 1985
- [Karlson 2008] A.M. Karlson, *Closure to "Discussion: 'On the Reference Length and Mode Mixity for a Bimaterial Interface'"*. J. Eng. Mater. Techno., vol. 130, 04502, 2008
- [Kim 2000] J-K. Kim, M. Leabbai, J.H. Liu, J.H. Kim, M.M.F. Yuen, *Interface Adhesion Between Copper Lead frame and Epoxy Molding Compound:*

- Effects of Surface Finish, Oxidation and Dimples*. Electronic Components and Technology Conference, IEEE, 2000
- [Kinloch 1987] A.J. Kinloch, *Adhesion and Adhesives*. Chapman and Hall ed., 1987
- [Krueger 2002] R. Krueger, *The Virtual Crack Closure Technique: History, Approach and Applications*. NASA/CR-2002-211628, ICASE Report No. 2002-10, 2002
- [Lam 2000] W.K. Lam, T.S. Yeung, A. Teng, M.M.F. Yuen, *A Method for Evaluating Delamination between Epoxy Moulding Compounds and Different Plated Leadframes*. International Symposium on Electronic Materials & Packaging, IEEE, 2000
- [Lemaitre 2007] J. Lemaitre, R. Desmorat, *Engineering Damage Mechanics – Ductile, Creep, Fatigue and Brittle Failures*. Springer Verlag, 2007
- [Liu 2002] W. Liu, F.G. Shi, *Effect of the Viscoelastic Behavior of Molding Compounds on Crack Propagation in IC Packages*. Electronic Components and Technology Conference, IEEE, 2002.
- [Luo 2000] S. Luo, M. Vidal, C.P. Wong, *Study on Surface Tension and Adhesion in Electronics Packaging*. Electronic Components and Technology Conference, IEEE, 2000
- [Malyshev 1965] B.M. Malyshev and R.L. Salganik, *The Strength of Adhesive Joints using the Theory of Cracks*. International Journal of Fracture, vol. 1, pp. 114-128, 1965
- [Mantič 2008] V. Mantič, *Discussion: "On the Reference Length and Mode Mixity for a Bimaterial Interface"*. J. Eng. Mater. Techno., vol. 130, 04501, 2008
- [Merrill 2004] C.C. Merrill, P.S. Ho, *Effect of Mode-Mixity and Porosity on Interfacial Fracture of Low-k Dielectrics*. Materials Research Society Symposia Proceeding, vol. 812, pp. 61-66, 2004
- [Muskhelishvili 1953] N.I. Muskhelishvili, *Some Basic Problems of the Mathematical Theory of Elasticity*. English Translation, P. Noordhoff and Company, New York, 1953
- [Nishimura 1992] A. Nishimura, I. Hirose and N. Tanaka, *A new test methods for measuring Adhesion Strength of IC Molding compounds*, Journal of electronic packaging, vol. 114, pp. 605-616, 1992

- [Reeder 1990] J.R. Reeder, J.H. Crews, *Mixed Mode Bending Method for Delamination Testing*, AIAA Journal, vol. 28, No. 7, pp. 1270-1276, 1990
- [Reeder 2002] J. Reeder et al., *Postbuckling and growth of delaminations in composite plates subjected to axial compression*. 43rd AIAA/ASME/ASCE/AHS/ASC Structures, Structural Dynamics and Materials Conference, Denver, Colorado, vol. 1746, p. 10, 2002
- [Rice 1965] J.R. Rice, G.C. Sih, *Plane Problems of Cracks in dissimilar media*. *Journal of Applied Mechanics*, vol. 32, pp. 418-423, 1965
- [Rice 1968a] J.R. Rice, *A path independent integral and the approximate analysis of strain concentration by notches and cracks*. *Journal of Applied Mechanics*, vol. 35, pp. 379-386, 1968
- [Rice 1968b] J.R. Rice, *Mathematical Analysis in the Mechanics of Fracture*. In *Fracture: An Advanced Treatise*, H. Liebowitz ed., vol. 2, pp. 191-311, 1968
- [Rice 1988] J.R. Rice, *Elastic Fracture Mechanics Concepts for Interfacial Cracks*. *Transaction of the ASME, Journal of Applied Mechanics*, vol. 55, pp. 98-103, 1988
- [Roger 2007] J. Roger, *On the investigation of experimental and numerical methods to characterize the fracture behaviour of epoxy resins: an approach to prevent failure in electronic component*. PhD thesis, University of Valenciennes, 2007
- [Rybicki 1977] E.F. Rybicky, M.F. Kanninen, *A Finite Element Calculation of Stress Intensity Factors by a modified Crack Closure Integral*. Pergamon Press, *Engineering Fracture Mechanics*, vol. 9, pp. 931-938, 1977
- [Schapery 1981] R.A. Schapery, *On viscoelastic Deformation and Failure Behavior of composite Materials with distributed Flaws*. *Advances in Aerospace Structures and Materials*, Winter Annual Meeting of the ASME, 1981
- [Schwarzl 1990] F.R. Schwarzl, *Polymermechanik – Struktur und mechanisches Verhalten von Polymeren, Lineares visko-elastisches Deformationsverhalten der Polymere*. Springer-Verlag, Berlin Heidelberg, 1990

- [Shen 1976] C.H. Shen, G.S. Springer, *Moisture Absorption and Desorption of Composite Materials*. J. of Composite Materials, vol. 10, No. 2, pp. 2-20, 1976
- [Shih 1991] C.F. Shih, *Cracks on bimaterial interfaces: elasticity and plasticity aspects*. Material Science and engineering, A143, pp. 77-90, 1991
- [Shirangui 2008] H. Shirangui, J. Auersperg, M. Koyuncu, H. Walter, W.H. Mller, B. Michel, *Characterization of Dual-Stage Moisture Diffusion, Residual Moisture Content and Hygroscopic Swelling of Epoxy Molding Compounds*, 9th. Int. Conf. on Thermal, Mechanical and Multiphysics Simulation and Experiments in Micro-Electronics and Micro-Systems, EuroSimE, 2008
- [Strobl 1996] G. Strobl, *The Physics of Polymers, Mechanical and Dielectric Response*. Springer-Verlag, Berlin Heidelberg, 1996
- [Sun 1987] C.T. Sun, C.J. Jih, *On Strain Energy Release Rate for Interfacial Cracks in Bimaterial Media*. Engineering Fracture Mechanics, vol. 28, pp. 13-20, 1987
- [Sun 1997] C.T. Sun, W. Qian, *The Use of Finite Extension Strain Energy Release Rates in Fracture of Interfacial Cracks*. International Journal of Solids and Structures, vol. 34, No. 20, pp. 2595-2609, 1997
- [Suo 1990] Z. Suo, J.W. Hutchinson, *Interface Crack between Two Elastic Layers*. International Journal of Fracture, vol. 43, pp. 1-18, 1990
- [Szeto 2000] W.K. Szeto, M.Y. Xie, J.K. Kim, M.M.F. Yuen, P. Tong, S. Yi, *Interface Failure Criterion of Button Shear Test as a Means of Interface Adhesion Measurement in Plastic Packages*. International Symposium on Electronic Materials & Packaging, IEEE, 2000
- [Tay 1999] A.A.O. Tay, Y.Y. Ma, S.H. Ong, T. Nakamura, *Measurement of interface toughness as a function of temperature, moisture concentration and mode mixity*, EEP-Vol. 26-2, Advances in Electronic Packaging, ASME 1999
- [Tay 2003] A.A.O. Tay, J.S. Phang, E.H. Wong, R. Ranjan, *A Modified Button-Shear Method for Measuring Fracture Toughness of Polymer-Metal Interfaces in IC Packages*. Electronic Components and Technology Conference, IEEE, 2003

- [Teverovsky 2002] A. Teverovsky, *A rapid Technique for Moisture Diffusion Characterization of Molding Compounds in PEM*, NASA Technical Report, 2002
- [The 2005] L.K. The, E. Anto, C. Wong, G. Mhaisalkar and E.H. Wong, *Moisture-induced Failures of Adhesive Flip Chip Interconnects*, IEEE Trans. Comp. Package. Technol., 2005
- [Wang 1990] J.-S. Wang, Z. Suo, *Experimental Determination of Interfacial Toughness Curves using Brazil-Nut-Sandwiches*. Acta Metallurgica et Materialia, vol. 38, No. 7, pp. 1279-1290, 1990
- [Williams 1959] M.L. Williams, *The stress around a fault or crack in dissimilar media*. Bulletin of the Seismological Society, Am. 49, pp. 199-204, 1959
- [Wittler 2004] O. Wittler, *Bruchmechanische Analyse von viskoelastischen Werkstoffen in elektronischen Bauteilen*. Fakultät Elektrotechnik und Informatik, Technical University of Berlin, 2004
- [Wu 1965] E.M. Wu and R.C. Reuter Jr., *Crack extension in fiberglass reinforced plastics*, T and M Report, University of Illinois, vol. 275, 1965
- [Wunderle 2003] B. Wunderle, *Thermo-Mechanical Reliability of Flip-Chip Assemblies with Heat-spreaders*, PhD Work, Fakultät Elektrotechnik und Informatik, Technical University of Berlin, , 2003
- [Xiong 2000] Z. Xiong and A.A.O. Tay, *Modeling of Viscoelastic Effects on Interfacial Delamination in IC Packages*. Electronic Components and Technology Conference, IEEE, 2000
- [Yeung 2000] D.T.S. Yeung, D.C.C. Lam, M.M.F. Yuen, *Interfacial Fracture Properties Measurement in Electronic Packages*. Journal of Electronic Packaging, vol. 122, pp. 67-72, 2000
- [Zhu 2005] W.H. Zhu, S. Ang, L. Gan, *Moisture effect on fracture strength of molding compounds for electronic packaging in a wide temperature range*, Proceeding of Assembly and Interconnect Technologie, pp. 1533-1537, 2005

Bibliothèque Universitaire de Valenciennes



00900762